TUM

TECHNISCHE UNIVERSITÄT MÜNCHEN

TUM School of Engineering and Design

Output-Only Aeroelastic Analysis of Helicopters in Atmospheric Turbulence

Willem Rex

Vollständiger Abdruck der von der <u>TUM School of Engineering and Design</u> der Technischen Universität München zur Erlangung des akademischen Grades eines Doktors <u>der Ingenieurwissenschaften (Dr.-Ing.)</u> genehmigten Dissertation.

Vorsitz: Prof. Dr. Klaus Bengler

Prüfende der Dissertation: 1. Prof. Dr.-Ing. Manfred Hajek

2. Prof. Dr. Carlo L. Bottasso

Die Dissertation wurde am <u>14.06.2021</u> bei der Technischen Universität München eingereicht und durch die <u>Fakultät für Maschinenwesen am 28.09.2021</u> angenommen.

Abstract

Aircraft testing is key for certification and the verification of models and assumptions inherently related with the aircraft's design. However, the in-flight quantification of properties like aeroelastic phenomena can be associated with considerable challenges, since deterministic testing is often beyond the technical limitations. This includes non-measurable inputs and insufficient excitation. A promising alternative is to exploit stochastic perturbations of the system during regular operation. Suitable approaches like Operation Modal Analysis and Blind Source Separation allow to compute eigenmodes from the stochastic structural response only. Based on simulations, this work demonstrates that atmospheric turbulence provides an adequate excitation of the elastic helicopter structure to enable in-flight output-only modal analysis. However, the identification of rotor modes in vicinity of the main-rotor blade-passing frequency is almost impossible, presumably due to the high main-rotor aerodynamic damping, which is supported by literature. This becomes relevant for the identification of airframe modes if the airframe's impedance at the main-rotor interface is comparably low. In this case, the helicopter tail-section subject to atmospheric turbulence is an important enabler of output-only helicopter modal analysis.

Acknowledgments

Contents

Contents

Abbreviations and Symbols

Acronyms

1/rev	Once-Per-Revolution
ALS	Alternating Least-Squares
ARMA	Autoregressive-Moving-Average
BE	Blade Element
BPF	Blade-Passing Frequency
BSS	Blind Source Separation
CETI	Control Equivalent Turbulence Input
CFD	Computational Fluid Dynamics
CLT	Central Limit Theorem
CMIF	Complex Mode Indication Function
CP	Complexity Pursuit
DAMVIBS	Design Analysis Methods for Vibrations
DFT	Discrete FOURIER-Transformation
DIC	Digital Image Correlation
DMD	Dynamic Mode Decomposition
DNS	Direct Numerical Simulation
DOF	Degrees of Freedom
DOR	Direction of Rotation
EMA	Experimental Modal Analysis
ERA	Eigensystem Realization Algorithm
FDD	Frequency Domain Decompositon
FullFT	Full-Field Turbulence
GVT	Ground Vibration Testing
HS	Horizontal Stabilizer
HubDT	Hub-Based DRYDEN Turbulence

Acronyms

IBC	Individual Blade Control
ICA	Independent Component Analysis
ITD	Ibrahim Time Domain
LD	Logarithmic Decrement
LES	Large Eddy Simulation
LSCE	Least-Squares Complex Exponential
LSCF	Least-Squares Complex Frequency
LTI	Linear Time Invariant
LTP	Linear Time Periodic
MAC	Modal Assurance Criterion
MAM	Mode Acceleration Method
METS	Mixer Equivalent Turbulence Simulation
mis	Mismatch
MLE	Maximum Likelihood Estimator
MR	Main-Rotor
MRC	Mode Rejection Criterion
MTN	Modal Transfer Norm
NExT	Natural Excitation Technique
NFAC	National Full-scale Aerodynamics Complex
NREL	National Renewable Energy Laboratory
OMA	Operational Modal Analysis
PCA	Principal Component Analysis
PDF	Probability Density Function
PEM	Parametric Time-Domain Method
PM	Pencil Method
POD	Proper Orthogonal Decomposition
PP	Peak Picking
PSD	Power Spectral Density
RANS	Reynolds-averaged Navier-Stokes
RBM	Rigid Body Mode
RMS	Root-Mean-Square
SDG	Statistical Discrete Gust
SEM	Synthetic Eddy Method
SOBI	Second-Order Blind Identification
SORBET	Simulation of Rotor Blade Element Turbulence
SSI	Stochastic Subspace Identification
SVD	Singular Value Decomposition
tot	Total

TR	Tail-Rotor
VAWT	Vertical Axis Wind-Turbine
VS	Vertical Stabilizer

List of symbols

C_P	Dimensionless power, $C_P = \frac{P}{\rho S(\Omega R)^3}$
C_P/σ	Power coefficient
C_T	Dimensionless thrust, $C_T = \frac{T}{\rho S(\Omega R)^2}$
C_T/σ	Blade-loading
E	Energy
J	Jacobi-Matrix
K	Number of harmonics
N_b	Number of rotor-blades
P	Power
R	Rotor radius
S	Area
T	Time period
T	Thrust
V	Velocity
X	Aerodynamic force
Ω	Spatial frequency
Ω_{MR}	Main-rotor speed
Ψ_k	Eigenvector of mode k of the time-continuous system
Θ	Helicopter pitch-attitude
α	Angle of attack
χ	Downwash skew-angle
η_{decay}	Decay-threshold
$\hat{\Psi}_k$	Eigenvector of mode k of the time-discrete system
$\hat{\lambda}_k$	Eigenvalue of mode k of the time-discrete system
$\hat{a}$	Perturbation magnitude
λ_k	Eigenvalue of mode k of the time-continuous system
$\mathbf{A}$	System matrix
$\mathbf{B}$	System matrix
$\mathbf{C}$	System matrix
$\mathbf{D}$	System matrix
$\mathbf{F}$	Force vector
$\mathbf{G}$	Gyroscopic matrix
$\mathbf{K}$	Stiffness matrix
$\mathbf{M}$	Mass matrix
$\mathbf{Q}$	Mixing matrix
$\mathbf{\Phi}$	Power Spectral Density
$\mathbf{\Psi}$	Modal matrix

List of symbols

f	Vector-valued function
q	Vector of generalized/modal coordinates
r	Position vector
s	Vector of sources
u	Vector of control inputs
v	Velocity vector
v	Measurement noise vector
$\mathbf{v}_t$	Vector of translational turbulence components
w	External noise vector
x	State vector
y	Measurements
μ	Advancing ratio, $\mu = \frac{V}{\Omega R}$
ω	Temporal frequency
$\omega_{0,k}$	Eigenfrequency of mode k of the undamped system
ϕ	Vector of rotational turbulence components
ψ	Phase-angle/azimuth
ρ	Air density
σ	Standard deviation
σ	Solidity, $\sigma = \frac{N_b c}{\pi R}$
θ	Azimuthal coordinate
ξ	Relative damping
c	Chord length
e	Error
g	Gain factor
i	Counter variable
j	Counter variable
k	Counter variable
l	Counter variable
m_k	Modal mass of mode k
n	Counter variable
q	Generalized/modal coordinate
r	Radial coordinate
t	Time
u	Length of a circle segment
v	Velocity component
v_i	Induced velocity
w	Vertical velocity component
x	Cartesian coordinate
y	Cartesian coordinate
z	Cartesian coordinate

List of Figures

List of Tables

1. Introduction and Motivation

The model extraction from test-data is an established method in rotorcraft engineering, like Ground Vibration Testing (GVT) or System Identification [135, 114]. These techniques are typically based on quantified inputs and outputs, however, in some cases the input loads leading to critical phenomena are inaccessible and remain unknown [115, 192]. This can e.g. be due to highly complex phenomena like air-resonance and flutter or distributed loads which cannot be measured properly. In addition, these phenomena cannot be reproduced via deterministic ground testing in general, since environmental aspects and boundary conditions can have a fundamental influence on the dynamics [202, 237]. However, by taking advantage of ambient loads naturally acting on the system during regular operation, output-only modal analysis techniques are designed to solve for the system's dynamics without involving knowledge about the inputs.

In this context, the in-flight output-only testing of aircraft based on vibrations induced by atmospheric turbulence is a well-known approach [192]. However, the modal analysis of helicopters operating in atmospheric turbulence is associated with particular challenges, since fundamental assumptions usually involved in output-only modal analysis approaches are violated. These algorithms typically assume GAUSSIAN white noise input, whereas atmospheric turbulence is not GAUSSIAN in general [155] and the turbulence spectrum is shaped according to KOLMOGOROV's law [78]. Another aspect is that the rotor revolution introduces both cyclostationary effects, resulting in a frequency shift of energy [61, 98] and specific periodic loads that distort the statistical properties [111]. In addition, the rotor involves intrinsic periodicity [87, 235] which is in general not in agreement with the typically involved assumption that the dynamics can be characterized by a Linear Time Invariant (LTI) system.

Based on simulations, this work investigates how atmospheric turbulence can be utilized as a suitable natural excitation for computing aeroelastic modes of airborne helicopters including coupled rotor-airframe phenomena. Therefor, an appropriate modal analysis procedure is developed, evaluated and demonstrated. Both Operational Modal Analysis (OMA) approaches as well as Blind Source Separation (BSS) techniques are employed for aeroelastic helicopter modal analysis. In this context, the coupled rotor-airframe dynamics are analyzed based on the results obtained from output-only modal analysis. Note that even simulations conducted in this work do not provide access to the input forces resulting from atmospheric turbulence, due to the non-linear and distributed airload models.

1.1. Influence of Atmospheric Turbulence on Helicopter Vibrations and Related Work

Helicopter vibrations are a result of different interacting phenomena, see Ref. [294]. Multiple sources and mechanisms of airframe vibrations exist, among which rotor airloads, aerodynamic forces acting on the airframe, drive system dynamics and engine vibrations are the most relevant contributors, see Refs. [291, 42, 105]. Although the vibrations are highly specific depending on the configuration, they can be classified into broadband vibrations and discrete harmonics in general. The main contributor to discrete harmonics is the Main-Rotor (MR), introducing vibrations predominantly at MR-Blade-Passing Frequency (BPF) and integer multiples, especially in high-speed flight through asymmetric flow conditions and low speed flight through rotor wake interaction, see Ref. [70]. Vibrations in hover conditions are comparably low, since the rotors experience less periodic variation of aerodynamic loads, see Ref. [291]. A thorough review on helicopter aeroelasticity and about its complexity is provided in Ref. [88].

Airloads varying over the MR azimuth and cyclic control input are extrinsic sources of periodicity. Another source for helicopter periodicity is the intrinsic parametric variation of the system. This stems from periodically varying structural properties of the rotor system e.g. due to centrifugal stiffening through blade flap and lead-lag motion as well as azimuthal variation of the control linkage support. At this point it is mentioned that different approaches exist to handle intrinsic periodicity explicitly. One approach is FLOQUET theory, see Refs. [87, 102] and another is the HILL approach, see e.g. Ref. [66]. The former one is based on computing a so called transition matrix via e.g. single-pass [89, 87] or N-pass [235] scheme, while the latter one transforms the Linear Time Periodic (LTP) system into a LTI formulation. In both cases, a stability analysis is conducted based on eigenvalue decomposition. However, compared to FLOQUET theory, the HILL approach requires to know the linearized system equations, see Ref. [235].

In general, vibration levels of modern helicopters are still high, although manufacturers are trying to tailor them more acceptable since decades [206, 284, 86]. In this context, one widely stated aim in the helicopter industry is to achieve jet-smooth-ride conditions which correspond to cabin acceleration levels below 0.05g in vertical direction, which has still today not been achieved [284, 65, 35]. In general, helicopter vibrations lead to discomfort, mental and structural fatigue, etc. [106]. At the same time it is still challenging to predict them sufficiently [291, 316, 70].

To reduce the vibrations regular maintenance procedures comprise rotor track&balance corrections by means of trim tabs, tuning masses, pitchlink length, etc. [152]. After the first flight of a prototype undesirable BPF vibrations are often encountered using additional passive and active systems [206, 167], whereas active systems are more effective than passive systems in general [42]. Active systems include Individual Blade Control (IBC) [210, 315], distributed force generators [65, 200], trailing-edge flaps [74], helicopter re-trim procedures [106], variable rotor-speed devices [40, 196], etc.. A detailed survey on helicopter specific vibration mitigation systems is provided in Ref. [6].

1. Introduction and Motivation

The integration of both passive and active devices is expensive, time-consuming and can create new problems [254]. However, as soon as the rotor-harmonics are successfully mitigated, broadband, aperiodic and random vibrations remain, which can still carry a significant amount of energy [252]. These components may not be effectively reducible by additional mitigation devices [80]. One important source for broadband vibrations is atmospheric turbulence, which is a driver for discomfort [252, 142], structural fatigue [116, 169] and increasing pilot workload [138, 151].

A handling quality analysis conducted in Ref. [150] reveals that the MR experiencing turbulence influences predominantly heave- and roll-motion control. Furthermore, turbulence excitation of the airframe is found to have a most dominant effect on pitch-motion control and the yaw-motion control is predominantly affected by the Tail-Rotor (TR) experiencing atmospheric turbulence. Hence, both rotors and the airframe are contributors to degraded handling qualities in atmospheric turbulence estimated by simulation. Ref. [67] states that a high flapping-hinge offset has better gust response in terms of controllability. At the same time, stabilizing effects of helicopters operating in atmospheric turbulence were found in previous studies, like an increase in aerodynamic damping [248, 247]. The flapping response of an isolated helicopter rotor-blade experiencing atmospheric turbulence is studied in Ref. [91]. The authors conclude that isolated flapping motion's stability is approximately unaffected by atmospheric turbulence. In Refs. [247, 188] low effects of in-plane turbulence components were detected, whereas the vertical turbulence component has most influential effect on the flap-lag motion.

The coupled flap-torsion stability of an isolated rotor-blade operating in atmospheric turbulence was investigated by several authors in the past. In Ref. [91] it is concluded that the stability of coupled flap-torsion motion of a rotor-blade operating in forward flight is significantly reduced by atmospheric turbulence. In Ref. [90] the authors conclude that turbulence induced vibrations measured by the Root-Mean-Square (RMS) value in trimmed rotor operation with suppressed Once-Per-Revolution (1/rev) flapping motion are of comparable magnitude as oscillations of twice the BPF in absence of atmospheric turbulence. The Lock-number is discovered to have particular influence on both blade-flap and blade-torsion response in presence of turbulence, see Ref. [90]. Ref. [26] summarizes that helicopter's sensitivity towards atmospheric turbulence increases with decreasing C_T/σ and is higher compared to fixed-wing due to lower disk-loading. Hence, disc-loading is concluded to be an important design driver for helicopter turbulence response. In addition, structural loads are found to be dominated by maneuver loads rather than turbulence loads [26]. By running linear coupled elastic rotor-airframe simulations, Ref. [80] concludes that turbulence is not relevant in the context of fatigue, since the RMS value of the blade-motion is approximately one order of magnitude below the amplitude of the BPF. In high-μ conditions, Refs. [103, 97] conclude that non-uniformity of atmospheric turbulence is negligible and Refs. [101, 94] conclude that the rotor-flapping response to atmospheric turbulence has narrow-band characteristic.

1.2. State of the Art Output-Only Modal Analysis in Structural Dynamics

In extension to the results summarized in the previous section 1.1, modal analysis provides an additional understanding of dominant underlying phenomena characterizing the helicopter's aeroelastic response to atmospheric turbulence. As long as the helicopter is operating close enough to a periodic reference orbit, linear approximation is reasonable to quantify the phenomena acting in the fundamentally nonlinear helicopter system [35, 88]. For linear systems, methods to characterize dynamic modes and to assess the system's stability are well-established. Typical helicopter aeroelastic modes and possible instabilities can generally be divided into phenomena only involving the rotor and phenomena resulting from rotor-airframe coupling [175]. The first category includes e.g. pitch-flap-lag instabilities. The second category includes e.g. ground-resonance, air-resonance and rotor whirl-flutter.

Depending on experimental limitations and limitations related to the capability to linearize the simulation model, modal approximation is in general not a straight-forward task. As a workaround Ref. [35] suggests to employ numerical treatment in the time-domain to resolve the nonlinear phenomena in a first step. In a second step, the system is analyzed towards the underlying phenomena. In this context the system's stability can be assesses via damping computation using e.g. Circle-Fit [135], PRONY method [145], Logarithmic Decrement (LD), Moving-Block approach, Randomdec [302, 59, 115, 141], Half-Power Bandwidth method, Pencil Method (PM), Eigensystem Realization Algorithm (ERA), Ibrahim Time Domain (ITD) method, etc. [35, 117]. Once the relevant phenomena are understood, Ref. [35] further suggests to establish a simplified model which allows linear treatment and enables a detailed stability analysis. However, finding a representative linear model can be a cumbersome task. Noteworthy, the approach used in this work follows the same logic but bypasses the difficulties of the second step by obtaining the linear model directly from the response obtained in the first step. In this work, the solution during the first step is computed using MONTE CARLO simulation.

The linear model is identified using two different modal analysis approaches in the scope of this work. The first approach is termed OMA, the second BSS. OMA techniques are an extension to the classical input-output modal analysis towards the case where no input data is available, whereas BSS techniques realize a de-mixing of underlying modes. Both approaches are mathematically related [17, 15]. In addition, both approaches are unable to recover a full model since modal masses or the absolute scaling of the eigenvectors respectively, cannot be computed [264, 273]. However, both approaches recover eigenfrequencies, modal damping ratios as well as unscaled eigenvectors of the system. Since a vast amount of different algorithms exists for both OMA and BSS techniques, only the most important algorithms and related references are reviewed in the following, along with a selection of appropriate algorithms further used in this work.

Some alternatives and extensions have been developed in the past related to the modal analysis problem of concern in this work, which are however not further considered. In Refs. [264, 192, 190] it is demonstrated that if measured input-data is available, it can be

combined with the output-only approach to improve the modal analysis and to obtain the modal masses. This allows to further compute modal participation factors, e.g. according to Ref. [209]. Another approach in output-only aeroelastic testing is to perform a modal analysis based on unsteady operation states. In this case the input remains unknown, however, not the continuous stochastic input is used but the fact that a changing dominant frequency is present during the unsteady phase. This idea allows for example a run-up based modal analysis of wind-turbines [184, 164] and turbomachines [122]. In Ref. [283] the modal analysis of a helicopter rotor-systems is developed based on least squares fitting of the transfer functions. Although the technique requires input data, the particular aspect is that the helicopter rotor system's intrinsic periodicity is explicitly included in the approach.

1.2.1. Random Signal Separation

Helicopters are subject to both periodic and random forcing at the same time, which complicates the output-only modal analysis and requires additional signal preprocessing steps to treat both components separately. This is because signals involving harmonic components do not agree with GAUSSIAN white noise ambient excitation, which is typically assumed by OMA algorithms. In Ref. [43] it is indicated that the excitation of the structure does not need to be close to white noise. However, it is more important that all modes of interest are excited at all to realize an output-only modal analysis. Coloring can be considered as a filter of white noise belonging to the identified system [43]. However, this does not include distinct harmonics. If the characteristic harmonics are not separated from the stochastic signal they introduce dominant so called *spurious* modes which deteriorates the identification of physical modes, see Refs. [182, 204]. In general, the frequencies of the harmonic signals vary with time and are not known in advance. Hence, the separation of deterministic and non-deterministic signal components is concerned with different tasks. The related frequencies have to be identified first and the signals can be separated subsequently. A brief survey of relevant processing steps is provided in the following.

1. *Identification of harmonic components*: In Ref. [12] an automatic procedure based on Kurtosis is introduced for the detection of harmonic components in the signal. Another metric to separate the harmonic and stochastic components is the entropy index which is used in several studies [110, 183, 7]. The entropy index is found to be more robust compared to the Kurtosis index, see Refs. [62, 7]. In Refs. [111, 176] a KALMAN-filter approach is used to identify and handle harmonics with frequencies not known in advance. For further reading Ref. [144] provides a detailed review of methods to identify harmonic components.

2. *Handling of time-varying harmonics*: If the rotational speed is changing with time, Refs. [228, 197, 183] employ a transformation to the azimuth domain, which is also referred to as angle-domain time synchronous averaging to compensate variational rotor-speed [13]. In Refs. [237, 238] different techniques in context of helicopters are discussed to handle harmonic components with varying frequency, which include notch-filtering as well as describing and identifying the variation of frequency with both parametric and non-parametric models.

3. *Separation of deterministic and non-deterministic harmonics*: After the harmonic components are identified, they can further be separated from the stochastic components. The separation problem can be approached following two fundamentally different philosophies. The first approach is to consider the signals as noise disturbed harmonic signals. Following the WOLD decomposition, which is in theory always unique and achievable [18, 13], the random components can theoretically be separated from the deterministic signals components. Multiple realizations exist for this separation, see Refs. [18, 5]. Another improved implementation is introduced and demonstrated in Refs. [19, 13] for the separation of periodic and stochastic signal components. The shortcoming of these approaches is that the stochastic signal components, which carry the modal information of the system, are extracted from the output signal by subtracting the noise-canceled signal in time-domain. Since the noise-cancellation is not optimal, the noise-canceled signal still carry modal information. By removing the noise-canceled components, important signal components which carry modal information are removed as well.

The other philosophy is to treat particular sinusoids as disturbances to be removed. An easy approach is to filter the signal appropriately, see e.g. Ref. [237]. The reference indicates however that masking a frequency range increases the involved uncertainty of subsequently identified modes. Refs. [198, 144] indicate that filter characteristics can perturb the identified frequencies and damping ratios. Hence, in the reference filtering is concluded to not be an adequate method to mask the periodic components. In Ref. [143] frequency based techniques are used to exclude harmonic signal components by spectrum curve-fitting. Another approach is based on the ceptrum, see e.g. Refs. [107, 251, 118, 119]. In Refs. [198, 181] the harmonic components are explicitly handled by a modified modal analysis algorithm. Other approaches are based on system's transmissibility [73] and on harmonic approximations in the frequency domain, see Ref. [204]. Once the harmonics are fitted, they are removed from the signals.

The first two steps described above can be skipped in this work, because the rotor-speed is known in advance and constant in time.

1.2.2. Operational Modal Analysis

Experimental Modal Analysis (EMA) is typically based on measured inputs as well as measured outputs. If the inputs cannot be quantified, OMA enables the modal analysis by compensating this lack of information with statistical assumptions, see Refs. [192, 225]. Established OMA techniques identify a LTI system, which is also referred to as stochastic state-space model, see Eq. 1.1 and Eq. 1.2 as well as Ref. [221]. These equations represent a typical discrete mathematical formulation of a linear dynamical system subject to both process and measurement noise $\hat{\mathbf{w}}_k$ and $\hat{\mathbf{v}}_k$. However, if the unknown system inputs $\mathbf{u}_k$ fulfill the assumption of GAUSSIAN white noise, they cannot be separated from the noise components $\hat{\mathbf{w}}_k$ and $\hat{\mathbf{v}}_k$ and are combined to $\mathbf{w}_k$ and $\mathbf{v}_k$, see Ref. [221]. Recovering the matrices $\mathbf{A}$ and $\mathbf{C}$ is sufficient to compute the modes of the related time-continuous system. Note that

extensions to LTP systems exist as well [148, 10]. Another representation of linear models, which has successful been used for modal analysis is the family of Autoregressive-Moving-Average (ARMA) models [219]. Since ARMA models can be shown to be mathematically equivalent to stochastic state-space models [225], the stochastic state-space formulation is preferred and exclusively used throughout this work. Overviews covering most popular OMA approaches and theory can be found in Refs. [225, 185, 319, 261], or in books, see Refs. [43, 217]. OMA techniques can be categorized as shown in the following table 1.1. In general, the techniques can be classified as frequency- and time-domain techniques. Some of the time-domain techniques have frequency-domain counterparts, see Ref. [225]. Likewise, some of the OMA techniques have input-output based counterparts [225]. In the time-domain, approaches can be further distinguished depending on whether correlations are computed as a first step during the modal analysis, which are consequently referred to as *covariance-driven* approaches.

$$\mathbf{x}_{k+1} = \mathbf{A}\mathbf{x}_k + \underbrace{\mathbf{w}_k}_{\mathbf{B}\mathbf{u}_k + \hat{\mathbf{w}}_k} \tag{1.1}$$

$$\mathbf{y}_k = \mathbf{C}\mathbf{x}_k + \underbrace{\mathbf{v}_k}_{\mathbf{D}\mathbf{u}_k + \hat{\mathbf{v}}_k} \tag{1.2}$$

frequency-domain		time-domain
spectrum-driven	*data-driven*	*covariance-driven*
LSCF	SSI-DATA	SSI-COV
PolyMAX	PEM	NExT
Hilbert transform		
PP		
CMIF/FDD		
MLE		

Table 1.1.: Overview OMA approaches.

A widely used frequency-domain method in output-only modal analysis is Peak Picking (PP), which is however reported not to be suitable in presence of rotating machinery [132], since PP identifies operational deflection shapes rather than mode shapes and involves some level of ambiguity due to manual selection steps [225, 260]. Other approaches are Frequency Domain Decompositon (FDD) [44] and Complex Mode Indication Function (CMIF) [43, 225] which are both closely related and both based on Singular Value Decomposition (SVD), as well as Maximum Likelihood Estimator (MLE) [123, 112]. Another example of a frequency based approach is PolyMAX [226, 229], which is an extension of the Least-Squares Complex Frequency (LSCF) technique. An improved version of PolyMAX is published in Ref. [222]. Other extensions to frequency-domain algorithms are e.g. developed in Ref. [52]. In Refs. [183, 7] a Hilbert transform is used to compute an approximation of the transfer function from which the modal parameters are found.

A widely used time-domain based Stochastic Subspace Identification (SSI) method is called SSI-DATA, which is originally introduced in Ref. [216]. The theory behind this approach is in particular described in Refs. [217, 45]. The approach is based on KALMAN-filtering. Particular extensions to this approach are available from literature regarding computational efficiency, uncertainty, etc., see Refs. [77, 320, 76, 75]. Another time-domain approach is Parametric Time-Domain Method (PEM) which is based on an ARMA model formulation, however, this approach is computationally complex, see Ref. [236].

Algorithms from both categories just described are not used in this work, since the approaches introduced in the following offer more design flexibility and less implementation effort [212, 265]. Two approaches which are used in this work belong to the covariance-based category of output-only modal analysis algorithms. The first approach exploits the Natural Excitation Technique (NExT) principle which takes advantage of the fact that the correlations of the response of linear dynamical systems subject to GAUSSIAN white noise are characterized by the modal properties of the structural system, see Ref. [146]. Hence, the NExT approach can directly be combined with deterministic algorithms typically used in EMA based on the system's free decay. In this context, the most popular deterministic algorithms are ERA, Least-Squares Complex Exponential (LSCE) and ITD. Other authors used PRONY series, etc. as well [109, 236]. The ERA method is e.g. explained in Refs. [198, 157]. Ref. [47] provides some practical information about ERA when used in combination with NExT. Ref. [198] provides compact introductions into LSCE and the ITD method in addition. Both ERA and ITD have been used e.g. for postprocessing Digital Image Correlation (DIC) data of rotor measurements, see Ref. [50, 269, 301].

Another covariance driven method is SSI-COV, which first computes the correlation signals but handles them slightly different compared to ERA. An introduction into SSI-COV is provided in Refs. [217, 224, 148]. The advantage of SSI-COV is its simple implementation [265]. Due to this fact this approach has been subject to several improvements and extensions, see e.g. Ref. [263]. An important extension developed in the context of helicopters, treats intrinsic periodicity explicitly within the modal analysis based on FLOQUET theory, see Ref. [148]. Within this publication the validity of the methodology is demonstrated based on a representative rotor model, however, with a rotational speed of approximately one order of magnitude below the rotor-speed of typical helicopters.

1.2.3. Blind Source Separation

From a mathematical perspective, BSS computes a mixing matrix $\mathbf{Q}$, see equation 1.3, such that the sources $\mathbf{s}(t)$ are separated as much as possible according to a certain separation measure [321]. Introductions into BSS are provided in Refs. [51, 56, 57]. A thorough overview of the most important BSS algorithms is available from Ref. [273]. BSS has been developed for communication problems which can be described as instantaneous mixing problems [240, 21]. In contrast, signals obtained from mechanical systems are much more complex than communication signals, because the dynamics are governed by differential equations involving signal convolution [13]. However, an agreement with instantaneous mixing can be achieved for

structural dynamical systems, since the sources $\mathbf{s}(t)$ can be interpreted as generalized modal coordinates $\mathbf{q}(t)$ and the mixing matrix $\mathbf{Q}$ as the modal matrix $\mathbf{\Psi}$ accordingly, see equation 1.4 and Ref. [21]. The suitability of BSS algorithms in context of structural dynamics depends strongly on the involved measures to separate the sources. Some algorithms exploit second-order statistics like Second-Order Blind Identification (SOBI), whereas others exploit higher-order statistics like Independent Component Analysis (ICA) [240] or even other complex measures, see Ref. [21]. In the following, several techniques are reviewed to spot some light on the selection of the SOBI algorithm further used in this work. Once the modal matrix $\mathbf{\Psi}$ is computed, the sources $\mathbf{q}(t)$ can be determined via modal transformation [189]. Subsequently, the relative damping ratios and the eigenfrequencies can be obtained from the sources, see Ref. [273].

$$\mathbf{x}(t) = \mathbf{Q}\mathbf{s}(t) \tag{1.3}$$

$$\mathbf{x}(t) = \mathbf{\Psi}\mathbf{q}(t) \tag{1.4}$$

$$\tag{1.5}$$

Proper Orthogonal Decomposition (POD) and Principal Component Analysis (PCA) are two closely related BSS approaches, computing a mixing matrix $\mathbf{Q}$ consisting of orthogonal eigenvectors [57]. In Ref. [217] it is demonstrated that PCA can be seen as a special case of SSI. The eigenvectors of the elastic helicopter structure are indeed linear independent but no necessarily orthogonal. Hence, POD and PCA are not further considered in this work. In contrast, ICA assumes linear independent but not necessarily orthogonal eigenvectors [240]. An additional statistical assumption involved in ICA is that the sources are statistically independent in terms of higher-order statistics, which corresponds to non-GAUSSIAN sources [140, 163, 162]. In Ref. [189] it is concluded that ICA is problematic in the context of damped mechanical systems. This is supported by Ref. [273] where ICA was discovered not to be suitable for the detection of modes associated with a relative damping ratio higher than 5%. Other authors indicate that an order of 1% relative damping should be guaranteed for successful modal analysis using ICA [15, 121], which makes ICA impractical in presence of aerodynamic damping in particular. A typical relative damping ratio of the flapping motion of helicopters is 50% [152] whereas the structural damping ratios of the elastic airframe used in this work are in the range of approximately 1%-3%. In addition to the high damping, another problematic aspect indicated later in section 4.2, is that the modal coordinates exhibit nearly GAUSSIAN behavior, which does not allow to exploit higher-order statistics. This is confirmed by tests conducted in the scope of this work and hence, ICA is not further considered.

SOBI [33, 250] and AMUSE [298] are other approaches closely related with each other, which employ second-order and no higher-order statistics. Hence, the methods work with GAUSSIAN distributed signals [240]. Although SOBI is not suited for highly damped structures, see Ref. [1], it is preferred over AMUSE, which is less stable and less robust than SOBI [17, 273]. At the same time SOBI is better suited for the identification of higher damped structural modes compared to ICA according to Ref. [121], hence SOBI is preferred over ICA as well. In this work it is demonstrated that SOBI separates modes with eigenfrequencies even close

to each other, which are typical for helicopter airframes, see e.g. section 4.5. This approach has been used already by other authors in the context of wind-turbine modal analysis, see Ref. [54]. SOBI is considered as a special case of Complexity Pursuit (CP) [14], while CP has equivalent shortcomings as SOBI [273]. CP is introduced in Refs. [139, 311] and has been used in the context of helicopter output-only modal analysis based on optical measurements, see Ref. [301]. In addition, good agreement between CP and NExT-ERA was found in Ref. [301]. Extensions to CP have been published in the past [278].

Dynamic Mode Decomposition (DMD) is another BSS approach. An extension of DMD is available from literature which allows to handle closed loop systems specifically [244]. The interpretation of DMD in context of mechanical systems is that the algorithm is supposed to identify the system matrix $\mathbf{A}$ given in Eq. 1.1. However, Ref. [46] reports that the mode extraction with DMD in presence of broadband signals is challenging. Consequently, this approach is not considered in this work. Another BSS approach is the KOOPMAN theory, see e.g. Refs. [201, 194]. The theory is based on introducing new coordinates that allow a linear representation of the dynamics. This approach has been used by several researchers for flow decomposition [193, 25, 309]. Although the governing equations of the rotor-system are nonlinear, this approach is not used in this work, since the states of the identified linear system are intended to have physical units.

Classical BSS algorithms are developed for over-determined problems and are not applicable to under-determined systems. Hence, modifications have been introduced to extend BSS approaches for solving under-determined problems, see Refs. [273, 173]. Examples of such algorithms are Alternating Least-Squares (ALS) [16], NoHeJAD [15] and approaches based on sparsity [249]. The method introduced in Ref. [317] even allows an explicit treatment of time varying modal parameters. Another extension to the BSS framework that explicitly handles cyclostationary processes which are typical for helicopter rotors operating in atmospheric turbulence is introduced in Ref. [20]. Due to the complexity to adapt this algorithm to the problem pursuit in this work, this approach is not further considered.

1.2.4. Applications

The most occurring applications of output-only modal analysis algorithms can be found in context of buildings, bridges, wind-turbines, cars, fixed-wing aircraft and helicopters as well as spacecraft, ships and maritime structures. Apart from helicopters, the following summary is concentrated on wind-turbines and fixed-wing aircraft, because both systems are most similar to helicopters operating in atmospheric turbulence. Consequently, civil engineering structures like buildings and bridges as well as cars, spacecraft and vessels, etc. are neglected.

The similarity between airplanes and helicopters is that both are exposed to the same power spectrum of atmospheric turbulence. During fixed-wing in-flight testing, turbulence conditions are typically avoided and deterministic excitation is used although this technique is bandwidth-limited and ambient excitation can extend the frequency range and improve the analysis [28]. This is confirmed by multiple authors who discovered that atmospheric turbu-

lence generates sufficient excitation to enable a modal analysis of airplanes based on in-flight measurements [227, 274, 207]. The quality of the identification of modes depends on the flight-conditions, see Ref. [165]. In particular low-speed and high-altitude conditions are discovered to excite all modes of interest [165]. Real-time execution of OMA algorithms to monitor aeroelastic modes involving flutter is realistic according to Refs. [293, 63]. In Ref. [63] a real-time modal analysis of a fixed-wing aircraft was established in combination with a clustering algorithm to process stabilization diagrams automatically. The approach was e.g. used for mode-tracking over varying flight-conditions. To generate appropriate atmospheric turbulence signals, in Ref. [293] DRYDEN models have been used in context of simulation-based output-only modal analysis of fixed-wing aircraft. OMA techniques have successfully been used in the context of GVT of small and large fixed-wing aircraft as well [39, 274]. This includes conditions like engine start and taxi, see Ref. [165]. Some authors discovered PolyMAX to be superior over SSI in context of fixed-wing aircraft modal analysis, see Ref. [72]. In contrast and more recently, other authors discovered SSI algorithms to be superior in case of atmospheric turbulence due to more robustness against nonstationarities [28, 207]. In Ref. [227] it is concluded that damping is highly uncertain in the context of fixed-wing modal analysis in atmospheric turbulence.

Although helicopters and wind-turbines have significant differences in their functions and due to their structural design concepts, the similarity between wind-turbines and helicopters is that both feature rotating parts, introducing rotor-harmonics in the vibratory spectrum. In analogy to fixed-wing GVT, wind-turbines are often analyzed in parked conditions to avoid rotor-harmonics in the response spectra [215]. In Ref. [215] EMA and OMA results obtained from experimental data in parked conditions at National Renewable Energy Laboratory (NREL) are compared. The EMA is based on shaker excitation while OMA is based on ambient wind excitation. The results of both approaches are in agreement. However, low wind-speeds lead to less excitation of the low frequency region, although the lower modes were still identified properly [215]. In Ref. [54] wind-turbines under parked conditions are identified successfully using both SSI and BSS techniques.

In extension to parked conditions, the analysis of wind-turbines in operation is state-of-the-art as well. However, OMA techniques cannot directly be used for the modal analysis of operating wind-turbines. This requires to separate the rotor-harmonics from the broadband spectrum. One finding of past research activities is that the rotation of the rotor introduces peaks at the rotor-speed and at integer multiplies, which are not sharp but broadband. This non-sharpness deteriorates the identification of modes existing in these regions, see Ref. [296]. A second aspect is the periodically variation of modal parameters in time due to the rotor rotation. As an approach to this problem a COLEMAN transformation is suggested in Ref. [297] to achieve a set of equations with constant parameters. However, in this case this is a typical misconception, see Ref. [36]. A proper treatment of intrinsic periodicity can only be achieved via periodic frameworks like e.g. FLOQUET theory or HILL approach [289]. A third aspect is the slow variation of mode shapes due to changing operating conditions like wind-speed and rotor-speed. In Ref. [34] the problem of time-variation of modal properties of wind-turbines is addressed by matching the identified modes for different operating states based on frequency tracking.

Apart from these limitations both LSCE and SSI were demonstrated to allow the extraction of modal frequencies and damping ratios of large wind-turbines based on simulations, see Ref. [191]. LSCE is less powerful in identifying modes with higher damping compared with SSI according to the authors, see Ref. [191]. LSCE requires to consider one order of magnitude longer time signals compared to SSI to enable an identification of higher damped modes, which is expected to be related to the NExT principle, see Ref. [191]. A number of at least 200 cycles and a corresponding size of the HANKEL matrices is reported to be required for successful modal analysis [191]. The reference reveals as well that flapping and lead-lag motion are always coupled in the simulations [191]. In Ref. [245] the natural excitation of wind-turbines by atmospheric turbulence is extended and combined with seismic excitation like earth-quake in the context of OMA based on experimental data and simulations. One conclusion is that seismic forces can result in higher structural loads compared to aerodynamic forces, which is however of less importance for rotor-blade design. A second conclusion is that modes with higher eigenfrequency are most relevant for seismic excitation and an appropriate level of simulation fidelity has to be provided in order to capture this influence. During operation an increase of distinct damping ratios was discovered which is considered to be due to aerodynamic effects. In some cases, however, a decrease in relative damping was discovered for other modes. The conducted simulations based on finite-element modeling using rotor-blade beam approximations are in good agreement with experimental data, see Refs. [245, 246]. According to Ref. [296] the forces acting on the blades underlie high correlations. For the output-only modal analysis of wind-turbines, strain as well as optical (photogrammetry and laser interferometry) measurements were used in the past, see Ref. [212]. This approach was found to be better suited than acceleration-sensing, which is unsuitable for the detection of low frequencies up to 1Hz according to the author, see Ref. [212]. In Refs. [218, 212] it is concluded that both strain and optical measurements enable proper output-only modal analysis of wind-turbines.

Based on simulation models and representative simulated changes in operating conditions such as icing events and damage, an OMA approach has been developed for the structural monitoring of wind-turbines in Refs. [178, 177]. One conclusion is that a high amount of energy in the power-spectrum is associated with rotor-harmonics, which has detrimental effects on the identification of physical modes. Within the scope of wind-turbine structural monitoring, another approach has been developed to detect long term changes in the structural behavior of wind-turbines based on modal parameters identified through OMA, see Ref. [214]. The modal analysis is therefor combined with an automatic tracking algorithm based on regression. The algorithms are able to detect the onset of typical damage phenomena of wind-turbines. To enhance the output-only modal analysis the free decay of structural oscillations due to shutdown events of wind-turbines are additionally exploited to quantify structural damping in Ref. [213], although the reference mentions the continuous operation data to entails much more information. In Ref. [212] it is concluded that high damping of wind-turbine modes in the range of 10%-60% makes it nearly impossible to detect them using output-only modal analysis.

Former studies use OMA in the context of helicopters as well, to determine modal parameters of both the airframe and the rotor-blades. Refs. [183, 223] are concerned with the OMA of the helicopter airframe based on GVT. Spectra recorded during flight-testing are used as

well as random signals. One conclusion is that an entropy index based removal of rotor-harmonics allows to properly recover the modal airframe parameters. In both Refs. [48, 49] OMA is employed to quantify the influence of helicopter payload on airframe dynamics. The tests include in-flight testing as well as GVT. The results agree with expectations according to the authors. Based on an ARMAX model, Ref. [202] concludes that the presence of rotor-harmonics has detrimental effects on both mode-shape and damping estimation. For different helicopter airframe (sub-)structures the difference in modal estimation via EMA and OMA in presence of rotor-harmonics is investigated in Ref. [110]. The analysis is based on GVT using white noise and sine signals as well as recorded flight-test data. The authors conclude that the identification and an appropriate treatment of the rotor-harmonics is possible. Forces introduced at the tail section during flight improve the modal analysis using OMA, see Ref. [110]. The modal behavior of an isolated helicopter tail section is studied in Ref. [53] via GVT as well. Here, OMA properly recovers the modal parameters compared to input-output EMA, although the applied signals include rotor-harmonics. Based on recorded in-flight test-data, Ref. [62] uses a HILBERT-transformation to improve the prediction of modal parameters using an elastic finite-element airframe model. The rotor-harmonics are identified and removed using an entropy index. The approach is found to be promising in the scope of model updating based on recorded flight-test data.

Based on experimental data, Ref. [8] compares frequency- and time-domain OMA approaches, based on reference structures like beams and plates and a full-scale helicopter rotor-blade. Even in presence of closely spaced and coupled modes the modal properties were properly extracted. In Ref. [290] OMA is used within the scope of determining structural properties of composite rotor-blades. Therefor, experiments are conducted in the non-rotating as well as in the rotating domain. The identified frequencies agree with simulation results up to the nominal rotor-speed and even slightly above. In Ref. [7] the modal properties of an operating rotor-blade are computed based on experimental data using OMA. The approach includes the removal of rotor-harmonics based on an entropy index. Frequencies and damping ratios are extracted for the first four eigenmodes up to the nominal rotor-speed. In Ref. [300] NExT-ERA is successfully used to extract the modal parameters of a flexible rotor-blade from DIC data in hovering conditions. However, only the two first elastic blade modes were identified and the need for an improvement of damping ratio determination is concluded. The method is used to determine the CAMPBELL diagram experimentally, which is demonstrated for 4 different rotor-speeds. In Ref. [301] the authors employ CP in addition to NExT-ERA in order to recover the modal parameters of the rotor-blade in hover conditions. The results of both approaches are in agreement, although CP is concluded to be superior over NExT-ERA due to much less required user-input. However, damping estimation is still most difficult. The damping ratios are determined from the separated source signals using curve fitting. Turbulence and basement vibration are assumed to introduce suitable broadband vibrations according to the authors. In Ref. [299] the work is continued to determine rotor-blade structural loads from correlation with numerical models. Since only the first three modes are identified the load distribution could not be computed in detail.

1.3. Research Objectives

The objectives of this work are twofold. The first objective is to evaluate if structural modes can be computed from the helicopter elastic response to atmospheric turbulence. If this can be achieved, the second objective is to quantify the contribution of rotor- and airframe-states to the structural mode-shapes and to assess the system's stability based on the relative damping ratios. This is performed for three different horizontal flight velocities as well as three different turbulence intensities. The approach used in this work is intended to be applicable to recorded flight-test data as well. Therefor, limitations inherent from flight-testing are respected, which includes a limited number of sensors, unmeasurable airloads as well as the fact that experiments in atmospheric turbulence once recorded cannot be reproduced exactly. The successful demonstration of the modal analysis approach based on simulations is considered as a promising indicator for its practical usability in context of helicopter flight-testing. To realize and evaluate the helicopter in-flight modal analysis based on simulations, this work aims for developing an approach, which includes appropriate treatment of helicopter-specific aspects. These aspects are summarized in the following.

1. *Intrinsic Periodicity:* This is a well-known property of helicopters, see Ref. [235]. Since the OMA algorithms used in this work assume LTI-specific dynamics, the assumption is assessed whether the helicopter structural dynamics can be described sufficiently by a LTI system.

2. *Extrinsic Periodicity:* In addition to intrinsic periodicity, the rotor experiences extrinsic periodic airloads. This deterministic influence has to be handled explicitly during the modal analysis and requires to include appropriate signal pre- and postprocessing steps or to use specific modal analysis approaches, see e.g. Refs. [198, 197]. This has to be realized even under the influence of cyclostationary effects of rotors encountering atmospheric turbulence and the related shift of energy from lower frequencies to rotor-harmonics.

3. *Simulation Approach:* The suitability of output-only modal analysis of helicopters operating in atmospheric turbulence can only be demonstrated within the limitations of the selected modeling approach. Hence the kinematic, aerodynamic, aeroelastic as well as the statistical and spectral properties of atmospheric turbulence that matter in particular are appropriately modeled.

1.4. Reference Aircraft and Flight-States

Although atmospheric turbulence is of concern for many rotorcraft configurations, see e.g. Refs. [270, 268], this work focuses on MR/TR configurations, since this is the most common helicopter configuration, see Ref. [152]. Furthermore, the MR/TR configuration is present in all weight categories, from ultra lightweight helicopters to heavy-lift configurations [152].

1. Introduction and Motivation

This work is fundamentally based on the UH-60A, a utility helicopter with a take-off weight approximately located in the middle of the weight range of existing MR/TR configurations, because the required data for model validation is available from literature. The UH-60A is not a modern helicopter but is still today an important reference for research activities, since this helicopter served in several flight-test campaigns and experiments like the Airloads Program [41] and a wind-tunnel test campaign, see Ref. [279]. In addition, the vast amount of secondary literature in conjunction with the UH-60A provides important references for comparison with the results obtained in this work, see e.g. Refs. [127, 286].

The UH-60A test campaigns are summarized in Ref. [258] and a thorough summary about the development and history of this helicopter is provided in Ref. [172]. A large amount of test-data has been published about this helicopter [291], including the structural, geometrical and aerodynamic properties. This includes all properties which are necessary to establish the models required according to the objectives formulated in the previous section 1.3. The model properties used in this work are taken from literature and are summarized in Ref. [258], except for the tail section. The properties of the TR and the empennage surfaces are observed from Ref. [136]. For two reasons, this work focuses on steady horizontal flight-states exclusively. First, the results obtained with the modal analysis methods are assumed to improve in stationary operating conditions and second, typical helicopter mission profiles are often characterized by steady flight-conditions. The necessary data to validate the steady horizontal flight-states is available from literature and summarized in Ref. [258] as well.

The flight-conditions tested during the Airloads Program, which is the reference test-campaign for this work, are categorized based on the blade-loading C_T/σ. The associated data-records comprise horizontal velocity-sweeps, see Ref. [41]. The higher the blade-loading of a helicopter, the more limited is the flight-envelope towards higher speeds, see e.g. Ref. [152]. In order to cover a wide range of horizontal flight-speeds, a lower blade-loading is selected as reference in this work. This allows to study both rotational effects most dominant at low speed as well as highly asymmetric flow-conditions introducing high structural oscillations at high speed. In addition, the low blade-loading allows a higher threshold towards significant unsteady effects like dynamic-stall, which are not modeled in this work. Consequently, a blade-loading of approximately $C_T/\sigma \approx 0.08$, which is associated with a velocity sweep of the flight-test campaign labeled nbr. 85, see Refs. [41, 314], is used in this work exclusively. Another argument for the selection of this flight-test counter is that turbulence encounters have been measured during this run, which serve as an additional opportunity for validation. In general, test-data recorded in turbulent conditions is rarely published and often avoided during flight-testing, see Ref. [41]. The test-counter 85 covers 19 recordings of different horizontal flight-velocities. The flight-levels of this sweep are considered to be located within the atmospheric boundary-layer, see Ref. [85]. From these points three different flight-speeds are selected. The selection of the lowest speed at $\mu \approx 0.076$, according to the Airloads Program flight test counter 8519, is based on the fact that rotor-specific turbulence effects are most pronounced at low horizontal flight-speed and that the speed is not violating TAYLOR's hypothesis even under severe turbulence conditions, according to Ref. [292]. The second horizontal flight-speed is selected approximately as twice the flight-speed of counter 8519, namely counter 8513 at $\mu \approx 0.149$ to include a reference point at medium horizontal speed. Note that this flight-states involves blade-vortex interaction which is not resolved by

the simulation approach used in this work. The third reference is approximately twice the speed of counter 8513, namely counter 8528 at $\mu \approx 0.308$ to include a data point with high horizontal flight-speed.

Based on the standard deviation of the turbulence velocity, atmospheric turbulence is typically classified into the four categories light, moderate, severe and extreme, see Ref. [134]. In this work extreme turbulence is neglected, since it is defined to harm the aircraft via loss of control or structural damage. The flight-conditions covered in this work are summarized in table 1.2. Beside the three different flight-speeds corresponding to the counters 8519, 8513 and 8528, three different levels of turbulence are investigated to study the influence of turbulence intensity on the aeroelastic phenomena and on the applicability of OMA and BSS techniques. The reference flight-condition of low horizontal speed in light turbulence is referred to as *baseline* throughout this work. The flight-conditions at increased turbulence intensity are labeled *moderate* and *severe* consistently. In addition, counter 8513 is referred to as *loiter*, since the flight-speed of counter 8513 is close to the velocity of best endurance and hence close to a reasonable loiter-speed. Counter 8528 is referred to as *cruise*, since this flight-state is close to the velocity of maximum range and hence a reasonable cruise-speed.

specifier:	*baseline*	*loiter*	*cruise*	*moderate*	*severe*
altitude $[m]$	762	762	762	762	762
turbulence intensity	light	light	light	moderate	severe
flight-speed $[m/s]$	16.79	32.93	68.06	16.79	16.79
reference flight-test counter*	8519	8513	8528	8519	8519

* *according to Airloads Program, see Ref.* [41].

Table 1.2.: Flight-conditions considered in this work. Both horizontal flight-speed and turbulence intensity are varied. The statistical turbulence properties are obtained from the specification MIL-F-8785C, see Ref. [24].

2. Helicopter Specific Modeling of Atmospheric Turbulence

Note that some of the result presented in this chapter are summarized and presented as well in the final report of the project CORINNE, German aviation research program LuFo, reference number 20K1702C.

Airborne helicopters are exposed to a highly dynamic and unsteady atmosphere which is relevant for the aircraft aeroelastic behavior, see section 1.1. The atmospheric dynamics are studied within the academic discipline called meteorology. Although the meteorological phenomena are complex and characterized by variations of different quantities like velocity, temperature, pressure, humidity, etc. [133], the motion of air-masses is most important from an aeroelastic perspective. Hence, the intention of this chapter is to summarize the most important related kinematic phenomena and to select and implement an appropriate atmospheric turbulence model into the simulation framework. For further reading, the following textbooks are recommended for introductions into meteorology [133], into turbulence [186] and into the statistical description of atmospheric turbulence [84, 78, 128]. A noteworthy and thorough review on atmospheric turbulence in the context of helicopters is provided in Ref. [98].

2.1. Meteorology and Turbulence Fundamentals

The forces governing the motion of fluid particles in the atmosphere are separated into *fundamental* and *apparent* forces in Ref. [133]. Fundamental forces include pressure gradients, gravitation and friction, see Refs. [134, 83]. In presence of pressure gradients, fluid particles are accelerated along the gradient in higher-to-lower pressure direction. Due to viscosity, frictional forces are acting on the surface of a fluid particle if it is in motion. Gravitation can be assumed as a constant acceleration acting towards the earth's center [133]. Apparent forces include both centrifugal forces and CORIOLIS forces. Apparent forces are referred to as inertial forces as well, because they are related to the fact that the atmosphere is carried with the earth's rotation with respect to a non-rotating inertial frame [133]. A fluid particle is subject to centrifugal forces if it moves along a curved slope measured in the non-rotating inertial frame. Note that gravity is defined as the superposition of both gravitational acceleration and centrifugal acceleration resulting from the earth's rotation. Geopotential height is an established concept to compensate that both components are in general not acting in the same direction, see Ref. [133]. Next to the earth's rotation, large-scale phenomena causing

17

curved motion are e.g. tornados and hurricanes. If the motion of a fluid particle results in a change of its distance to the current rotation axis measured in the non-rotating frame, it is subject to a CORIOLIS force due to conservation of momentum.

The motion of fluid particles is in general unsteady and entails statistical fluctuations, periodic oscillations, short-term accelerations, steady components, etc.. Complex models are necessary to simulate this motion holistically. Hence, different heuristic logics exist to distinguish the underlying components, which allows to formulate specific component models of less complexity. One postulation, known as the REYNOLDS decomposition, separates turbulent motion into mean and stochastic motion, see Ref. [23]. In addition, regular periodic patterns of the mean motion are explicitly referred to as waves in Ref. [292]. An analogue and established aeronautical terminology separates the atmospheric motion into mean wind, stochastic turbulence and discrete gusts, see Ref. [24]. Following this reasoning discrete gusts are timely limited events, continuous turbulence represents stochastic atmospheric motion and mean wind characterizes the averaged velocity with slow variation in time.

These components are physically related with each other, since e.g. mean wind leads to shear effects generating turbulent phenomena [292]. However, since this work focuses on atmospheric turbulence, the separation of these components allows to isolate the modeling of atmospheric turbulence and to exclude mean wind and discrete events from the analysis. Steady wind is neglected, since it is not relevant for aircraft aeroelastic analysis, see Ref. [203]. Discrete atmospheric events like timely-limited gusts and wind shear are excluded in this work as well, because related aeroelastic responses do not contribute to structural loads exploited by OMA and BSS techniques.
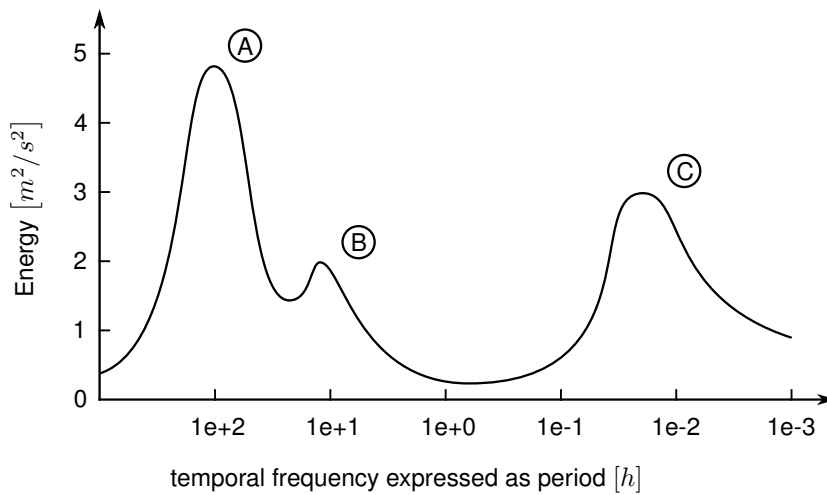
Figure 2.1.: VAN DER HOVEN wind spectrum. Figure schematically adopted from Ref. [84].

A different view on the mixture of components of atmospheric motion is available from the frequency-domain. Evident from the VAN DER HOVEN wind spectrum is that the underlying phenomena are acting at significantly different time-scales, see Fig. 2.1 and Ref. [84]. The spectrum reveals that slow weather cycles with a time-period of 3-4 days (peak A) coexists with phenomena resulting from the 24hour day-night-cycle (peak B). In addition, atmospheric turbulence (peak C) in present at even higher frequencies. Not all of these time-scales are of importance for aeroelastic analysis, since structural eigenfrequencies of the aircraft are multiple orders of magnitude higher than the earth's rotational speed introducing the day-night-cycle. In this regard, the time-scales of atmospheric turbulence are most relevant for aircraft aeroelastic phenomena.

In general, turbulence can be characterized as an irregular and random motion which is a superposition of structures of different length-scales ranging from 10^{-3}m to 10^{3}m, see Ref. [85]. A concept to describe these structures is to treat them as eddies, see Ref. [292]. The two most important sources generating these eddies in the atmosphere are wind-shear and convection, see Ref. [134]. Shear effects are e.g. present in the atmospheric (planetary) boundary layer which ranges up to 1-2km of altitude above ground level over land and up to 0.5km over seas [85, 128]. Other effects are thunderstorms and man-made wake effects generated e.g. by airborne aircraft [134, 128].
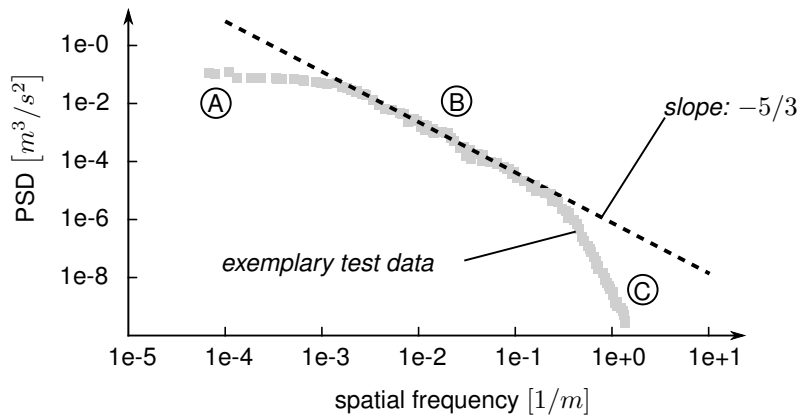
Figure 2.2.: Energy cascade of turbulent eddies. Figure schematically adopted from Ref. [78].

Energetically, the eddies are related with each other, since larger eddies separate into smaller ones until the smallest eddies dissipate into heat, see Fig. 2.2 and Refs. [85, 78]. Fig. 2.2 indicates three phases of energy decay. In segment A, eddies with comparable energy exist at different frequencies. In segment B, the decay follows KOLMOGOROV's law until in segment C the steeper negative slope characterizes the energy dissipation into heat resulting from viscosity effects [78].

2.2. **Stochastic Turbulence Simulation and Rotational Sampling Effects**

Based on the insights from the previous section 2.1, the following three requirements are defined in the scope of this work, for the selection of an appropriate turbulence model in conjunction with helicopter aeroelastic simulation.

1. *Spectrum:* Kolmogorov's law shall be satisfied in order to maintain a correct representation in terms of energy introduced into the elastic helicopter structure depending on the frequency.

2. *Bandwidth:* Length-scales shall match the helicopter dimensions and relevant eigenfrequencies. Both very low length-scales associated with very low energy and very large length-scales, are assumed to have a negligible effect on the dynamics. Hence, the analysis focuses on intermediate frequencies. The frequency range of interest is approximately 10^{-1}Hz to 10^2Hz. The related length-scales of the turbulence eddies over all flight-speeds considered in this work range from approximately 10^{-1}m to 10^2m. This is considered as an appropriate range, since the helicopter dimensions range from 1m to 10m approximately.

3. *Cyclostationarity:* Due to kinematic characteristics, the simulation of atmospheric turbulence in context of helicopters is more complex compared to fixed-wing aircraft, see Ref. [26]. Approaches employed in fixed-wing turbulence simulation are a good approximation for helicopter high-speed flight but not for low-speed and hover conditions [26]. Depending on the rotor-radius and the turbulence wavelengths, it is possible that more than one blade passes a characteristic turbulence pattern, which introduces periodic effects. These are referred to as cyclostationary effects and hence, corresponding rotational blade-element sampling shall be used in this work for the simulation of rotors experiencing atmospheric turbulence, see Refs. [98, 104, 242]. To resolve this effect a spatially distributed turbulence field has to be included in the analysis, represented by an at least two-dimensional vector-field of turbulent fluctuations **v** distributed along x- and y-coordinate, see Fig. 2.3. The horizontal flight velocity is indicate by V. Since the inter-blade-correlation is high, it is sufficient to only select the 75% radial station as representative sampling-point for each rotor-blade, see Refs. [98, 270].

Different modeling approaches of atmospheric turbulence satisfy the requirements specified above. Turbulence models reviewed in this work are classified as *physical* or *empirical* models, although these models are in general developed iteratively in close interaction with measurements and theoretical analysis, see Ref. [79]. However, this classification intends to express to which extend the approaches involve comprehensive models. Models referred to as physical turbulence model are based on the Navier-Stokes equations. In this context, it is assumed in literature that turbulence processes are inherently described by the Navier-Stokes equations, which is however not an incontestable assumption, see Ref. [79]. In fact, this approach is more general compared to empirical modeling, because it involves much more physical in-
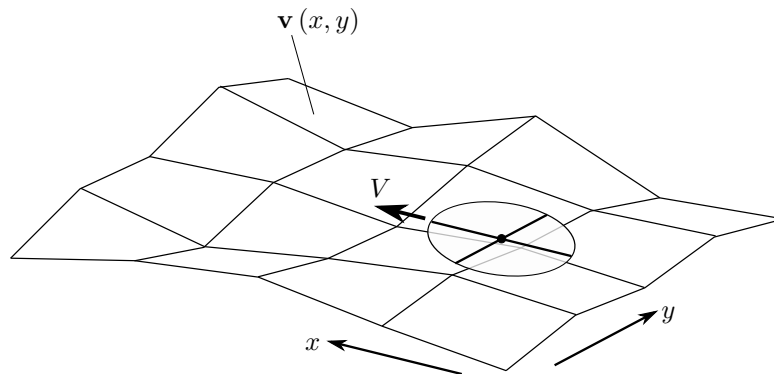
Figure 2.3.: Two-dimensional vector-field of the three atmospheric turbulence velocities. Since no temporal variation is involved, the variation of turbulence velocity is a result of both rotor-rotation and flight-speed following TAYLOR's hypothesis. The two-dimensional field allows to account for cyclostationary effects, experienced by an observer fixed on a rotor-blade. Figure adopted from Ref. [258].

formation. In contrast, models referred to as empirical models are directly based on measured test-data and involve only very little physical information. Table 2.1 provides an overview over most relevant models that appropriately represent atmospheric turbulence in the context of helicopter in-flight simulation. The table indicates that different types of empirical models exist depending on the outputs of the model. Control-equivalent models mimic aircraft operation in atmospheric turbulence via stochastic aircraft control inputs, while kinematic models compute turbulence velocities, which are further processed by aerodynamic models.

physical	empirical	
CFD	*control-equivalent*	*kinematic*
DNS	METS	SDG
LES	CETI	SEM
RANS		FullFT
		HubDT
		SORBET
		SNLWIND(-3D)

Table 2.1.: Overview turbulence models representing cyclostationary effects.

Computational Fluid Dynamics Modeling

A holistic approach for helicopter simulation in atmospheric turbulence is Computational Fluid Dynamics (CFD) analysis, involving a comparably high level of physical modeling governed by the NAVIER-STOKES equations. The turbulent phenomena can e.g. be computed by approximating the NAVIER-STOKES equations via Direct Numerical Simulation (DNS), see Ref. [78]. This approach is however impractical in the context of helicopter simulation.

This is due to the fact that the required discretization to resolve atmospheric turbulence sufficiently, is multiple orders of magnitude less than the dimensions of the aircraft. This is indicated in Ref. [78] for the application of DNS in engineering in general and causes a non-manageable computational expense. Another approach is to approximate the NAVIER-STOKES equations using Large Eddy Simulation (LES), which originates from meteorological modeling and weather forecasting, see Ref. [79]. An approximation for the stress tensor to incorporate turbulence is e.g. provided by SMAGORINSKY's model [79, p.56]. Another widely used approach is referred to as Reynolds-averaged Navier-Stokes (RANS). In this context, typically the BOUSSINESQ's hypothesis is involved and isotropic surrogate turbulence models like SPALART-ALLMARAS, k-omega, k-epsilon, MENTER's-SST are included to represent turbulent phenomena. The fundamental advantage of CFD modeling is that the air-masses can develop freely, which allows to account for the interaction of different objects. The disadvantage is the high computational effort.

Empirical Modeling via Equivalent Input

One empirical helicopter-specific turbulence modeling approach that allows real-time simulation is based on equivalent stochastic aircraft control-inputs extracted from helicopter flight-test results. In Ref. [277] two approaches based on an observer and on model inversions are introduced to compute turbulence-equivalent control input perturbations $\delta\mathbf{u}$. Both approaches require to measure both the control inputs of the pilot and the response of the helicopter during flight-testing in atmospheric turbulence in a first step. In a second step, the control input perturbations $\delta\mathbf{u}$ are computed such that the simulated response matches with the response recorded during flight-testing. Subsequently, filters are parameterized such that the spectra of the computed perturbations $\delta\mathbf{u}$ can be approximated at each time-step k during real-time simulation. The reproduced perturbations are finally superimposed with the control input vector $\mathbf{u}_k$, see exemplarily Eq. 1.1 and Eq. 1.2. Two examples of this type of model are the UH-60A Mixer Equivalent Turbulence Simulation (METS) model [168, 179] and the Control Equivalent Turbulence Input (CETI) model [277, 276]. These approaches are focusing on hover and low-speed flight, because in these flight-conditions other established models have the most drawbacks [277]. However, control-equivalent models can be derived and used for higher flight-speeds as well, see Ref. [276]. They are e.g. in good agreement with experimental data recorded in hover as well as during ship-deck operations, see Refs. [168, 208]. A drawback of this approach is that it cannot be generalized for other configurations, see Ref. [124]. However, by introducing an advanced modeling approach, see e.g. Ref. [125], the models could be generalized within a limited range to other flight-states and turbulence intensities [124]. Another drawback is that both CETI and METS models are designed such that the measured states are reproduced, which typically include vertical acceleration, helicopter rates and rotor-states, see e.g. Ref. [276]. It is not guaranteed that the equivalent control inputs generate representative responses of quantities not considered during model parameterization, like pilot seat or rotor-hub vibrations.

Empirical Kinematic Modeling

A more general empirical turbulence modeling approach does not involve aircraft specific characteristics by solely being based on meteorological and fluid-dynamical investigations. One-, two- and even three-dimensional models of this type exist, see Ref. [310]. The statistical and spectral properties are typically represented by the Probability Density Function (PDF) and the Power Spectral Density (PSD). During simulation, turbulence velocities are computed such that they follow both the governing statistics and spectra, see Ref. [78]. Different techniques can be employed for computational realization. The first approach is frequency-domain analysis, which is applicable if a transfer-function of the aircraft is available in the frequency-domain, see Ref. [128]. In the time-domain the alternative is to employ MONTE CARLO simulation. An established approach to simulate atmospheric turbulence is to pass white noise through shaping-filters. An alternative is to linearly superimpose fundamental functions. One kind of these fundamental functions are sinusoids with amplitudes weighted according to the governing turbulence PSDs, see Refs. [32, 267, 270]. Another kind of fundamental functions is used by the Statistical Discrete Gust (SDG) method, see Refs. [153, 154]. This model generates turbulence by a superposition of multiple discrete events of ramp-shape under the assumption that the sum resolves continuous turbulence appropriately. In Ref. [231] PSD- and SDG-based methods are compared with the result that the signals generated with both approaches agree with each other but PSD-based methods are computationally more efficient. Kinematic turbulence models only resolve the spatial domain and involve the TAYLOR's hypothesis, which neglects the time-variation of turbulence. According to TAYLOR's hypothesis the temporal frequency ω is expressed by the product of flight-speed V and spatial frequency Ω, see equation 2.1. Hence, turbulence is only properly modeled by kinematic approaches, while the aircraft is moving sufficiently fast and relatively to the turbulence pattern. In consequence, this simulation approach fails to simulate atmospheric turbulence in hover, see Ref. [67].

$$\omega \left[\frac{\text{rad}}{\text{s}}\right] = V \left[\frac{\text{m}}{\text{s}}\right] \cdot \Omega \left[\frac{\text{rad}}{\text{m}}\right] \tag{2.1}$$

Although GAUSSIAN distribution is often assumed by kinematic turbulence models, measurements indicate that the statistics of atmospheric turbulence are in general non-GAUSSIAN, which is recognized by pilots as *patchiness* in the context of flight-simulators and known as *intermittency*, see Refs. [153, 270]. Several authors were concerned with designing non-GAUSSIAN models, see Refs. [155, 153]. In Refs. [253] two independent stochastic processes are multiplied, to generate non-GAUSSIAN turbulence signals. In Ref. [306] even more independent stochastic signals are used. In Ref. [239] a new non-GAUSSIAN method based on filtered POISSON-processes is introduced.

The statistical and spectral properties of the stochastic processes that represent turbulence can be obtained from established turbulence models, experiments or CFD analysis. Two well-established one-dimensional atmospheric turbulence models in context of helicopters are the VON KÁRMÁN model, see Refs. [80, 268] and the DRYDEN model, see Refs. [187, 136,

295], which both generate homogeneous and isotropic turbulence. The statistical and spectral properties of both models can be found in Ref. [24]. In wind-energy engineering often KAIMAL turbulence models are used which better represent the atmospheric turbulence properties in close proximity to the ground, see Refs. [34, 82]. Specific standardized spectra for helicopter ship-deck operation have been established as well, see Ref. [24, 95].

For simulating complex and highly specific environments in real-time, several authors used CFD results for the extraction of statistical and spectral properties to establish empirical turbulence models. In Ref. [58] properties observed from CFD analysis are used for ship-airwake modeling in the context of the UH-60A. Comparable work is conducted in Refs. [171, 170] in the context of the UH-60A as well. In Ref. [138] a model referred to as Synthetic Eddy Method (SEM) is used to model turbulence experienced by a simulated helicopter rotor for real-time simulation. The SEM approach is presented in Ref. [147] and generates stochastic signals representing turbulence components based on TAYLOR's frozen field hypothesis, while the statistical properties are extracted from pre-computed CFD simulations or experiments.

As multi-dimensional kinematic turbulence models can be established from CFD results, one-dimensional turbulence models can be expanded into two or three dimensions as well. In Refs. [100, 99] the authors published an approach to model the longitudinal variation of vertical turbulence velocity over the helicopter rotor-disk. Later the approach was extended for variations of non-uniform turbulence in longitudinal and lateral direction, see Ref. [96]. In Ref. [64] a new blade-element turbulence model was presented in the frequency-domain. At the same time a new time-domain approach for modeling cyclostationary processes based on SHINOZUKA algorithm, see Refs. [282, 281], was developed, see Refs. [267, 241]. Based on these references, Ref. [270] further developed a full-field turbulence simulation method for rotorcraft applications, which is in this work referred to as Full-Field Turbulence (FullFT) model. The approach, which is based on the VON KÁRMÁN model and the BORGMAN method, see Ref. [38], digitally realizes two-dimensional turbulence fields. Since real-time execution was necessary for a flight-simulator test campaign, parallel computation was developed and employed in context of two-dimensional turbulence models in Refs. [69, 68].

Another approach to describe the variation of turbulence in the rotor-disc is provided by the Simulation of Rotor Blade Element Turbulence (SORBET) model, see Ref. [188]. Within the model two uncorrelated stochastic processes, generated at points moving with the aircraft are used to generate turbulence signals via shaping-filters. The two points are located in front of the rotor and are positioned symmetrically left and right in the rotor-plane with a distance of the rotor diameter. Following TAYLOR's hypothesis, the generated velocities are convected rearward with aerodynamic horizontal flight-speed V, which represents the longitudinal distribution. The lateral distribution is realized using what is referred to as GAUSSIAN interpolation which maintains GAUSSIAN distribution in lateral direction, see Ref. [188]. This scheme is applied to all three turbulence components. Turbulence velocities are subsequently sampled at each individual aerodynamic rotor-blade station and superimposed with the local flow velocities. The advantage compared to the FullFT model is the higher computational speed. This modeling approach is used e.g. in Refs. [150, 149] as well. In Ref. [149] the approach is improved by using VON KÁRMÁN spectra, which is found to improve the simulation of handling quality aspects of helicopters.

Parallel to two-dimensional turbulence models developed for helicopter applications, an equivalent model has evolved as a standard model for wind-turbine turbulence simulations, which is today distributed as *TurbSim* and provided by NREL [161, 156]. *TurbSim* contains several stochastic turbulence models, e.g. two of which, namely SNLWIND [303] and SNLWIND-3D [160] are two-dimensional turbulence models. The two models generate a vertical plane of random turbulent fluctuations. In SNLWIND only turbulence components in flow direction are considered [303], whereas SNLWIND-3D covers all three components, see Ref. [160]. The generation of the statistical processes in time-domain is based on sum-of-sinusoids, see Ref. [160]. To enable the simulation of atmospheric turbulence in case of a Vertical Axis Wind-Turbine (VAWT), the vertical convection of turbulence fluctuations in combination with interpolation is used, see Ref. [303]. In theory, SNLWIND in combination with this approach can be used accordingly in context of helicopters operating in close proximity to the ground.

Turbulence Model Selection

Essentially three different approaches are discussed above to model the atmospheric turbulence appropriately in the context of helicopters. The disadvantages of CFD simulation are the significant meshing effort and the high computational cost, which are both considered not to be proportionate to the objectives mentioned in the beginning of this section 2.2. The disadvantages of control-equivalent models is that they are not available for the variety of flight-states of interest in this work. In addition, they do not guarantee to excite the helicopter structure sufficiently for a modal analysis based on the structural response only. Hence, empirical kinematic modeling of atmospheric turbulence is selected in this work. Since, the SEM approach is based on data from high fidelity turbulence simulation, this approach is not further considered in this work, since CFD approaches are not further considered as discussed above. Since the SDG approach was found to be computationally less efficient compared to PSD-based approaches, SDG is not further considered as well. SNLWIND(-3D) is not applicable to the flight-conditions of interest in this work, although the modeling approach is indeed promising to be adapted to helicopters. Among the remaining kinematic models, the FullFT model is preferred over the SORBET model, because the FullFT model employs VON KÁRMÁN-spectra which satisfy the KOLMOGOROV law. Note that extensions of the SORBET approach exist, which employ VON KÁRMÁN-spectra, see Ref. [149]. However, the implementation proposed in Ref. [270] based on the BORGMAN approach is considered to be very promising. In addition, the FullFT model fulfills the initially specified requirements in this section. Additionally, the model is valid for all flight-conditions specified in table 1.2 and has a low computational cost. This model is described in the following section 2.3. For comparison a second model is selected and implemented in this work, namely the DRYDEN model, including both translational and rotational components, see section 2.4. Based on the comparison with the FullFT it can be evaluated whether in particular cyclostationary effects are appropriately represented by including rotational turbulence components. Both models allow to appropriately simulate the time-delay between the MR and the tail section. The two models are both realized in *C* and wrapped to *Python* using *SWIG* to realized a connection to other models.

2.3. Full-Field Turbulence Model

The FullFT model is fundamentally adopted from Ref. [270], while the adoptions and the validation of the implementation are already published in Ref. [257]. Hence, only the most important aspects are repeated in this work. Refs. [270, 257] are recommended for more fundamental insights. The FullFT model describes a two-dimensional vector-field of three translational turbulence velocities, see Fig. 2.3, based on the VON KÁRMÁN model. An exemplary two-dimensional PSD according to the VON KÁRMÁN model is shown in Fig. A.1 for the vertical atmospheric turbulence velocity. According to the PSD most energy is approximately located at spatial frequencies of 10^{-4} to 10^{-3}rad/m. The two-dimensional PSD can e.g. be realized numerically using the SHINOZUKA algorithm in time- or spatial-domain, see Ref. [266]. The superposition according to the SHINOZUKA algorithm is shown in equation 2.2. Accordingly, each turbulence velocity-component is based on a superposition of K^2 harmonic functions at a specific longitudinal coordinate x and lateral coordinate y. The harmonic functions are associated with an equally distributed random phase-shift ψ_{ij} in the interval $[0, 2\pi[$, see Eq. 2.2 and Ref. [280].

$$w\left(x, y\right) = 2\sqrt{2} \sum_{i=1}^{K} \sum_{j=1}^{K} \sqrt{\Phi_w\left(\Omega_{x,i}, \Omega_{y,j}\right) \Delta\Omega_{x,i}\Delta\Omega_{y,j}} \cdot \sin\left(\Omega_{x,i} \cdot x + \Omega_{y,j} \cdot y + \psi_{ij}\right) \quad (2.2)$$

In the context of the VON KÁRMÁN PSD, the SHINOZUKA algorithm leads to a large number of required harmonics with equidistantly distributed frequencies. This is because the lower harmonics require a fine frequency resolution, and consequently the number of harmonics increases to realize an appropriate representation of the higher harmonics due to the logarithmic scales of the VON KÁRMÁN PSD. Truncation of higher frequencies would lead to an under-representation of energy. In Ref. [270] another realization algorithm is used instead, which better fits the logarithmic scales of the VON KÁRMÁN PSD, namely the BORGMAN approach, see Ref. [38]. This approach has been developed in context of ocean-wave simulation and incorporates a different discretization logic of the PSD. In contrast to the SHINOZUKA algorithm, where equally spaced harmonics are distributed, the BORGMAN approach uses discrete frequencies that are related to constant fractions of energy, see Eq. 2.3 and Ref. [38]. This formulation is computationally more efficient, since the PSD does not have to be evaluated for each element during the summation, since the magnitude of the harmonics is constant per se. In addition, a much lower number of harmonics can be selected, while the contribution of higher frequencies is covered appropriately, see Ref. [270].

$$w\left(x, y\right) = \sqrt{2}\frac{\sigma_w}{K} \sum_{l=1}^{K^2} \sin\left(\Omega_{x,l} \cdot x + \Omega_{y,l} \cdot y + \psi_l\right) \quad (2.3)$$
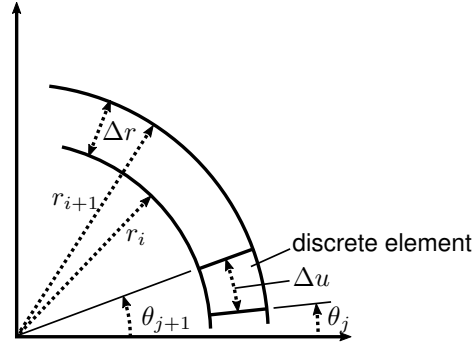
Figure 2.4.: Element used for the discretization of the VON KÁRMÁN PSDs.

The discrete frequencies have to be computed in advance, which takes some computational time but this can be executed once during a preprocessing step of the turbulence simulation. The developed algorithm to distribute the harmonics is described in Fig. A.2. The algorithm uses polar coordinates, because this is in better geometrical agreement with the shape of the VON KÁRMÁN PSDs, see e.g. Fig. A.1. This idea is proposed in Ref. [270] and adopted in this work. The corresponding VON KÁRMÁN PSDs expressed in polar coordinates are available from Ref. [270] as well. The geometry of one discrete element expressed in polar coordinates is shown in Fig. 2.4. The algorithm consists of two iteration cascades, while the inner cascade consists of two consecutive loops. The first inner loop searches for an integer value of n azimuthal elements of shape $\Delta r = \Delta u$ with $\Delta u = (r_{i+1} + r_i) \frac{\pi}{n}$ and $\Delta r = r_{i+1} - r_i$, see Fig. 2.4, such that the sum of energy represented by the n elements corresponds to the energy located between r_i and r_{i+1}, see box C in Fig. A.2. The geometrical constraint $\Delta r = \Delta u$ is satisfied by the expression in box B. Note that this expression is a first estimation. The azimuthal distribution of the n elements is refined later by the second inner loop. Since the energy associated with the n elements is not necessarily equivalent to the n/K^2-fraction of the overall energy due to discretization inaccuracies, the energy-mismatch E_{mis} is computed in box D to be compensated during the subsequent outer iteration. Once the radial coordinate r_{i+1} and the associated number n of azimuthal elements is found, the second inner loop distributes the azimuthal stations θ_j. This is required since the PSD $\mathbf{\Phi}$ is not necessarily rotationally symmetric. Once the next station θ_{j+1} is found based on the associated energy fraction computed in box E, the step is repeated $n - 1$ times by incrementing j, since the last station is located at 2π and does not have to be computed. Note that the j is counted starting with 0 hence the measure $n-2$ is used in box F to track if all azimuthal stations θ_j of the n elements are computed. Once one ring-element is computed, the outer loop increments the radius and the procedure is repeated until the total energy E_{tot} is fully distributed both radially and azimuthally by the K^2 elements, which is computed in box G. Subsequently, the coordinates are mapped to the center of each element which is not indicated in Fig. A.2. Finally, the polar coordinates are transformed into cartesian coordinates.

In Fig. 2.5 the obtained frequencies using the algorithm from Fig. A.2 are compared with reference values obtained from Ref. [270]. In general, the discretization of higher-dimensional PSDs involves some level ambiguity related to the aspect-ratio of the discrete elements. The algorithm used in this work seeks for equal lengths of Δr and Δu for each individual element

approximately as described above. Note that in Ref. [270] a different logic is used. However, the radial cumulative distribution of energy is in agreement with the reference, see Fig. 2.5(a). Note that only the lower and upper 10% of the distribution are available from Ref. [270]. In contrast, the normalized harmonics differ from each other expressed in cartesian coordinates, see Fig. 2.5(b). The involved frequency normalization is described in Ref. [270] in detail. Since discrete harmonics are computed in the range of 0% to 99.9% of total energy, the frequency bandwidth covered in this work is slightly higher than in Ref. [270], see Fig. 2.5(b).
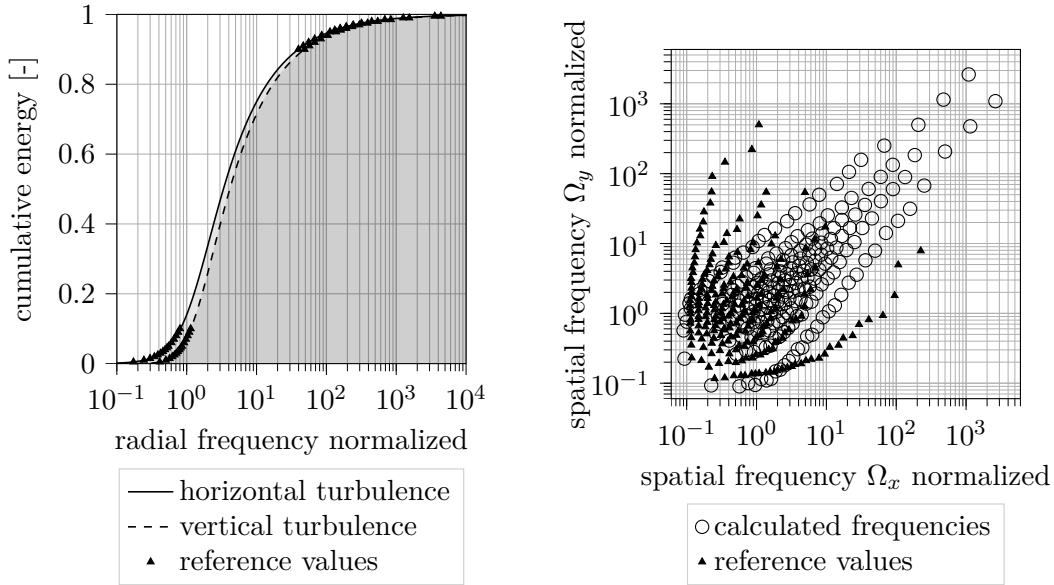
(a) Energy distributed along radial normalized frequency compared to Ref. [270].

(b) Discrete normalized harmonics in cartesian coordinates compared to Ref. [270].

Figure 2.5.: Distribution of energy according to the VON KÁRMÁN spectrum along the radial coordinate and discrete frequencies expressed in cartesian coordinates obtained with the algorithm depicted in Fig. A.2. Figures adopted from Ref. [258].

The baseline flight-condition selected for this work is specified in table 1.2. For this flight-condition, the PSD of the vertical turbulence component obtained from the FullFT model is shown in Fig. 2.6(a) for a non-rotating observer. Obviously, the numerical time-domain based solution and the theoretical slope of the VON KÁRMÁN PSD are in agreement up to at least 100Hz if $K = 2500$ BORGMAN-harmonics are selected. If the number of BORGMAN-harmonics is reduced, the individual harmonics are visible in the spectrum, see Ref. [257]. However, 2500 harmonics approximate the spectrum up to 100Hz appropriately for a non-rotating observer.

In Fig. 2.6(b) the PSD of the vertical turbulence component recorded by a rotating observer is illustrated. Rotational sampling-effects are clearly visible, introduced at rotor-speed and integer multiples. This induces a visible shift of energy from lower to higher frequencies, which is in agreement with physics, see e.g. Ref. [98]. Since the higher frequencies are predominantly characterized by rotational sampling effects, the number of BORGMAN har-

(a) Hub-element sampled, baseline.

(b) Blade-element sampled, baseline.

(c) Blade-element sampled, loiter.

(d) Blade-element sampled, cruise.
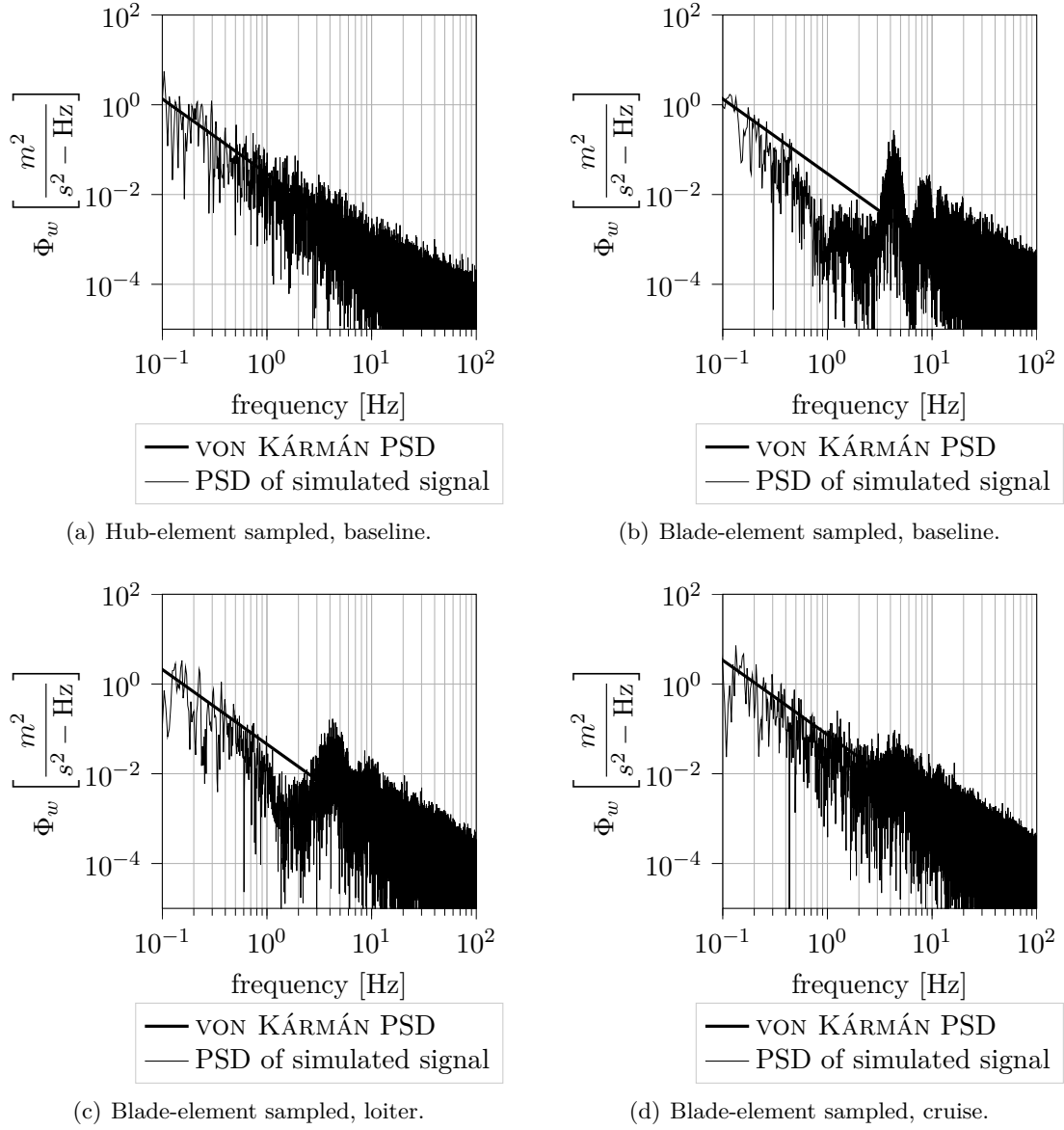
Figure 2.6.: PSDs of atmospheric turbulence velocity in vertical direction simulated with the FullFT model using 2500 BORGMAN harmonics. The atmospheric conditions are summarized in table 1.2. The blade-element sampling is carried out at 75% radial station. Figures adopted from Ref. [258].

monics is less influential on the spectrum compared to hub-element sampling. In this case the number of harmonics can be decreased to $K = 500$ without a significant change in the spectrum. If the flight-speed is increased as specified in table 1.2, the rotational sampling effects are less pronounced, see Fig. 2.6(c) and Fig. 2.6(d), because with increasing advancing ratio, the turbulence fluctuations are convected faster through the rotor plane. Hence, cyclostationarity becomes less relevant. Note that with increasing speed the reference slope of the VON KÁRMÁN model slightly increases, which is a result of the velocity dependency of the VON KÁRMÁN PSDs. Similar results, not explicitly shown in this work, are obtained for the other two turbulence components and other turbulence intensities.

The simulation of atmospheric turbulence over at least 10 minutes allows to fully cover the harmonics which are associated with atmospheric turbulence according to the VAN DER HOVEN wind spectrum, see Fig. 2.1. In Fig. 2.7(a) it is shown that the normalized probability distribution of the turbulence velocities sampled over 10 minutes at the MR hub are close to GAUSSIAN distribution. If the turbulence velocities are sampled at a rotating blade-element, the probability distribution shows a light level of skewness, see Fig. 2.7(b). According to table A.1, the statistical parameters obtained from a simulation over 10 minutes are in agreement with the VON KÁRMÁN reference values.

If the simulation time is reduced to 4 minutes, the normalized probability distributions of the turbulence velocities show increased kurtosis compared to 10 simulated minutes, see Fig. 2.8. In case of blade-element sampling the probability distribution is characterized to some extend by skewness again, see Fig. 2.8(b). The statistical properties of turbulence simulated over 4 minutes are summarized in table A.1 as well. Hub-element sampling over 4 minutes shows the largest discrepancies from the reference values. Interestingly, both first- and second-order statistics remain close to the reference even in case of blade-element sampling. In nearly all cases, v_x shows a positive mean value bias, which is however still below 1m/s. This effect is slightly reduced if the simulation time is increased.

In Fig. A.3(a) and Fig. A.3(b) the auto-correlations over time are depicted. The correlations are characterized by a decay in the first seconds of the simulation. This indicates that during 4 minutes of simulation the turbulence signals do not repeat. Based on the results provided in this section, the FullFT model is considered to be valid when used in context of at least 4 minutes of simulation time.

2.4. Rotor-Hub Based Turbulence Model

For comparison, a second model referred to as Hub-Based DRYDEN Turbulence (HubDT) model is used in this work, which is governed by the DRYDEN turbulence model and does not satisfy KOLMOGOROV's law. The *continuous* DRYDEN model implementation from Ref. [313] is used. The implementation of the model is already validated in Ref. [257], hence only the most important fundamentals are repeated in this work. The underlying concept is to pass GAUSSIAN white noise through filters that color the spectrum according to the DRYDEN

(a) Hub-element sampled.

(b) Blade-element sampled.
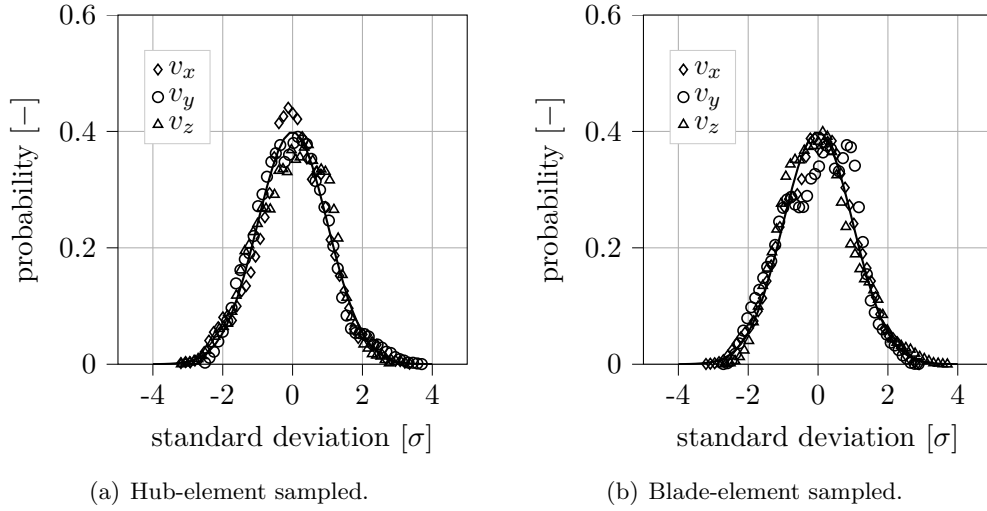
Figure 2.7.: Normalized histogram of turbulence velocities simulated for the baseline flight-condition over 10 minutes with the FullFT model. The corresponding mean values and standard deviations are summarized in table A.1.

(a) Hub-element sampled.

(b) Blade-element sampled.
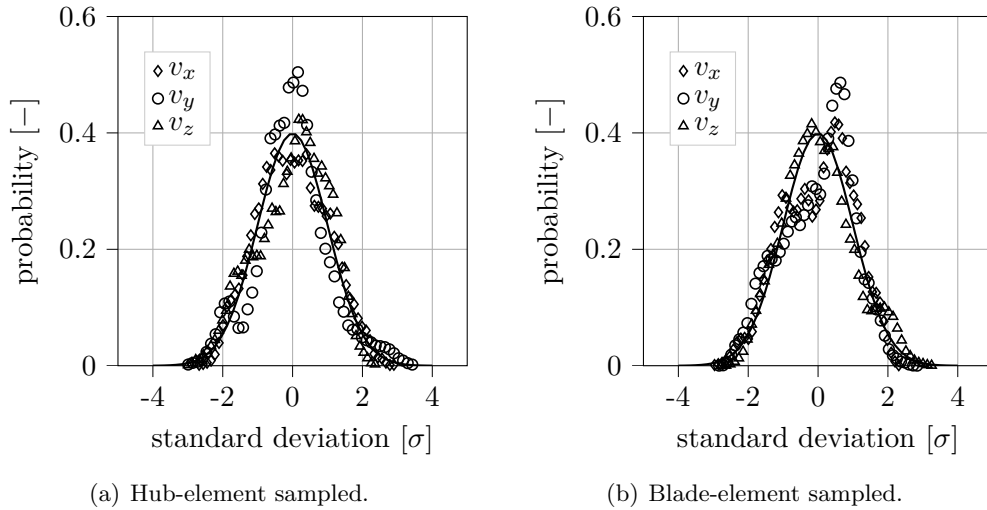
Figure 2.8.: Normalized histogram of turbulence velocities simulated for the baseline flight-condition over 4 minutes with the FullFT model. The corresponding mean values and standard deviations are summarized in table A.1.

PSDs, see Fig 2.9. Note that this converges the signal's probability distributions towards GAUSSIAN distribution due to the Central Limit Theorem (CLT). Online-filtering is possible since the DRYDEN PSDs are characterized by rational functions and the corresponding filters can be determined in the time-domain exactly by analytical transformation. Note that approximations of the irrational VON KÁRMÁN PSD functions have been published, which allow to realize equivalent online-filters in time-domain, see e.g. Ref. [149]. The filter-states are integrated in time using an explicit EULER-scheme. The approach realizes six turbulence components in the non-rotating domain at the MR hub, namely three translational components $\mathbf{v}_t$ and three rotational components ϕ. The sampling in the two-dimensional turbulence plane according to Fig. 2.3 is realized using Eq. 2.4. $\mathbf{v}_{BE}$ represents the velocity sampled at a rotating blade-element located at $\mathbf{r}_{BE}$ with respect to the MR hub. Within the DRYDEN model the MR diameter is selected as equivalent wing-span.

Figure 2.9.: Illustration of atmospheric turbulence simulation using a shaping filter. Figure taken from Ref. [258].

$$\mathbf{v}_{BE} = \mathbf{v}_t + \phi \times \mathbf{r}_{BE} \tag{2.4}$$

The PSD obtained from time-domain turbulence simulation with the HubDT model and recorded by a non-rotating observer is in agreement with the reference DRYDEN PSD, see Fig. 2.10(a). The turbulence properties are computed for the baseline flight-conditions specified in table 1.2. In Fig. 2.10(a), the steeper negative slope of the DRYDEN PSD compared to the VON KÁRMÁN PSD is visible. At lower frequencies the DRYDEN PSD is a good approximation, however, at higher frequencies the discrepancy with KOLMOGOROV's law increases. If the turbulence velocities are sampled at 75% radial station of the rotating blade, Fig. 2.10(b) indicates that the HubDT model introduces rotational sampling effects. The magnitude at rotor rotational frequency is comparable to the FullFT model, while the peak is more narrow, see Fig. 2.6(b). The significant difference to the FullFT model is that no energy is shifted from lower to higher frequencies. Hence, cyclostationarity is not resolved appropriately by the HubDT model, see e.g. Ref. [98]. Instead, additional energy is introduced by the modeling approach. If the advancing ratio is increased, the rotational sampling effects are less pronounced, see Fig. 2.10(c) and Fig. 2.10(d). This result is already discussed in the context of the FullFT model, see section 2.3. Note that with increasing speed the reference slope of the DRYDEN model slightly increases, which is a result of the velocity dependency of the DRYDEN PSDs, which is obtained for the VON KÁRMÁN model as well. An equivalent agreement visible in Fig. 2.10 is found for all turbulence components and all investigated turbulence intensities. Hence, they are not shown explicitly.

(a) Hub-element sampled.

(b) Blade-element sampled, baseline.

(c) Blade-element sampled, loiter.

(d) Blade-element sampled, cruise.
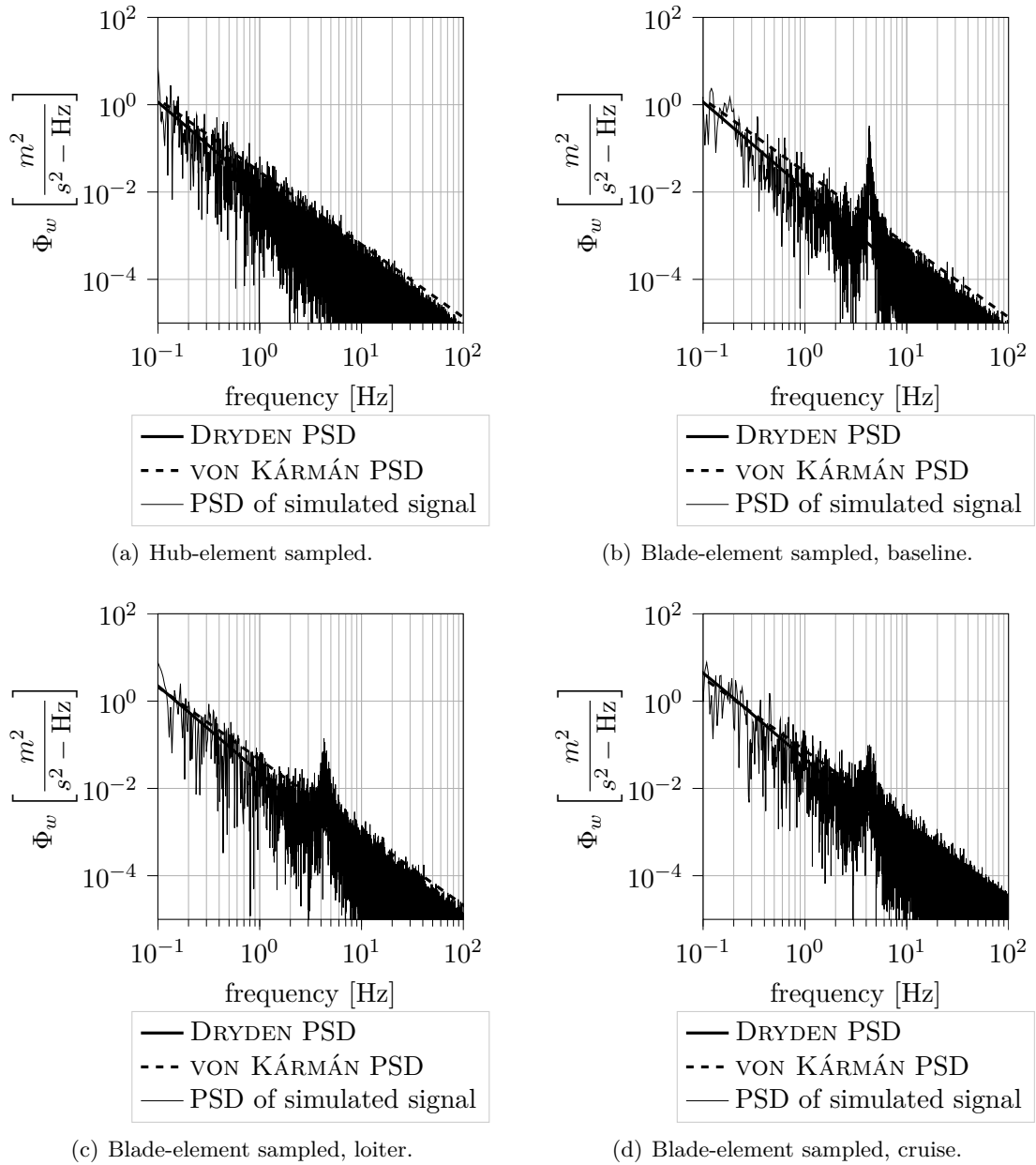
Figure 2.10.: PSDs of atmospheric turbulence velocity in vertical direction simulated with the HubDT model. The atmospheric conditions are summarized in table 1.2. The blade-element sampling is carried out at 75% radial station. Figures adopted from Ref. [258].

Like the FullFT model, the turbulence velocities generated with the HubDT model over 10 minutes show GAUSSIAN behavior in case of hub-fixed sampling, see Fig. 2.11(a) as well as in case of blade-element sampling, see Fig. 2.11(b). The comparison of both sampling strategies reveals that the kurtosis is increased if the turbulence velocities are sampled at the rotating blade but not the skewness, like it is obtained for the FullFT model. In general, the rotational components are closer to GAUSSIAN PDF than the translational components. This is assumed to result from the CLT. In particular, the components ω_y and ω_z involve more processing steps than the other components since the filters of both components are fed with the turbulence components v_z and v_y respectively, rather than independent GAUSSIAN white noise signals.

If the simulation time is reduced to 4 minutes the normalized probability distribution of the hub-sampled signals show an increased kurtosis compared to the data obtained from 10 simulation minutes, see Fig. 2.12. The probability distribution of blade-element sampled signals is not much affected by reduced simulation time, see Fig. 2.11(b) and Fig. 2.12(b) in comparison. The statistical properties are compared with the theoretical values according to the DRYDEN model in table A.2 for the baseline flight-condition specified in table 1.2. Mean value and standard deviation are approaching the reference values, with increasing simulation time. Blade-element sampling is not identified to introduce a larger mismatch compared to hub-element sampling.

The auto-correlation of hub-fixed sampled turbulence velocities show a clear decay, see Fig. A.4(a) This is true for blade-element sampling as well, see Fig. A.4(b). Hence, the signals do not repeat during the considered time. In particular, the rotational components exhibit a fast decay. The lateral translational component v_y shows the largest oscillations even after several minutes if hub-element sampling is employed. Based on the results presented in this section, the HubDT model is interpreted to be correctly implemented and suitable for aeroelastic analysis of at least 4 simulated minutes.

(a) Hub-element sampled.

(b) Blade-element sampled.
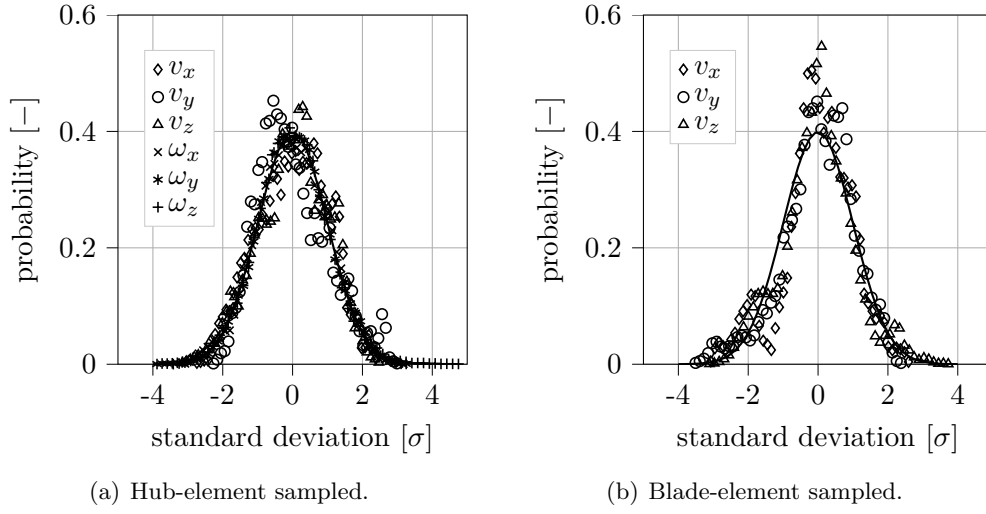
Figure 2.11.: Normalized histogram of turbulence velocities simulated for the baseline flight-condition over 10 minutes with the HubDT model. The corresponding mean values and standard deviations are summarized in table A.2.

(a) Hub-element sampled.

(b) Blade-element sampled.
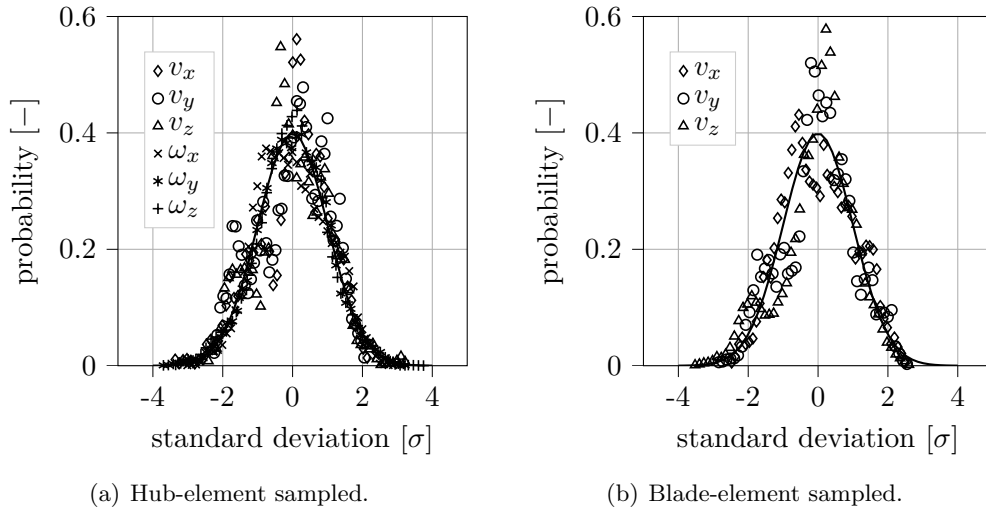
Figure 2.12.: Normalized histogram of turbulence velocities simulated for the baseline flight-condition over 4 minutes with the HubDT model. The corresponding mean values and standard deviations are summarized in table A.2.

3. Helicopter Model

Note that some of the result presented in this chapter are summarized and presented as well in the final report of the project VARI-SPEED, German aviation research program LuFo, reference number 20E1506.

The concept of modal analysis is to extract a linear representation of a structural system from its response to some input. Whether or not the input is measured, modal analysis requires most importantly sufficient excitation of the system in the frequency range of interest. In this work, the input includes both atmospheric turbulence as well as the helicopter-induced flow field. While the atmospheric turbulence modeling is described in the previous chapter 2, the current chapter introduces the aerodynamic models. However, the prediction of the helicopter structural response is not only concerned with appropriate input modeling but with appropriate transfer-path modeling as well. In this sense, next to the aerodynamic models, this chapter introduces the structural models to describe the transfer-path mathematically.

Important aspects to be modeled for the prediction of helicopter vibrations are summarized in Ref. [70], although the aim of the modeling approach established in this work is not the accurate prediction of structural vibrations. Since the modal analysis, see the next chapter 4, can only be demonstrated within the limitations of the modeling approach, effects known to characterize the helicopter structural response in atmospheric turbulence are explicitly included in the simulation models. In addition, the computational scheme to solve the governing equations is selected such that all relevant effects are resolved appropriately. The related frequency range of interest ranges up to 30Hz which covers all relevant airframe eigenfrequencies. Vibrations arising from the dynamical system like the gearbox, the shafts, the engines, etc. as well as acoustics are neglected within this study because they are expected to be related with significantly higher frequencies compared to the eigenfrequencies of the airframe considered in this work.

Apparently, the response of a dynamical system to random loading is random as well, see e.g. Ref. [205]. For linear systems under random loading, stochastic solutions can be obtained analytically, which can be solved either in frequency- or time-domain [205, 180]. Periodically time-varying systems subject to random loading are treated e.g. in Refs. [243, 159]. It is concluded in Ref. [243] that LTP systems subject to random input can mathematically be treated equivalently to LTI systems. More specifically, closed-form solutions have been used to study the influence of atmospheric turbulence on helicopter rotors as well, see Refs. [174, 93, 131, 104].

In this work time-domain based MONTE CARLO simulation is used to solve the helicopter dynamics subject to atmospheric turbulence, see e.g. Ref. [128]. This approach is selected, because it resolves the aperiodic processes introduced by atmospheric turbulence and allows to couple the different non-linear models. A synchronous time-step width for all models is selected such that the phenomena of interest are resolved sufficiently and that the forward-stepping exchange between the models is an appropriate approximation such that an inter-time-step-iteration of the solution can be avoided. This is found to be achieved with a time-step width of 10^{-3}s. The involved solvers all converge using this time discretization. Since the approach selected involves both temporal and spatial discretization, the solutions are only an approximation within certain limits. The limitations include e.g. the frequency content, the spatial resolution of atmospheric turbulence waveforms, as well as the number of structural modes.

Fig. 3.1 provides an overview of the modeling framework. The structural model consists of the MR model (section 3.2) and the modal airframe (section 3.5). The modal airframe includes the structural representation of both the Vertical Stabilizer (VS) and the Horizontal Stabilizer (HS), which are together referred to as empennage. An additional model is included to represent the empennage aerodynamics, see section 3.4. The purely aerodynamic TR model is introduced in section 3.4 as well. The TR model includes a uniform and time-invariant inflow model. In contrast, the MR inflow model is non-uniform and dynamic, described in section 3.1 and explicitly depicted in Fig. 3.1. The MR inflow velocities are computed based on the MR airloads, which are computed using airfoil-table interpolation. The resulting MR inflow averaged over the MR but varying in time is respected by the HS aerodynamics depending on the rotor-wake skew-angle. The atmospheric turbulence model introduced in chapter 2, calculates turbulence velocities for all aerodynamic reference points involved in the simulation. This includes the MR blades, the TR as well as the empennage. The turbulence velocities are superimposed with the absolute velocity of each aerodynamic element individually. To operate the MR in trimmed conditions under the influence of unsteady atmospheric turbulence, a trim-controller is used, see section 3.3. The MR thrust as well as the roll- and pitch moments, which are passed to the controller, are low-pass filtered.

Both the MR and airframe models are formulated in separated mathematical frameworks. This allows to solve the MR with a solver that appropriately handles the inherent non-linearities, see Eq. 3.1, where $\mathbf{x}_{MR}$ represents the MR states and $\mathbf{u}_{MR}$ comprises the MR control inputs. The separated mathematical formulation of the elastic airframe allows to efficiently solve each mode independently. The elastic airframe is represented by 8 modes governed by second-order ordinary differential equations, see Eq. 3.2. $\omega_{0,k}$ is the eigenfrequency of the undamped system, ξ_k is the relative damping ratio, m_k the modal mass and Ψ_k the eigenvector of mode k. The eigenvector Ψ_k projects the external forces $\mathbf{F}(t)$ onto the mode k. The external forces are computed from Eq. 3.3 based on the MR hub loads, the TR hub loads, the distributed VS airloads and the distributed HS airloads. All forces are therefor transformed into a common airframe-fixed reference coordinate system. The computation of the interface loads of all components is described in the following sections. The airframe displacements, velocities and accelerations are computed based on Eq. 1.4 given in the introduction.

$$\mathbf{f}_{\mathrm{MR}}\left(\ddot{\mathbf{x}}_{\mathrm{MR}}, \dot{\mathbf{x}}_{\mathrm{MR}}, \mathbf{x}_{\mathrm{MR}}, \mathbf{u}_{\mathrm{MR}}\right) = \mathbf{0} \tag{3.1}$$

$$\ddot{q}_k + 2\xi_k \omega_{0,k} \dot{q}_k + {\omega_{0,k}}^2 q_k = {\Psi_k}^T \frac{\mathbf{F}\left(t\right)}{m_k} \tag{3.2}$$

$$\mathbf{F}\left(t\right) = \mathbf{F}_{\mathrm{MR}}\left(t\right) + \mathbf{F}_{\mathrm{TR}}\left(t\right) + \mathbf{F}_{\mathrm{VS}}\left(t\right) + \mathbf{F}_{\mathrm{HS}}\left(t\right) \tag{3.3}$$

At the interface between the elastic airframe and an attached device like a rotor, loads are exchanged in both directions, which need to be accounted for in the helicopter model, see Ref. [70]. If both directions are accounted for in the simulation, this is referred to as two-way coupling in literature, whereas one-way coupling considers only loads acting on the airframe and neglects the response of the airframe in the attached components, see e.g. Ref. [255]. This terminology is used in the following as well. In particular, the bidirectional relationships between the airframe and the MR are an important property of helicopters. To account for the airframe impedance in the rotor simulation, so called impedance-matching methods have been used in the past, see Refs. [130, 137, 92]. This approach employs one-way coupled simulation, where interface loads computed by the rotor model are introduced into the elastic airframe, while the impedance is accounted for by including pre-computed corrections. A monolithic approach to account for the airframe impedance is e.g. HERTING's method, which includes the modal airframe model, see Eq. 3.2, into the solution process of the non-linear rotor model, see Eq. 3.1 and Ref. [31]. Another alternative used in literature is to assume an infinite airframe impedance in the rotor simulation by using one-way rotor-airframe coupling. In Refs. [92, 55, 4, 258] this approach was previously found to over-predict the elastic airframe response, while the two-way coupling approach shows better agreement with flight-test data. In Ref. [65] higher hubloads are obtained with one-way simulation as well, but the difference to two-way simulation is small. Next to the MR modeling, the airframe impedance is a relevant property for the stabilizer dynamics as well. In Refs. [256, 255] aeroelastic studies are conducted based on a helicopter very similar to the one used in this work. These studies focus on the aerodynamic load-path, while the structural load-path is neglected. In addition, broadband vibrations are not analyzed. A conclusion of the studies is that two-way coupling is preferred over one-way coupling, although not all sensors show an improvement using two-way coupling in comparison with flight-test data.

In this work, the bidirectional relationships between the elastic airframe and the attached components are resolved by time-domain based iteration, indicated by the structural feedback-loop in Fig. 3.1. The two-way coupling procedure in this figure is iterated at each time-step. As long as the time-step width is small compared to the time scales of the oscillating phenomena of interest, the airframe impedance is assumed to be appropriately resolved. This is because the elastic airframe dynamics are than respected by the attached components with a negligible time-delay. The coupled simulation approach is further validated in section 3.5 based on MR hub accelerations. The structural feedback-loop can be deactivated via the switch indicated in Fig. 3.1, which allows to run a one-way coupled airframe simulation and to consider the modal airframe as an independent model. This is particularly useful in the context of output-only modal analysis, since the modal properties of the airframe are in this case known a priori.
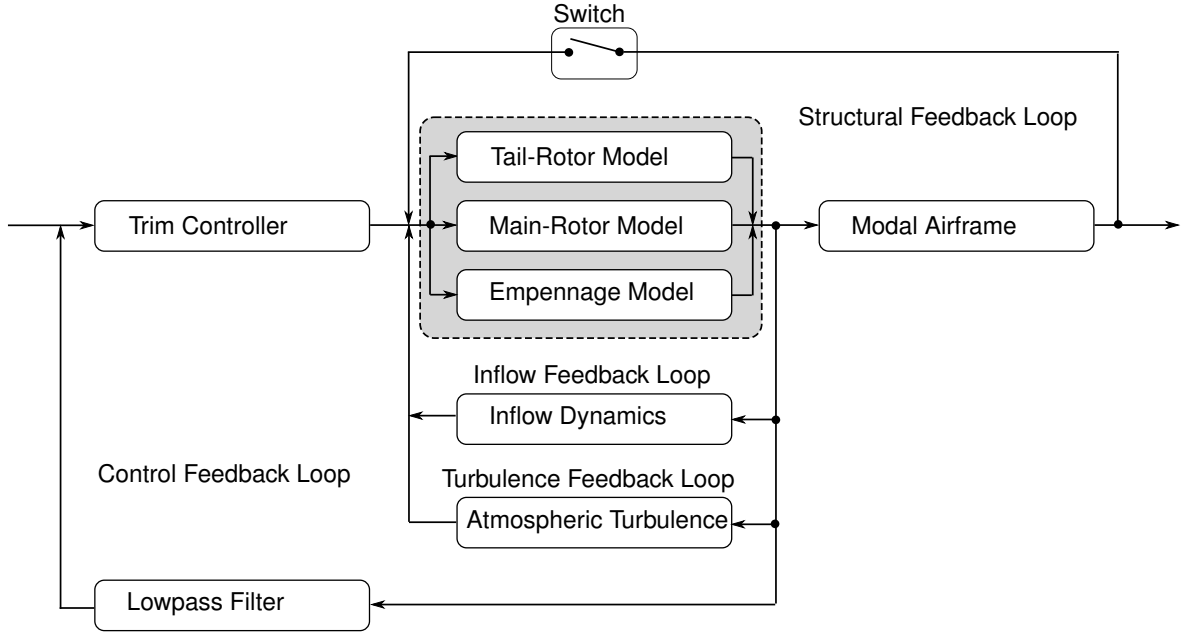
Figure 3.1.: Coupling-scheme and involved simulation models. The coupling strategy can be switched between one-way and two-way coupling using the depicted switch.

Dymore, see Ref. [30], is selected to model the MR, which includes the dynamic inflow, the airloads, the structure and the controller, due to mainly three reasons. First, *Dymore* provides adequate solvers that allow transient analysis of the non-linear rotor in time-domain. Second, during the simulation the rotor-states can be accessed and variables can be modified, which allows to coupled the rotor with the turbulence model and the elastic airframe. Third, the rotor aerodynamics and inflow dynamics can be modeled appropriately in conjunction with the structural dynamics. *Dymore*, the elastic airframe model and the atmospheric turbulence models are written and realized in *C*. To enable time-synchronous coupling they are wrapped to *Python* using *Swig*. The coupling of the TR model and the empennage aerodynamics is straightforward, since both are written in *Python*. For more details about the implementation see Ref. [258].

3.1. Inflow Model and Superposition with Turbulence Velocities

Since the MR is constantly operating in its own downwash, an appropriate model is used to resolve the radial, azimuthal and temporal variations of the inflow velocity. The selection of the inflow model significantly affects the simulated MR-airframe coupled vibration levels, see Ref. [65]. This is because helicopter vibrations are e.g. induced by complex aerodynamic phenomena, which are only resolved by models with higher fidelity, see Refs. [285, 70]. In this work, an accurate prediction of the structural vibrations is considered to be of no advantage in the scope of output-only modal analysis based on broadband vibrations. Additional arguments why specifically CFD methods are not used in this work are discussed in section 2.2.

Although the surrounding flow is affected by MR self-generated turbulence, see Refs. [158, 134, 166], this effect is neglected in this work, since it is assumed to provide no significant benefit for the output-only modal analysis.

In this work, a two-dimensional finite-state PETERS-HE dynamic inflow model is used, see Ref. [234]. The model represents the rotor-disc as a time-varying velocity field along both, radial and azimuthal coordinate. In agreement with Ref. [126], 12 states are selected to represent the dynamic inflow disc. An explicit RUNGE-KUTTA algorithm of 4th order is used to solve the inflow dynamics. The inflow velocities are superimposed with the turbulence velocities, which is assumed to be supported by the REYNOLDS decomposition, see Ref. [23]. The summation of the velocity components is carried out for each aerodynamic blade-element individually, in agreement with previous approaches from literature, see Refs. [188, 270]. After the summation, element-wise airloads are computed based on the total element velocity.

Although the inflow and turbulence velocities are superimposed, the inflow velocities are indirectly affected by atmospheric turbulence through induced MR oscillations and rotor re-trim to compensate the influence of atmospheric turbulence. The following table 3.1 compares the differences with a reference simulation in calm air. In light atmospheric turbulence the model predicts 3.74% less mean inflow velocity and correspondingly 2.84% less MR torque, while the MR trim-controller maintains the MR thrust up to an accuracy of 0.15%. The same tendency is discovered in moderate turbulence, see table 3.1. The explanation for this behavior is that during the considered simulation time the averages of the turbulence velocities are not equal to zero but can be biased up to 1m/s, see e.g. table A.1. These biased mean values can introduce power into the rotor system depending on the turbulence direction. In this context, the vertical turbulence velocity has the most dominant influence. However, asymmetric in-plane components with respect to the helicopter x-z-plane can influence the MR shaft-power as well.

	calm air	light turbulence	moderate turbulence
mean inflow [m/s]	8.458	8.141 (-3.74%)	8.273 (-2.18%)
mean thrust [N]	66767.300	66664.667 (-0.15%)	66643.729 (-0.19%)
mean torque [Nm]	35412.020	34405.254 (-2.84%)	35099.604 (-0.88%)

Table 3.1.: Difference between MR inflow, thrust and torque in calm air compared to light and moderate turbulence.

3.2. Elastic Main-Rotor and Airloads Model

The MR introduces the most significant amount of vibration, see section 1.1. Consequently, a MR model is included in the modeling framework to account for related loads. The model consists of structural and aerodynamic sub-models. Both domains are closely related since aerodynamic loads are influenced by the rotor motion and vice versa. The structural model is depicted for one reference rotor-blade in Fig. 3.2, which is adopted from Ref. [258]. The total number of rotor-blades is $N_b = 4$. The geometrical properties indicated in Fig. 3.2 can be found in Ref. [258]. The model consists of an elastic rotor-shaft with a rigid rotor-head attached to it on top. The blade-attachment is modeled as a rigid body as well and connects the elastic rotor-blade with the rotor-head via a spherical joint, which allows flap-, lead-lag- and feathering-motion. This represents the UH-60A elastomeric bearing assembly reasonably, see Ref. [272]. The lead-lag damper is connected to both the blade-attachment and the MR hub. The non-linear slope of the damper is depicted in Fig. A.8 and available from Ref. [136]. The pitchlink connects the blade-attachment with the rotating part of the swashplate and transfers control inputs from the swashplate to the rotor-blade. The rotating part of the swashplate is carried by two scissors. Note that only one scissor is indicated in Fig. 3.2. The non-rotating part of the swashplate is supported by three actuators, which are used for controlling the MR system. On top of the assembly, one of four bifilar absorbers is illustrated.

The model allows both rigid and elastic rotor-blade motion. Rigid motion is included because it is essential for rotor trim and it characterizes the rotor response towards atmospheric turbulence. Elastic blade modes are incorporated in the model to resolve elastically transferred vibrations of higher frequencies, see Refs. [90, 268]. An implicit time-integration scheme called *generalized-alpha* is used to solve the non-linear rotor dynamics, which provides sufficient numerical robustness, see Refs. [22, 29].

The elastic rotor-blades are modeled using finite-element models based on HODGES' beam theory, which covers important non-linear effects, see Ref. [129]. A number of 14 elements is equidistantly distributed in radial direction, which is discovered to resolve the eigenmodes up to the maximum frequency of interest of 30Hz appropriately. In Fig. 3.3 the simulated eigenfrequencies agree with data obtained from EMA, see Ref. [113]. For better comparison, the EMA setup is fully modeled, which includes the rotor-blade, the bungee chord attachment and the shaker, see Ref. [113]. The corresponding mode-shapes are depicted in Fig. A.5. These are in good agreement with the experimental test data from Ref. [113]. Note that the three upper flap-modes are not precisely resolved. For structural validation, the three upper flap modes are computed in Ref. [258] with an increased structural resolution of 40 finite elements. In comparison it is anticipated that increasing the number of elements results is much better agreement of the higher flap-modes, while the lower modes are not much affected. Hence, the mismatch obtained in Fig. A.5(b) is in fact rather attributed to the coarse discretization than to inaccurate structural properties. However, in this work 14 beam elements are sufficient, since centrifugal stiffening effects increase the flap frequencies such that the upper three flap-modes are located above 30Hz once the rotor operates at nominal speed, see Fig. A.6(b).
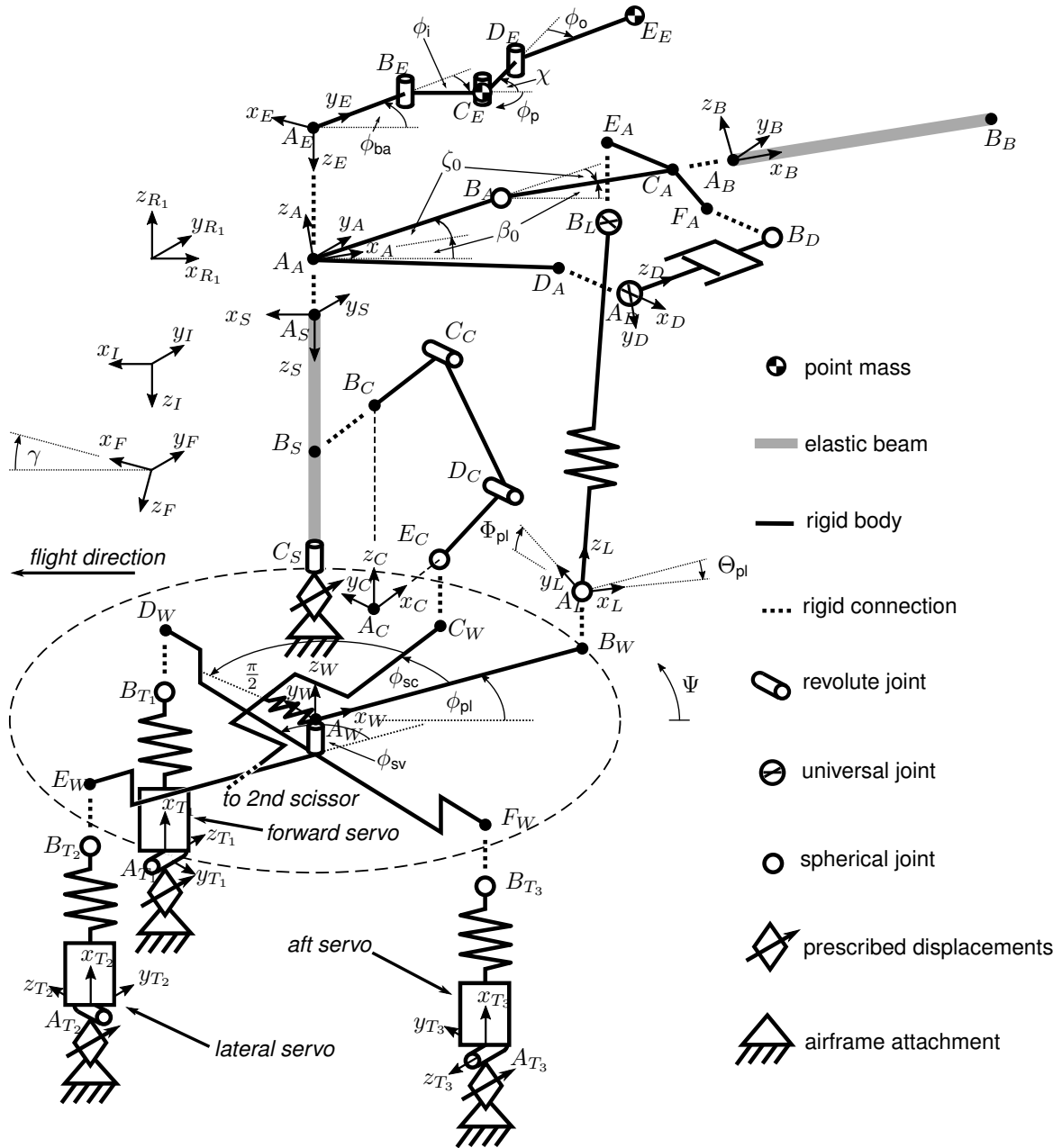
Figure 3.2.: Mechanical MR model. See Ref. [258] for structural and geometrical properties. Figure adopted from Ref. [258].
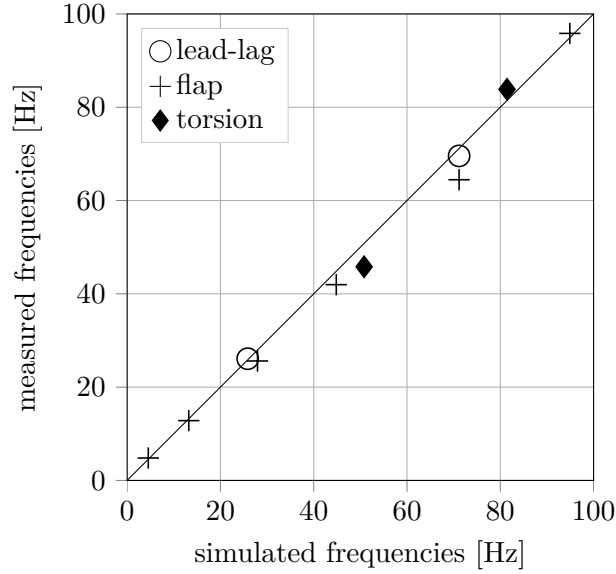
Figure 3.3.: Eigenfrequencies of the non-rotating MR blade. Calculation involves 14 beam elements with linear shape-function. In Ref. [258] the equivalent figure is published computed with 40 elements.

Since no experimental data is available from the rotating domain, the effects of centrifugal stiffening are compared to reference simulations based on the CAMPBELL diagram shown in Fig. A.6. Two setups, one with soft and the other with nominal pitchlink stiffness are compared. The nominal stiffness is the actual stiffness of the UH-60A MR pitchlinks, while the soft parameterization is obtained from literature for comparison only, see Ref. [127]. In particular, the model is in agreement with Reference 1 and mostly in agreement with Reference 2 for both pitchlink stiffnesses. Hence, the stiffening effects due to rotation and the structural properties of the rotor-blades are considered to be represented correctly.

Since the elasticity of the control-linkage has an effect on the vibratory mechanisms, see Ref. [70], an elastic MR primary control system is included in the structural model. This includes components in the rotating domain as well as in the non-rotating domain. The elasticity of the control linkage in the rotating domain is modeled close to the actual geometry, see Fig. 3.2, while the elasticity of the non-rotating linkage is incorporated by equivalent servo elasticity. The elasticity of the pitchlinks and the servos is approximated by one-dimensional spring elements. The masses of the pitchlinks, the rotor-blades and the swashplate are included in the multi-body model, whereas the masses of the blade-attachments and the rotor hub are represented by the modal airframe model. This is a reasonable approximation, since the rotor hub cannot move freely during the rotor computation, because its motion is fully prescribed by the elastic airframe response. Hence, only the inertias of the blade-attachments are theoretically relevant for the dynamic states of the MR model. However, neglecting these inertias in the multi-body simulation is acceptable with regard to the much higher inertias of the attached rotor-blades. The rotor-shaft elasticity and mass are covered in the elastic airframe model as well, see section 3.5, and the shaft is included in Fig. 3.2 only for better understanding. The actuators of the MR, see Fig. 3.2, are not connected with the elastic
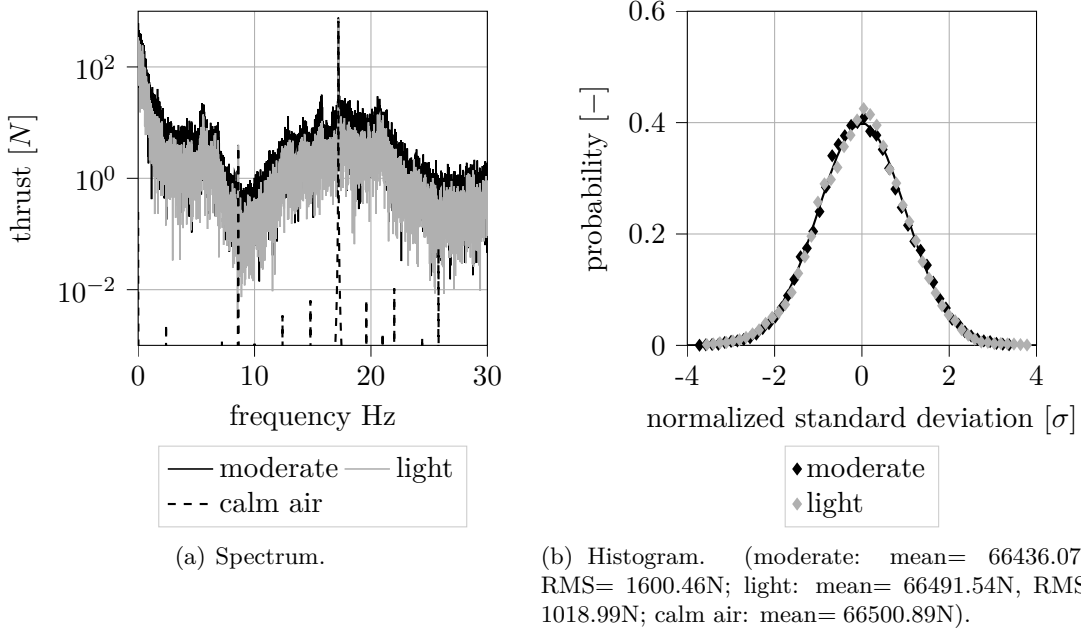
airframe, which would be important to cover mechanical control feedback-effects, see e.g. Ref. [211]. The coupling between the MR and the elastic airframe is further elaborated in section 3.5. The bifilar absorbers tuned towards 3/rev in-plane frequency and depicted in Fig. 3.2 are not used in this work. The reason is that the 3/rev vibrations are already sufficiently predicted without the absorbers compared to flight-test data, whereas other harmonics show higher discrepancies which would not improve if the bifilar absorbers are considered, see Fig. A.13.

To model the rotor aerodynamics, blade element theory in conjunction with airfoil table interpolation is used. The aerodynamic rotor-loads are determined in combination with the finite-state inflow model, which is introduced in the previous section 3.1. In Fig. A.7 the simulated MR shaft power coefficient C_P/σ is compared with test-data obtained e.g. during the Airloads Program and in the 80x120ft National Full-scale Aerodynamics Complex (NFAC) wind-tunnel, where C_P is the dimensionless MR power required P. Consistently, C_T is the dimensionless MR thrust T and σ is the MR solidity. The solidity is computed based on geometrical properties of the MR according to $\sigma = N_b c/(\pi R)$. In Fig. A.7 a correction according to literature of the MR download during flight-testing is involved. For further details see Ref. [258], where the model was validated previously. The MR hover-polar is in agreement with both flight and wind-tunnel test-data for the complete thrust range of interest, see Fig. A.7(a).

In forward flight an agreement between flight and wind-tunnel test-data as well as free-wake simulations is obtained, see Fig. A.7(b). This result was previously published in Ref. [258] as well and includes different advancing ratios as well as different blade-loading levels. Note that wind-tunnel wall-effects influence the power prediction at higher thrust levels, see Ref. [305]. Hence, a discrepancy between simulation and the wind-tunnel test-data is visible. However, the simulation is in better agreement with a reference simulation using free-wake analysis which explicitly neglects the wall-effects. Details about the reference data can be found in Ref. [258]. Note that all flight-states are properly trimmed. The trim process is outlined in the next section 3.3. The aerodynamics including the airfoil tables, the aerodynamic radial discretization, as well as the selected number of inflow-states is considered to be suitable in terms of MR power prediction over the helicopter flight-envelope of interest for this work.

The MR hub loads are significantly affected by atmospheric turbulence, which was analyzed in more detail previously in Ref. [257]. Fig. 3.4 reveals that the MR thrust is significantly characterized by broadband harmonics in atmospheric turbulence. Broadband oscillations are predominantly attracted by the BPF, while the amplitude at the BPF is not much affected by turbulence in comparison with simulation results in calm air. Hence, vibrations with BPF are first of all a result of deterministic airloads. The standard deviation of the MR thrust introduced by atmospheric turbulence is small compared to the mean thrust. Note that the BPF oscillations have no significant influence on the probability distributions. This is concluded since the distribution shows approximately GAUSSIAN characteristic, see Fig. 3.4. This slope is in agreement with expectations with regard to the CLT, because different stochastic processes are mixed while translating through the elastic MR system.

(a) Spectrum.

(b) Histogram. (moderate: mean= 66436.07N, RMS= 1600.46N; light: mean= 66491.54N, RMS= 1018.99N; calm air: mean= 66500.89N).

Figure 3.4.: Spectrum and histogram of the simulated MR thrust in presence of light and moderated atmospheric turbulence as well as in calm air.

3.3. Main-Rotor Trim

An essential aspect for the correct prediction of helicopter vibrations is the computation of an accurate trim-state according to Ref. [70]. Multiple approaches exist to obtain a trimmed solution, see Ref. [233], which are not all applicable in this work. An important requirement is that the trim-solver preserves aperiodic signal components which are introduced by atmospheric turbulence. Although they are time-domain based, approaches like harmonic balance or periodic shooting are not suitable for the problem of concern in this work, because they assume periodic behavior per se and do not account for unsteady processes, see Refs. [65, 233]. The method used in this work is described in Ref. [233] as auto-pilot trim approach. The approach is to maintain the trim-state by a linear control-law based on an inverse JACOBI matrix J in time-domain, see Eq. 3.4 and Eq. 3.5. This functionality is provided by *Dymore.*

$$\Delta \mathbf{u} = \Delta t J^{-1} g_s \cdot \begin{bmatrix} \ddots & & \\ & g_i & \\ & & \ddots \end{bmatrix} \Delta \mathbf{y} \tag{3.4}$$

with: $J = \dfrac{\partial \mathbf{y}}{\partial \mathbf{u}}$ (3.5)

The control inputs $\Delta\mathbf{u}$ are computed based on the inverse of the Jacobi matrix J multiplied with the time-step width Δt. Close to the trim-state, the control authority is faded out using the gain factor g_s according to the law in eq. 3.6. In this work $e_{\min} = 5 \cdot 10^{-4}$ is used and the gains g_i are all set to unity. The computed control inputs $\Delta\mathbf{u}$ include the three displacements of the actuators in the order *forward, lateral, aft* which are depicted in Fig. 3.2. The trim states $\mathbf{y}$ include the MR thrust, roll- and pitch-moment. Note that the wind-tunnel trim is achieved based on MR thrust and lateral as well as longitudinal flap motion in agreement with literature, see e.g. [279]. This is involved in the computation of wind-tunnel trim conditions in Fig. A.7(a) and Fig. A.7(b) in section 3.2. For more details see Ref. [258].

The trim-task is decomposed into two steps. In the first step, the gain matrix J is computed based on finite control perturbations. In the second step, the inverted control matrix is applied to drive the rotor-system into the trim-state by using the control-law in eq. 3.4. The controlled rotor-states are low-pass filtered using a Butterworth-filter of 4th order, see Fig. A.9. The main purpose is to mask dominant MR-BPF oscillations. However, the cut-off frequency is selected such that the MR speed and the first elastic airframe eigenfrequency are filtered as well, see Fig. A.9. The intention is to reduce the coupling between the trim-controller and aeroelastic modes as much as possible, while the controller is still able to maintain the trim-state. The filtered signals are passed to the controller.

$$g_s = \tanh\left(4e/e_{\min}\right) \tag{3.6}$$

$$\text{with: } e = \frac{\|\Delta\mathbf{y}\|}{\|\mathbf{y}_{\text{target}}\|} \tag{3.7}$$

The trim controller allows to maintain the trim-state during operation in atmospheric turbulence. Note that no fundamental controller optimization is conducted in this study to improve the MR response to atmospheric turbulence. The obtained trim-results during operation in atmospheric turbulence are depicted in Figs. 3.5 which are taken from Ref. [257]. In general, the trim-targets are properly met. However, an increase in turbulence intensity leads to more disagreement of MR thrust, see Fig. 3.5(a). In contrast, the shaft bending-moments are in good agreement independent from turbulence intensity, see Fig. 3.5(b). The blade feathering, flap and lead-lag motions are in agreement with test-data as well but not explicitly shown in this work. For more details see Ref. [258]. The helicopter attitude including the rotor-shaft orientation is prescribed according to the reference flight-conditions defined in table 1.2.

The following figures show the spectrum of control activity measured by actuation power, see Fig. 3.6. The actuators are labeled according to Ref. [3] and the labels are indicated in Fig. 3.2. In general, control activity increases with turbulence intensity especially at higher frequencies. However, the actuation power is predominantly associated with low frequencies which is a result from the included low-pass filter. Although significantly filtered, an increased level of control power is nonetheless associated with harmonics in close proximity to MR-BPF. In comparison, the forward actuator shows higher actuation activity, see Fig. 3.6(a). The two marked frequencies are further discussed later in this work is section 4.7. According to the

(a) MR thrust.

(b) MR shaft moments.
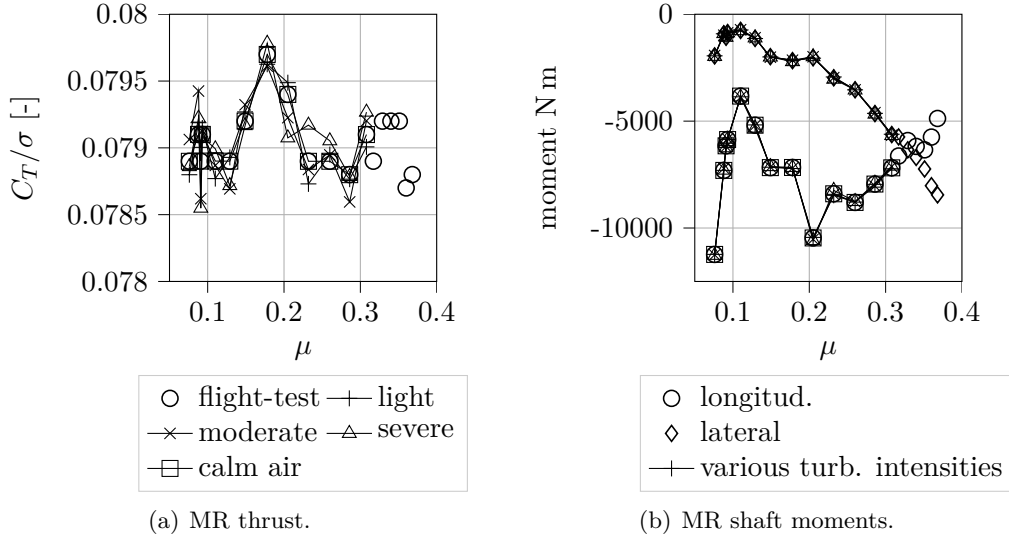
Figure 3.5.: Trim-values obtained from simulation for different turbulence intensities compared to reference values. Flight-state according to baseline case from table 1.2. Figure taken from Ref. [257].

JACOBI matrix, see Eq. 3.8, which is computed for the baseline flight-condition, the forward actuator shows the highest sensitivity towards MR thrust. This is interpreted to be related with the higher discrepancies of the MR thrust in atmospheric turbulence, see Fig. 3.5(a), compared to the MR shaft bending moments, see Fig. 3.5(b).

$$J = \frac{\partial \mathbf{y}}{\partial \mathbf{u}} = \begin{bmatrix} 1.409e + 6\,\mathrm{N/m} & -5.090e + 4\,\mathrm{N/m} & 9.630e + 5\,\mathrm{N/m} \\ -1.038e + 6\,\mathrm{N\,m/m} & 2.187e + 6\,\mathrm{N\,m/m} & -9.431e + 5\,\mathrm{N\,m/m} \\ 1.104e + 6\,\mathrm{N\,m/m} & 1.928e + 5\,\mathrm{N\,m/m} & -1.079e + 6\,\mathrm{N\,m/m} \end{bmatrix} \tag{3.8}$$

3.4. Tail-Rotor and Aerodynamic Empennage Model

The TR and the empennage section are important components with regard to the prediction of airframe vibrations as well, see Ref. [70]. Other authors identified the loads introduced at the tail section to have a beneficial influence on the airframe output-only modal analysis, see Ref. [110]. Hence, the helicopter tail section is included in the simulation framework. In general, the TR and the stabilizer models used in this work are much simpler compared to the MR model. The aerodynamic stabilizer models employ airfoil-table interpolation based on Ref. [136]. It was shown previously that concentrated empennage loads are not representative in terms of airframe excitation and distributed airloads are more realistic, see Ref. [259]. Hence, spanwise distributed aerodynamic panels are used to approximate the influence of spanwise atmospheric turbulence variation, see Fig. 3.7.

(a) Forward servo.

(b) Lateral servo.

(c) Aft servo.
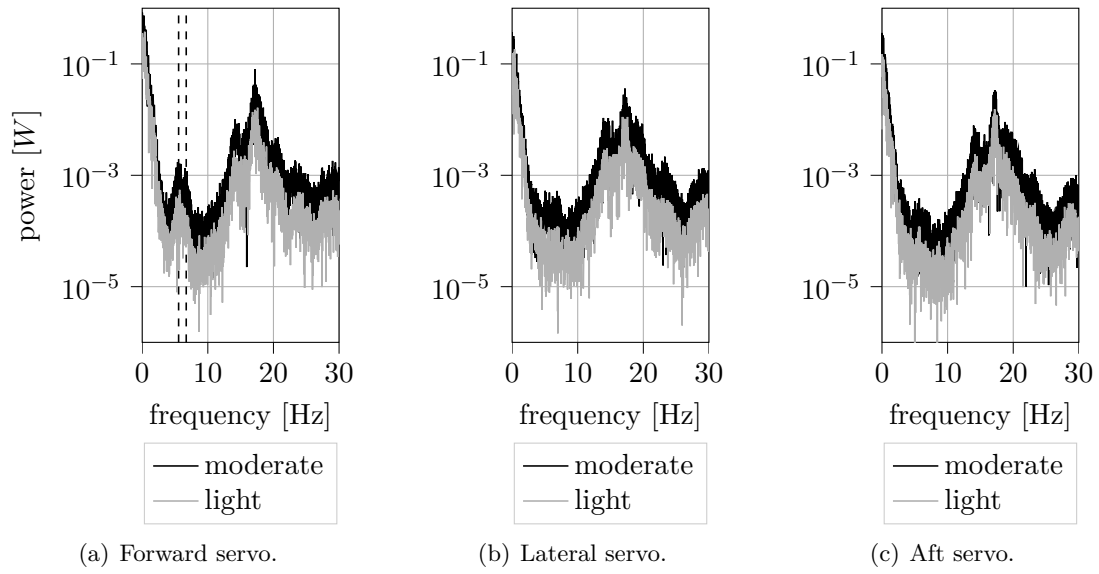
Figure 3.6.: Spectrum of the actuation power of the three servos. Flight-state according to baseline case, see table 1.2.
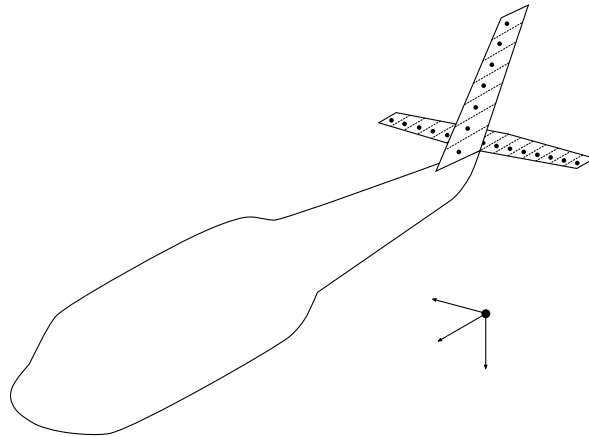
Figure 3.7.: Aerodynamic empennage discretization. Each stabilizer surface is discretized by 7 elements.

As an approximation, this is realized by computing the airloads for each individual panel i based on the aerodynamic polars $C_X(\alpha)$ that actually represent the complete stabilizer. The approach is used for both the VS and the HS. Note that the index X represents both the lift and the drag components. Hence, four different polars are involved. The computation of the total airloads is indicated in Eq. 3.9. This equation is generalized to account for the spanwise variation of turbulence velocities by introducing a variable chord-length c, a velocity V and an angle of attack α along the spanwise coordinate x, see Eq. 3.10. The quantities $V(x_i)$ and $\alpha(x_i)$ take the local flow conditions into consideration. These are composed of the turbulence velocities, the flight velocity, the elastic motion of the individual panel if two-way coupling is used and of the MR and TR inflow velocity if the stabilizer is located in the downwash of the respective rotor, see below. The panel loads are computed for each element i indicated in Fig. 3.7. The total airloads computed according to Eq. 3.11 agree approximately with the forces computed for the complete component directly, see Eq. 3.9, within geometrical discretization errors and as long as the panels are subject to the same global flow conditions. Note that this is not a valid approximation of the spanwise aerodynamic load distribution, since circulation-effects at the stabilizer-tips are not respected. However, the objective with regard to output-only modal analysis is the representative modeling of broadband and distributed loads introduced by atmospheric turbulence rather than the accurate modeling of spanwise load distribution.

$$X = \frac{\rho}{2} S V^2 C_X(\alpha) \tag{3.9}$$

$$X'(x) = \frac{\rho}{2} c(x) V(x)^2 C_X(\alpha_Y(x)) \tag{3.10}$$

$$\tilde{X} = \sum_i X'(x_i) \Delta x \tag{3.11}$$

The stabilizers are structurally represented by the elastic airframe model, see the next section 3.5. Since only a coarse spatial discretization of the airframe structure in modal space is available from literature, additional points matching with the aerodynamic panels, are linearly interpolated along the stabilizers in spanwise direction according to Fig. 3.7. This follows the assumption that the lower modes are approximately characterized by rigid stabilizer motion locally. This is in agreement with the mode-shapes visualized in Ref. [135]. The elastic motion of the stabilizers is respected in the aerodynamic simulation in principle. However, note that in particular the torsional degrees of freedom, which are an important contributor to wing flutter [37], are not included in the modal airframe, because this motion was not recorded during airframe GVT, see Ref. [135]. Hence, it is assumed that stabilizer flutter is not modeled.

In contrast to the flexible MR, the TR is modeled as a rotating mass-less rigid body. Hence, flapping dynamics of the TR are neglected, since the UH-60A TR flap motion is mechanically realized via rotor-blade flexibility. With regard to the coupled MR-airframe modeling, the integration of the TR does not aim for improving the structural representation, but to include a representative aerodynamic model to account for related loads later in the in-flight modal analysis. In addition, the TR-BPF is outside the frequency range of interest of this work.

Hence, a structural modeling of the TR is assumed to only provide a limited improvement of the structural representation. The TR cant angle of 20° is respected, see Ref. [136]. The aerodynamic modeling is based on airfoil table interpolation and blade-element theory equivalently to the MR. The aerodynamic profile SC1095 is used to model the TR, although Ref. [2] indicates that the TR profile varies in radial direction from SC1095 to SC1095R8. The elastic motion of the TR attachment is respected by the aerodynamic TR model. The TR thrust is properly trimmed in calm air such that the MR torque is balanced. The trim solution includes the computation of a steady uniform inflow velocity and the TR collective control input. During the TR trim-task the advancing-ratio is respected. However, no closed-loop trim-controller is employed to maintain the TR thrust during operation in atmospheric turbulence.

Since the TR radius is approximately one order of magnitude below the MR radius, the turbulence simulation is realized using hub-based sampling and hence, rotational sampling effects are neglected at the TR. Since the turbulence model spans a two-dimensional vector-field of velocities, turbulence encounters are determined at the tail section by vertical projection of all aerodynamic points into the turbulence plane. During the time-domain simulation the TR and the empennage loads are applied on the airframe simultaneously with the MR loads. A simple approximation is used to include the influence of the MR downwash in the aerodynamic simulation of the empennage and the TR. The MR downwash is assumed to be non-contracted when passing the tail section and skewed by the angle χ resulting from the horizontal flight-speed V and the MR inflow velocity $v_{i,\mathrm{mean}}$ averaged over the rotor-disc, see Fig. 3.8. The calculation of χ is given in Eq. 3.12, where Θ is the helicopter pitch-attitude. Since $v_{i,\mathrm{mean}}$ is perpendicular to the rotor-plane, the velocity is separated into the x-component aligned with V and the z-component perpendicular to V and pointing downward. If the reference point of one component is within the skewed rotor-wake geometry, the MR inflow velocity averaged over the MR disc is superimposed with the other velocities during the computation of aerodynamic forces of the complete component. The TR inflow impingement on the vertical stabilizer is considered likewise.
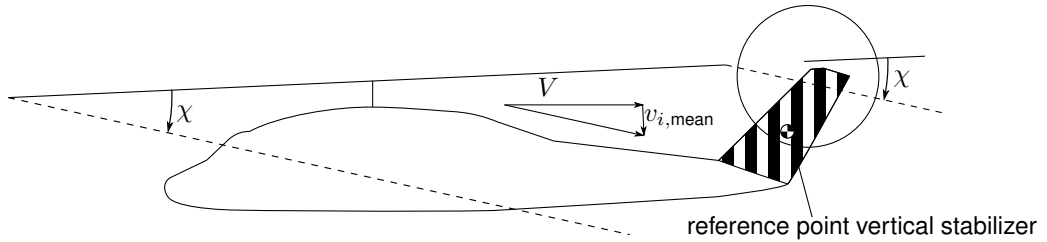
Figure 3.8.: MR downwash geometry.

$$\chi = \arctan\left(\frac{v_{i,\mathrm{mean,z}}}{V + v_{i,\mathrm{mean,x}}}\right) - \Theta \tag{3.12}$$

For the aerodynamic TR model validation, Fig. A.10 shows the TR power coefficient C_P/σ in hover and forward flight. Obviously, the TR shaft power is over-estimated in hover at higher thrust levels in comparison with test-data obtained from a scaled UH-60A MR with
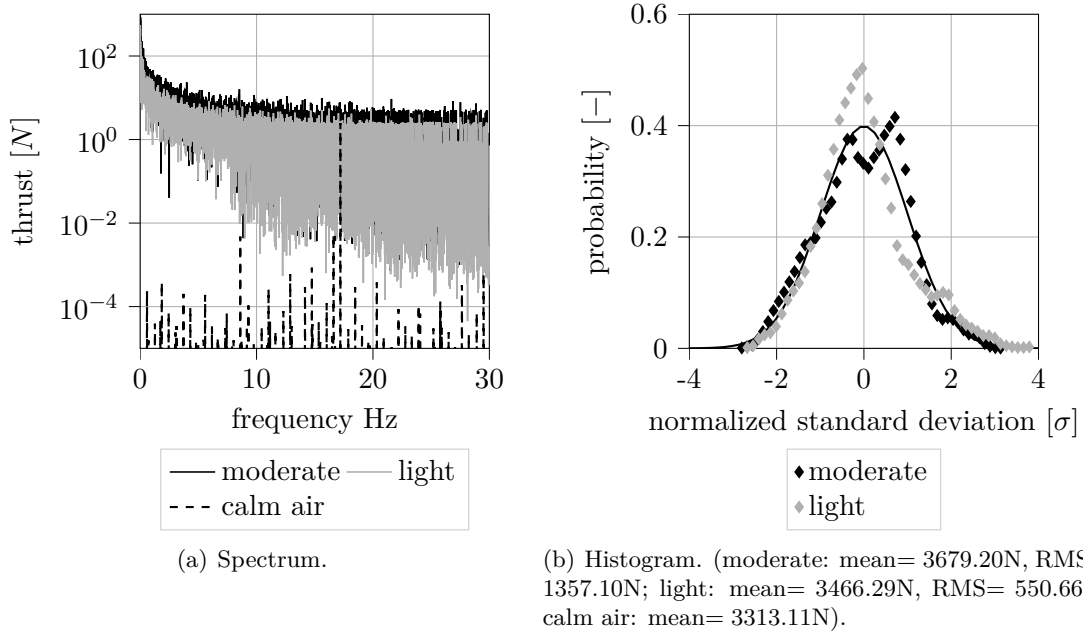
comparable TR dimensions, see Ref. [27]. However, the reference rotor features both a different radial airfoil and twist distribution. In forward flight the TR power is compared to flight-test data recorded during the Airloads Program flight-test counter 85 and trimmed correspondingly, see Ref. [314]. Three different advancing-ratios are computed for comparison, which agree with the flight states selected in this work, see table 1.2. In forward flight the TR power is under-estimated at lower speeds and over-estimated at higher speeds compared to the flight-test data. Note that the reference data itself shows some level of fluctuation. The discrepancy to flight-test data is assumed to result from discrepancies in helicopter trim, aerodynamic interaction, as well as non-uniform dynamic TR inflow. In comparison with the reference simulation obtained from Ref. [314] the results are under-estimated but follow a comparable trend. Finally, the TR performance is considered to be acceptable with regard to in-flight modal analysis.

Fig. 3.9 shows the spectrum and the histogram of the TR thrust. The spectrum decays with increasing frequency, see Fig. 3.9(a). The highest amplitude in calm air is associated with the MR-BPF structurally introduced via two-way coupling. The amplitude is less than the broadband amplitudes in presence of atmospheric turbulence. At increased flight-speeds the magnitude of the MR-BPF increases and becomes higher than the broadband spectrum, which is not shown explicitly. The TR-BPF is located at approximately 79.3Hz and is not within the frequency range of interest. The magnitude at TR speed at approximately 19.8Hz is not amplified in the spectrum. Fig. 3.9(b) shows a discrepancy of the probability distribution from Gaussian distribution for both turbulence intensities. The minimum of the distribution in case of moderate turbulence is not characteristic for the TR as repeated simulations indicate. In comparison with the probability distribution of the MR thrust, see Fig. 3.4(b), the discrepancy is explained by two aspects. First of all, the TR model is much simpler and the CLT, converging the solution towards Gaussian distribution, is less relevant, since hub-element turbulence sampling involves less stochastic processes. The second aspect is, that the TR loads are dominated by low-frequency oscillations and hence, the comparable short simulation time does not further converge the solution towards Gaussian distribution. Note that the standard deviation of the TR thrust is comparable with the the standard deviation of the MR thrust, see Fig. 3.4(b). Hence, the TR model used in this work is considered to over-predict the turbulence response, which is assumed to result from neglecting flapping as well as inflow dynamics. The mean TR thrust is increased with increasing atmospheric turbulence intensity because the TR thrust is not constantly retrimmed in contrast to the MR.

The resulting total loads of the VS and HS are shown in Fig. 3.10 and Fig. 3.11. The decay of the spectra with increasing frequency is characterized by the von Kármán turbulence spectra. In comparison of the two spectra, see Fig. 3.10(a) and Fig. 3.11(a) multiple harmonics are visible in the spectrum of the HS. This cannot be explained by the MR wake only, since the spectrum of the mean MR wake does not show such a high number of harmonics but one peak at MR-BPF. Instead, the high number of distinct harmonics is concluded to be related with the FullFT model, since they do not appear when using the HubDT model. At 30Hz the distinct harmonics are approximately one order of magnitude above the broadband spectrum. Up to 10Hz the distinct harmonics are assumed not to influence the broadband spectrum. The harmonics do not have an influence on the modal analysis conducted in

(a) Spectrum.

(b) Histogram. (moderate: mean= 3679.20N, RMS= 1357.10N; light: mean= 3466.29N, RMS= 550.66N; calm air: mean= 3313.11N).

Figure 3.9.: Spectrum and histogram of the simulated TR thrust in presence of light and moderated atmospheric turbulence as well as in calm air.

the next chapter 4, as the comparison with the HubDT model reveals. However, to avoid the occurrence of the harmonics, an increased number of Borgman-harmonics would be necessary as discussed in Ref. [257]. The number of harmonics is selected as $K = 500$ based on the results obtained for the MR in chapter 2 in comparison with Ref. [257]. However, the VS does not show such harmonics. The probability distributions of the overall stabilizer forces reveal a discrepancy from Gaussian distribution, see Fig. 3.10(b) and Fig. 3.11(b). Equivalent to the TR this is attributed to less relevance of the CLT, since the involved stochastic processes are correlated due spatial proximity. In addition, both spectra are again dominated by low frequencies and the comparable short simulation time does not further converge the distributions towards Gaussian distribution as well. In presence of atmospheric turbulence the mean values of both the VS and HS change, because the surfaces are not re-trimmed. Since rigid motion of the airframe is neglected in this work, the accurate prediction of mean loads is not important, because no free-flight trim is involved and the elastic airframe is linear. The standard deviation increases with turbulence intensity within a reasonable physical range. The validity of the stabilizer aerodynamics is concluded based on the both the mean-values and the standard deviation indicated in Fig. 3.10 and Fig. 3.11.

Not explicitly shown are the following results. The overall longitudinal force of the HS is more than one order of magnitude below the vertical force, whereas the model calculates forces of zero magnitude in lateral direction. The longitudinal force of the VS points rearwards and is of the same order of magnitude than the lateral forces, whereas the model calculates forces of zero magnitude in vertical direction. The HS generates an overall down-force in agreement with the helicopter trim-state and the VS generates drag and a force in opposite direction

(a) Spectrum.

(b) Histogram. (moderate: mean= 872.65N, RMS= 157.01N; light: mean= 692.20N, RMS= 76.07N; calm air: mean= 756.05N).
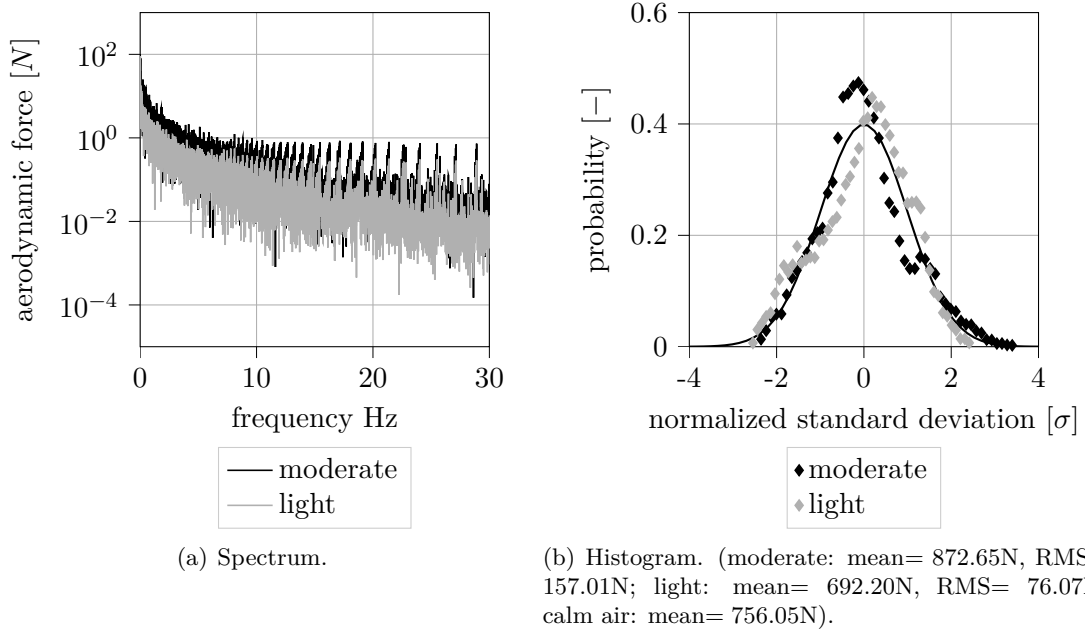
Figure 3.10.: Spectrum and histogram of the simulated total aerodynamic loads in vertical direction of the HS in presence of light and moderated atmospheric turbulence.

(a) Spectrum.

(b) Histogram. (moderate: mean= −742.15N, RMS= 127.65N; light: mean= −633.05N, RMS= 85.27N; calm air: mean= −730.84N).
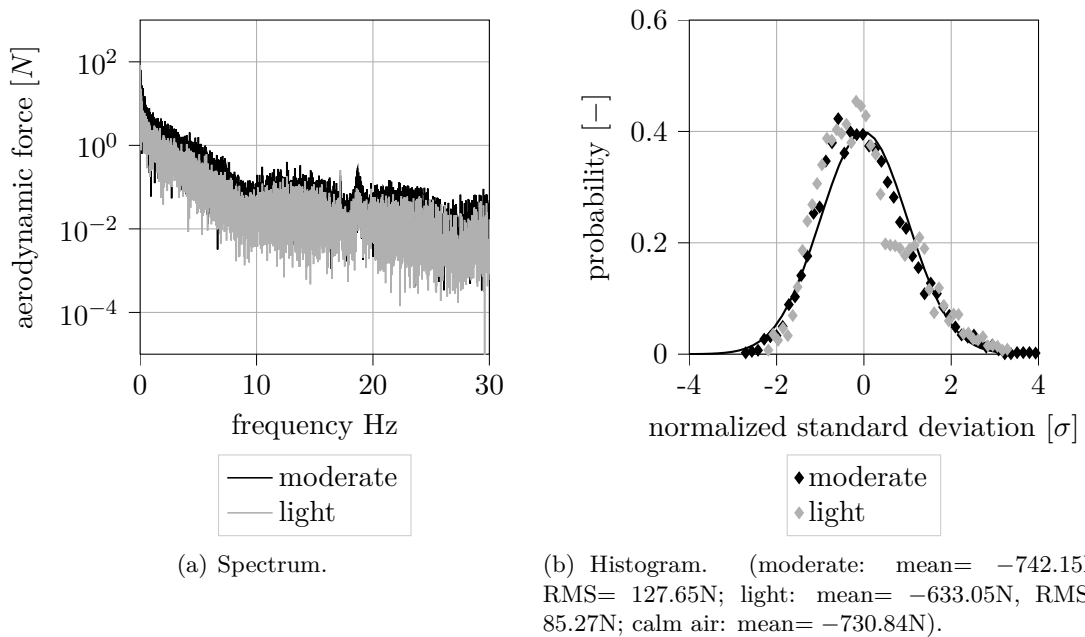
Figure 3.11.: Spectrum and histogram of the simulated total aerodynamic loads in lateral direction of the VS in presence of light and moderated atmospheric turbulence.

to the TR thrust, because it is located in the TR downwash. The results obtained in this chapter are depicted for the two-way airframe coupling, see Fig. 3.1. In case of one-way coupling, the results shown in this chapter change negligibly. The models described in this section are realized in *Python* using *NumPy* and are coupled and synchronously computed with the other models in this work.

3.5. Airframe Modal Approximation and Coupled Results

The elastic airframe is included in the modeling framework, since it is the most relevant component in terms of the helicopter modal analysis conducted in this work. In addition, an elastic airframe is required for the prediction of helicopter vibrations, see Refs. [70, 318, 55]. In Ref. [268] it is conclude that an elastic airframe should be included for the prediction of tilt-rotor loads in presence of atmospheric turbulence with short wavelengths in particular. In this work it is assumed that the elastic oscillations remain small enough to use component mode synthesis, see Refs. [31, 4, 65]. This approach allows to linearly superimpose the rigid and the elastic motions. In addition, the elastic oscillations are assumed to be sufficiently represented by modal approximation. The modes are governed by Eq. 3.2, which is solved in time-domain using a RUNGE-KUTTA scheme of 4th order.

In Ref. [258] two independent elastic airframe models of the UH-60A are reviewed that provide the modal quantities required by Eq. 3.2. While the the first airframe only provides 6 dimensions at the MR hub node, see Ref. [195], the airframe published in the context of the Design Analysis Methods for Vibrations (DAMVIBS) program includes nodes distributed over the entire airframe, but does not include rotational dimensions, see Ref. [135]. The influence of elastic rotational airframe dimensions on the MR hub vibrations is studied in Ref. [258]. The conclusion is that rotational dimensions do not have a significant influence on the MR hub vibrations. Since in this work the influence of the tail section is to be included in the analysis and rotational degrees of freedom are estimated to have not an important influence at least for the MR coupling, the DAMVIBS airframe is used in this work.

The effect of Rigid Body Mode (RBM) on the elastic transfer functions within the frequency range of interest is exemplarily shown for the MR hub in Fig. A.11. The effect is found to be negligible, which supports that rigid body motion is not included in this work. In addition, only the first 8 airframe modes are included in this work. The neglected higher modes are not corrected e.g. via Mode Acceleration Method (MAM) [308] or residual modes [271]. The correction is assumed to have only a small influence on the solution, which is supported by the agreement up to 30Hz of the experimentally determined transfer functions with the simulations including 8 modes, see Fig. A.11. Note that the transfer functions from test data are inconsistent in some cases, see especially Fig. A.11(b) and Ref. [135, p.158 vs p.167]. Hence the agreement found with the simulation model is considered to be appropriate. The 8 modes are listed in table 3.2 and depicted in Fig. A.12. Note that these modes differ slightly from the mode shapes depicted in Ref. [135] since the experimentally determined transfer function are re-evaluated for the computation of the eigenvectors and modal masses. The

eigenfrequency of mode 2 is selected as a compromise of both Ref. [135] and Ref. [195]. The modal properties of the elastic airframe are taken from Ref. [258]. Note that mode 6 is slightly corrected at the horizontal stabilizer for better agreement with the mode-shapes from Ref. [135].

mode	frequency $\omega_{0,k}$ [Hz]	damping ξ_k [%]	description
1	5.5	1.0	first lateral bending
2	6.6	1.0	first vertical bending
3	10.1	2.9	stabilator rigid body 1
4	12.3	1.4	transmission pitch
5	13.8	2.7	transmission roll
6	14.0	2.6	second vertical bending
7	15.4	2.8	cockpit/cabin roll
8	19.3	2.1	third vertical bending

Table 3.2.: Eigenfrequencies and damping ratios of the elastic airframe. The modal masses m_k are scaled to unity. For further details see Refs. [135, 258]
.

The mass of the MR head is included in this model since the airframe was tested with the MR head attached to the structure, see Ref. [135]. In addition, 50% equivalent rotor-blade mass is attached during GVT. Hence the rotor-blade mass is included in the MR model with 100%, see chapter 3.2, and in addition in the airframe model with 50%. In Ref. [120] an approach based on equivalent negative mass is introduced to correct the MR mass in the elastic airframe model. However, this correction is only necessary if the coupling involves participation factors according to Ref. [120], which are neglected in this work. The suspension during the airframe GVT was selected such that modes are introduced at frequencies of less than 20% of the second elastic eigenfrequency (vertical bending), see Ref. [135]. Hence, a negligible influence of the suspension system on the elastic modes is assumed. The elastic model of the airframe includes the elastic MR shaft as well, which is indicated in Fig. 3.2 as part of the MR assembly. Hence, the MR shaft is not modeled as a rotating part, which is assumed to be appropriate since this component does not undergo large off-axis rotations and consequently gyroscopic effects and shaft rotation are assumed to be negligible.

In Fig. A.13 the simulated hub acceleration levels obtained for different turbulence intensities are compared with flight-test data obtained from Refs. [291, 41]. A reasonable agreement between the flight-test data and simulated MR hub vibrations is found for the in-plane vibrations. In contrast, the out-of-plane accelerations at BPF (4/rev) and the mean half peak-to-peak accelerations are under-predicted over the entire flight-speed range. In general, an increase of vibration level is visible with increasing turbulence intensity in both in-plane and out-of-plane direction. While the out-of-plane mean half peak-to-peak vibrations show a clear trend, see Fig. A.13(f), e.g. the 3/rev in-plane vibrations do not, see Fig. A.13(c). Two outliers in this figure at severe turbulence intensity are visible in Fig. A.13(e) as well. The turbulence encounters recorded during flight-testing are subject to a higher level of variation than the vibration levels obtained for the different simulated turbulence intensities, see Fig.

A.13(a). At low speed the vibration levels are under-estimated in comparison with flight-test data. While the simulated results indicate an increase with flight-speed, the rapid increase indicated by the test-data at higher velocities is not resolved. Nevertheless, discrepancies of simulated hub vibrations in comparison with flight-test results are expected, since relevant aerodynamic phenomena are not modeled in this work, see Ref. [70]. More specifically Ref. [200] indicates that the secondary load-path, namely MR-wake impingement at the tail, which is not modeled in this work as well, contributes to vibrations in the forward airframe. Regarding the inaccuracies associated with the aerodynamic modeling, the structural model used in this work is considered to be appropriate for the simulation of the structural response to atmospheric turbulence. The elastic airframe solver is verified independently in another context concerned with load estimation of helicopter T-tail configurations subject to rotor-wake impingement, see Ref. [259]. The elastic airframe model is realized in *C* and wrapped to *Python* using *Swig* to enable time-synchronous and coupling with the associated models.
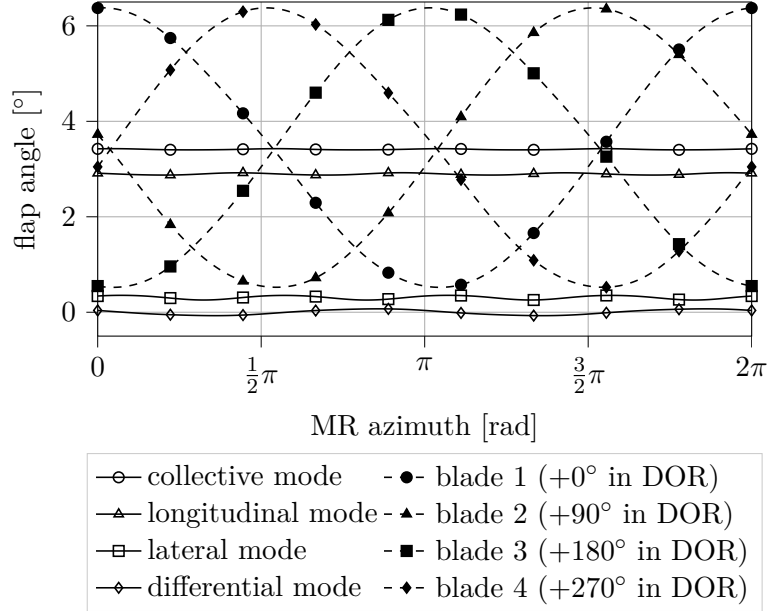
3.6. Multi-Blade Coordinates

To enable a modal analysis of coupled rotor-airframe phenomena, all states involved have to be expressed in one coordinate system, see Refs. [232, 212]. Therefor, the non-rotating helicopter body-frame is selected. This requires to transform rotor-states like flapping motion into the non-rotating domain, which is realized using COLEMAN transformation in this work, see Ref. [60]. This results in four new coordinates corresponding to the number of four main-rotor blades of the UH-60A, which are referred to as *collective*, *longitudinal*, *lateral* and *differential* mode, see Refs. [152, 71]. Sometimes the collective mode is referred to as umbrella mode and the differential mode is referred to as scissor mode in literature. If the rotor exhibits a 1/rev flap motion for illustration, this movement can be described in a non-rotating coordinate system as a room-fixed orbit with longitudinal and lateral tilt-angle. Since the new coordinates describe the motion of all blades, because they operate approximately on the same orbit with uniform phase-offset in trimmed conditions, the new coordinates are termed multi-blade coordinates. The exact computation of the multi-blade coordinates according to COLEMAN is available from Ref. [152]. Note that COLEMAN transformation does not handle intrinsic periodicity, hence, e.g. FLOQUET analysis is still necessary to account for the system's intrinsic periodicity even if COLEMAN transformation is applied, see Ref. [36]. COLEMAN transformation has been used for OMA in the context of wind-turbines previously, see Refs. [288, 287].

For illustration of the transformation, Fig. 3.12 depicts the flapping motion computed for the main-rotor in calm air over one revolution in trimmed conditions. The baseline flight state from table 1.2 is used. The figure shows both the properties recorded in the rotating domain and the associated multi-blade coordinates. The four individual blades exhibit approximately the same flapping motion with a phase offset of 90°. The blades numbering is conducted in direction of rotation, hence the blades pass a certain azimuth in reverse numbering order. The flapping angles of the four individual blades are transformed into four approximately steady multi-blade coordinates. The collective coordinate agrees reasonably with the mean value of

the harmonic oscillations. The differential mode remains close to zero, while the longitudinal motion is higher than the lateral motion, which agrees with the forward tilt of the main-rotor tip-path-plane in the considered trim state, see Ref. [314]. The multi-blade coordinates show a small level of oscillation. This is due to the fact that the COLEMAN transformation does not account for all periodic components.

Figure 3.12.: Flapping motion measured in the rotating domain for each rotor-blade individually and corresponding multi-blade coordinates. Flight-state according to baseline condition in table 1.2.

In this work, the aeroelastic analysis is based on the states summarized in table 3.3. The main- and tail-rotor hub motion as well as the horizontal stabilizer motion and the actuator displacement are expressed in non-rotating coordinates per se. The states measured in the rotating domain are expressed in multi-blade coordinates. This includes blade flapping and lead-lag motion as well as elastic rotor-blade torsion, the feathering motion and elastic pitchlink displacement. Since the closed-loop system is analyzed, the feathering motion is interpreted as an internal state and a measure for controller activity. Note that the actuator travel of the servos is commanded in the non-rotating domain. However, this command is translated via the swashplate into the rotating domain resulting in the feathering motion.

Note that the transformation from the non-rotating into the rotating domain changes the involved frequencies. As an example, a property oscillating with ω is transformed from a frame rotating with the MR-speed Ω_{MR} into the non-rotating domain. If the quantity is measured in direction of the rotating axis, like in-plane lead-lag motion or rotor-thrust, it is not subject to a frequency shift. In contrast, if the property is not measured in direction of the rotating axis, like flapping and pitch motion, it is subject to a frequency shift, see e.g. Eq. 3.13. In this equation the oscillation with a frequency ω, carried with Ω_{MR}, is transformed into two oscillations with frequencies $\Omega_{\mathrm{MR}} \pm \omega$. In both cases, in-plane as well as out-of-plane oscillation, the phase-shift ψ_i between the blades cancels out specific oscillations

name	DOFs	multi-blade	motion	unit
MR hub	3	no	elastic displacement	m
TR hub	3	no	elastic displacement	m
HS right	3	no	elastic displacement	m
HS left	3	no	elastic displacement	m
MR lead-lag	4	yes	rotation	rad
MR flapping	4	yes	rotation	rad
MR feathering (control input)	4	yes	rotating	rad
MR blade torsion	4	yes	elastic torsion	rad
MR pitchlink	4	yes	elastic displacement	m
MR actuators	3	no	elastic displacement	m

Table 3.3.: Helicopter states selected for aeroelastic analysis.

in trimmed rotor conditions. A hands-on introduction into these phenomena is provided in chapter 12 in Ref. [105]. Later in this work the rotor dynamics are expressed in terms of eigenvectors, associated with individual eigenfrequencies and damping ratios. Hence, if a multi-blade coordinate oscillates with an arbitrary eigenfrequency, the mode does no longer represent azimuthally fixed motion but consequently an asynchronous motion.

$$2\cos\left[\Omega_{\mathrm{MR}}t\right]\cos\left[\omega t + \psi_i\right] = \cos\left[\left(\Omega_{\mathrm{MR}} + \omega\right)t + \psi_i\right] + \cos\left[\left(\Omega_{\mathrm{MR}} - \omega\right)t - \psi_i\right] \qquad (3.13)$$

4. Helicopter Aeroelastic Analysis

This chapter is concerned with the computation and the analysis of helicopter aeroelastic modes. The computation is based on output-only modal analysis enabled by natural excitation of the helicopter structure through atmospheric turbulence. The development and the validation of the modal analysis framework as well as the analysis of the helicopter aeroelasticity are based on results obtained using MONTE CARLO simulation. The involved atmospheric turbulence models are introduced and validated in chapter 2, while the helicopter model is introduced and validated in chapter 3. For the modal analysis, OMA as well as BSS methods are used in comparison. Except for the introduction in section 1.2, the mathematics of the methods are not explained in this work, because excellent references exist, which are presented in section 1.2.

The first OMA approach used in this work is referred to as NExT-ERA in literature. One reason for its selection is that the ERA algorithm is an established technique for the conventional input-output EMA. Another reason for the selection of ERA is that an extension has been published that is able to handle harmonic signal components explicitly, see Refs. [199]. In this context ERA was found to be slightly superior to other investigated methods. The ERA algorithm is implemented according to Ref. [198] and the modified ERA method presented in the reference was implemented for comparison during the course of this work as well.

The second OMA approach used in this work is referred to as SSI-COV in literature. It has been shown to be very similar to NExT-ERA as it is based on the correlations of the signals as well and is accordingly categorized as covariance-based approach. In addition, the similarity between the methods is that they are both fundamentally based on HANKEL expansion. The reason for choosing SSI-COV is that the algorithm is comparable easy to implement and in consequence easy to modify, see section 1.2. In addition, SSI-COV does not require long time series for the modal analysis. The suggested minimum of 200 cycles, which in indicated in Ref. [212] is met throughout this work. Another aspect is that a modification of SSI-COV has been published in the past that is able to handle system-intrinsic periodicity, see Ref. [148]. Note that this extension is very different from the extension proposed in Ref. [199] in context of NExT-ERA, which is highlighted above. This modified approach was tested as well during the course of this work. However, the approach is not further considered, since MR intrinsic periodicity is found in the previous section 4.4 to be negligible. SSI-COV is implemented in this work according to Ref. [148].

Based on the discussion presented in section 1.2, the BSS technique called SOBI is used as well in this work, which serves as a reference to the OMA methods. The advantage of the BSS approach compared to OMA is that no manual selection of the modes from the stabilization diagram is necessary, since the order of the system is predefined. However, at the same time this is a significant limitation, since no under-determined systems can be solved, which is theoretically not a limitation in this work, since the number of elastic airframe modes is less than the number of physical airframe states. In this work, SOBI is implemented according to Ref. [17]. Note that this implementation involves several steps which are assigned to the AMUSE algorithm in Ref. [17]. The algorithm to realize the joint diagonalization is obtained from Ref. [307].

Although OMA and BSS are fundamentally different, see section 1.2, the first preprocessing steps are equivalent and introduced in section 4.1. The OMA algorithms used in this work require an additional preprocessing step, namely the computation of the correlations subsequently, see Fig. 4.1. After the modal analysis is performed, both methods, OMA and BSS require different postprocessing steps, which are introduced in section 4.3 and indicated in Fig. 4.1 as well. In the context of OMA the results are further processed via eigenvalue decomposition. The obtained modes are filtered to exclude non-physical, so called *spurious* modes. After the successful separation of the modal coordinates $\mathbf{q}$ using BSS, the mode-shapes Ψ_k can directly be extracted from the modal matrix $\mathbf{\Psi}$. The modal coordinates $\mathbf{q}$ are subsequently computed using modal transformation via multiplying the input signals $\mathbf{x}$ with the inverse of the modal matrix $\mathbf{\Psi}$, see e.g. Eq. 1.4. From the modal coordinates $\mathbf{q}$, the damping ratios and the eigenfrequencies are obtained by further processing with an OMA method. Note that OMA algorithms are used in this work for two different tasks. On the one hand the approach is used standalone for output-only modal analysis and on the other hand in combination with BSS. The two different OMA algorithms employed in this work are NExT-ERA and SSI-COV. In addition, one BSS approach is used, namely SOBI. The methods are realized in *Python* using *NumPy* and *SciPy* linear algebra toolboxes.

(a) OMA. (b) BSS.
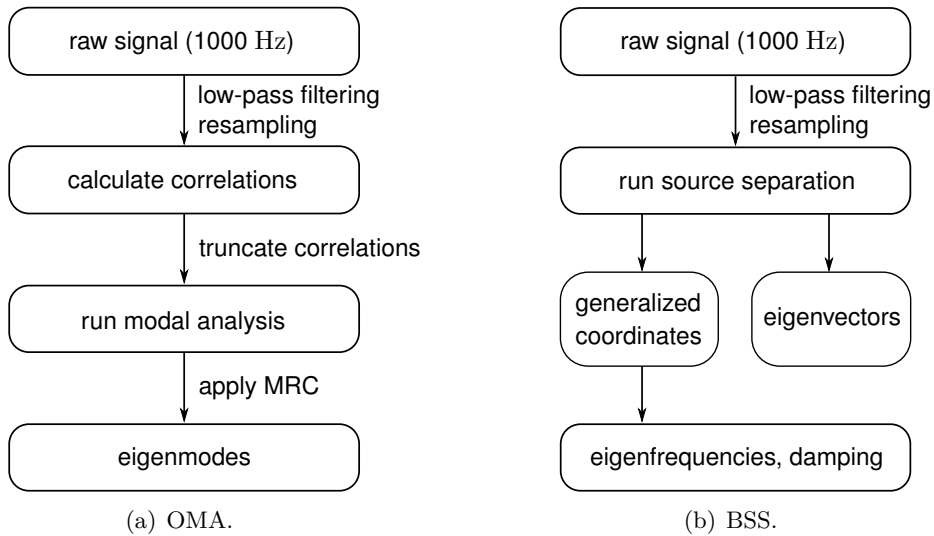
**Figure 4.1.:** Overview data-processing in the context of OMA and BSS.

After the preprocessing steps are introduced in section 4.1, in section 4.2 the obtained signals are analyzed towards their statistical and periodic properties as well as their applicability for OMA and BSS. As the MR system is in general not time-invariant but time-periodic, this property is assessed in section 4.4 in context of output-only modal analysis. The validity and suitability of both OMA and BSS are subsequently demonstrated in section 4.5 based on the isolated time-invariant elastic airframe subject to GAUSSIAN white noise. Afterwards an output-only modal analysis of the one-way coupled rotor-airframe system is conducted in section 4.6 exclusively focusing on the elastic airframe. This allows to treat the elastic airframe as a separated LTI system with modal properties known in advance. In addition, it allows to study the differences if GAUSSIAN white noise is replaced by the loads of the MR, TR and the empennage, all subject to atmospheric turbulence. Subsequently, in section 4.7 the two-way coupled system is analyzed including the MR states. Two-way coupling accounts for the airframe impedance compared to the one-way coupling in section 4.6.

4.1. Signal Preprocessing

Before the modal analysis is conducted, the signals are preprocessed to reduce the computational expense by removing unnecessary information from the signals. Since the mean value of the signals is of no relevance for the modal analysis methods used in this work, the signals are first of all centered by removing the mean. The frequency range of interest in this work is 0-30Hz as indicated in Fig. 4.2. This includes all airframe eigenfrequencies and the MR-BPF. Excluded are consequently integer multiples of the MR-BPF, in particular the MR-2BPF. The second postprocessing step is to low-pass filter the signals, to remove high frequencies which are beyond the frequency range of interest. The selected low-pass cutoff frequency is 30Hz accordingly. Note that the atmospheric turbulence spectra are characterized by a low magnitude at high frequencies in agreement with KOLMOGOROV's law, see Fig. 2.6(a). Hence, at high frequencies the system is not significantly excited anyway. Since no online-processing of the simulation results is necessary, the frequencies are low-pass filtered in frequency domain using forward and backward Discrete FOURIER-Transformation (DFT). Associated numerical inaccuracies observed at the end of the filtered signals are removed by excluding the last 2 seconds from the analysis.

The removal of higher frequencies allows to down-sample the signal consistently to reduce the amount of data that is processed by the modal analysis algorithms. This step is important because the required computational resources scale with the signal length squared. The selected re-sampled frequency is at least twice the NYQUIST-frequency, see e.g. Fig. 4.2. As practical frequency of the re-sampled signals 125Hz is selected, because every 8th step is kept and the intermediate time-steps are removed. A negligible difference is observed if the down-sampling is conducted after the correlations are computed, see Fig. 4.1(b). Hence, to reduce the computational cost during the computation of the correlations, the signal is down-sampled in advance.
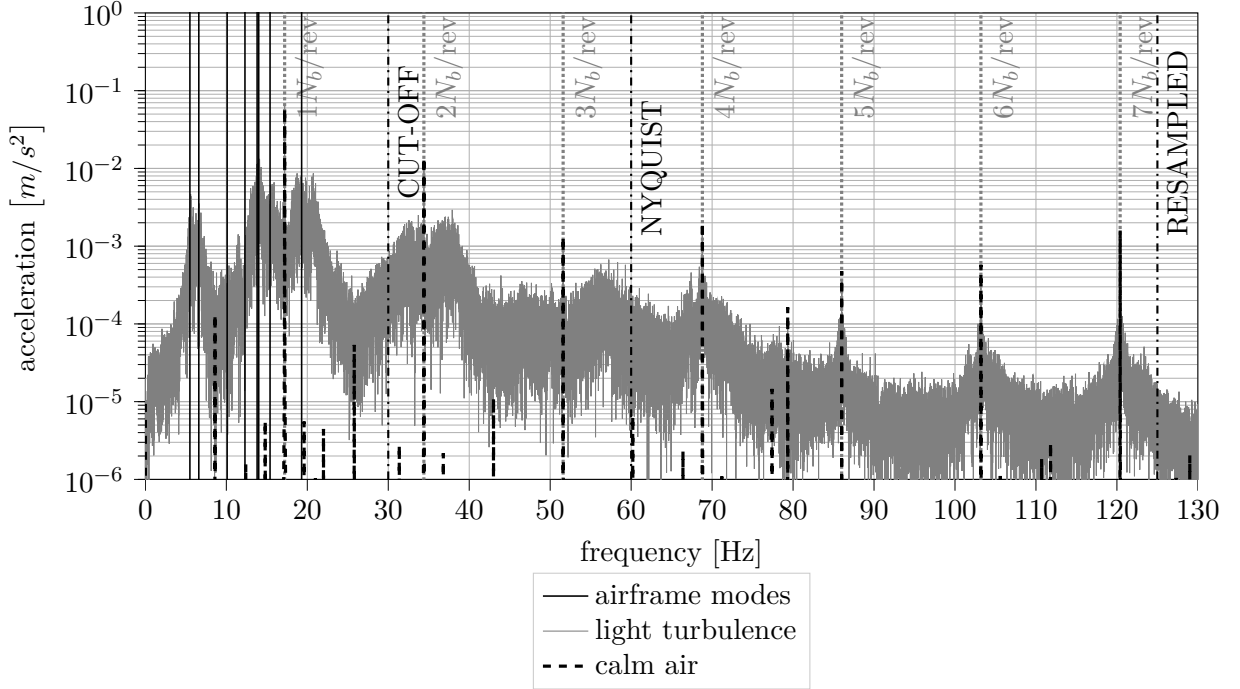
Figure 4.2.: Spectrum of the elastic MR hub accelerations in vertical direction computed for the baseline flight-state using two-way coupling in comparison with calm air.

To enable a modal analysis of the non-linear helicopter system, it is assumed that close enough to a steady operation state, the behavior of a dynamic system can be linearized and appropriately characterized as a LTI system. Since the rotor does not settle to rest even in steady operation, the state is described as a periodic trajectory. It is assumed that this periodic state exists and that it is superimposed with a *distortion* motion if the rotor is subject to random perturbations through atmospheric turbulence, see e.g. Ref. [81]. The extraction of the distortion motion, which is considered to carry the modal information, is achieved by removing the periodic reference trajectory from the solution. In theory, this results in randomly distributed and centered signals, which are considered as the motion *around* the steady reference state, see e.g. Ref. [185].

Hence, after the signals are low-pass filtered and down-sampled, the next processing step handles the presence of dominant rotor-harmonics contaminating the stochastic signals, see section 1.2. In this work, only the MR-BPF is removed from the signals using notch-filters. This approach is selected because it is obtained to be the most robust and effective way to remove the dominant MR harmonics. The removal of integer multiples is not included, since they are of less relevance in the frequency range of interest. A discarded alternative is the time-domain based fitting of harmonic functions with frequencies corresponding to the rotor-harmonics and the removal of these components subsequently. This approach is found to not remove the particular frequencies sufficiently. Another alternative implemented and tested but discarded in the context of this work is a modification of the ERA method

obtained from literature, see Ref. [199]. Although promising results were obtained to handle the periodic rotor loads, the approach was not found to be superior over notch-filtering the MR-BPF. The advantage of notch-filtering in the frequency domain is that a sharp cutout can be realized. In this work a bandwidth of $\pm 10^{-1}$Hz is selected. This ensures that airframe eigenfrequencies close to the MR-BPF are not affected. The concern mentioned in Ref. [144] that filtering perturbs the poles of the system is reduced to an minimum by applying the filters in the frequency domain. In addition, the selected approach conserves the phases. The notch-filtering is done simultaneously with the low-pass filtering step described above.

Another preprocessing step in the context of the OMA methods used in this work is the computation of the correlations. Since the correlations decay according to the NExT principle, see section 1.2, the most relevant information are located at the beginning of the correlations. Hence, without a significant loss of information, the correlations are truncated at time T_{decay}, see Fig. 4.3. In this figure the auto-correlation of an elastic airframe coordinate is exemplary depicted. The time T_{decay} is estimated based on the LD. Therefor, a decay-threshold η_{decay}, a reference damping ξ_{ref} and a minimum reference frequency $\omega_{\text{ref,min}}$ are introduced. In this work, $\omega_{\text{ref,min}}$ is selected as the eigenfrequency of the first mode of the elastic airframe and ξ_{ref} is selected as 1% corresponding to the modal damping ratio of the first mode of the elastic airframe as well. The decay-threshold η_{decay} describes the decay of the amplitude in percent at T_{decay} and is selected in this work as 50% associated with the lowest frequency $\omega_{\text{ref,min}}$ involved. Note that harmonics with a frequency higher than $\omega_{\text{ref,min}}$ exhibit faster decay ending with an amplitude ratio of less than 50%. The computation of T_{decay} is given by equation 4.1. Fig. 4.3 reveals that this logic allows to truncated the signal appropriately. An additional processing step which is suggested by other researchers in context of both OMA and BSS methods is to scale the input signals, see Refs. [144, 33]. However, this is not used in this work, since promising results are obtained even without scaling.

$$T_{\text{decay}} = \frac{\ln\left(1/\eta_{\text{decay}}\right)}{\xi_{\text{ref}} \cdot \omega_{\text{ref,min}}} \tag{4.1}$$
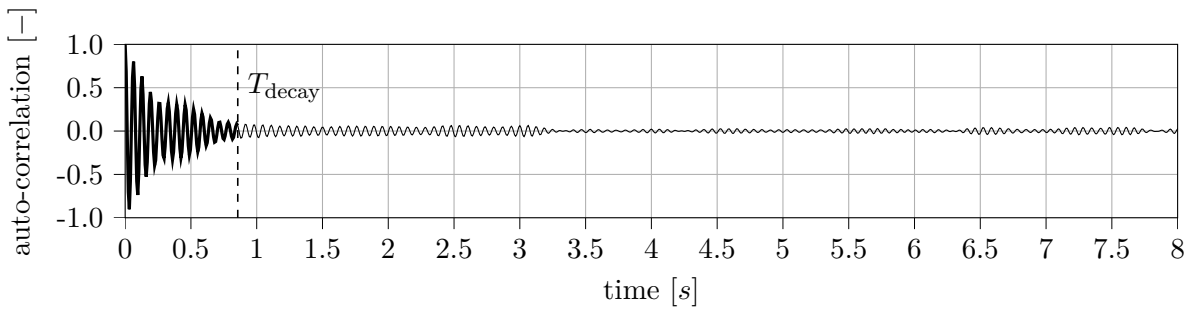
Figure 4.3.: Auto-correlation of the elastic airframe subject to GAUSSIAN white noise. The considered component is the translational vertical displacement at the MR hub.

4.2. Structural Response to Atmospheric Turbulence

In comparison with the simulation results obtained in calm air, Fig. 4.2 reveals that in presence of light turbulence significant broadband vibrations are characterizing the spectrum, while the MR harmonics remain nearly unaffected. The broadband vibrations are particularly amplified in close proximity to MR harmonics. Three effects are considered to cause this characteristic. First of all, the eigenfrequencies of the four higher elastic airframe modes are located rather close to the MR-BPF. Second, the MR blade flapping resonance is located in close proximity to the MR speed, see Fig. A.6(b). Third, turbulence encountered by rotating rotors causes cyclostationary effects, which accumulates energy at MR-speed integer multiples, see Ref. [98]. However, the first two aspects result from the transfer behavior of the helicopter structure itself and only the third aspect introduces coloring effects which disagree with OMA theory. At higher frequencies the broadband vibrations are multiple orders of magnitude below the lower frequencies located in particular within the frequency range of interest up to 30Hz, see Fig. 4.2. This is related to the turbulence spectrum which carries less energy at higher frequencies according to KOLMOGOROV's law. The spectra of the elastic MR hub motion are discussed in more detail in Ref. [257].

To evaluate the assumption that the system perturbed by atmospheric turbulence is nonetheless operating close to a reference motion in atmospheric turbulence, the simulated output signals including the generalized coordinates and the states specified in table 3.3 are studied based on a statistical analysis over one MR revolution. In general, the MR states are expressed in multi-blade coordinates, according to section 3.6. This analysis is based on both the mean values and standard deviations computed for each azimuthal position over all revolutions in light turbulence compared to calm air. The related results are shown in Fig. A.14 to Fig. A.21. In general, the mean values of the response in light turbulence do not agree with the results obtained in calm air. Consequently, the reference trajectory is altered by atmospheric turbulence. Note that in most cases the mean value shows oscillation at MR-BPF for both calm air and light turbulence. These oscillations are approximately biased with a constant offset over all azimuthal stations if turbulence is activated. An exception to this is the lateral elastic pitchlink motion, which shows an increased level of MR-2BPF, see Fig. A.20(c). Another exception to this are all differential modes, which exhibit MR-0.5BPF motion, see e.g. Fig. A.16,

The standard deviation of the signals in calm air is zero, due to the computed periodic trim-state and the fact that the motion after one MR revolution is repeated approximately. In fact, light atmospheric turbulence introduces a standard deviation, because a subsequent revolution undergoes not the same motion as the revolutions before. However, the standard deviation does not change azimuthally. Although the mean values are altered in presence of light turbulence compared to calm air, it is anticipated that in all cases the trajectory in calm air remains within the standard deviation introduced by light atmospheric turbulence. In this sense the disturbed solution is considered to stay close to the undisturbed reference.

Fig. A.14 reveals that the first three airframe modes oscillate rather randomly. The closer the eigenfrequency of an airframe mode is to the MR-BPF, the more dominant oscillations with MR-BPF are characterizing the modal coordinate approximately. Depending on the contribution of individual modes to the structural response of physical nodes, they exhibit rather stochastic or deterministic motions, see Fig. A.15. As an example, the lateral TR hub motion is in particular governed by the first elastic mode, see Fig. A.12. Since the first mode exhibits rather stochastic motion, the lateral TR motion is rather stochastic consistently, see Fig. A.15(h). Theoretically, a physical state dominantly characterized by mode 8, see Fig. A.14(h), would be rather periodic. However, note that all physical airframe states involve a high level of the stochastic content compared to the mean motion over one revolution due to the superposition of all modes.

To mask the periodic reference oscillation visible in the figures just discussed, notch-filtering of the MR-BPF is used as described in the previous section 4.1. The expectation is that the remaining distortion motion only includes stochastic signals components. The resulting statistics are studied in Fig. A.22 based on the probability distributions of the notch-filtered signals. In addition to notch-filtering, the other preprocessing steps introduced in section 4.1 are executed as well, except for the computation and truncation of the correlations. Figure A.22(a) indicates the probability distribution of the generalized airframe coordinates scaled with the norm of each related eigenvector. The modes show Gaussian behavior, while the mode with the larges discrepancy from the Gaussian distribution is mode 7. Note that the eigenfrequency of mode 7 is the closest to the MR-BPF. The probability distributions of the physical airframe states are close to Gaussian distribution as well, see Fig. A.22(b). Obviously, dominant periodic oscillations can indeed be removed from the airframe states by notch-filtering the MR-BPF. The remaining Gaussian distribution is resulting from the Gaussian distributed turbulence signals and the involved CLT due to the mixing of the elastic airframe modes.

In the following figures, see Fig. A.22(c) to Fig. A.22(h), significant discrepancies from Gaussian distribution are visible for some multi-blade coordinates, indicating that the periodic components included in these signals are not properly removed by the notch-filtering approach. In particular, this is true for all differential modes. This is explained with the dominant oscillation of the differential modes with MR-0.5BPF frequency, see Fig. A.16 to Fig. A.20. This component is not removed by notch-filtering. In addition, Fig. A.22(c) and Fig. A.22(e) show both a discrepancy of the collective mode from Gaussian distribution. However, neither the distributions nor the azimuthal average shown in Fig. A.16(a) and Fig. A.18(a) indicate that this discrepancy is due to distinct harmonics. Hence, it is expected that the related distortion motion is predominantly stochastic, however, in both cases the simulation time is not long enough to converge the probability distribution to Gaussian distribution. This is supported by the spectrum of the collective lead-lag and the collective feathering mode, since both states show an amplified level below 0.2Hz compared to the other coordinates, see Fig. 4.4(a) and Fig. 4.4(b). In particular, the slow harmonics involved in the feathering motion are interpreted to be related with the slow dynamics of the trim-controller, see section 3.3. In addition, two amplified frequencies in the feathering spectrum are highlighted, see Fig. 4.4(b), which are further discussed in section 4.7. The elastic servo displacement is close to Gaussian distribution, see Fig. A.22(h). With regard to the low

magnitude of the differential modes compared to the other multi-blade coordinates, the differential mode is excluded from the following analysis. Consequently, it is not necessary to mask the MR-0.5BPF. The other signals are considered to be suitable for output-only modal analysis using only MR-BPF notch-filtering.

(a) Lead-lag motion.

(b) Feathering motion.
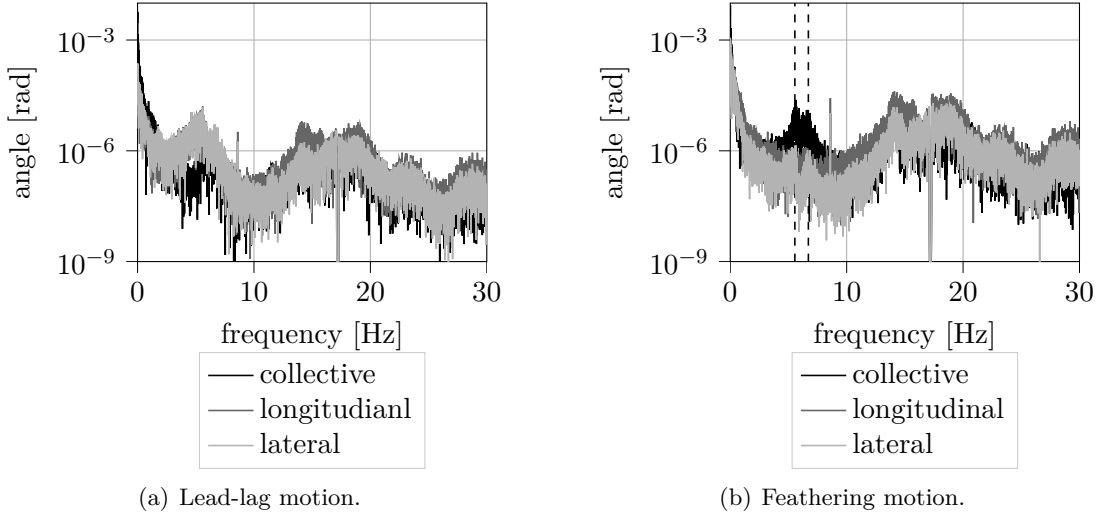
Figure 4.4.: Spectrum of lead-lag and feathering motion expressed in multi-blade coordinates obtained for the baseline flight condition using two-way coupled rotor-airframe simulation.

4.3. Mode Rejection and Signal Postprocessing

As explained in the introduction, OMA algorithms compute the system matrices of the corresponding time-discrete linear system, see Eq. 1.2. However, the modal properties of the time-continuous system are of practical relevance. These properties can be obtained based on the time-discrete model following Eq. 4.2 and Eq. 4.3 available from Refs. [264, 263], where $\hat{\cdot}$ represents the properties of the time-discrete system.

$$\lambda_k = \frac{\ln\left(\hat{\lambda}_k\right)}{\Delta t} \tag{4.2}$$

$$\Psi_k = \mathbf{C}\hat{\Psi}_k \tag{4.3}$$

Once a number of modes has been computed for the time-continuous system using eigenvalue decomposition, not all identified modes are physical. This is because the order of the system is in general not known in advance. Hence, the number of modes that is returned by the algorithm has to be defined explicitly and may exceed the number of physical modes. Even knowing the exact number of modes hidden in the system does not guarantee that all physical modes are returned properly, since spurious modes can indeed exist among the modes, see

Ref. [108]. Hence, a larger system order is required to be selected to return all physical modes. The typical procedure is to successively increase the system order and to track the recovered modes in a so called *stabilization diagram.* Spurious modes can be identified, since physical modes are assumed to remain constant in frequency with increasing system order. Therefor, automated clustering and selection procedures of stable modes have been demonstrated in the past, see Refs. [262, 304]. However, the selection throughout this work is conducted manually, which leaves indeed some level of ambiguity, see Ref. [219].

One source of spurious modes discussed above is external periodic forcing, which results in permanent oscillations. Hence, related components can be identified and removed from the stabilization diagram based on associated low damping values, see Ref. [108]. This criterion is used although the MR-BPF is removed from the signals, see section 4.1, since other permanent oscillations are characterizing the helicopter response as well. In addition, there are other criteria which help to identify spurious modes. In literature these criteria are called mode validation, Mode Rejection Criterion (MRC) or consistent mode indicator [262, 220]. Table 4.1 provides an overview of selected MRCs. This table follows a classification into hard and soft criteria according to Ref. [262]. Hard criteria are returning a boolean measure and soft criteria a gradual measure. Hence, a threshold in conjunction with soft criteria is typically used to transform them to an boolean indicator, corresponding to whether or not the particular mode is to be rejected. The first of the two hard criteria looks for the existence of a complex conjugate mode, which is characteristic for oscillating modes. The second one excludes modes with very low and even negative damping ratio and a ratio exceeding a maximum damping threshold. The soft criteria used in this work are the modal contribution of a single mode to the overall structural response measured by the Modal Transfer Norm (MTN), see Ref. [263] and Modal Assurance Criterion (MAC)-based mode rejection, see Ref. [274]. Because the eigenvectors returned by SSI-COV and NExT-ERA are complex in general, an appropriate formulation of the MAC criterion is used that handles complex vectors, see Ref. [9]. The MTN-criterion is implemented in this work based on Ref. [263]. Other criteria have been published as well like phase collinearity, etc., see Refs. [220, 263, 275], which are however not used in this work.

	description	threshold
hard criteria	complex conjugate pairs	any i with $|\Psi_k| - |\Psi_i| < 10^{-9}$
	damping ratio	$10^{-3} \leq \xi_k \leq 10^{-1}$
soft criteria	modal contribution	MTN $\geq 10^{-2}$
	MAC	any MAC ≥ 0.8

Table 4.1.: Overview MRCs.

Although the mode-shapes identified via BSS can be pre-selected using MRC as well, which is used later in section 4.6, other post-processing steps are required to obtain the relative damping ratios and the eigenfrequencies. This is because BSS does not identify system matrices which can be further processed using eigenvalue decomposition. BSS requires to extract these quantities from the separated generalized coordinates. A robust and classical approach to compute the eigenfrequencies is to use FOURIER-transformation. To determine

the eigenfrequencies, the dominant peaks are identified from the spectrum. In addition, several approaches to compute the damping are summarized in section 1.2. However, before well-known approaches can be applied to compute the damping based on the free decay, the NExT principle has to be involved, because the generalized coordinates exhibit no free decay but continuous stochastic motion. In comparison with other methods, Ref. [145] states that PM is to be preferred over e.g. LD in context of aeroelasticity. The PM is a SVD-based approach comparable to ERA, see Refs. [145, 11]. Since ERA is already implemented in the context of OMA in this work, this approach is used to compute the damping ratios of the separated source. In fact, this results in stabilization diagrams as well. However, the approach is found to be more robust compared to e.g. LD, which is found to have low robustness when applied to the noise contaminated correlations. Next to the damping ratios, ERA computes the eigenfrequencies which are obtained from the stabilization diagram as well. The rejection of modes computed with SOBI is based on the obtained spectra of the modal coordinates. In general, modes are rejected with more than one particular frequency characterizing the spectrum, which is assessed manually.

4.4. Main-Rotor Intrinsic Periodicity

Although the MR is characterized by intrinsic periodicity, see section 1.2, the modal analysis approaches used in this work assume linear time-invariant behavior. Hence, this section studies if the MR system's intrinsic periodicity requires explicit treatment during the course of MR output-only modal analysis. To quantify the periodicity of the MR over one rotor revolution, the linear matrices which are used during the non-linear MR simulation using generalized alpha, see section 3.2, are extracted at different MR azimuth angles. These matrices include the stiffness matrix $\mathbf{K}(\psi)$, the mass matrix $\mathbf{M}(\psi)$ and the gyroscopic matrix $\mathbf{G}(\psi)$. Note that the matrices $\mathbf{M}$ and $\mathbf{G}$ are singular, which results e.g. from constraints, which are only associated with the $\mathbf{K}$ matrix. Accordingly, pure zero block matrices can be identified in the matrices $\mathbf{M}$ and $\mathbf{G}$, see Eq. 4.4. Note that damping devices included in the MR simulation, like the lead-lag dampers, are not linearized and represented instead by the external forces $\mathbf{F}_1$ and $\mathbf{F}_2$. Hence the eigenvalues computed based on the system matrices do not represent the structural damping completely. Thus, structural damping is excluded from the analysis in this section.

$$\underbrace{\begin{bmatrix} \mathbf{M}_{11} & \mathbf{O} \\ \mathbf{O} & \mathbf{O} \end{bmatrix}}_{\mathbf{M}} \begin{bmatrix} \ddot{\mathbf{x}}_1 \\ \ddot{\mathbf{x}}_2 \end{bmatrix} + \underbrace{\begin{bmatrix} \mathbf{G}_{11} & \mathbf{O} \\ \mathbf{O} & \mathbf{O} \end{bmatrix}}_{\mathbf{G}} \begin{bmatrix} \dot{\mathbf{x}}_1 \\ \dot{\mathbf{x}}_2 \end{bmatrix} + \underbrace{\begin{bmatrix} \mathbf{K}_{11} & \mathbf{K}_{12} \\ \mathbf{K}_{21} & \mathbf{K}_{22} \end{bmatrix}}_{\mathbf{K}} \begin{bmatrix} \mathbf{x}_1 \\ \mathbf{x}_2 \end{bmatrix} = \begin{bmatrix} \mathbf{F}_1 \\ \mathbf{F}_2 \end{bmatrix} \tag{4.4}$$

$$\mathbf{M}_{11}\ddot{\mathbf{x}}_1 + \mathbf{G}_{11}\dot{\mathbf{x}}_1 + \underbrace{\left(\mathbf{K}_{11} - \mathbf{K}_{12}\mathbf{K}_{22}^+\mathbf{K}_{21}\right)}_{=:\tilde{\mathbf{K}}_{11}} \mathbf{x}_1 = \mathbf{0} \tag{4.5}$$

In Eq. 4.4 the state vector $\mathbf{x}_1$ can be identified to carry physical states and the $\mathbf{x}_2$ to be associated with constraints. Eliminating the states $\mathbf{x}_2$ in the upper row in combination with zeroing $\mathbf{F}_1$ and $\mathbf{F}_2$ to investigate the eigendynamics, leads to the following equation Eq. 4.5. In this equation $\mathbf{K}_{22}^+$ is the MOORE-PENROSE pseudoinverse since the matrix $\mathbf{K}_{22}$ has in general not full rank. Introducing the variable $\tilde{\mathbf{x}}$, see Eq. 4.6, leads to the equation 4.7, which describes the MR dynamics linearly at one particular azimuth.

$$\tilde{\mathbf{x}} = \begin{bmatrix} \mathbf{x}_1 \\ \dot{\mathbf{x}}_1 \end{bmatrix} \tag{4.6}$$

$$\begin{bmatrix} \mathbf{I} & \mathbf{O} \\ \mathbf{O} & \mathbf{M}_{11} \end{bmatrix} \dot{\tilde{\mathbf{x}}} + \begin{bmatrix} \mathbf{O} & \mathbf{I} \\ \tilde{\mathbf{K}}_{11} & \mathbf{G}_{11} \end{bmatrix} \tilde{\mathbf{x}} = \mathbf{0} \tag{4.7}$$

To obtain a suitable quantification of the periodicity of the system described by the equation Eq. 4.7, eigenvalue decomposition is used. Note that the real part of the eigenvalues does not represent the damping of the system appropriately as described above. The variation of the obtained eigenfrequencies over one revolution is depicted in Fig. 4.5. These vary approximately between $\pm 2\%$. The eigenfrequencies depicted in Fig. 4.5 are found four times in the linear periodic system with an offset of 90° each, which corresponds with the four blades of the MR. In fact, much more information can be extracted from the eigenvalues and -vectors varying with azimuth, however, this is beyond the scope of this work.
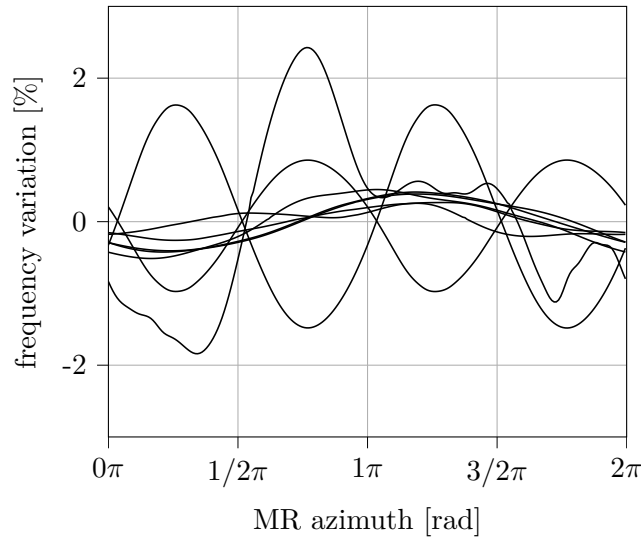
Figure 4.5.: Variation of the dominant MR eigenfrequencies over the MR azimuth.

To further assess this variation of $\pm 2\%$ in terms of an LTI-based modal analysis, the elastic airframe introduced in section 3.5 is modified such that it exhibits intrinsic periodicity. The selected approach is close to Ref. [10], where a MATHIEU oscillator is employed, see Eq. 4.8. In this section the MATHIEU oscillator is slightly modified, such that the value $\hat{a}$ is directly related to the variation of eigenfrequency for better comparison with the variation of the frequencies, observed in Fig. 4.5, see Eq. 4.9.

$$\ddot{q}_k + 2\xi_k\omega_{0,k}\dot{q}_k + \omega_{0,k}{}^2\left(1 + \hat{a}\cos\left(\Omega_{\mathrm{MR}}t\right)\right)q_k = {\Psi_k}^T\frac{\mathbf{F}\left(t\right)}{m_k} \tag{4.8}$$

$$\ddot{q}_k + 2\xi_k\omega_{0,k}\dot{q}_k + \omega_{0,k}{}^2\left(1 + \hat{a}\cos\left(\Omega_{\mathrm{MR}}t\right)\right)^2 q_k = {\Psi_k}^T\frac{\mathbf{F}\left(t\right)}{m_k} \tag{4.9}$$

As an approximation, all modes of the elastic airframe are varied in phase with the same perturbuation magnitude $\hat{a}$. A sensitivity study is conducted to evaluate up to which magnitude $\hat{a}$ the modal analysis is still able to return the modal properties of the assumed LTI system. To assess these variations the eigenfrequencies of the elastic airframe are periodically varied with increasing magnitude in the range $\hat{a} = 0.0...0.1$ (0%...10%). The eigenfrequencies and the MAC-values are evaluated for each $\hat{a}$. Since a diagonal structure of the MAC is observed in comparison with the time-invariant modal airframe properties, corresponding to the MAC-values found in the next section 4.5, only the diagonal MAC-values are further considered. According to Fig. 4.6(a), the computed eigenfrequencies of the system are all close to the reference and rather invariant towards the variation of $\hat{a}$. Fig. 4.6(b) reveals a similar result for the MAC-values, although some of the obtained MAC-values are smaller than 0.8, which indicates that the corresponding mode is not in agreement with the reference mode. However, in both cases no systematic dependency on the eigenfrequency variation is found and hence, it is assumed that the intrinsic periodicity has not to be handled explicitly in the following.
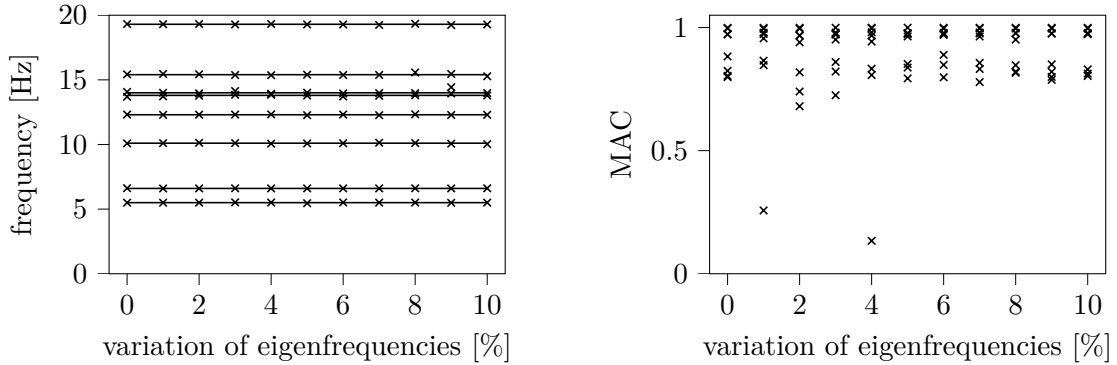

(a) Identified frequencies for different variations of frequency.

(b) Identified MAC-values (diagonal elements only) for different variations of frequency.

Figure 4.6.: Identified eigenfrequencies and MAC-values of the periodically varied elastic airframe. The airframe is modified such that the eigenfrequencies of all modes vary in phase over the MR azimuth angle.

## 4.5. Modal Analysis of the Airframe Subject to White Noise

The validity and performance of the three output-only modal analysis approaches are analyzed and demonstrated in this section. The selection of the methods is based on the overview and the discussion provided in the introduction, see section 1.2. All three approaches are time-domain based methods. In this section the analysis is based on the elastic airframe introduced in section 3.5, subject to GAUSSIAN white noise. The standard deviation of the introduced forces in each direction is 1000.0N at the the MR hub, 100.0N at the TR hub and 10.0N for each aerodynamic empennage element. All processes are independent and the simulation is conducted over 4 minutes. The eigenfrequencies, relative damping ratios and mode shapes of the elastic airframe are known a priori, serving as a validation reference. In addition, the elastic airframe is used, because the isolated treatment of the elastic airframe provides important insights to the helicopter-specific airframe modal analysis.
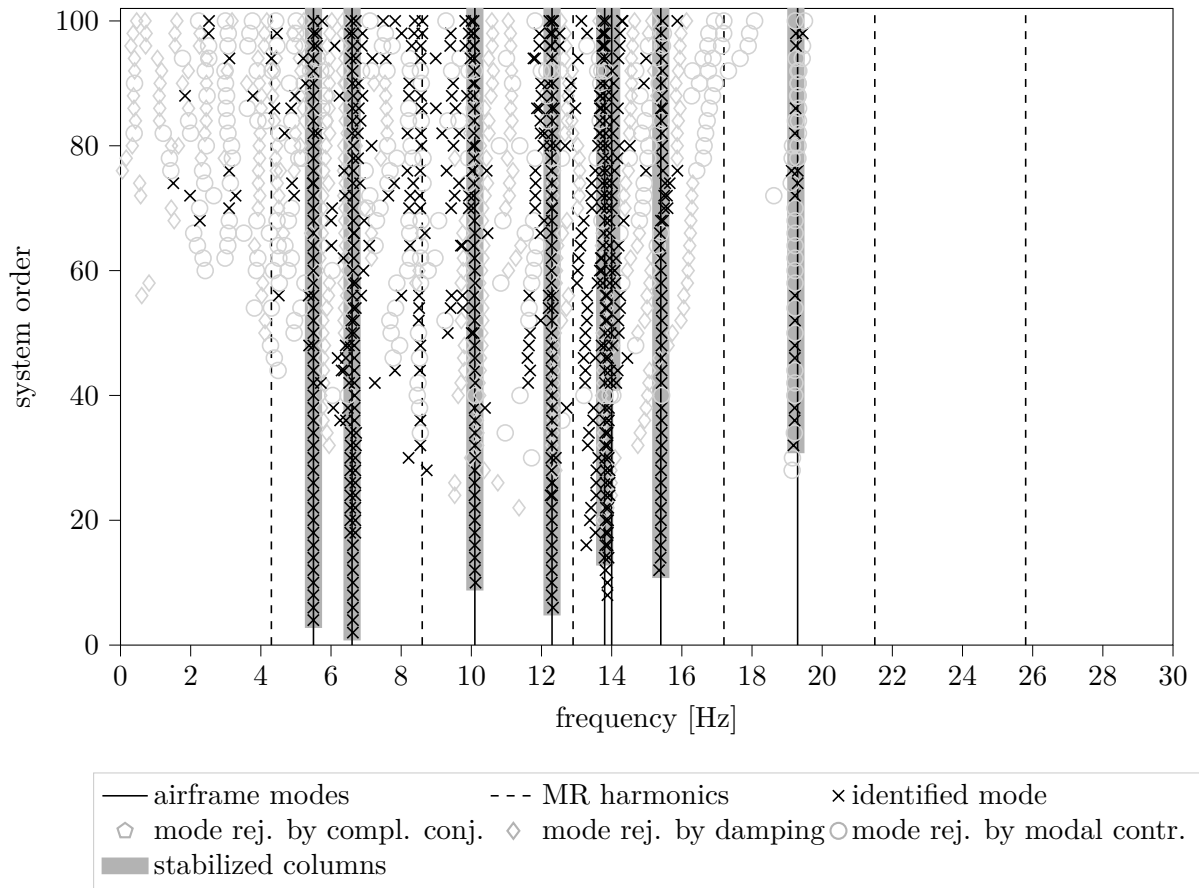
Figure 4.7.: Stabilization diagram obtained for the elastic airframe subject to GAUSSIAN white noise using NExT-ERA.

The stabilization diagrams obtained with NExT-ERA and SSI-COV for the elastic airframe subject to white noise are depicted in Figs. 4.7 and 4.8, which are both very similar. In both cases non-physical modes are properly rejected, which are indicated in grey. Most of the modes are rejected based on the damping ratio (diamond), followed by the modal contribution (circle) and finally by the complex conjugate criterion (pentagon). Note that in this section the MAC-based mode rejection criterion is not used. The remaining modes cluster in close proximity to the airframe eigenfrequencies. In Fig. 4.9 the corresponding damping ratios for selected modes are indicated. The overall trend of the reference damping is covered correctly, however, the damping ratios are subject to a higher level of inaccuracy compared to the eigenfrequencies. The MAC-values in Fig. 4.10(a) and Fig. 4.10(b) show good agreement with the reference mode shapes for both OMA approaches. Some off-diagonal elements are visible, since the modes 3,5 and 7 are very similar in particular at the horizontal tail, see Fig. A.11.
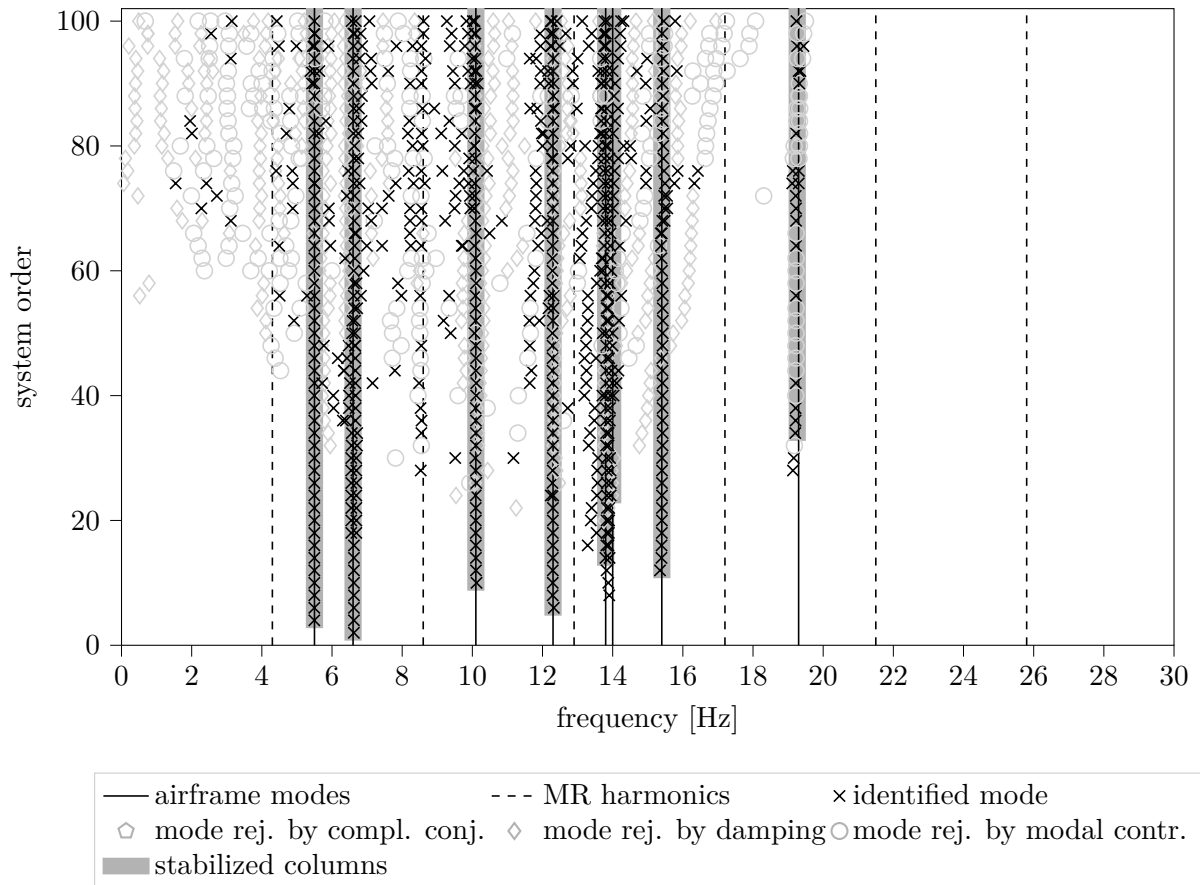

Figure 4.8.: Stabilization diagram obtained for the elastic airframe subject to GAUSSIAN white noise using SSI-COV.
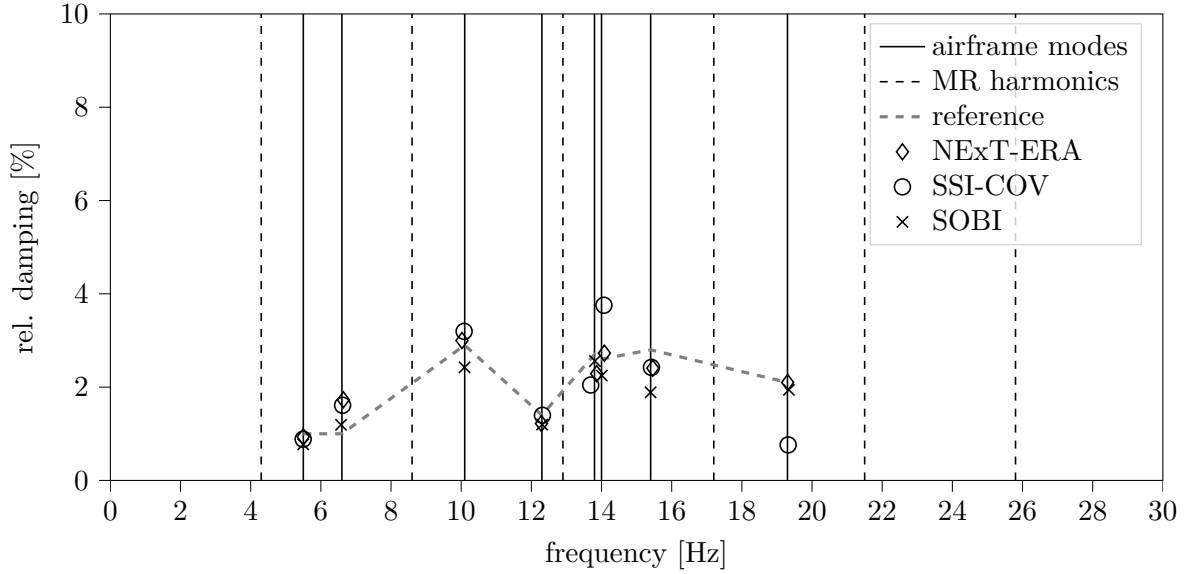
Figure 4.9.: Modal damping and eigenfrequencies obtained for the elastic airframe subject to Gaussian white noise using NExT-ERA, SSI-COV and SOBI in comparison with the exact airframe quantities.

The spectra of the separated modal coordinates obtained with SOBI are indicated in Fig. A.23. Obviously, the separation can be accomplished successfully and the dominant frequency of each source is in agreement with another eigenfrequency of the airframe. The four remaining sources (difference between 12 considered airframe states and 8 airframe modes) contain Gaussian white noise. In this case no modal rejection criteria are used and the modes are selected manually. The extracted damping ratios from the separated sources via NExT-ERA are indicated in Fig. 4.9. In comparison with NExT-ERA and SSI-COV, no fundamental differences are visible and the damping estimation is subject to a similar level of inaccuracy.
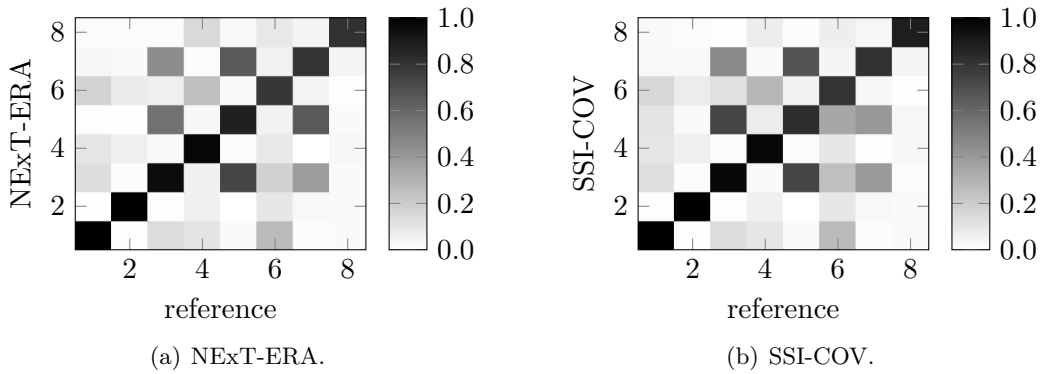
(a) NExT-ERA.

(b) SSI-COV.

Figure 4.10.: MAC-values obtained for the elastic airframe subject to Gaussian white noise. The eigenvectors are computed using NExT-ERA and SSI-COV and are compared to the exact eigenvectors of the airframe.

In Fig. 4.11 the MAC-values for the eigenvectors obtained with SOBI are depicted. They indicate a good correlation with the reference mode shapes. In comparison with the results obtained with NExT-ERA and SSI-COV, the off-diagonal elements are less pronounced, which indicates a slight improvement in terms of eigenvector computation. From the results presented in this section it is anticipated that the algorithms are implemented correctly. One important conclusion is that the considered methods are all able to identify the airframe modes appropriately, even if some of the modes are very close to each other, which is typical for helicopter airframes having comparable stiffness and mass properties in lateral and vertical direction.
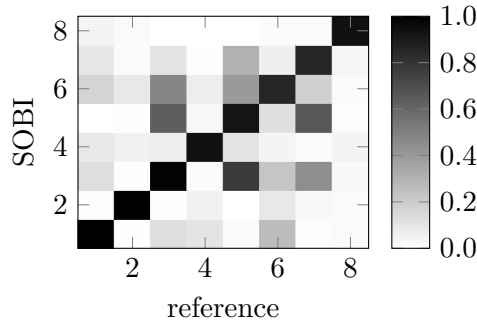
Figure 4.11.: MAC-values obtained for the elastic airframe subject to Gaussian white noise. The eigenvectors are computed using SOBI and are compared to the exact eigenvectors of the airframe.

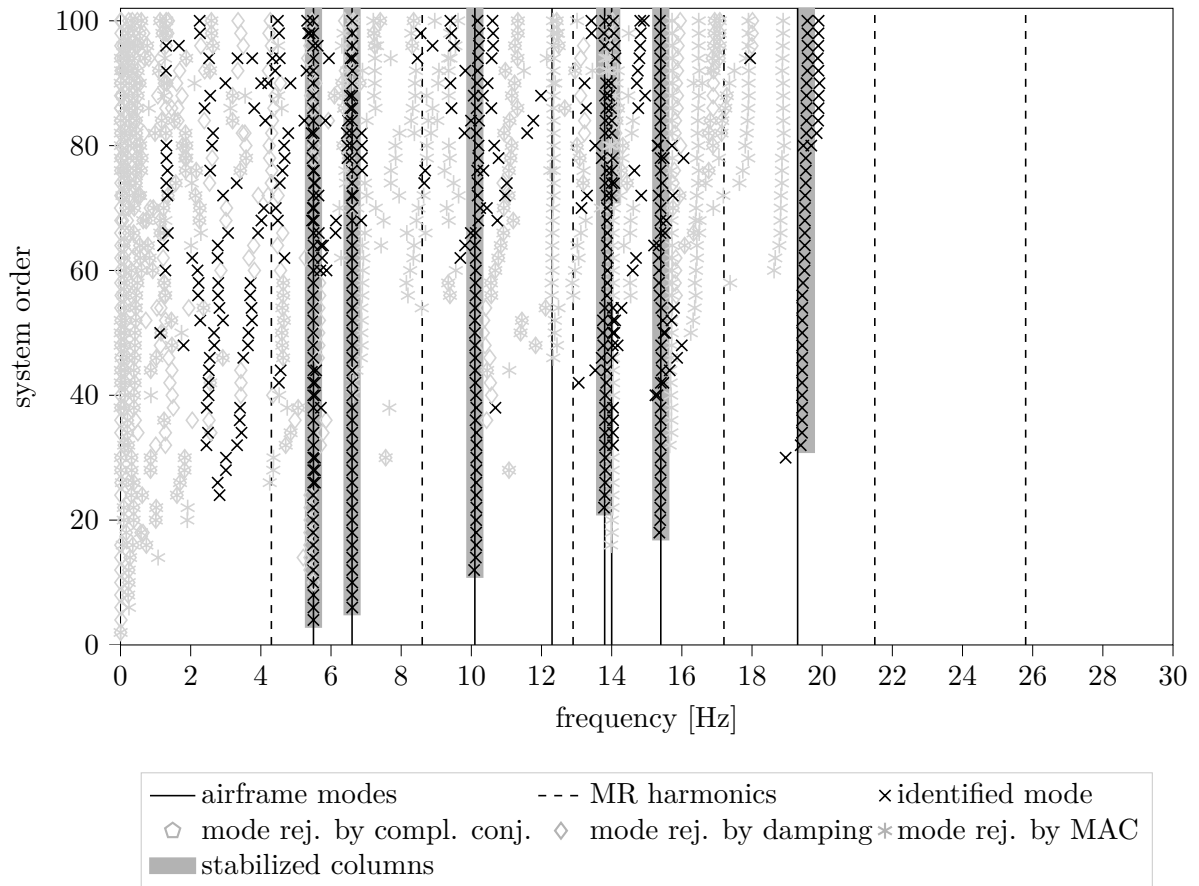## 4.6. One-Way Coupled Airframe Modal Analysis

In this section the output-only modal analysis is conducted based on the airframe vibrations obtained from one-way coupled rotor-airframe simulation in atmospheric turbulence. This coupling approach allows to interpret the airframe as a subsequent independent linear system. Hence, the modal properties of the airframe dynamics are known a priori and serve as a reference of the identified modal properties. In literature, one-way rotor-airframe coupling is as well referred to as hub-fixed simulation, because the rotor dynamics are not influence by the elastic airframe motion at the hub interface connection. Hence, this approach neglects the structural impedance of the elastic airframe in the MR simulation. However, it was found to be a reasonable approximation of the MR hub loads previously, see e.g. Ref. [65]. The MR is interpreted as an non-linear filter of the stochastic signals from atmospheric turbulence. The loads of the MR, the TR and the stabilizers are applied to the elastic airframe simultaneously. Compared to the excitation with Gaussian white noise, see section 4.5, this has some consequences. In particular, the MR characteristic transfer-path introduces additional coloring, amplifies the vertical direction and introduces specific rotor-harmonics.

Since NExT-ERA and SSI-COV are found to be very similar in section 4.5, which is confirmed for the coupled rotor-airframe analysis as well, in the following work only SSI-COV is used. For comparison with SSI-COV, SOBI is used. Before the methods are applied, the input

signals are preprocessed according to section 4.1. Note that in the current section the modal contribution rejection criterion is replaced by the MAC, see table 4.1. The identified modes are always sorted with increasing frequency for both SSI-COV and SOBI. If not specifically highlighted, the results computed in this section are based on the FullFT turbulence model, see section 2.3.

The stabilization diagram obtained with SSI-COV for the baseline flight-condition described in table 1.2 is shown in Fig. 4.12. At low frequencies up to 1Hz, a high number of modes is rejected. The diagram indicates the proper stabilization of 6-7 modes. Note that the airframe mode 4 is indeed identified but rejected based on MAC-values. The modes 5 and 6 are very close and not always both are identified. In addition, an offset to higher frequency of mode 8 is visible. Finally, 7 modes are obtained from the highest system dimension shown in the stabilization diagram. The stabilization diagrams obtained for the other flight conditions are not explicitly shown in this work. However, properly stabilized modes are obtained in these cases as well, similar to Fig. 4.12.

Figure 4.12.: Stabilization diagram obtained for the one-way coupled elastic airframe using SSI-COV. MAC-based mode rejection criterion is applied.

During the modal analysis using SOBI it is found that this method identifies spurious components of very low frequency, which deteriorates the determination of the physical modes. This is consistent with the high number of spurious modes at low frequency detected when using SSI-COV, see Fig. 4.12. However, in this case the spurious modes are successfully rejected by appropriate criteria. These criteria are applicable in the context of BSS as well, however, since only a small number of modes can be obtained, limited by the number of states included in the analysis, the spurious sources prevent the identification of physical modes. The occurrence of spurious sources associated with low frequency when using SOBI is prevented by introducing a high-pass filter with a cutoff-frequency of 1Hz. In this context it is emphasized that the masking the MR-BPF is much more relevant for the SOBI algorithm compared to SSI-COV. If the MR-BPF is not properly masked during the modal analysis using SOBI, the algorithm predominantly steers towards identifying many spurious sources related with the MR-BPF. SSI-COV is more robust in this context and is still able to properly identify physical modes even in presence of the MR-BPF. Spurious modes associated with the MR-BPF can alternatively be removed successfully by applying the mode rejection criterion based on damping, since the spurious modes with MR-BPF are associated with damping close to zero due to permanent oscillation.

The frequencies and damping ratios obtained with SSI-COV, for all flight conditions specified in table 1.2, are depicted in Fig. 4.13 in comparison with the exact modal parameters of the elastic airframe. In addition, a simulation based on the baseline flight-conditions is included, which only accounts for MR loads introduced into the elastic airframe. The two-way coupled results shown in Fig. 4.13 are discussed later in section 4.7. The identified frequencies based on one-way coupled simulation show a reasonable agreement with the reference values. Note that the mode 4 which is not identified for the baseline simulation, see Fig. 4.12, is however identified under different simulation settings. Hence, the quality of the identification depends on the flight condition. In contrast to the frequencies, the damping ratios are subject to higher inaccuracies, in particular the damping ratios obtained for modes 3, 5 and 6. The variation in damping for the other modes is smaller. Note that the trend of modal damping is however covered appropriately. In general, relative damping tends to be under-estimated. Compared with the GAUSSIAN white noise driven simulation in the previous section 4.5, the inaccuracies in damping ratio obtained with the one-way coupled helicopter simulation are not significantly higher, see Fig. 4.9 for comparison.

Similarly, in Fig. 4.14 the eigenfrequencies and relative damping ratios obtained with SOBI are depicted. The two-way coupled results are discussed in the following section 4.7 as well. In comparison with the results obtained with SSI-COV, see Fig. 4.13, the computation of the frequencies is similarly accurate, while the damping ratios are subject to less inaccuracies in general. However, note that less modes are identified using SOBI and in particular mode 7 is only identified from a one-way coupled simulation at cruise-speed.

To investigate the agreement of the identified eigenvectors with the exact mode-shapes, the MAC-values for all different simulations covered in Fig. 4.13 are shown in Fig. A.24. Again the two-way coupled results are discussed later in chapter 4.7. In general, not all modes are properly identified in terms of the MAC. Note that modes with no agreement in MAC are rejected anyway by the corresponding rejection criterion, see table 4.1. In all cases the first
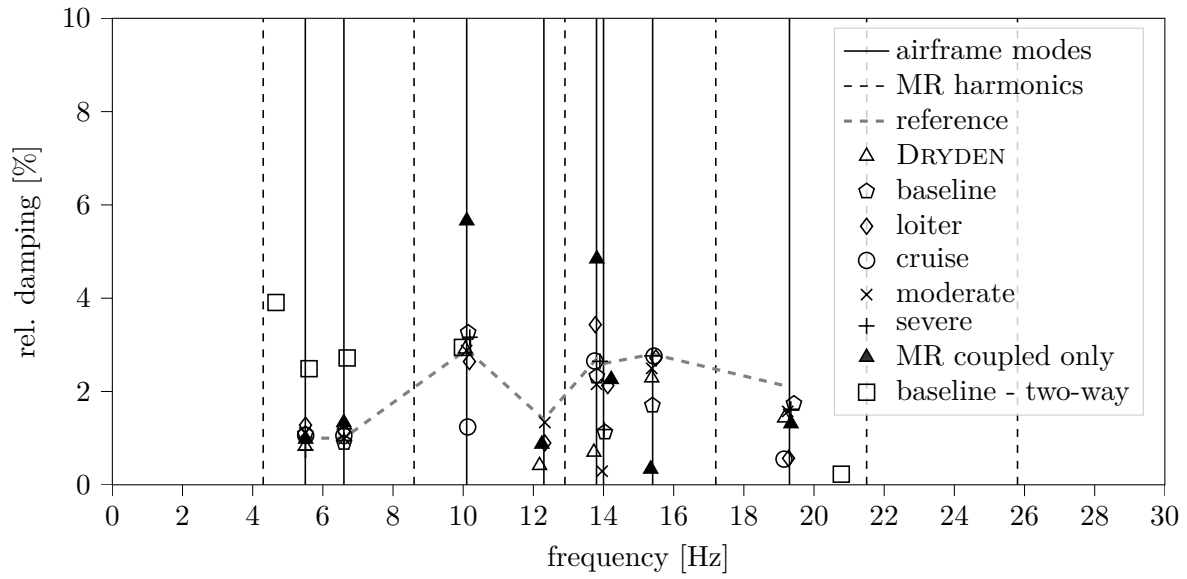
Figure 4.13.: Modal damping and eigenfrequencies obtained for the one-way coupled elastic airframe using SSI-COV in comparison with the exact airframe quantities.
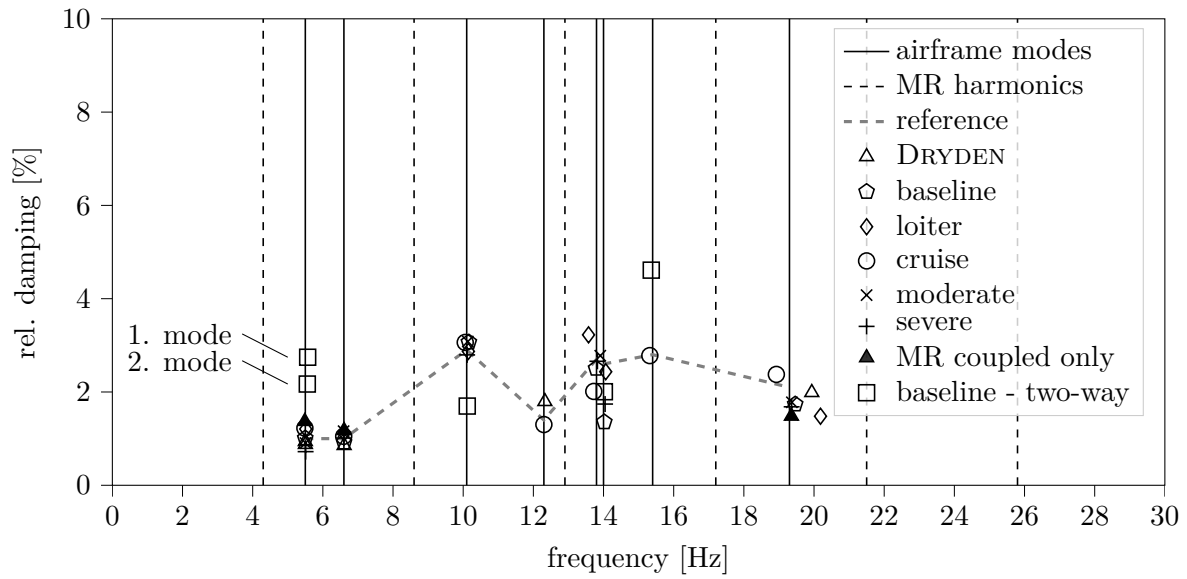
Figure 4.14.: Modal damping and eigenfrequencies obtained for the one-way coupled elastic airframe using SOBI in comparison with the exact airframe quantities.

3-4 modes are properly identified. In some cases the modes 4 to 6 are not found. When using the DRYDEN turbulence model, mode 8 cannot be identified. An explanation for this might be that the shift of energy towards higher frequencies via cyclostationary effects is not modeled by the DRYDEN model. This shift of energy can be relevant for the identification of the highest considered mode 8. The flight condition at loiter-speed, see table 1.2, allows to identify all airframe modes. The advancing ratio corresponding to the loiter-speed flight condition is expected to represent a beneficial relationship between rotor induced vibrations and rotational sampling effects. At higher speeds, higher asymmetric flow conditions are expected to deteriorate the modal analysis due to more pronounced rotor-harmonics. At lower speeds, a higher influence through cyclostationary effects and the related shift of energy is expected to deteriorate the modal analysis as well. Although this result is confirmed by repeated simulations it is not evident whether this result is physical or due to modeling and numerical characteristics.

In Fig. A.25 the MAC-values of the modes obtained using SOBI are depicted, corresponding to the modal properties shown in Fig. 4.14. In this case no simulation run allows to identify all reference modes. Except for the case where the MR is coupled only, SOBI computes the first 3 modes. For the baseline flight-condition, in comparison with SSI-COV, SOBI fails to identify mode 7. Furthermore, the agreement with the exact mode shapes is found to be lower compared to the vectors identified with SSI-COV. In particular, if only MR forces are introduced, the algorithm is able to only separate 3 modes. A slight improved identification using SOBI compared to SSI-COV is obtained in cruise-flight conditions.

A concluding remark of this section is that the both algorithms are able to identify airframe modes excited by the atmospheric turbulence spectra in principle. In particular, the first three modes are robustly identified. In addition, both algorithms are able to identify modes in close proximity to the MR-BPF. The picture changes if the MR-BPF is not removed from the spectrum especially in the context of SOBI. In general, SSI-COV is found to be slightly preferred over SOBI. First of all, SSI-COV is able to return more physical modes and second, spurious modes can be handled more appropriately using SSI-COV. This is because the limited number of sources separated using SOBI provides not much room to cope with spurious source. In the context of SOBI, these are required to be known in advance in order to preprocess the input signals appropriately.

4.7. Two-Way Coupled Rotor-Airframe Dynamics

This section is concerned with the modal analysis of the two-way coupled rotor-airframe system, which accounts for the airframe impedance. Two-way coupling is realized by closing the switch indicated in Fig. 3.1. Consequently, the airframe cannot be considered as a linear subsequent independent system, since its response is fed back into the MR simulation and into the TR and stabilizer aerodynamics. Hence, the MR and the TR as well as the stabilizers depend on the elastic airframe motion. Consequently, the two-way coupled elastic helicopter structure exhibits dynamic modes which are not known a priori.

Fig. 4.15 depicts the stabilization diagram obtained with SSI-COV from the two-way coupled simulation. Compared to the one-way coupling, see Fig. 4.12, a reduced number of spurious modes is rejected, because the MAC is the most effective criterion to remove spurious modes, however, this criterion cannot be applied in case of two-way coupling, because the modes are not known in advance. Many modes are identified and not rejected in close proximity to the MR-BPF. In particular, three modes are considered as physical modes since they show sufficient stabilization. This includes the modes identified close to the first and second eigenfrequency of the isolated airframe as well as a third modes slightly below the first eigenfrequency, which are highlighted in grey, see Fig. 4.15. In vicinity of the isolated airframe modes 3 and 4, no modes are identified. Most of the modes identified in proximity to the MR-BPF are not in agreement with the concept of stabilized modes. However, three additional modes are selected from the stabilization diagram which are considered as rather stabilized modes. Accordingly, these six modes are selected from the stabilization diagram for further analysis. All modes discussed in this section are always sorted with increasing frequency.
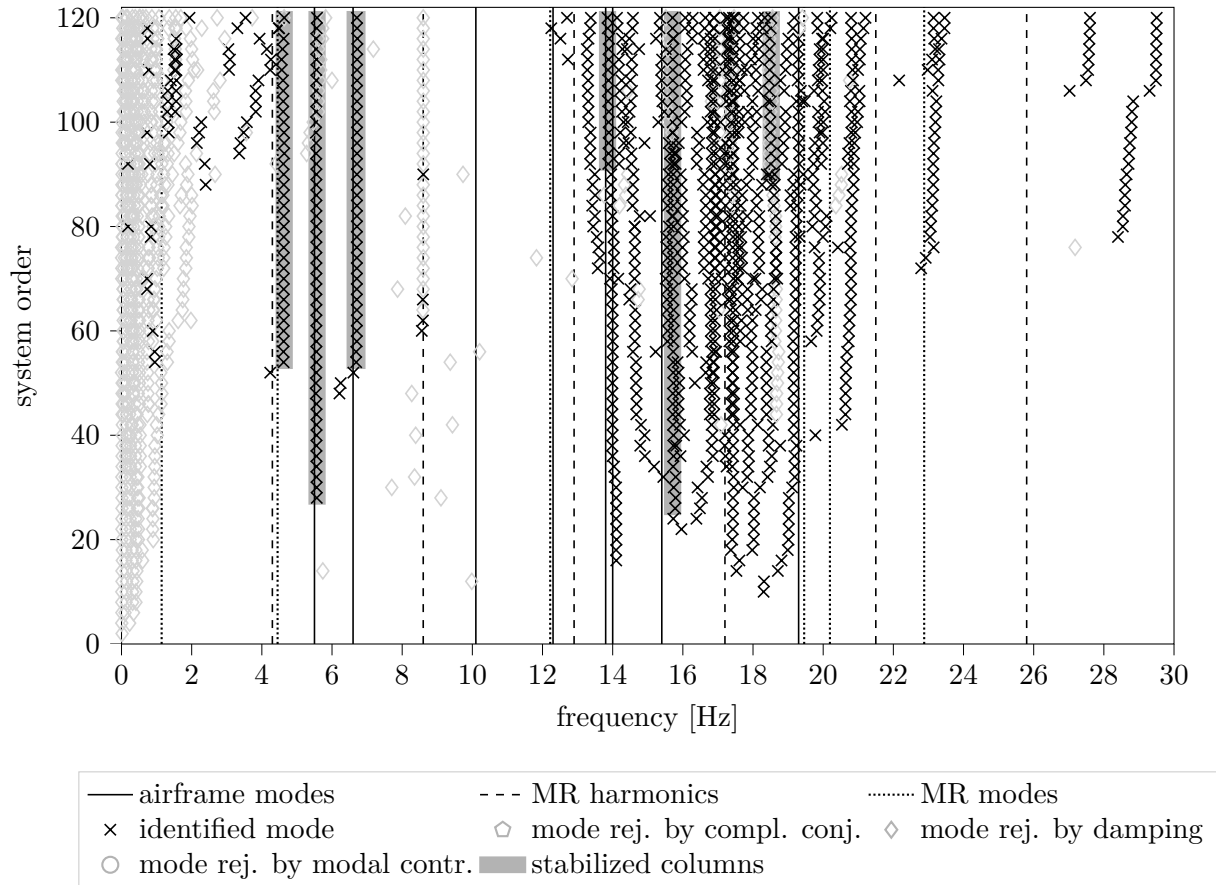
Figure 4.15.: Stabilization diagram obtained for the two-way coupled helicopter system using SSI-COV. Only MR states and the elastic motion of the MR hub are included.

The further discussion of the identified modes follows two perspectives. The first perspective is to only include the airframe coordinates into the analysis. This allows to compare the eigenvectors with those of the isolated airframe. The second perspective is to exclude the elastic airframe coordinates from the analysis of the eigenvectors except for the MR interface node to focus on the MR-airframe coupling. The stabilization diagram in Fig. 4.15 is obtained for this second perspective. The modal analysis is conducted with the selected minimum number of coordinates only, because it is found to improve the modal analysis. Hence, both perspectives do not necessarily identify the same modes.

If only the airframe states are included in the analysis, the comparison of the eigenvectors with the isolated airframe modes based on the MAC shows as degraded agreement compared to one-way coupled simulation. This is indicated for the baseline flight-condition in Fig. A.24(h) for the modal analysis with SSI-COV and in Fig. A.25(h) for the modal analysis with SOBI. In case of SSI-COV only the first three modes are in agreement. In case of SOBI, significant MAC-values are only found for mode 1 and mode 3. Fig. 4.13, which is obtained using SSI-COV, reveals that the associated damping ratios of the modes located closely to the first and the second airframe eigenfrequency are increased. This is assumed to result from additional aerodynamic damping. In Fig. 4.14 a similar result for the first airframe mode is obtained using SOBI. In this case, two modes with a frequency close to the first isolated airframe eigenfrequency are identified. The eigenfrequencies are slightly increased compared to modes of the isolated airframe. The increase is not considered to be significant, however, a physical explanation for an increase in frequency are MR centrifugal forces introducing additional stiffening to the system.

In the following, the entries in the eigenvectors belonging to the airframe tail section are excluded from the analysis and the MR states are included in the eigenvectors to focus on the MR-airframe coupling. In addition, the elastic pitchlink and elastic actuator displacement are excluded from the analysis, since the contribution of these states to the equivalent feathering motion is one order of magnitude below the feathering motion itself, see section 4.2. Hence, the states included in the following analysis are the elastic MR hub displacement as well as MR flapping, lead-lag and feathering motion and elastic MR blade torsion.

The frequencies and damping ratios of the stabilized modes of five different flight-conditions specified in table 1.2 are indicated in Fig. 4.16 and in Fig. 4.17. In both figures, the damping ratios and eigenfrequencies of the isolated airframe are depicted as reference. The selection of the 6 modes for the baseline flight-condition from the stabilization diagram is representatively shown in Fig. 4.15. It is found that the lower modes are associated with a higher damping ratio compared to the structural damping of the isolated airframe, whereas modes closer to the MR-BPF are associated with low damping. While the modes close to the first and second airframe mode obtained by SSI-COV are obtained by SOBI as well, see Fig. 4.17, this is not the case for the higher modes. In general, SOBI identifies again a reduced number of modes compared to SSI-COV. In both cases no clear dependency on modal damping is found with either turbulence intensity or flight-speed due the inaccuracies related with the damping prediction. The eigenfrequencies of the lower modes are consistent by comparing different flight-speeds and turbulence intensities. One particular finding is that in case only MR loads are two-way coupled with the airframe, these lower frequencies in vicinity of airframe mode
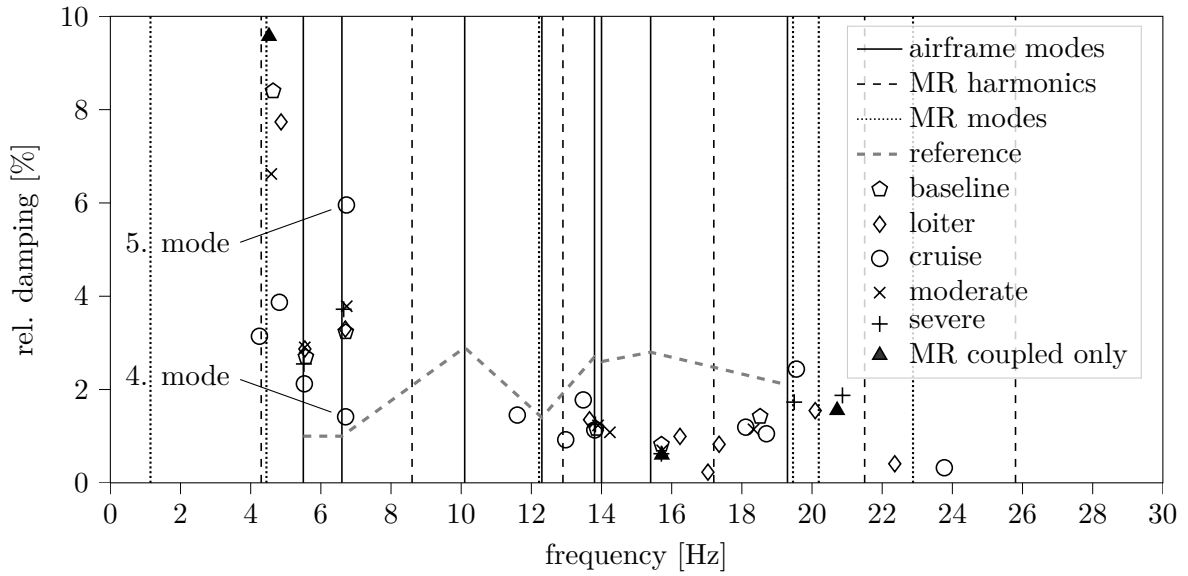
Figure 4.16.: Modal damping and eigenfrequencies obtained for the two-way coupled helicopter system using SSI-COV. Only MR states and the elastic motion of the MR hub are included.
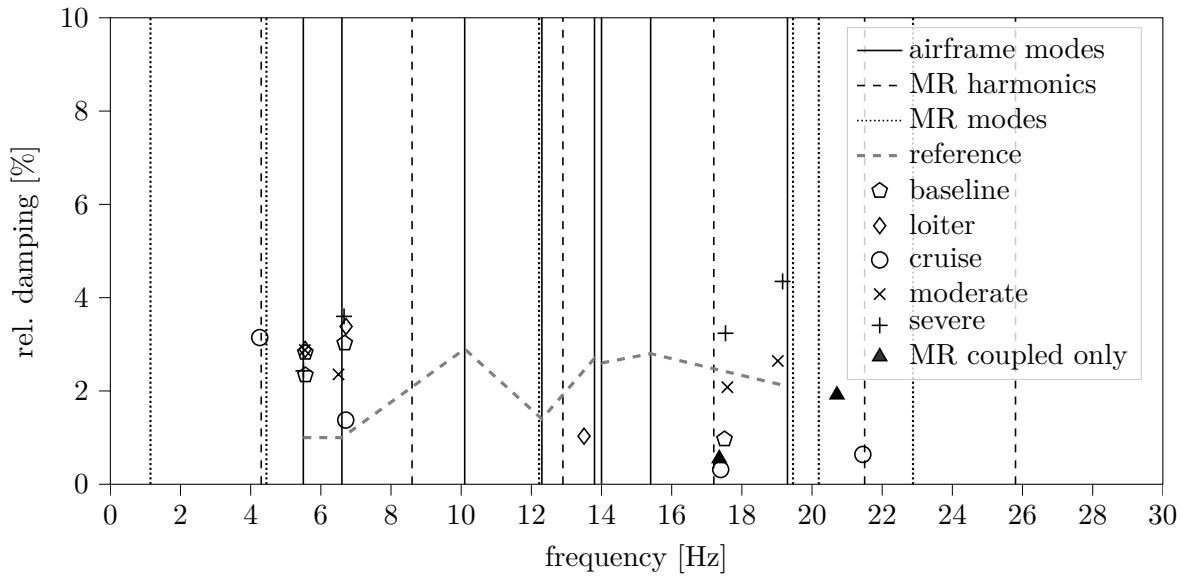
Figure 4.17.: Modal damping and eigenfrequencies obtained for the two-way coupled helicopter system using SOBI. Only MR states and the elastic motion of the MR hub are included.

1 and 2 are not found. Note that in Fig. 4.16 modes with a frequency higher than the third eigenfrequency of the elastic airframe are not consistent in frequency when comparing different flight-conditions, which is true for the modes identified with SOBI as well, see Fig. 4.17. The higher frequencies in proximity to the MR-BPF are assumed to be subject to detrimental effects through a high level of MR aerodynamic damping. Note that all modes identified with SSI-COV stem from stabilized columns in corresponding stabilization diagrams.

To further assess the identified modes, the MAC-values are studied in the following. However, since no reference mode shapes are available for comparison, the agreement of the eigenvectors obtained from two-way coupled analysis is determined based on MAC-values computed in comparison of different flight-conditions identified with SSI-COV, see Fig. A.26 and SOBI, see Fig. A.27, as well as in comparison of SSI-COV and SOBI, see Fig. A.28.

The MAC-values in Fig. A.26 are computed using SSI-COV, with the results obtained for the baseline flight-condition selected as reference. As indicated by the MAC-values shown in the figure, an agreement of the lower 2-3 modes is found, except for the case where only the MR is coupled with the airframe, see Fig. A.26(e). This is because the lower modes, which show an agreement for different flight-speeds and turbulence intensities are not identified if the MR is coupled only, as already discussed in context of Fig. 4.16. Apparently, due to the airframe impedance, isolated MR-airframe coupling does not enable the identification of these modes. This result is confirmed by SOBI in Fig. A.27(e). Due to the agreement found for the lower modes in the other cases in Fig. A.26, the first 3 modes identified for the baseline flight-condition are assumed to be physical. The agreement of the higher modes is poor in contrast, see e.g. Fig. 4.16. Hence, the higher modes are not considered to be physical. Note that the selection of the upper 3 modes for the baseline flight-conditions is in fact questionable, since the modes are not strictly stabilized, see Fig. 4.15. The equivalent MAC-values obtained with SOBI are indicated in Fig. A.27. The poor agreement in case only the MR is coupled is discussed already. The other MAC-values show degraded agreement in comparison with SSI-COV. However, for the higher turbulence intensities a consistent agreement with the baseline flight-condition is found. Poor agreement is found for the comparison of different flight-speeds.

In particular, the modes 1,3 and 4 obtained for the baseline flight-conditions are interpreted to be physical in case of SOBI, see Fig. A.27. In case of SSI-COV the corresponding physical modes are labeled 1,2,3 obtained for the baseline flight-condition as well. Note that in particular the SOBI-baseline modes 1,3 and the SSI-COV-baseline modes 2,3 have comparable frequencies. To further study the relationship between these modes, in Fig. A.28 the modes identified with SSI-COV are compared with the modes identified with SOBI. Apparently, in all cases no significant agreement between the modes is found. The degraded agreement between the eigenmodes obtained in comparison of SSI-COV with SOBI is expected to result from the difference that SOBI computes real-valued eigenvectors, while SSI-COV computes complex-valued eigenvectors. In case of one-way coupling this is not an issue, see section 4.6, because the eigenvectors computed with SSI-COV are indeed complex but the imaginary parts have comparable low magnitude. In case of two-way coupling the imaginary part increases, which is assumed to result from the complex interaction between the airframe and the MR and an associated increased level of aerodynamic damping. Hence, the physical rel-

evance of identified coupled MR-airframe modes cannot be confirmed by comparison of the eigenvectors based on the MAC, although some frequencies are in agreement as mentioned above.

Based on the discussion above two modes are selected for further aeroelastic analysis which are computed using SSI-COV. Corresponding to the agreement in terms of MAC indicated in Fig. A.26, the modes baseline-2&-3 are closer analyzed, which are referred to as mode A and mode B in the following. These modes are found to agree in particular with modes loiter-2&-3, cruise-3&-4, moderate-2&-3 and severe-1&-2. Note that the modes cruise-3 and moderate-3 are included, although the related MAC-values indicate poor agreement, see Fig. A.26. However, this discrepancy can be further analyzed by including the two modes as well. In Fig. 4.18 the magnitude of the eigenvector entries is indicated. Note that the 5 different flight-conditions are computed and analyzed in terms of OMA independently from each other. Due to the inaccuracies in damping estimation and the relationship between the damping and the imaginary parts of the eigenvectors, the phases of the modes are not further investigated.

Apart from a dominant collective feathering motion, mode A is characterized by a longitudinal and lateral elastic motion of the MR hub in combination with longitudinal as well as lateral lead-lag motion and collective flapping, see Fig. 4.18(a). Since both longitudinal and lateral lead-lag motion are involved in the mode operating at a frequency of 5.55Hz, this indicates a lead-lag whirl mode, coupled with a horizontal motion of the MR hub. Note that this result is visible for all different flight speeds and turbulence intensities, while the cruise-speed flight-state shows the highest disagreement with the baseline flight-state, which is in agreement with the MAC-values indicated in Fig. A.26. Apart from collective feathering motion, mode B is characterized by longitudinal elastic MR hub motion in particular, see Fig. 4.18(b). Again longitudinal and lateral lead-lag motion as well as collective flapping and lateral MR hub motion are pronounced, however, to a much lower extend compared to collective feathering motion than in mode A. The eigenvector obtained from cruise-flight shows the highest disagreement with the baseline case, which is again in agreement with the obtained MAC-values, see Fig. A.26. Note that both modes are properly damped, indicated by the mean damping computed for the all 5 cases. However, note that in cruise-flight a particularly low damping ratio is obtained, see Fig. 4.16.

Independent of the flight-condition, both modes involve a dominant collective feathering motion, see Fig. 4.18. With regard to Fig. A.22(e) and Fig. 4.4(b), the collective feathering exhibits a rather slow motion. Hence, statistical treatment of this component might lead to inaccurate results. However, since the modes are identified independently from each other for different flight-conditions, they are assumed to represent indeed physical modes. The contribution of the collective feathering motion indicates an involved aeroservoelastic phenomenon. Since the controller activity is represented by the feathering motion, this phenomenon is induced via the closed-loop trim controller. Note that this contribution is in fact supported by the discussion in section 3.3. In particular, Fig. 3.6(a) confirms that the forward actuator which has the highest influence on the MR thrust, shows two peaks at approximately the same frequency of the two aeroelastic modes A&B at 5.55Hz and 6.71Hz. In addition, the spectrum of the collective feathering motion shows the two peaks as well, see Fig. 4.4(b).
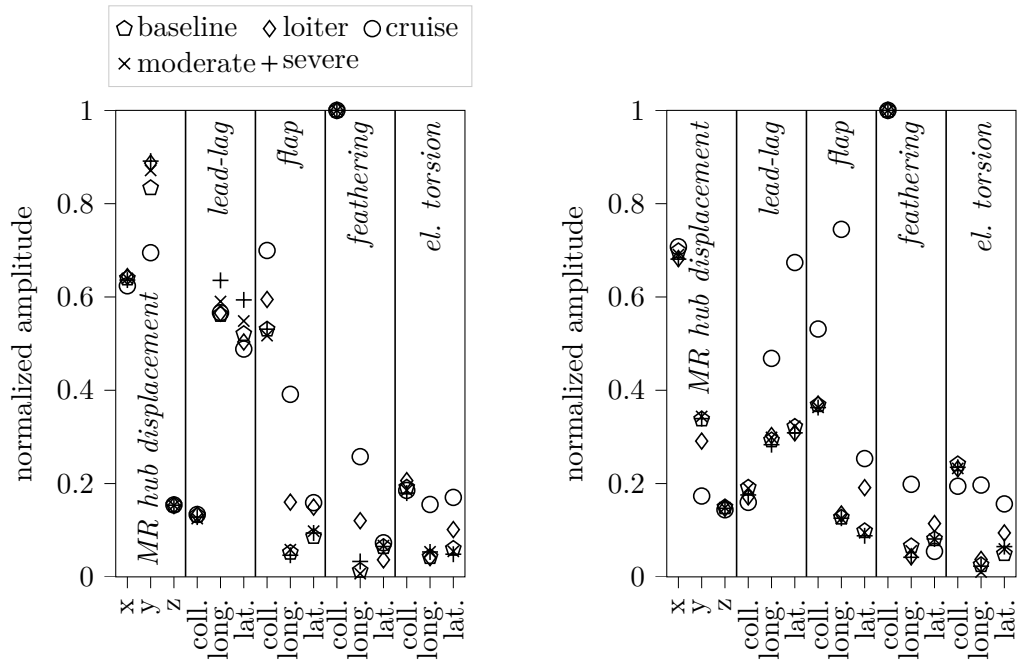
(a) Mode A. Mean eigenfrequency and damping ratio computed for five flight conditions: 5.55Hz, 2.63% relative damping.

(b) Mode B. Mean eigenfrequency and damping ratio computed for five flight conditions: 6.71Hz, 3.09% relative damping.

Figure 4.18.: Mode shapes of the two-way coupled helicopter system computed using SSI-COV.

5. Conclusion and Future Work

The results obtained in the previous chapter 4 indicate that light atmospheric turbulence excites the elastic helicopter structure sufficiently to perform an output-only modal analysis. In principal, the approach allows to compute isolated airframe modes, isolated rotor modes or coupled rotor-airframe modes from regular helicopter operation in atmospheric turbulence. The coupling between the airframe and rotor modes is strongly governed by the airframe impedance at the MR interface. High airframe impedance is represented in this work by one-way rotor-airframe coupling and low airframe impedance is represented by two-way coupling respectively. If the impedance is high, the airframe modes are rather decoupled from the rotor modes. In this case the modal analysis of the airframe allows to extract airframe modes even close the MR-BPF and at loiter-speed, all modes are identified using OMA. At higher or lower speeds compared to loiter-speed, a reduced number of modes is obtained. Increasing the turbulence level does not allow to identify additional modes and does not improve the modal analysis in general. Replacing the natural excitation of the airframe by GAUSSIAN white noise, shows that both OMA and BSS are able to identify all airframe modes. While the eigenfrequencies and eigenmodes can be extracted accurately, the computed relative damping is associated with considerable inaccuracies, which is discovered in Ref. [301] as well. Next to distinct rotor-harmonics introduced in the response spectrum, which can be removed appropriately, atmospheric turbulence introduces broadband components that are attracted by the rotor-harmonics due to cyclostationarity, which cannot be handled straightforward. In the context of wind-turbines this is supported by Ref. [296].

Independent of the airframe impedance at the MR interface, the identification of isolated rotor modes in proximity to the MR-BPF is problematic. It is assumed to be a result of the high aerodynamic damping of the MR. This is supported by previous publications in the context of scaled helicopter rotor testing, see Ref. [299] and in the context of wind-turbines, see Refs. [212, 245]. If the airframe impedance at the MR interface is low, than high aerodynamic MR damping affects the airframe modes as well. This results in three consequences, namely that airframe modes, ...

1. ... which can be identified and found to be in agreement with the standalone airframe according to the MAC, show a significant increase in damping.
2. ... which are in proximity of the MR-BPF cannot be identified.
3. ... even with some distance to the MR-BPF are not excited properly by the MR.

Hence, the MR aerodynamic damping is concluded to deteriorate the identification of both rotor and airframe modes. This was found in Ref. [245] in the context of wind-turbines as well. Note that two-way coupling is of more practical relevance with regard to flight-testing,

since loads in real helicopters are exchanged in both directions between the airframe and the MR. However, the identification of modes with some distance to the MR-BPF is still enabled via loads introduced by atmospheric turbulence at the tail section of the helicopter. The improved output-only modal analysis of helicopters by loads introduced at the tail section is supported by Ref. [110]. Hence, critical aeroelastic modes of helicopters having a comparable low frequency can be identified even if the airframe impedance at the MR interface is small and although the MR damping deteriorates the identification of airframe modes in this case significantly. The considered frequency range in this work ranges up to 30Hz. Above this frequency, no conclusions about the suitability of the output-only modal analysis from excitation through atmospheric turbulence are drawn. However, additional findings within this frequency range are concluded in the following.

- *Helicopter stability:* For the considered flight-conditions in this work, no unstable modes are obtained by studying the system's response in time-domain. Consequently, modes with negative damping are rejected in this work during the output-only modal analysis. The inaccuracies associated with the computed damping values do not allow to study the influence of turbulence intensity or flight-speed on damping. In section 4.7, two coupled rotor-airframe modes are obtained from a two-way coupled MR-airframe simulation. The mode A indicates a classical air-resonance phenomenon, where lead-lag whirl motion interacts with an elastic MR hub motion in MR in-plane direction. However, both modes indicate a significant contribution from the control system. In future, a more advanced control-law can be included to reduce this influence or to even mitigate the MR turbulence response and control activity.

- *OMA versus BSS:* Although all methods are comparably promising as long as the structure is subject to GAUSSIAN white noise, it is observed that in general less modes are identified by SOBI compared with the two OMA approaches, in case the helicopter is excited by atmospheric turbulence. Hence, the OMA techniques used in this work are found to be more robust against both cyclostationary effects and the coloring inherent from the atmospheric turbulence spectra. Consequently, the two OMA approaches are found to be slightly superior over SOBI from a user perspective and as well in terms of robustness. In general, SSI-COV and NExT-ERA are found to be very similar. It is concluded that BSS algorithms based on higher-order statistics are not applicable in this work, since the generalized coordinates are found to be characterized by second-order statistics, since they are approximately GAUSSIAN after the MR-BPF is removed. However, it is emphasized that using BSS in addition to OMA allows to verify identified modes which are not known in advance. A discrepancy between the two approaches in this context is that OMA methods compute complex-valued eigenvectors and BSS methods compute real-valued eigenvectors. Under the influence of numerical inaccuracies and from the violation of mathematical assumptions, the eigenvectors obtained with OMA and BSS are not directly comparable. Note that none of the approaches allows to extract a full model, since they are not able to compute the absolute scaling of the eigenvectors or the modal masses respectively.

- *Practical aspects of the modal analysis approaches:* The stabilization diagrams in context of the OMA approaches require indeed manual user input, which is however found

to be a helpful tool, because it simplifies the (pre-)selection of physical modes. At a first glance, SOBI promises not to require manual user input to such an extent, which is however not supported by the experience made throughout this work. The first aspect is that only a very limited number of modes can be identified, corresponding to the number of sensor signals. This requires additional signal preprocessing effort to mask components which prevent the identification of physical modes. In some cases this results in an iterative task. The second aspect is that SOBI returns separated sources, which have to be further processed in order to extract the modal damping and the eigenfrequencies. For this task, a hybrid approach is used in this work and found to be most robust, which employs NExT-ERA to extract the modal quantities from the sources. This step is in fact based on stabilization diagrams again, hence the seemingly advantages of SOBI vanish if modal damping is supposed to be extracted. This is true as well if the LD is used instead to extract the relative damping values.

- *Signal processing:* The selected approach to notch-filter the MR-BPF is appropriate to mask this frequency and enables the identification of the airframe modes. It is not necessary to remove additional sub-harmonics or integer multiples of helicopter states used in this work during aeroelastic analysis. Consequently, the linearization of the helicopter system with respect to a MR-BPF periodic orbit is a reasonable approximation. This is supported by the probability distributions of the output signals after removing the MR-BPF in section 4.2, which show GAUSSIAN distribution. However, notch-filtering sometimes results in spurious modes at the edges of the masked frequency band. The LTI approximation of the helicopter system investigated in this work is found to be appropriate, since the MR intrinsic periodicity is estimated to be small and to influence the modal analysis not significantly. It is discovered that it makes a difference if only airframe states are included in the modal analysis or both airframe and rotor states. The identification of airframe modes is in general improved if only airframe states are included. The loads introduced at the empennage and the TR improve the modal analysis compared to an rotor-only coupling with the elastic airframe. Multi-blade coordinates obtained via COLEMAN transformation are found to be a suitable way to represent both the airframe and rotor dynamics in one common coordinate system. If a reference for the mode shapes is available, spurious modes can be identified efficiently based on the MAC. In addition, mode rejection based on the damping ratio and on the modal contribution are found to be efficient as well.

- *Helicopter model:* The models used in this work are found to represent the helicopter aerodynamics and the associated aerodynamic damping sufficiently in the context of output-only modal analysis. In addition, the structural transmissibility of broadband vibrations is considered to be represented appropriately by the helicopter model used in this work. An exception to this is the rigid TR model, which is assumed to overestimate the broadband loads in terms of standard deviation. Although the integral MR and TR loads are reasonably predicted, the aerodynamic models are expected to be associated with inaccuracies towards the prediction of local stresses and vibrations. As an example, the MR wake, which impinges the tail section and which introduces characteristic sectional rotor blade loads is not modeled in this work. Both phenomena can lead to significant periodic oscillations, which are considered to have a potential detrimental influence on the output-only modal analysis.

- *Turbulence model:* Cyclostationary effects, which are important to be covered, are represented more appropriately with the FullFT turbulence model compared to the HubDT model. Consequently, the modal analysis is slightly influenced by the turbulence model, since the FullFT model shifts energy from lower to higher frequencies. This improves the identification of higher modes, whereas the identification of lower modes is improved by using the HubDT model, where the shift of energy to rotor-harmonics and higher frequencies due to cyclostationary effects is not represented appropriately. The superposition approach used by the FullFT model increases the computational expense significantly. The HubDT model is in contrast suited even for real-time applications. A compromise for future research projects might be the SORBET model, see section 1.2. Improving the atmospheric turbulence simulation can be further directed to the following aspects. In Ref. [310] an approach to span the turbulence model in the vertical direction is described, which is also proposed in Ref. [230]. This dimension could be used to approximate turbulence encounters in hover conditions by convecting the third dimension with MR inflow velocity in agreement with Taylor's hypothesis. A further improvement is high fidelity aerodynamic modeling using CFD methods to incorporate e.g. tail-shake, the interaction with obstacles like vessels, buildings, etc. and distributed airloads of the airframe. Another improvement is to replace the inflow model used in this work by a free-wake simulation, to account for MR wake effects. In the context of complex simulation models, the approach used in this work can be adapted as linearization technique of simulation models in general. This requires to introduce stochastic processes in the simulation, small enough not to alter the operating state significantly, but strong enough to enable an output-only modal analysis.

The application of output-only modal analysis to flight-test data is promising. The time-windows of some minutes used in this work are assumed to be of sufficient length. This is a reasonable time-period to keep the helicopter trim state during flight-testing as well. Except for the MR blade elastic torsion, which is complex to be measured, the quantities used in this work can be determined during flight-testing in principal as well. During flight-testing an improvement in output-only modal analysis compared to the simulation in this work can be the fact that broadband vibrations are introduced e.g. by the engines, by the transmission system and by unsteady aerodynamic effects like tail-shake in addition to atmospheric turbulence. This is because increasing the number of uncorrelated stochastic inputs improves the output-only modal analysis, see Ref. [43]. It is expected that the identification of rotor-modes is complicated in vicinity to MR-BPF due to the high aerodynamic damping of the rotor. Most importantly this requires to further improve the modal analysis in presence of highly damped oscillations like the rotor-blade flapping motion, which is concluded in Ref. [300] as well. In the past, some work dedicated to this issue has been presented. Ref. [312] is e.g. concerned with the improvement of the modal analysis of structures with high damping using BSS. To further investigate the applicability of output-only modal analysis in context of flight-test data based on simulations, measurement noise can be added. In general, measured input-data should be processed during the modal analysis as well if available, to improve the identification of modes, see Refs. [192, 190]. A robust analysis method of elastic helicopter modes might be further used for helicopter condition monitoring. Work in this research field was presented previously in Refs. [28, 274, 63].

A. Appendix
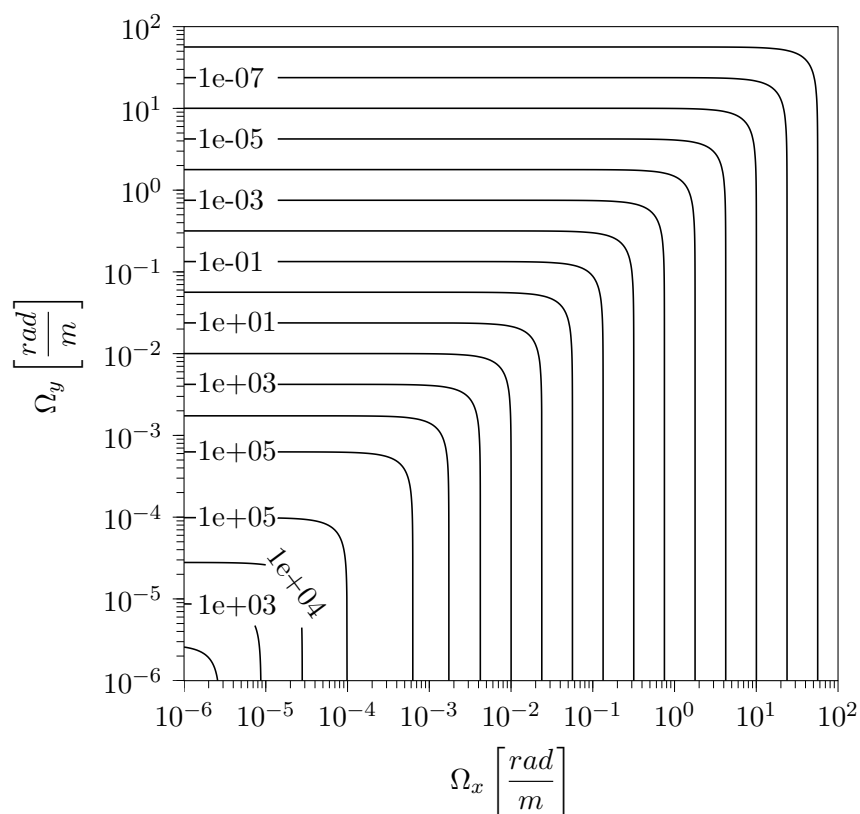
Figure A.1.: Power spectral density $\Phi_w \left[\frac{m^2}{s^2 - rad/m} \right]$ of the vertical atmospheric turbulence velocity according to the VON KÁRMÁN spectrum. The spectrum is shown with respect to spatial frequency for light turbulence intensity at an altitude of 762m (2500ft).
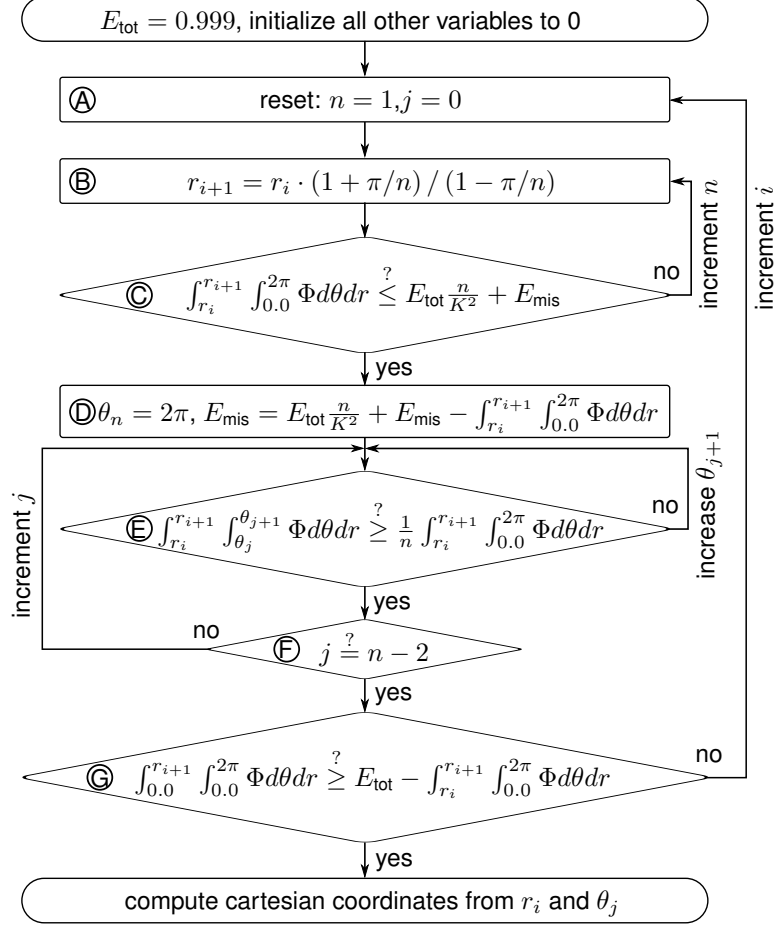
Figure A.2.: Algorithm to discretize the VON KÁRMÁN PSDs, see e.g. Fig. A.1. The algorithm computes frequencies associated with approximately equal energy and elements with approximately equal edge length. Figure adopted from Ref. [258].
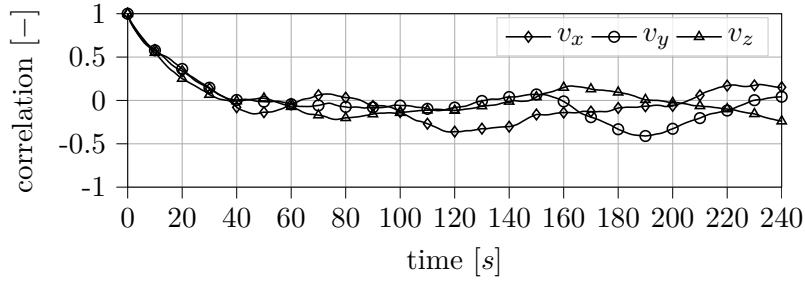
simulation time [s]:		600	*240*	600	*240*
RMS	reference	hub element		blade element	
v_x [m/s]	1.55	1.577	*0.932*	1.430	*1.654*
v_y [m/s]	1.55	1.400	*1.243*	1.577	*1.309*
v_z [m/s]	1.55	1.371	*1.185*	1.526	*1.250*
mean					
v_x [m/s]	0	+5.277e-01	*+7.710e-01*	+5.557e-01	*+8.684e-01*
v_y [m/s]	0	-1.742e-02	*+3.002e-01*	-1.181e-00	*-4.825e-01*
v_z [m/s]	0	-2.108e-03	*+2.096e-01*	+9.049e-01	*+5.437e-01*

Table A.1.: First- and second-order turbulence statistics obtained with the FullFT model for both ten and four minutes of simulated time. The reference values are computed according to the governing VON KÁRMÁN model for the baseline flight-condition summarized in table 1.2.
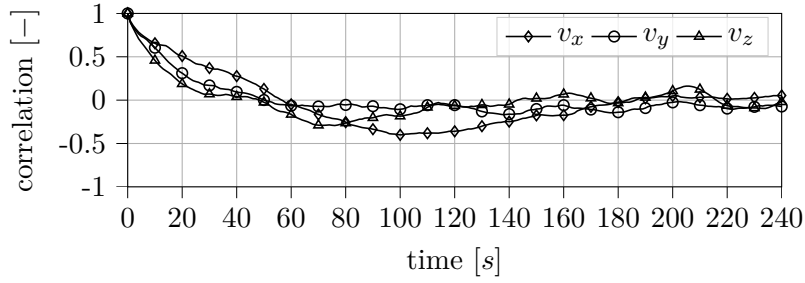
(a) Hub-element sampled.
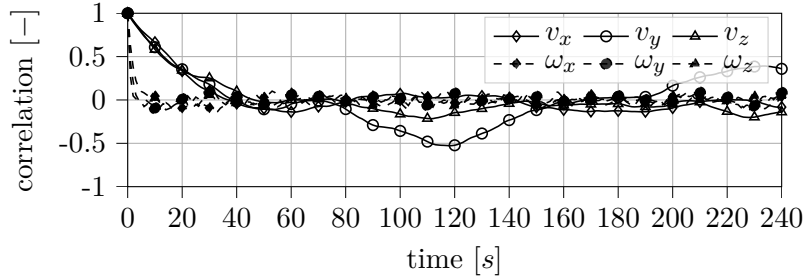

(b) Blade-element sampled.

Figure A.3.: Auto-correlations of turbulence velocities generated with the FullFT model for the baseline flight-condition summarized in table 1.2.

simulation time [s]:		600	*240*	600	*240*
RMS	reference	hub element		blade element	
v_x [m/s]	1.55	1.518	*1.084*	1.593	*0.982*
v_y [m/s]	1.55	1.745	*1.523*	1.565	*1.397*
v_z [m/s]	1.55	1.383	*1.317*	1.159	*0.979*
ω_x [1/s]	3.16e-02	3.312e-02	*3.352e-02*	-	-
ω_y [1/s]	2.09e-02	1.735e-02	*1.883e-02*	-	-
ω_z [1/s]	2.41e-02	2.103e-02	*1.969e-02*	-	-
mean					
v_x [m/s]	0	-8.513e-01	*-9.579e-02*	+1.324e-01	*+4.500e-01*
v_y [m/s]	0	-6.709e-01	*+9.094e-02*	+2.577e-01	*+1.634e-01*
v_z [m/s]	0	+2.775e-01	*+5.866e-01*	+6.754e-01	*+5.001e-01*
ω_x [1/s]	0	-4.097e-03	*-7.258e-03*	-	-
ω_y [1/s]	0	-1.468e-04	*+1.713e-03*	-	-
ω_z [1/s]	0	-1.999e-04	*+3.087e-05*	-	-

Table A.2.: First- and second-order turbulence statistics obtained with the HubDT model for both ten and four minutes of simulated time. The reference values are computed according to the governing DRYDEN model for the baseline flight-condition summarized in table 1.2.
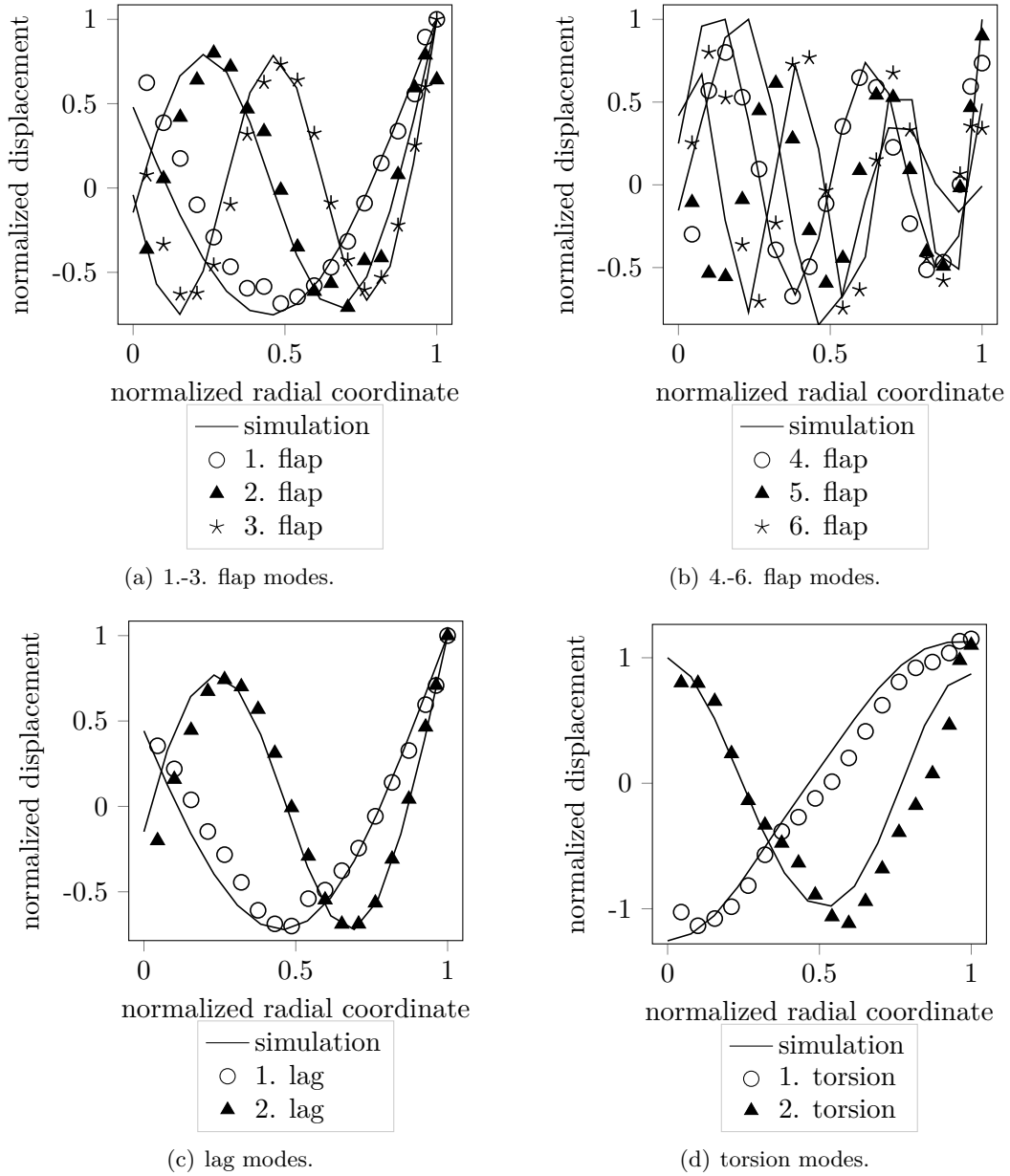


(a) Hub-element sampled.
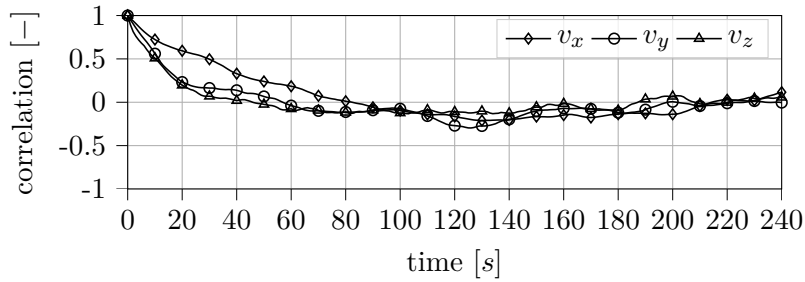
(b) Blade-element sampled.

Figure A.4.: Auto-correlations of turbulence velocities generated with the HubDT model for the baseline flight-condition summarized in table 1.2.

(a) 1.-3. flap modes.

(b) 4.-6. flap modes.

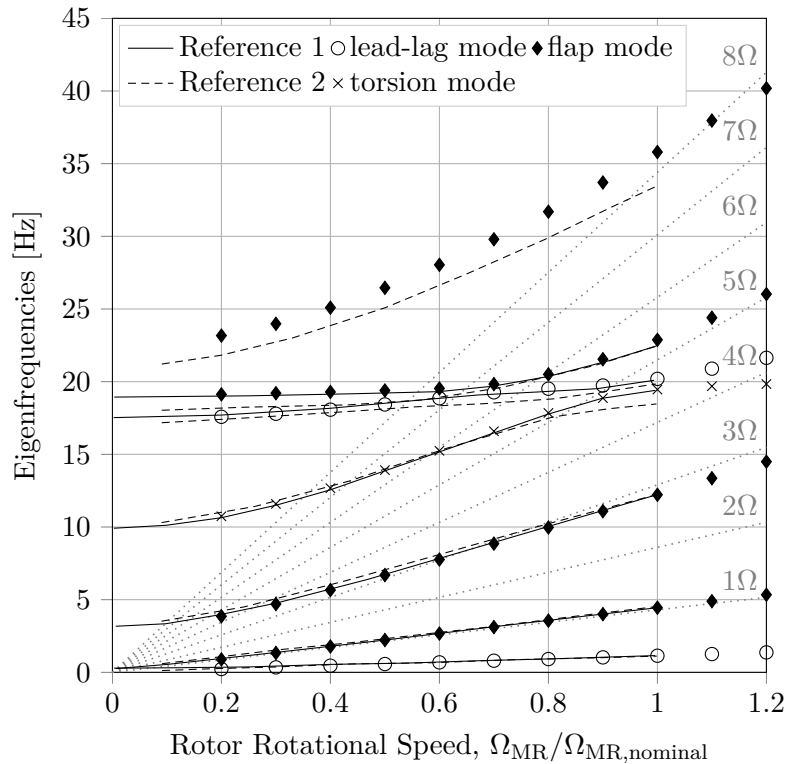(c) lag modes.

(d) torsion modes.

Figure A.5.: Mode shapes of the non-rotating MR blade. Calculation involves 14 beam elements with linear shape-function. In Ref. [258] the same figures are published but computed with 40 elements.
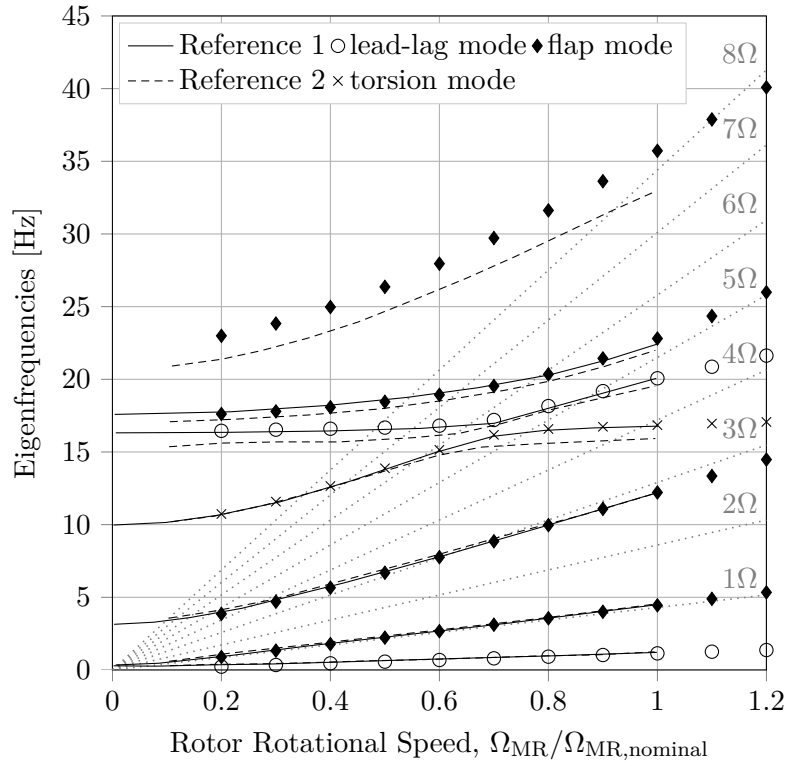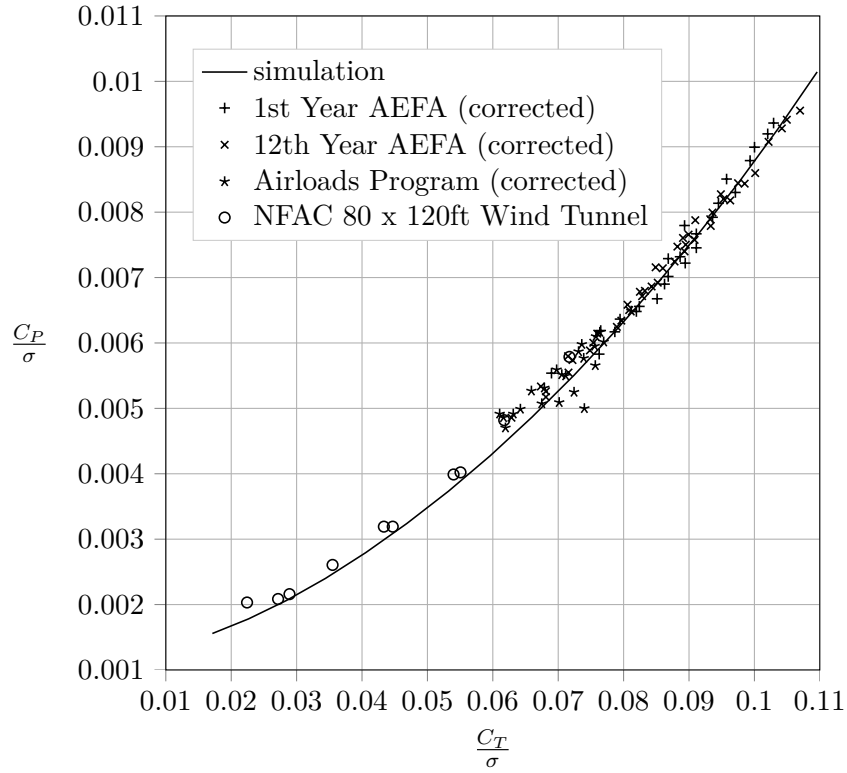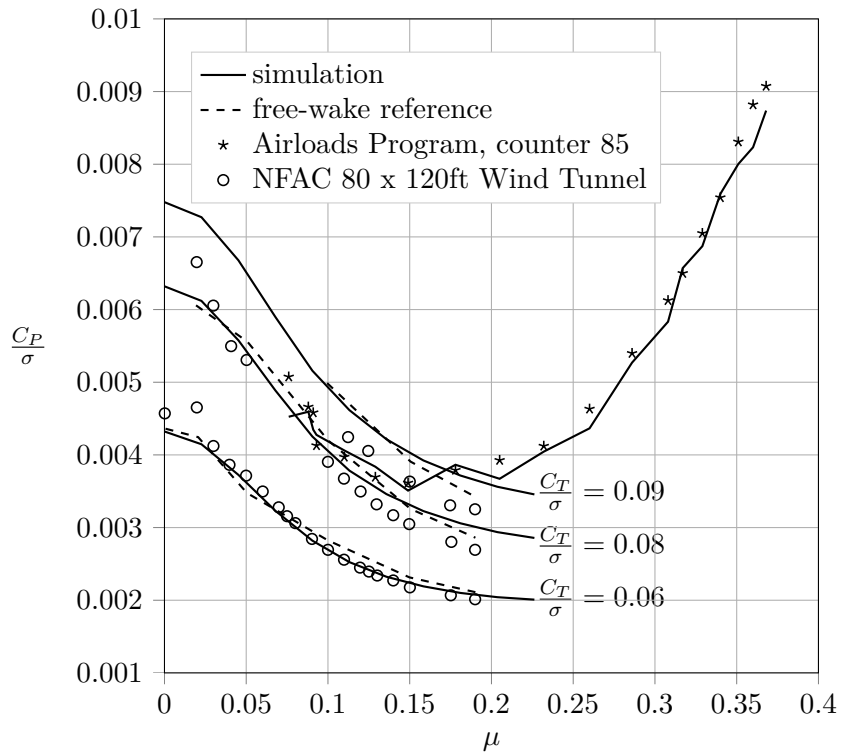
(a) Soft pitchlink stiffness.

(b) Nominal pitchlink stiffness.

Figure A.6.: Campbell diagram of the MR blade. Calculations involve 14 beam elements with linear shape-function. In Ref. [258] the same figures are published but computed with 40 elements.

(a) MR power in hover.

(b) MR power in forward flight.

Figure A.7.: Simulated MR performance in comparison with test-data for both hover and forward flight conditions. Figures taken from Ref. [258].
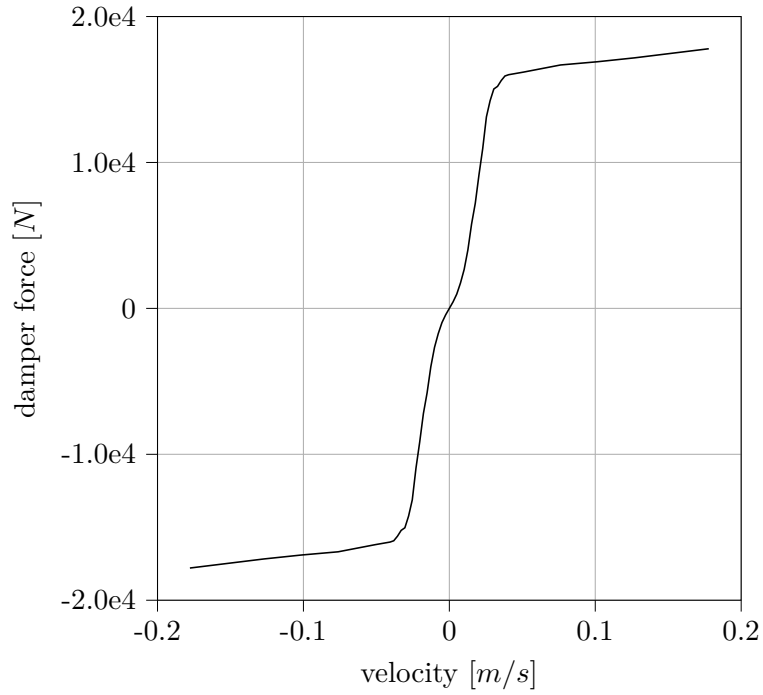
Figure A.8.: Slope of the non-linear lead-lag damper.

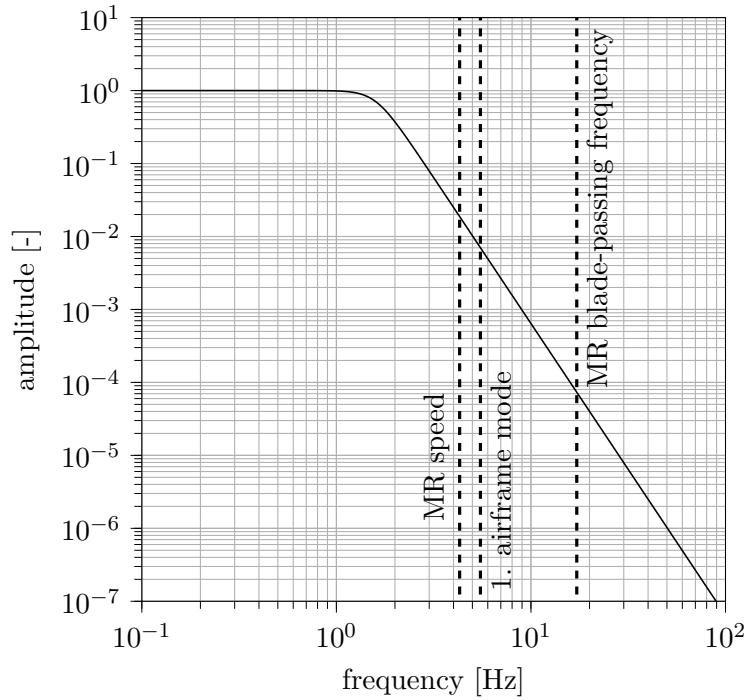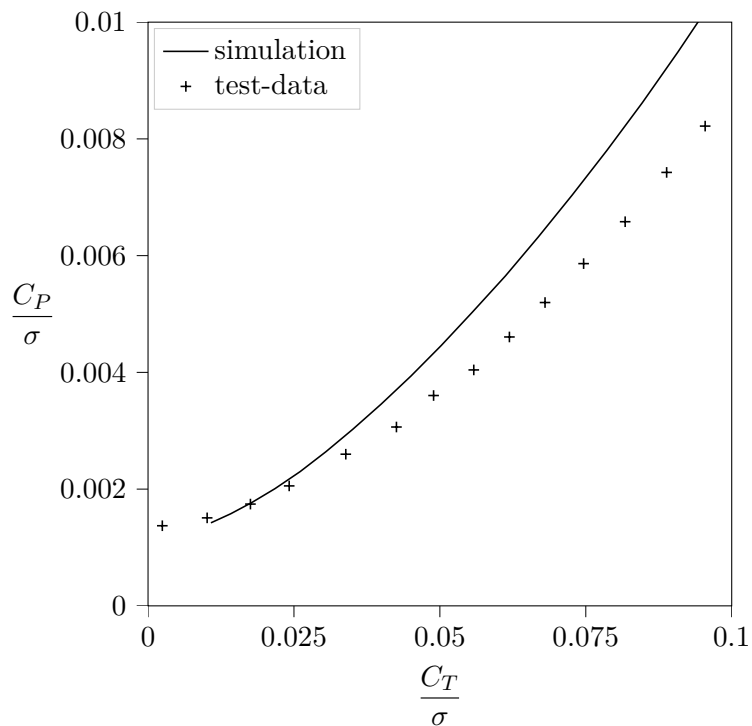**Figure A.9.:** Low-pass BUTTERWORTH-filter to suppress the MR-harmonics with a cut-off frequency of 1.59Hz (10 rad/sec).

(a) TR power in hover in comparison with a UH-60A MR scaled to 1:5.7 (equal airfoils), see Ref. [27].
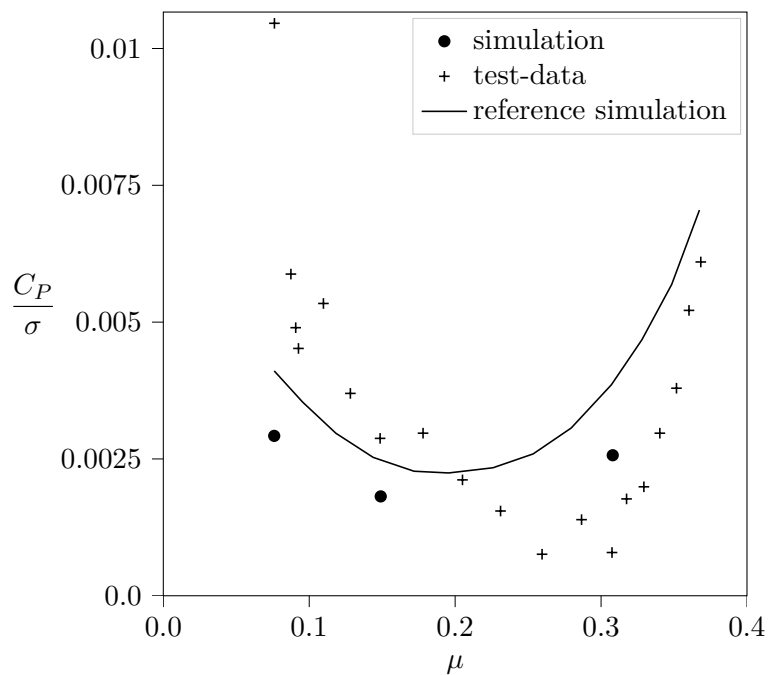
(b) TR power in forward flight in comparison with the Airloads Program flight-test counter 85, see Ref. [314].

Figure A.10.: TR power in comparison with test-data and a reference simulation.
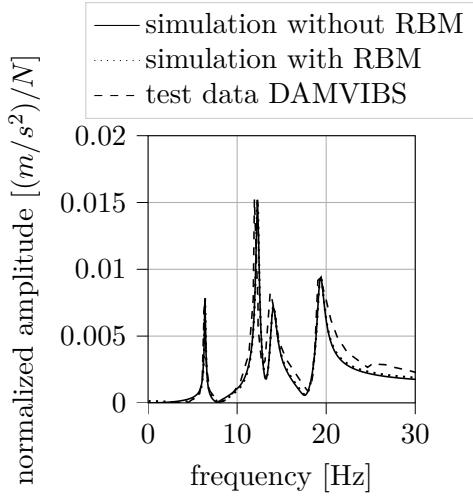
(a) Longitudinal response to longitudinal force.
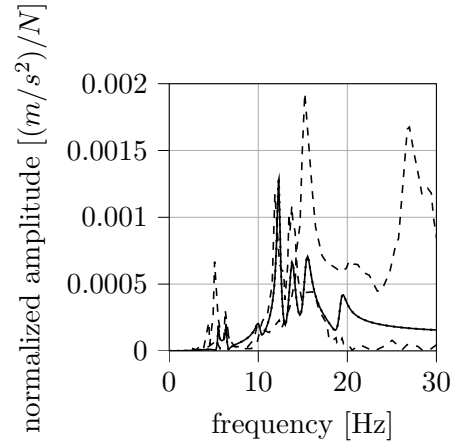
(b) Lateral response to longitudinal force.
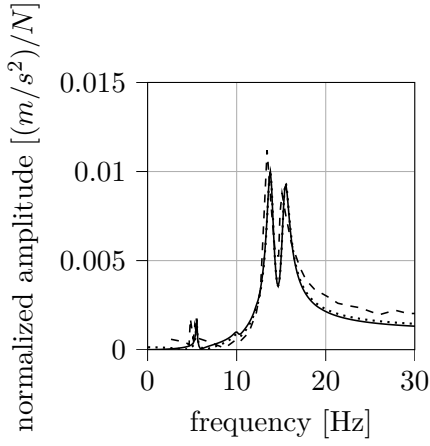
(c) Lateral response to lateral force.
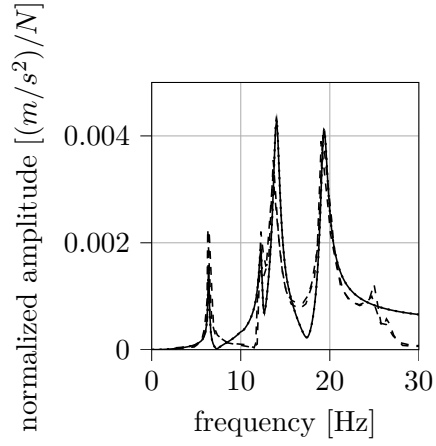
(d) Vertical response to longitudinal force.
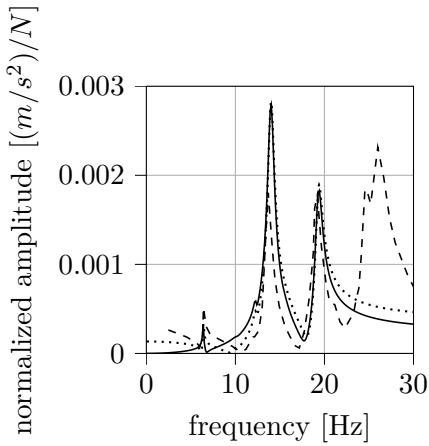
(e) Vertical response to vertical force.
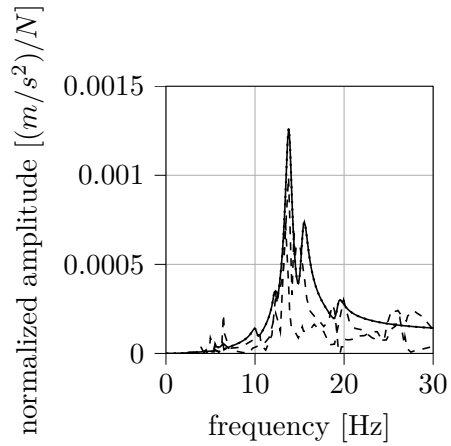
(f) Vertical response to lateral force.

Figure A.11.: Transfer functions of the modal airframe at the MR hub in comparison with the DAMVIBS program. Figures taken from Ref. [258].

(a) mode 1: first lateral bending.

(b) mode 2: first vertical bending.

(c) mode 3: stabilator rigid body 1.

(d) mode 4: transmission pitch.

(e) mode 5: transmission roll.

(f) mode 6: second vertical bending.

(g) mode 7: cockpit cabin roll.

(h) mode 8: third vertical bending.
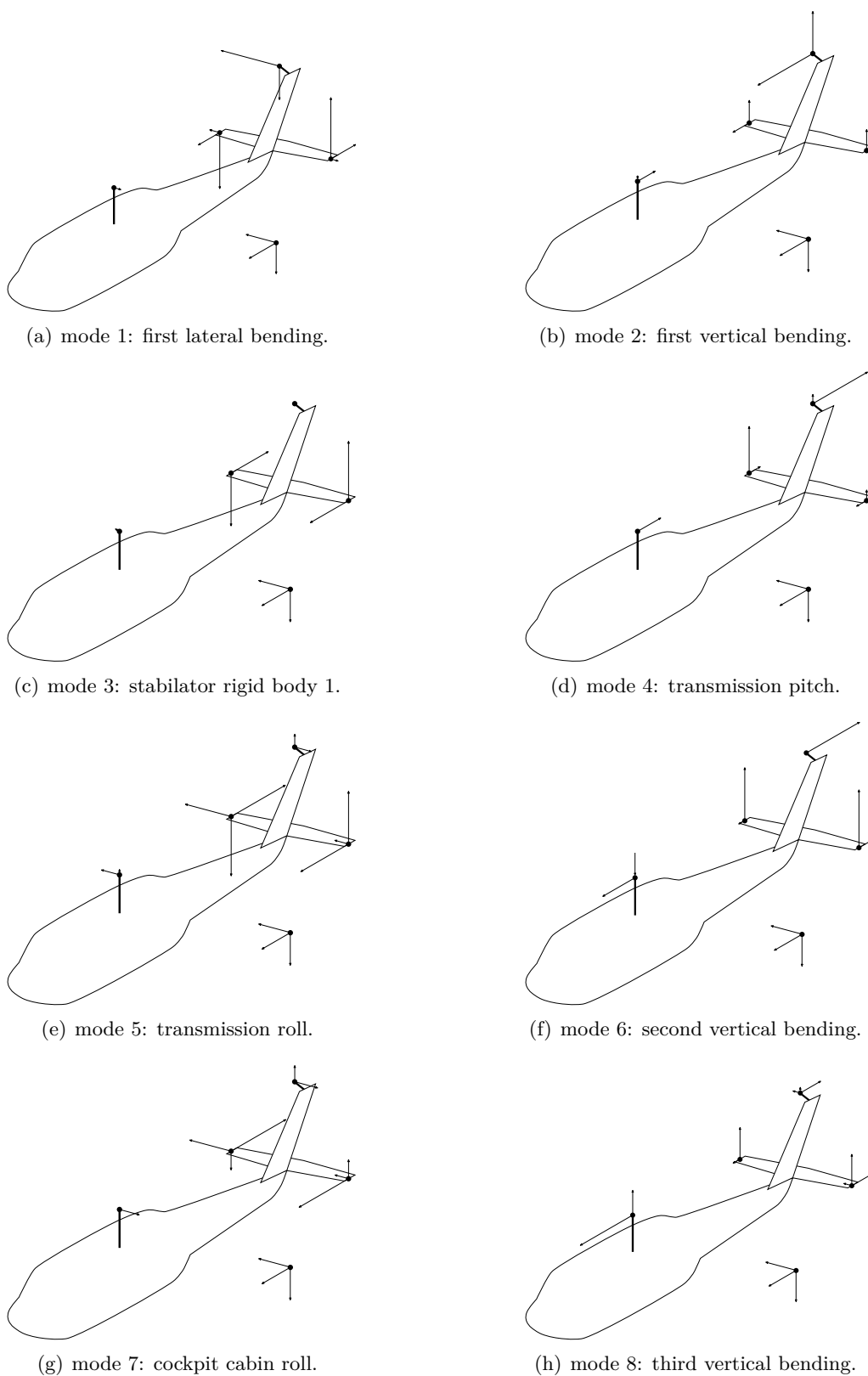
Figure A.12.: Mode shapes of the elastic airframe model according to the DAMVIBS program. Modes are adapted from Ref. [258] and are based on Ref. [135].

(a) 4/rev out-of-plane.

(b) 8/rev out-of-plane.

(c) 3/rev in-plane.

(d) 5/rev in-plane.

(e) mean half peak-to-peak in-plane.

(f) mean half peak-to-peak out-of-plane.
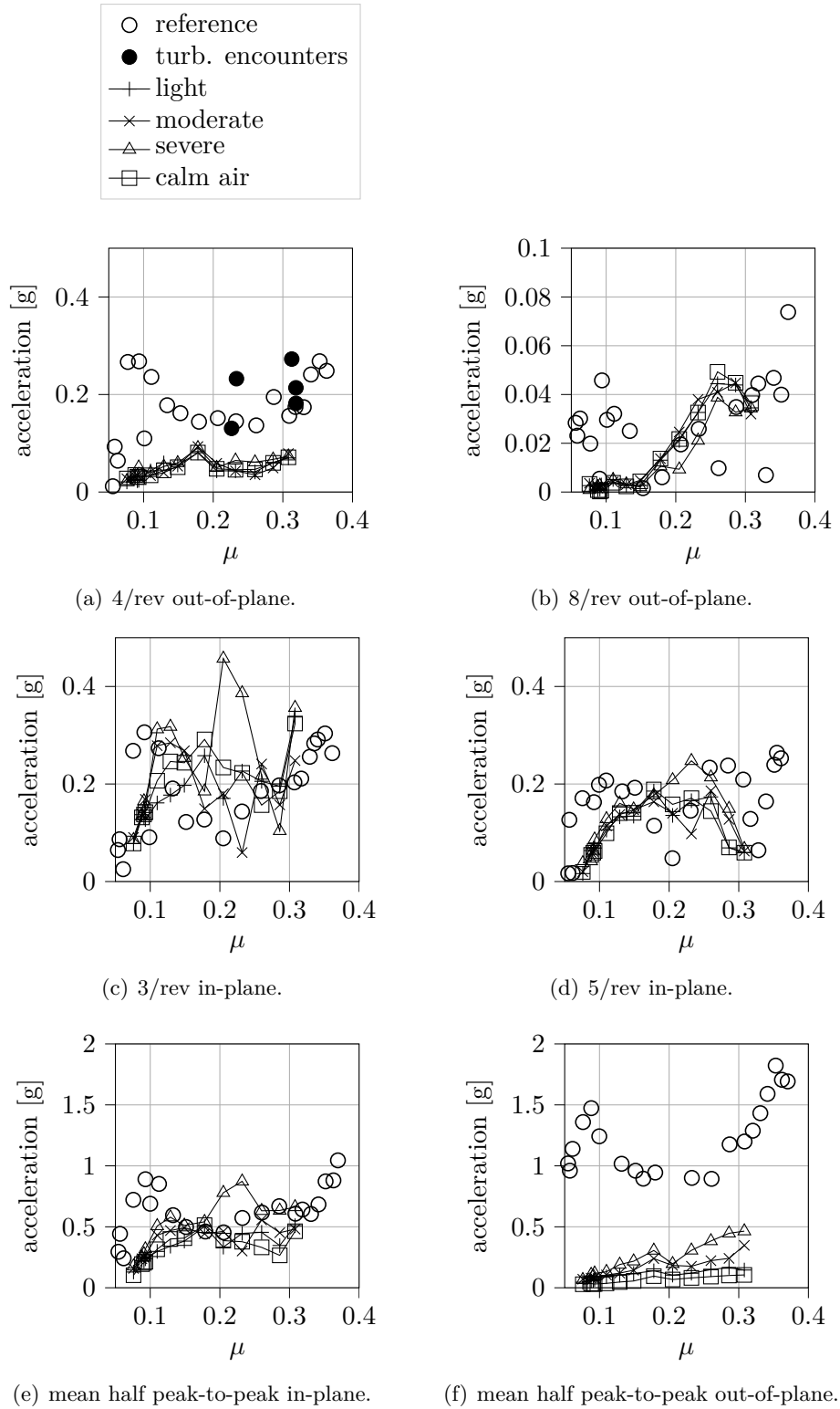
Figure A.13.: Simulated MR hub accelerations in presence of different levels of atmospheric turbulence compared to flight-test data, see Ref. [291], for a blade loading of $C_T/\sigma \approx 0.08$. Figure adapted from Ref. [257].

(a) mode 1.

(b) mode 2.

(c) mode 3.

(d) mode 4.

(e) mode 5.

(f) mode 6.

(g) mode 7.

(h) mode 8.
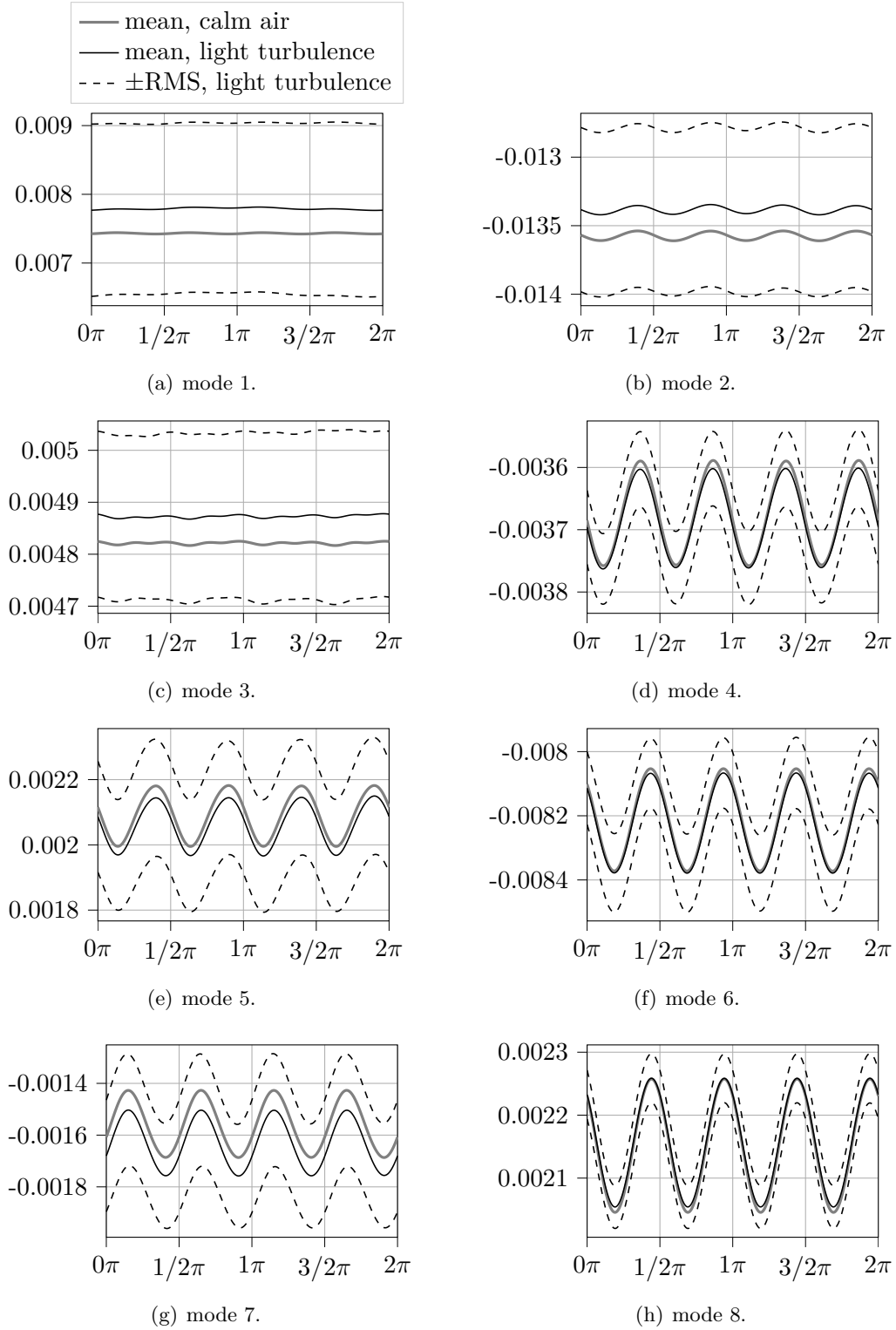
Figure A.14.: Mean and standard deviation of the generalized coordinates q_k projected onto the norm of the associated eigenvector $|\Psi_k|$ over one MR revolution.

(a) MR hub, x-direction

(b) MR hub, y-direction

(c) MR hub, z-direction

(d) TR hub, x-direction

(e) TR hub, y-direction

(f) TR hub, z-direction

(g) Right HS tip, x-direction

(h) Right HS tip, y-direction

(i) Right HS tip, z-direction

(j) Left HS tip, x-direction

(k) Left HS tip, y-direction

(l) Left HS tip, z-direction
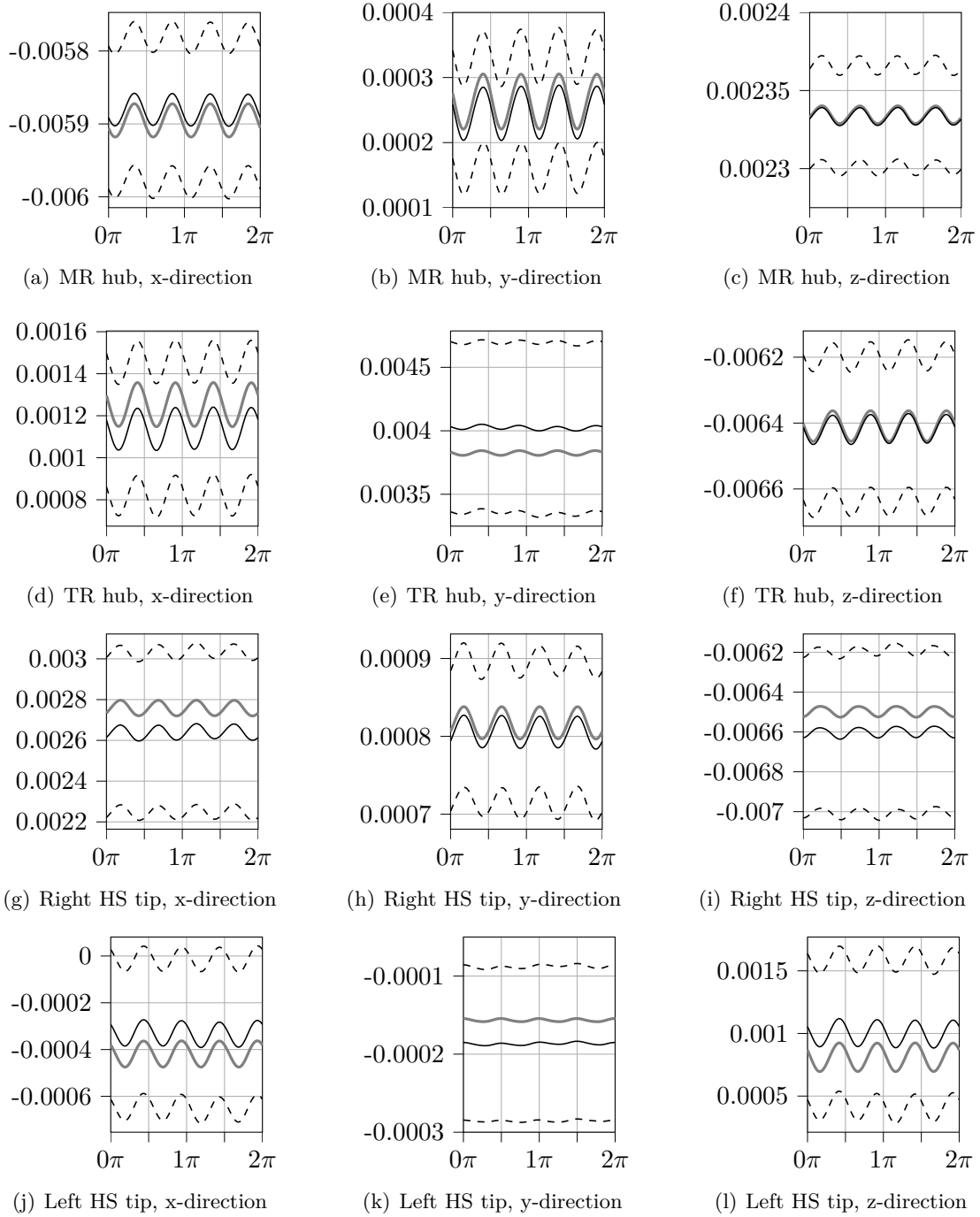
Figure A.15.: Mean and standard deviation of the translational elastic airframe displacement [m] at four different locations over one MR revolution. See legend in Fig. A.14.

(a) Collective mode.

(b) Longitudinal mode.

(c) Lateral mode.

(d) Differential / scissor mode.
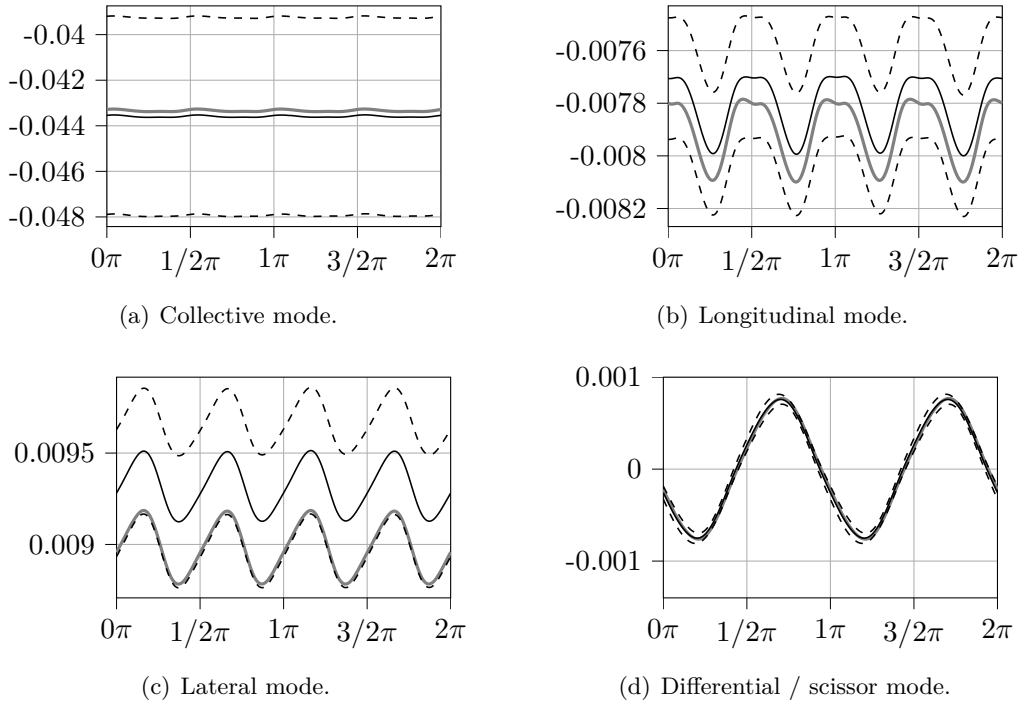
Figure A.16.: Mean and standard deviation of the lead-lag motion [rad] expressed in multi-blade coordinates over one MR revolution. See legend in Fig. A.14.

(a) Collective mode.

(b) Longitudinal mode.

(c) Lateral mode.

(d) Differential / scissor mode.
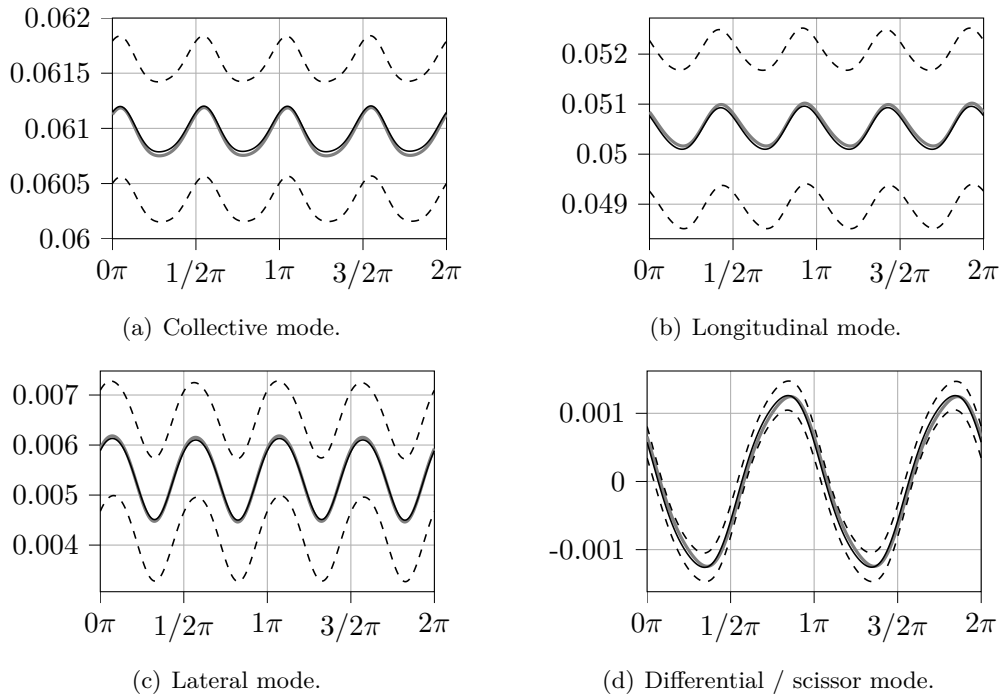
Figure A.17.: Mean and standard deviation of the flapping motion [rad] expressed in multi-blade coordinates over one MR revolution. See legend in Fig. A.14.

(a) Collective mode.

(b) Longitudinal mode.

(c) Lateral mode.

(d) Differential / scissor mode.
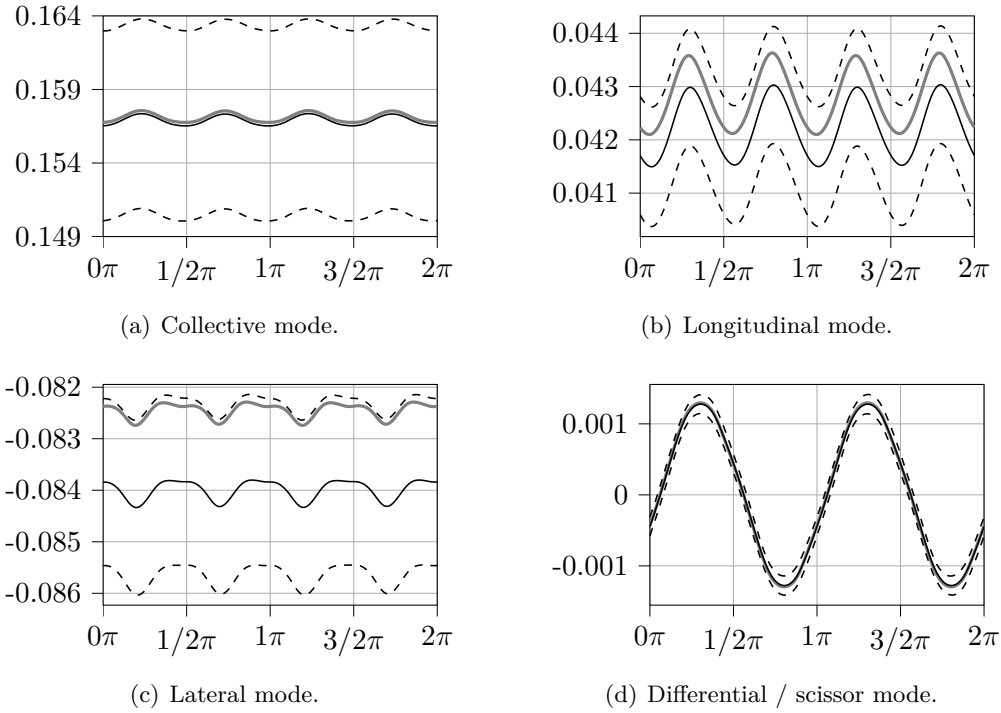
Figure A.18.: Mean and standard deviation of the feathering motion [rad] expressed in multi-blade coordinates over one MR revolution. See legend in Fig. A.14.

(a) Collective mode.

(b) Longitudinal Mode.

(c) Lateral Mode.

(d) Differential / Scissor mode.
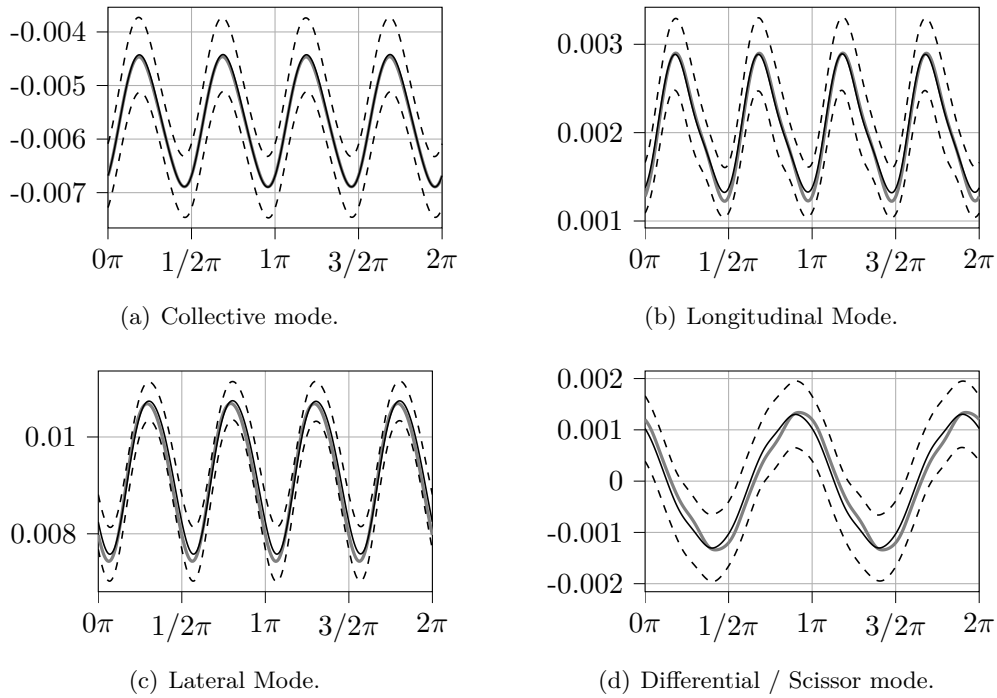
Figure A.19.: Mean and standard deviation of the elastic rotor-blade torsion [rad] expressed in multi-blade coordinates over one MR revolution. See legend in Fig. A.14.

(a) Collective mode.

(b) Longitudinal mode.

(c) Lateral mode.

(d) Differential / scissor mode.
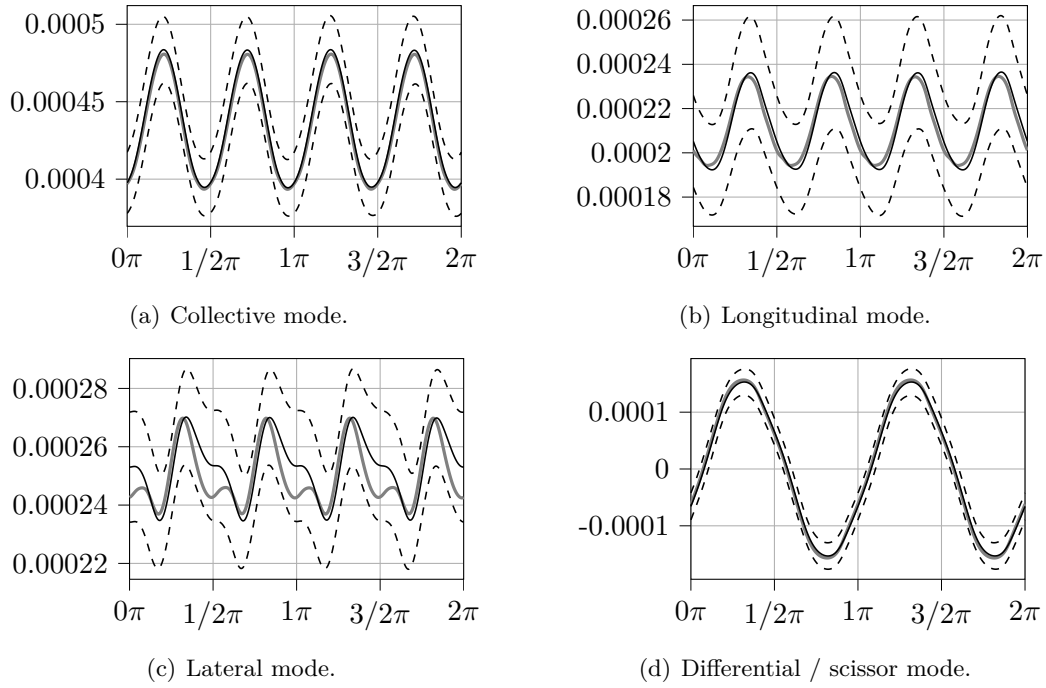
Figure A.20.: Mean and standard deviation of the elastic pitchlink displacement [m] expressed in multi-blade coordinates over one MR revolution. See legend in Fig. A.14.

(a) Forward servo.

(b) Lateral Servo.

(c) Aft servo.
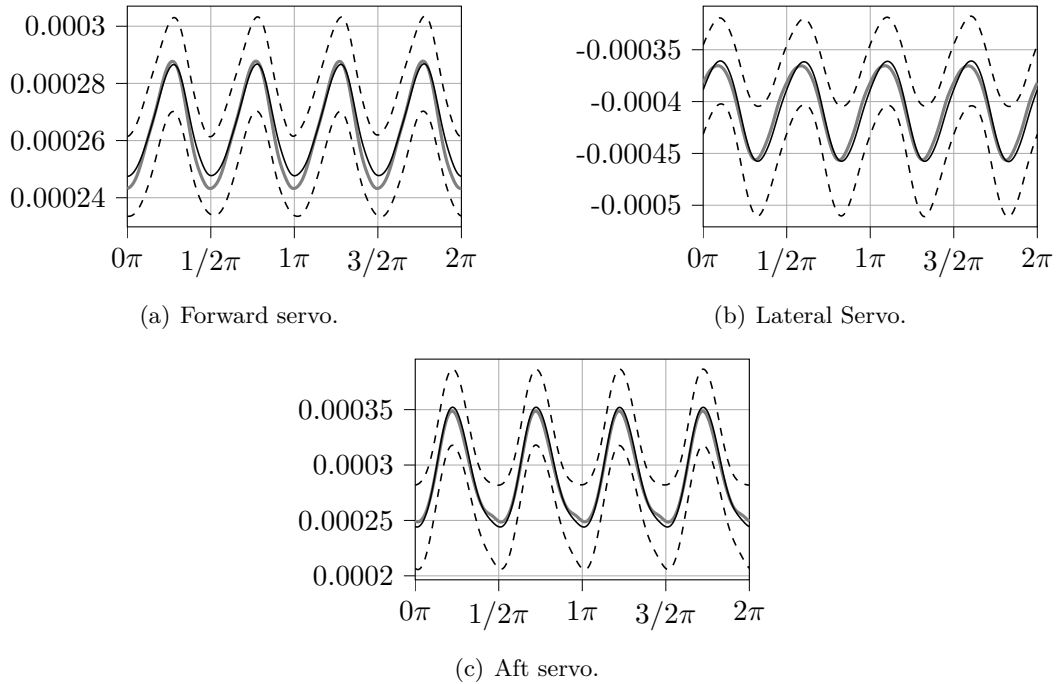
Figure A.21.: Mean and standard deviation of the elastic actuator displacement [m] over one MR revolution. See legend in Fig. A.14.
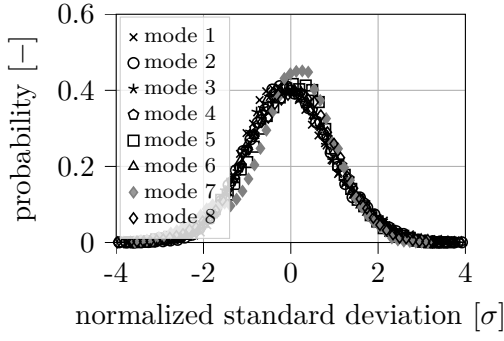
(a) Modal airframe coordinates q_k scaled.
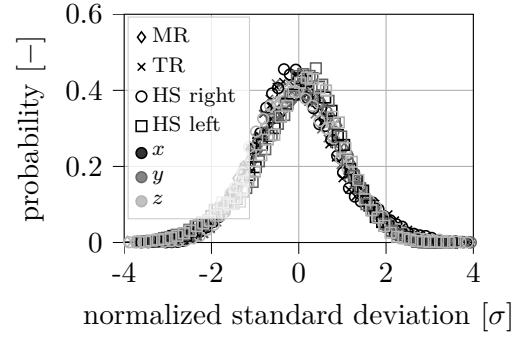
(b) Airframe elastic displacement.
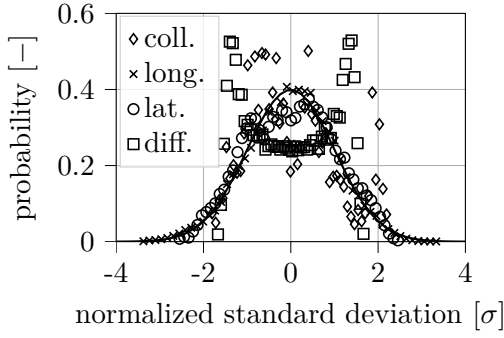
(c) MR lead-lag motion.
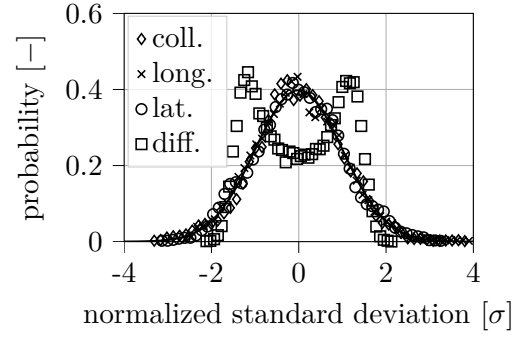
(d) MR flapping motion.
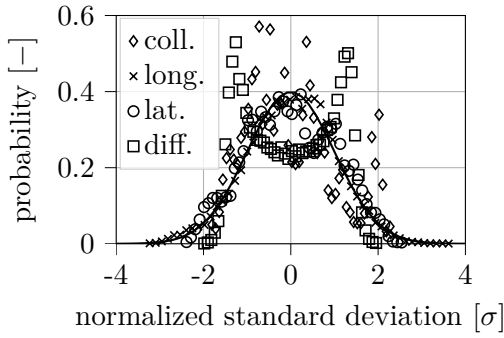
(e) MR feathering motion.
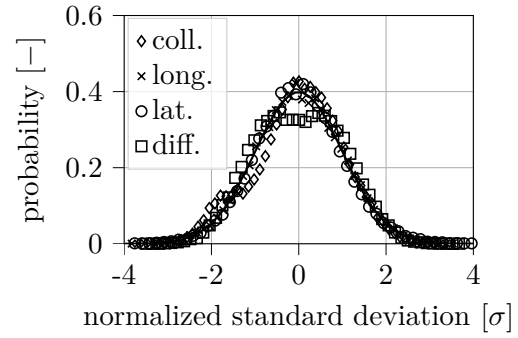
(f) MR elastic rotor-blade torsion.
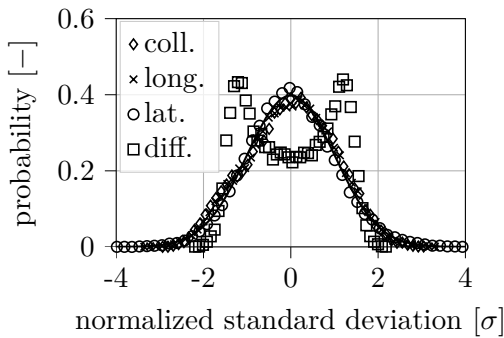
(g) MR elastic pitchlink displacement.
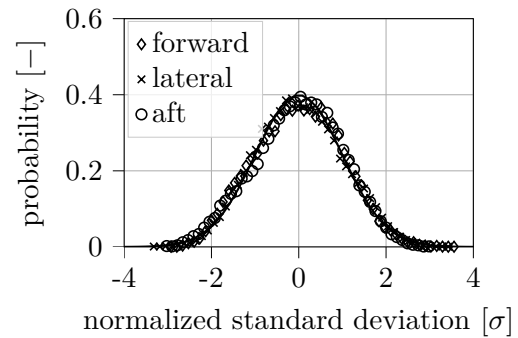
(h) MR elastic actuator displacement.

Figure A.22.: Normalized histogram of aeroelastic helicopter states versus GAUSSIAN distribution. The generalized coordinates are scaled with the norm of the eigenvectors. The standard deviations are indicated in Fig. A.14 to Fig. A.21. All mean values are close to zero since the signals are centered during the preprocessing.

(a) Mode 1.

(b) Mode 2.

(c) Mode 3.

(d) Mode 4.

(e) Mode 5.

(f) Mode 6.

(g) Mode 7.

(h) Mode 8.
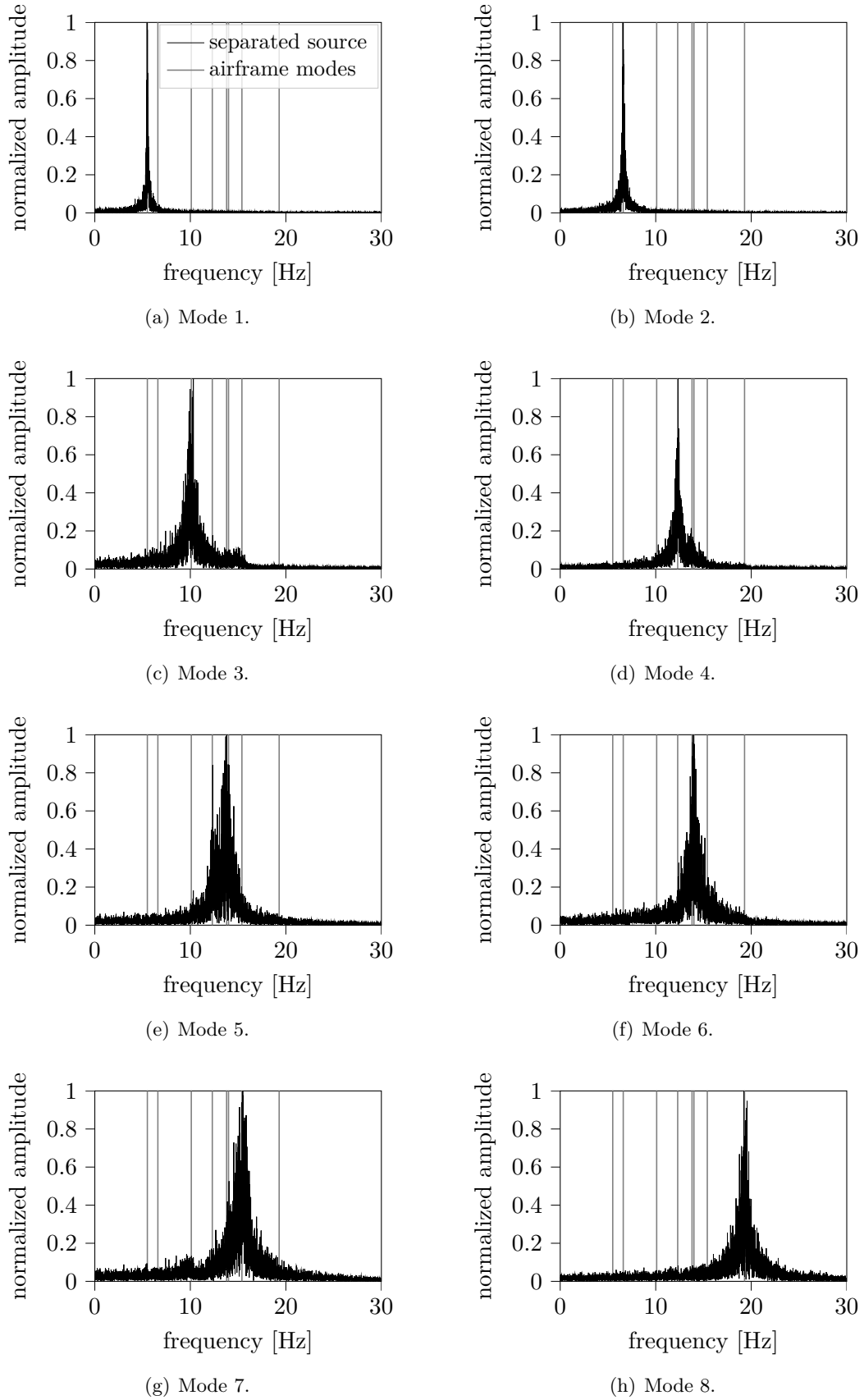
Figure A.23.: Spectra of the separated sources obtained for the elastic airframe subject to GAUSSIAN white noise using SOBI.

(a) DRYDEN.

(b) Baseline.

(c) Loiter.

(d) Cruise.

(e) Moderate.

(f) Severe.

(g) MR coupled only.

(h) Baseline two-way coupled.
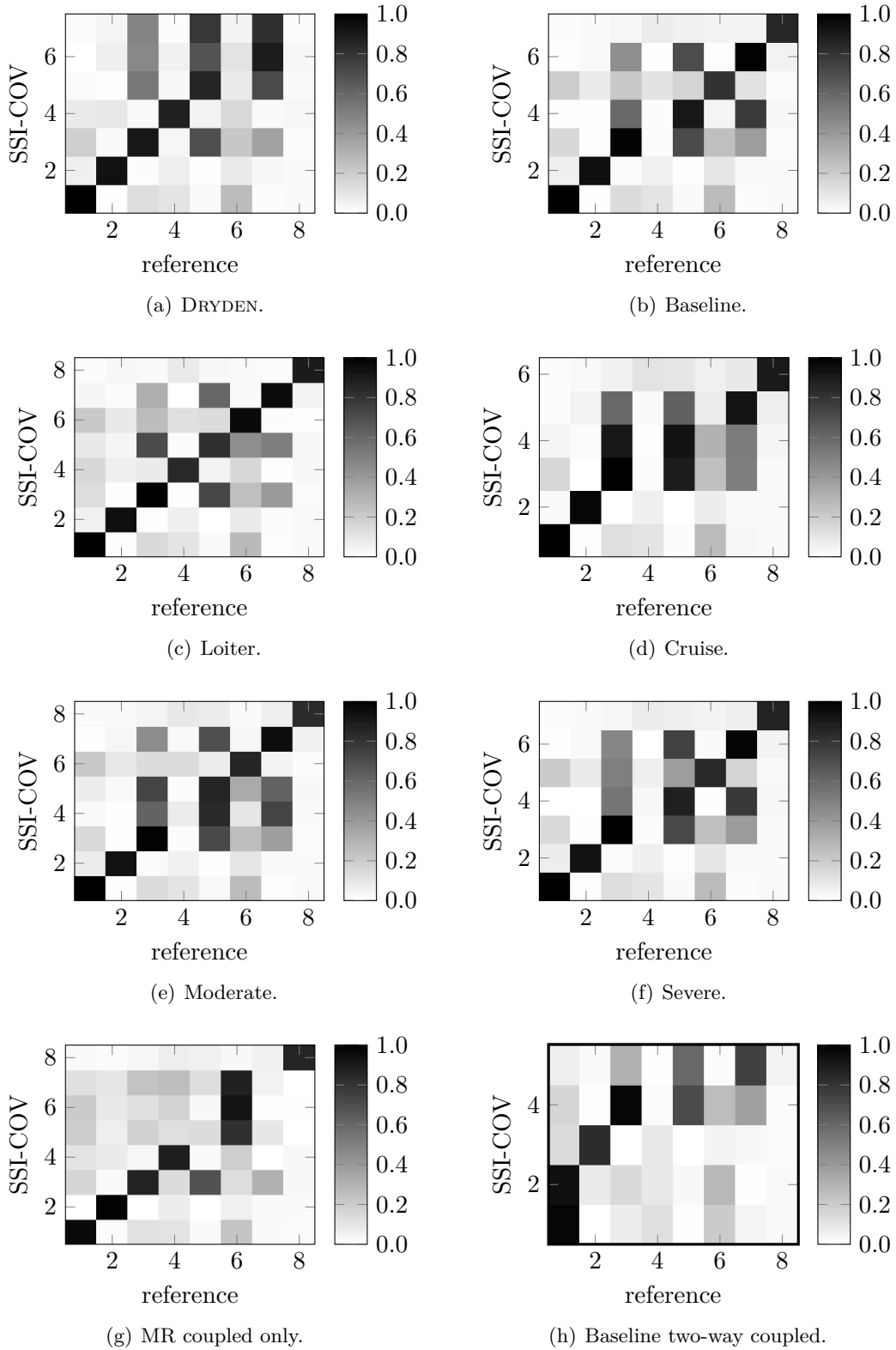
Figure A.24.: MAC-values obtained for the one-way coupled elastic airframe for different simulation scenarios. Note that the last figure is obtained from two-way coupling. The eigenvectors are computed using SSI-COV and are compared to the exact eigenvectors of the airframe.

(a) DRYDEN.

(b) Baseline.

(c) Loiter.

(d) Cruise.

(e) Moderate.

(f) Severe.

(g) MR coupled only.

(h) Baseline two-way coupled.
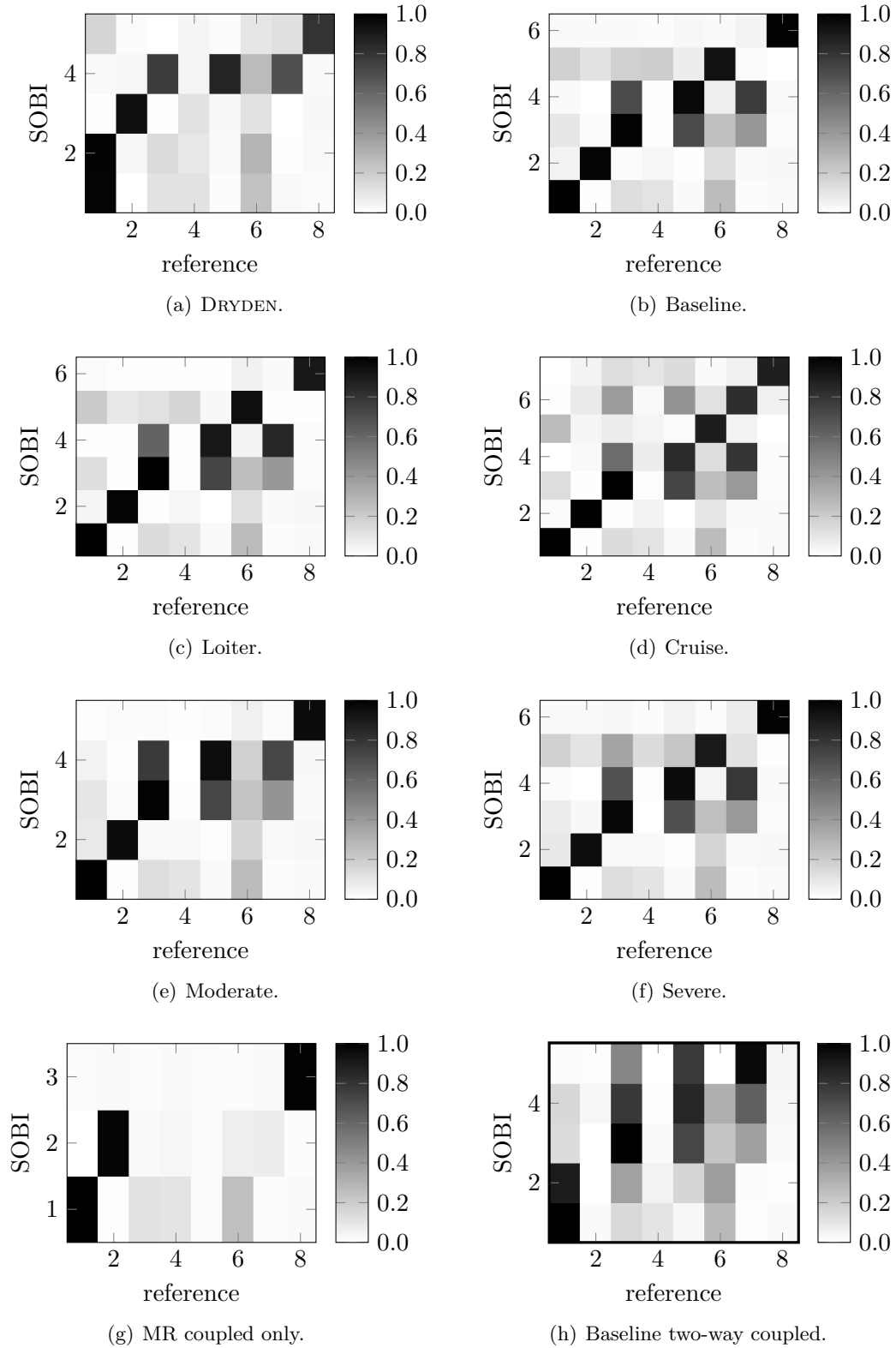
Figure A.25.: MAC-values obtained for the one-way coupled elastic airframe for different simulation scenarios. Note that the last figure is obtained from two-way coupling. The eigenvectors are computed using SOBI and are compared to the exact eigenvectors of the airframe.

109

(a) Loiter.

(b) Cruise.

(c) Moderate.

(d) Severe.

(e) MR coupled only.
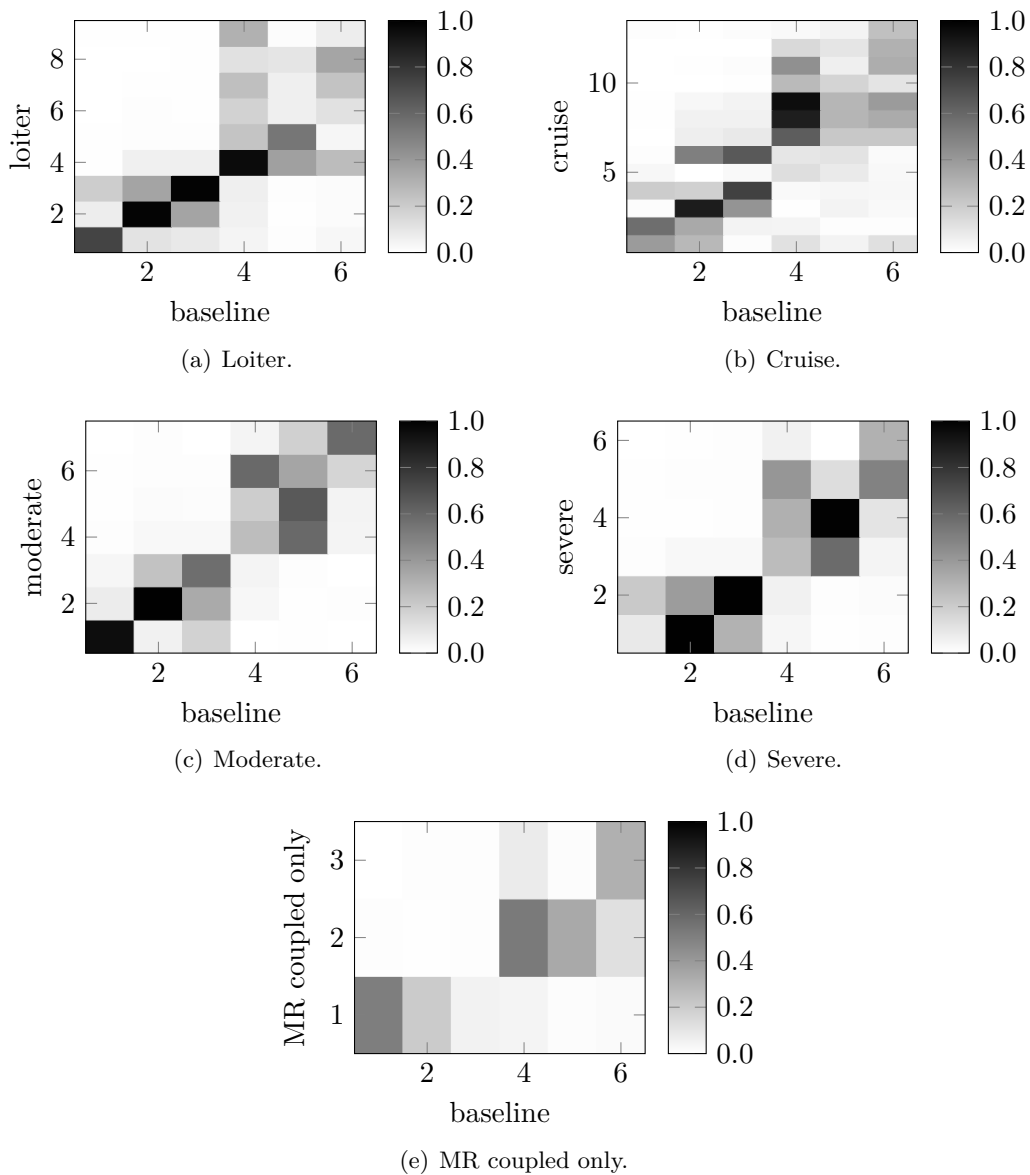
Figure A.26.: MAC-values obtained for the two-way coupled helicopter system using SSI-COV. The computed MAC-values compare different simulation scenarios. Only MR states and the elastic motion of the MR hub are included.

(a) Loiter.

(b) Cruise.

(c) Moderate.

(d) Severe.

(e) MR coupled only.
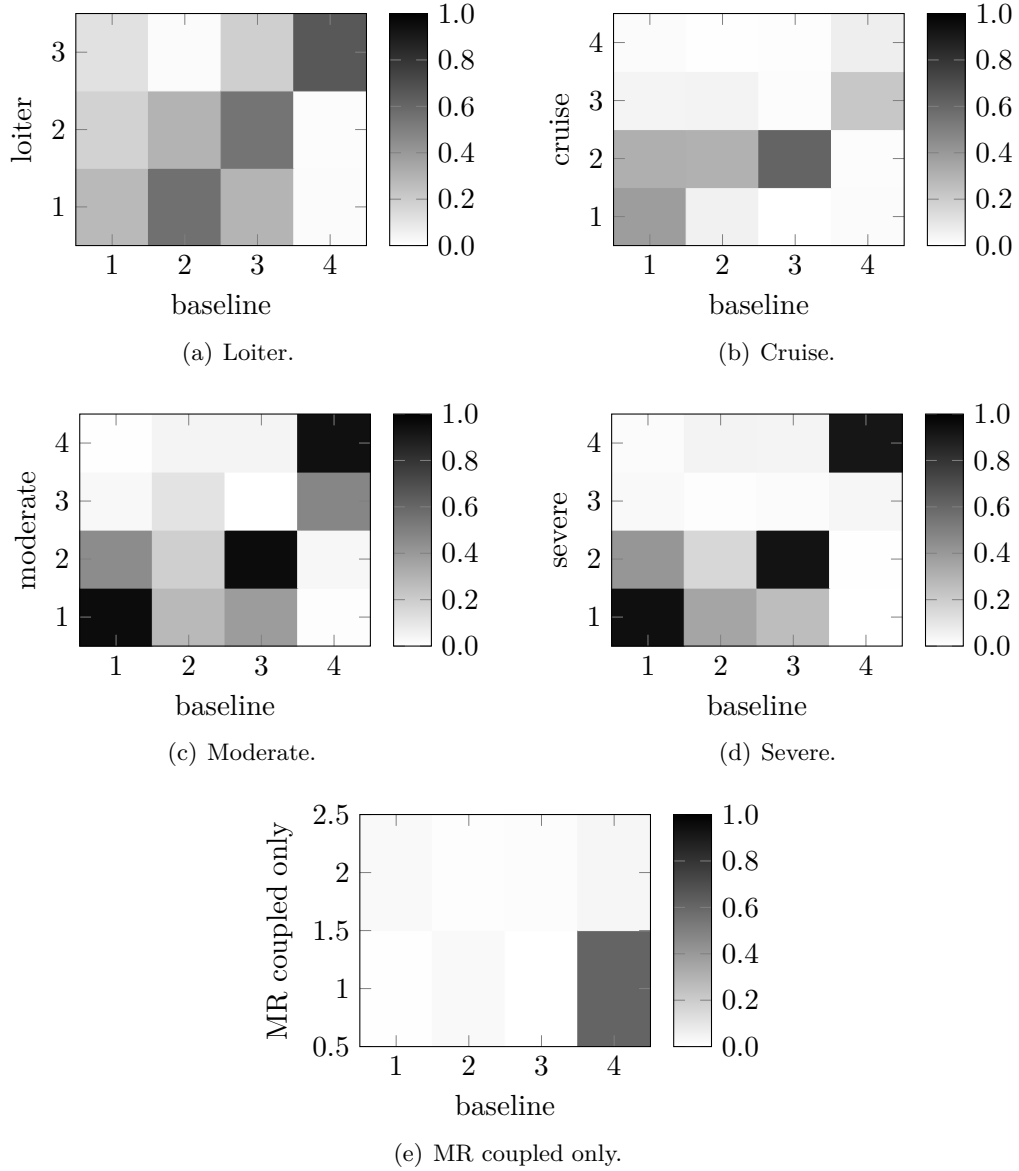
Figure A.27.: MAC-values obtained for the two-way coupled helicopter system using SOBI. The computed MAC-values compare different simulation scenarios. Only MR states and the elastic motion of the MR hub are included.

(a) Baseline.

(b) Loiter.

(c) Cruise.

(d) Moderate.

(e) Severe.

(f) MR coupled only.
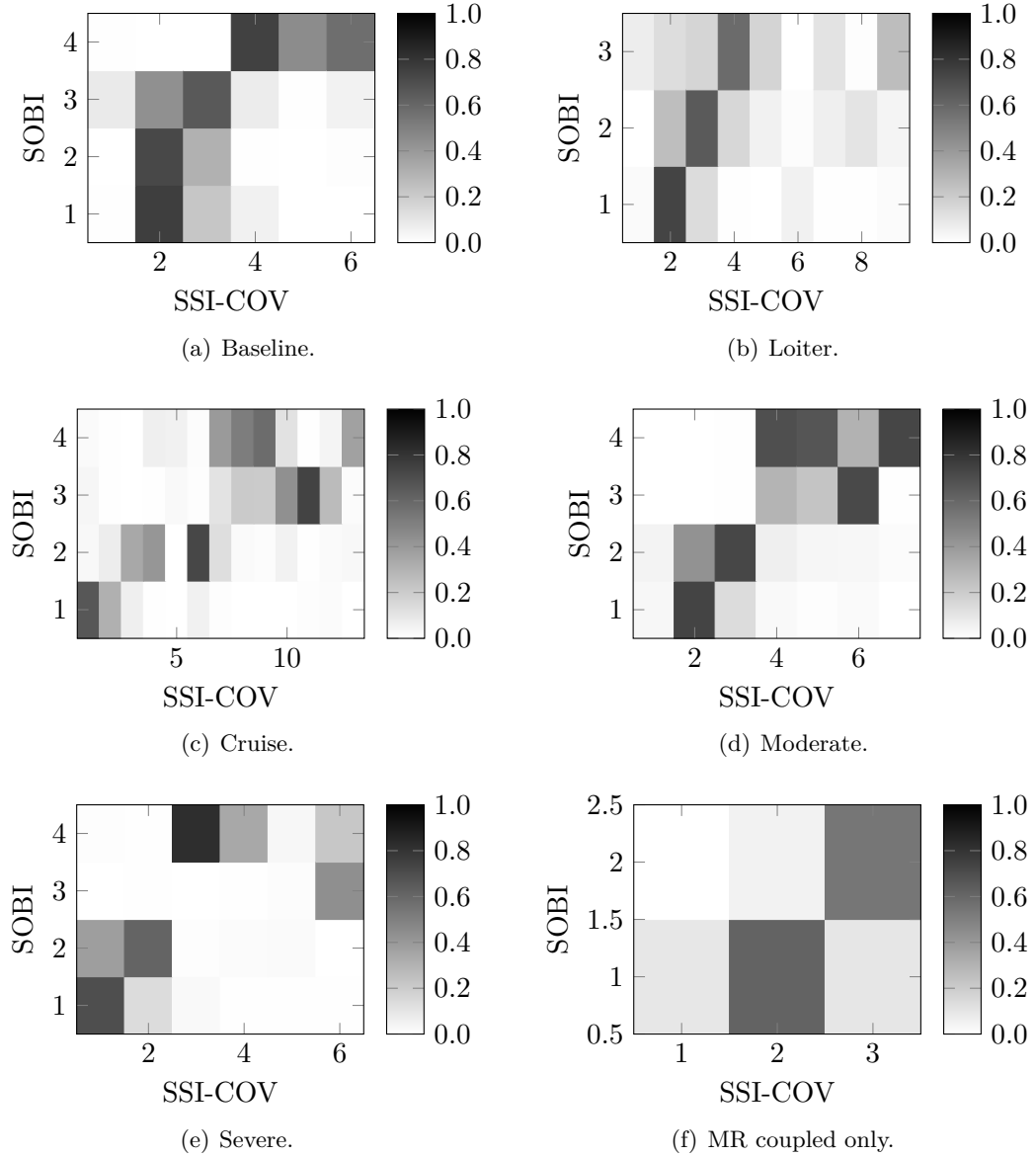
Figure A.28.: MAC-values obtained for the two-way coupled helicopter system for different simulation scenarios. The MAC-values compare the results obtained with SSI-COV and SOBI. Only MR states and the elastic motion of the MR hub are included.

Bibliography

[1]   Abazarsa et al. "Response-Only Modal Identification of Structures Using Limited Sensors". In: *Structural Control and Health Monitoring* (2012).

[2]   Abbott et al. *Validation Flight Test of UH-60A for Rotorcraft Systems Integration Simulator (RSIS)*. Tech. rep. US Army, 1982.

[3]   Abhishek, Datta, and Chopra. "Prediction of UH-60A Structural Loads Using Multi-body Analysis and Swashplate Dynamics". In: *Journal of Aircraft* (2009).

[4]   Abhishek et al. "Rotor Load Prediction using Coupled Rotor-Fuselage Model and Sensor Data". In: *American Helicopter Society Annual Forum*. 2012.

[5]   Aczel and Vajk. "Separation of Periodic and Aperiodic Sound Components by Employing Frequency Estimation". In: *16th European Signal Processing Conference*. 2008.

[6]   Agarwal. "Aeromechanical Stability Augmentation Using Semi-Active Friction-Based Lead-Lag Damper". PhD thesis. Georgia Institute of Technology, 2005.

[7]   Agneni, Coppotelli, and Grappasonni. "Operational Modal Analysis of a Rotating Helicopter Blade". In: *International Conference on Noise and Vibration Engineering ISMA, USD*. 2010.

[8]   Agneni, Crema, and Coppotelli. "Output-Only Analysis of Structures with Closely Spaced Poles". In: *Mechanical Systems and Signal Processing* (2010).

[9]   Allemang. "The Modal Assurance Criterion - Twenty Years of Use and Abuse". In: *Journal of Sound and Vibration* (2002).

[10] Allen et al. "Output-Only Modal Analysis of Linear Time Periodic Systems with Application to Wind Turbine Simulation Data". In: *Proceedings of the IMAC conference*. 2010.

[11] Almunif, Fan, and Miao. "A Tutorial of Data-Driven Eigenvalue Identification - Prony Analysis, Matrix Pencil, and Eigensystem Realization Algorithm". In: *International Transactions on Electrical Energy Systems* (2020).

[12] Andersen et al. "Estimating Modal Parameters of Civil Engineering Structures Subject to Ambient and Harmonic Excitation". In: *International Conference of Experimental Vibration Analysis for Civil Engineering Structures*. 2007.

[13] Antoni. "Blind Separation of Vibration Components - Principles and Demonstrations". In: *Mechanical Systems and Signal Processing* (2005).

[14] Antoni, Castiglione, and Garibaldi. "Interpretation and Generalization of Complexity Pursuit for the Blind Seperation of Modal Contributions". In: *Mechanical Systems and Signal Processing* (2017).

[15]   Antoni and Chauhan. "A Study and Extension of Second-Order Blind Source Separation to Operational Modal Analysis". In: *Journal of Sound and Vibration* (2013).

[16]   Antoni and Chauhan. "An Alternating Least Squares (ALS) based Blind Source Separation Algorithm for Operational Modal Analysis". In: *XXIX International Modal Analysis Conference*. 2011.

[17]   Antoni and Chauhan. "Second Order Blind Source Separation Techniques SO-BSS and their Relation to Stochastic Subspace Identification SSI Algorithm". In: *Proceedings of the IMAX-XXVIII*. 2010.

[18]   Antoni and Randall. "Unsupervised Noise Cancellation for Vibration Signals - Part I - Evaluation of Adaptive Algorithms". In: *Mechanical Systems and Signal Processing* (2004).

[19]   Antoni and Randall. "Unsupervised Noise Cancellation for Vibration Signals - Part II - A Novel Frequency-Domain Algorithm". In: *Mechanical Systems and Signal Processing* (2004).

[20]   Antoni et al. "Blind Separation of Convolved Cyclostationary Processes". In: *Signal Processing* (2005).

[21]   Antoni et al. "Least Action Criteria for Blind Separation of Structural Modes". In: *Mechanics and Industry* (2013).

[22]   Arnold and Bruels. "Convergence of the generalized-alpha scheme for constraint mechanical systems". In: *Multibody System Dynamics*. 2007.

[23]   Aubinet, Vesala, and Papale. *Eddy Covariance*. Springer, 2012.

[24]   *Background Information and User Guide for MIL-F-8785C, Military Specification - Flying Qualities of Piloted Airplanes*. Moorhouse and Woodcock, 1981.

[25]   Bagheri. "Koopman-Mode Decomposition of the Cylinder Wake". In: *Journal of Fluid Mechanics* (2013).

[26]   Bailey. "Helicopter-V-STOL Dynamic Wind and Turbulence Design Methodology". In: *NASA Langley Research Center Turbulence Inputs to Flight Simulation and Systems Certification Conference*. 1987.

[27]   Balch, Saccullo, and Sheehy. *Experimental Study of Main Rotor-Tail Rotor-Airframe Interactions in Hover - Volume I*. Tech. rep. NASA Contractor Report, 1983.

[28]   Basseville et al. "In-Flight Vibration Monitoring of Aeronautical Structures". In: *IEEE Control Systems Magazine* (2007).

[29]   Bauchau. "Computational Schemes for Flexible Nonlinear Mulit-Body Systems Multibody System Dynamics". In: *Kluwer* (1998).

[30]   Bauchau, Bottasso, and Nikishkov. "Modeling Rotorcraft Dynamics with Finite Element Multibody Procedures". In: *Mathematical and Computer Modelling* (2001).

[31]   Bauchau, Rodriguez, and Chen. "Coupled Rotor-Fuselage Analysis with Finite Motions Using Component Mode Synthesis". In: *Journal of the American Helicopter Society* (2004).

[32]   Beal. "Digital Simulation of Atmospheric Turbulence for Dryden and von Karman Models". In: *Journal of Guidance, Control, and Dynamics* (1993).

114

[33] Belouchrani et al. "A Blind Source Separation Technique Using Second-Order Statistics". In: *IEEE Transactions on Signal Processing* (1997).

[34] Bertha, Rios, and Golinval. "Modal Identification of Time-Varying Systems Using Simulated Response on Wind Turbines". In: *International Conference on Noise and Vibration Engineering ISMA, USD.* 2012.

[35] Bielawa. *Rotary Wing Structural Dynamics and Aeroelasticity.* AIAA, 2006.

[36] Bir. "Multiblade Coordinate Transformation and Its Application to Wind Turbine Analysis". In: *ASME Wind Energy Symposium.* 2008.

[37] Bisplinghoff, Ashley, and Halfman. *Aeroelasticity.* Dover Publications, 1983.

[38] Borgman. *Ocean Wave Simulation for Engineering Design.* Tech. rep. University of California, 1967.

[39] Böswald et al. "A Review of Experimental Modal Analysis Methods with Respect to their Applicability to Test Data of Large Aircraft Structures". In: *International Conference on Noise and Vibration Engineering ISMA.* 2006.

[40] Bottasso et al. "A Tunable Mast Vibration Absorber for Variable RPM Rotorcraft". In: *European Rotorcraft Forum.* 2016.

[41] Bousman and Kufeld. *UH-60A Airloads Catalog.* Tech. rep. NASA, 2005.

[42] Bramwell, Done, and Balmford. *Bramwells Helicopter Dynamics.* Butterworth-Heinemann, 2001.

[43] Brincker and Ventura. *Introduction to Operational Modal Analysis.* John Wiley and Sons, 2015.

[44] Brincker, Zhang, and Andersen. "Modal Identification of Output-Only Systems Using Frequency Domain Decomposition". In: *Smart Materials and Structures* (2001).

[45] Brincker et al. "Understanding Stochastic Subspace Identification". In: *Proceedings of the IMAC conference.* 2006.

[46] Brunton and Kutz. *Data-Driven Science and Engineering Machine Learning, Dynamical Systems, and Control.* Cambridge Universtiy Press, 2019.

[47] Caicedo. "Practical Guidelines For the Natural Excitation Technique (NExT) And the Eigensystem Realization Algorithm (ERA) for Modal Identification Using Ambient Vibration". In: *Experimental Techniques* (2011).

[48] Camargo, Jacobsen, and Strafacci. "Operational Modal Analysis on two Different Helicopter Configurations". In: *International Operational Modal Analysis Conference.* 2011.

[49] Camargo, Jacobson, and Strafacci. "Operational Modal Analysis on a Modified Helicopter". In: *Proceedings of the IMAC conference.* 2011.

[50] Cameron et al. "Measurement of Transient Loads and Blade Deformation in a Coaxial Counter-Rotating Rotor". In: *American Helicopter Society Annual Forum.* 2017.

[51] Cardoso. "Blind Signal Separation - Statistical Principles". In: *Proceedings of the IEEE* (1998).

[52] Cauberghe. "Applied Frequency-Domain System Indentification in the Field of Experimental And Operational Modal Analysis". PhD thesis. Vrije Universiteit Brussel, 2004.

[53] Cavagnino and Fosco. "Operational Modal Analysis of a Leightweight Helicopter Tail". In: *European Rotorcraft Forum*. 2006.

[54] Chauhan, Hansen, and Tcherniak. "Application of Operational Modal Analysis and Blind Source Separation Idenpendent Component Analysis Techniques to Wind Turbines". In: *Proceedings of the IMAC conference*. 2009.

[55] Chiu and Friedmann. "A Coupled Helicopter Rotor-Fuselage Aeroelastic Response Model for ACSR". In: *36th Structures, Structural Dynamics and Materials Conference*. 1995.

[56] Choi et al. "Blind Source Separation and Independent Component Analysis - A Review". In: *Neural Information Processing-Letters and Reviews* (2005).

[57] Cichocki and Amari. *Adaptive Blind Signal and Image Processing Learning Algorithms and Applications*. John Wiley and Sons, 2003.

[58] Clement, Gorder, and Jewell. "Development of a Real-Time Simulation of a Ship-Correlated Airwake Model Interfaced with a Rotorcraft Dynamic Model". In: *Flight Simulation Technologies Conference*. 1992.

[59] Cole. *On-Line Failure Detection and Damping Measurement of Aerospace Structures by Random Decrement Signatures*. Tech. rep. Nielsen Engineering and Research Inc., 1973.

[60] Coleman. *Theory of Self-Excited Mechanical Oscillations of Hinged Rotor Blades*. Tech. rep. NACA Report, 1943.

[61] Connell. "The Spectrum of Wind Speed Fluctuations Encountered by a Rotating Blade of a Wind Energy Conversion System". In: *Solar Energy* (1982).

[62] Conti, Coppotelli, and Van Tongeren. "Modal Parameters Estimate of AH64D Apache Helicopter from Flight Data and Correlation with Numerical Model". In: *AIAA SciTech Forum*. 2018.

[63] Coppotelli et al. "Real-Time System Identification for Fixed and Rotary Wing Aircraft". In: *AIAA Scitech Forum*. 2019.

[64] Costello et al. "Some Issues on Modeling Atmospheric Turbulence Experienced by Helicopter Rotor Blades". In: *Journal of the American Helicopter Society* (1992).

[65] Cribbs, Friedmann, and Chiu. "Coupled Helicopter Rotor-Flexible Fuselage Aeroelastic Model for Control of Structural Response". In: *AIAA Journal* (2000).

[66] Crimi. *A Method for Analyzing the Aeroelastic Stability of a Helicopter in Forward Flight*. Tech. rep. NASA Contractor Report, 1969.

[67] Dahl and Faulkner. "Helicopter Simulation in Atmospheric Turbulence". In: *European Rotorcraft Forum*. 1978.

[68] Dang, Gaonkar, and Prasad. "Parallel Methods for Turbulence Simulation and Helicopter-Response Prediction". In: *Journal of the American Helicopter Society* (1996).

[69]   Dang et al. "Parallel Computing of Helicopter Response to Turbulence Toward Real-Time Implementation". In: *American Helicopter Society Annual Forum*. 1994.

[70]   Datta. "Fundamental Understanding, Prediction and Validation of Rotor Vibratory Loads in Steady Level Flight". PhD thesis. University of Maryland, 2004.

[71]   Davis, Bennett, and Blankenship. *Rotorcraft Flight Simulation with Aeroelastic Rotor and Improved Aerodynamic Representation - Volume I*. Tech. rep. Bell Helicopter Company, 1974.

[72]   Debille, Pauwels, and Peeters. "The Benefits of Operational Modal Analysis of Aircraft and Spacecraft Structures". In: *European Test and Telemetry Conference*. 2005.

[73]   Devrient et al. "Operational Modal Analysis in the Presence of Harmonic Excitation by the Use of Transmissibility Measurements". In: *Mechanical Systems and Signal Processing* (2009).

[74]   Ding and Shen. "Helicopter Rotor Infield Tracking with a Trailing-Edge Flap and Adaptive Closed-Loop Regulator". In: *American Helicopter Society Annual Forum*. 2018.

[75]   Döhler, Lam, and Mevel. "Uncertainty Quantification for Modal Parameters from Stochastic Subspace Identification on Multi-Step Measurements". In: *Mechanical Systems and Signal Processing* (2013).

[76]   Döhler and Mevel. "Efficient Multi-Order Uncertainty Computation for Stochastic Subspace Identification". In: *Mechanical Systems and Signal Processing* (2013).

[77]   Döhler and Mevel. "Fast Multi-Order Computation of System Matrices in Subspace-Based System Identification". In: *Control Engineering Practice* (2012).

[78]   Durbin and Petterson-Reif. *Statistical Theory and Modeling for Turbulent Flow*. Wiley, 2011.

[79]   Dwoyer, Hussaini, and Voigt. *Theoretical Approaches to Turbulence*. Applied Mathematical Sciences Vol. 58, 1985.

[80]   Elliott and Chopra. "Helicopter Response to Atmospheric Turbulence in Forward Flight". In: *Journal of the American Helicopter Society* (1990).

[81]   Elliott and Chopra. "Hingeless Rotor Response to Random Gusts in Forward Flight". In: *28th Structures, Structural Dynamics and Materials Conference*. 1987.

[82]   Emeis. *Wind Energy Meteorology*. Springer, 2013.

[83]   Etele. *Overview of Wind Gust Modelling with Application to Autonomous Low-Level UAV Control*. Tech. rep. Defence R&D Canada, 2006.

[84]   Etkin. *Dynamics of Atmospheric Flight*. Dover Publications, 2000.

[85]   Foken. *Micrometeorology*. Springer, 2017.

[86]   Friedmann. "Helicopter Vibration Reduction Using Structural Optimization with Aeroelastic Multidisciplinary Constraints". In: *Journal of Aircraft* (1991).

[87]   Friedmann. "Numerical Methods for the Treatment of Periodic Systems with Application to Structural Dynamics and Helicopter Rotor Dynamics". In: *Computers and Structures* (1990).

[88] Friedmann. "Rotary-Wing Aeroelasticity - Current Status and Future Trends". In: *AIAA Journal* (2004).

[89] Friedmann, Hammond, and Woo. "Efficient Numerical Treatment of Periodic Systems with Application to Stability Problems". In: *International Journal for Numerical Methods in Engineering* (1977).

[90] Fuh et al. "Coupled Flap-Torsional Response of a Rotor Blade in Forward Flight Due to Atmospheric Turbulence Excitations". In: *Journal of the American Helicopter Society* (1983).

[91] Fujimori, Lin, and Ariaratnam. "Rotor Blade Stability in Turbulent Flows - Part II". In: *AIAA Journal* (1979).

[92] Gabel and Sankewitsch. "Rotor-Fuselage Coupling by Impedance". In: *American Helicopter Society Annual Forum*. 1986.

[93] Gaonkar. "A Study of Lifting Rotor Flapping Response Peak Distribution in Atmospheric Turbulence". In: *Journal of Aircraft* (1974).

[94] Gaonkar. "Gust Response of Rotor and Propeller Systems". In: *Journal of Aircraft* (1981).

[95] Gaonkar. "Nonlinear Stochastic Modeling of Airwake Turbulence for Helicopter Shipboard Operations". In: *American Helicopter Society Annual Forum*. 2006.

[96] Gaonkar. "Random Vibration Peaks in Rotorcraft and the Effects of Nonuniform Gusts". In: *Journal of Aircraft* (1977).

[97] Gaonkar. "Review of Nonstationary Gust-Responses of Flight Vehicles". In: *21st Structures, Structural Dynamics and Materials Conference*. 1980.

[98] Gaonkar. "Review of Turbulence Modeling and Related Applications to Some Problems of Helicopter Flight Dynamics". In: *Journal of the American Helicopter Society* (2008).

[99] Gaonkar and Hohenemser. "An Advanced Stochastic Model for Threshold Crossing Studies of Rotor Blade Vibrations". In: *AIAA Journal* (1972).

[100] Gaonkar and Hohenemser. "Comparison of two Stochastic Models for Threshold Crossing Studies of Rotor Blade Flapping Vibrations". In: *12th Structures, Structural Dynamics and Materials Conference*. 1971.

[101] Gaonkar and Hohenemser. "Stochastic Properties of Turbulence Excited Rotor Blade Vibrations". In: *AIAA Journal* (1971).

[102] Gaonkar, Prasad, and Sastry. "On Computing Floquet Transition Matrices of Rotorcraft". In: *Journal of the American Helicopter Society* (1981).

[103] Gaonkar and Subramanian. "A Study of Feedback, Blade and Hub Parameters on Flap Bending Due to Non-Uniform Rotor Disk Turbulence". In: *Journal of Sound and Vibration* (1977).

[104] George et al. "On the Adequacy on Modeling Turbulence and Related Effects on Helicopter Response". In: *AIAA Journal* (1992).

[105] Gessow and Myers. *Aerodynamics of the Helicopter*. Frederick Ungar Publishing Co., 1985.

[106]   Ghandi and Sekula. "Helicopter Vibration Reduction Using Fixed-System Auxiliary Moments". In: *AIAA Journal* (2004).

[107]   Gioia et al. "Identification of Noise, Vibration and Harshness Behavior of Wind Turbine Drivetrain und Different Operating Conditions". In: *Energies* (2019).

[108]   Goethals and De Moor. "Model Reduction and Energy Analysis as a Tool to Detect Spurious Modes". In: *International Conference on Noise and Vibration Engineering ISMA*. 2002.

[109]   Goodell. "Dynamic Analysis of Multi-Degree-Of-Freedom Systems Using a Pole-Residue Method". MA thesis. University of Rhode Island, 2016.

[110]   Grappasonni et al. "Dynamic Identification of Helicopter Structures Using Operational Modal Analysis Methods in the Presence of Harmonic Loading". In: *International Conference on Noise and Vibration Engineering ISMA, USD*. 2012.

[111]   Gres et al. "Kalman Filter-Based Subspace Identification for Operational Modal Analysis under Unmeasured Periodic Excitation". In: *Mechanical Systems and Signal Processing* (2020).

[112]   Guillaume, Verboven, and Vanlanduit. "Frequency Domain Maximum Likelihood Identification of Modal Parameters with Confidence Intervals". In: *Proceedings of the International Seminar on Modal Analysis*. 1998.

[113]   Hamade and Kufeld. *Modal Analysis of UH-60A Instrumented Rotor Blades*. Tech. rep. NASA Technical Memorandum, 1990.

[114]   Hamel and Jategaonkar. "Evolution of Flight Vehicle System Identification". In: *Journal of Aircraft* (1996).

[115]   Hammond and Doggett. "Determination of Subcritical Damping by Moving-Block Randomdec Applications". In: *NASA Symposium of Flutter Testing Techniques*. 1975.

[116]   Han, Mongeau, and Bernhard. "Energy Flow Analysis of Beams and Plates For Random Distributed Loading". In: *Journal of Fluids and Structures* (1998).

[117]   Hansen, Thomsen, and Fuglsang. "Two Methods for Estimating Aeroelastic Damping of Operational Wind Turbine Modes from Experiments". In: *Wind Energy* (2006).

[118]   Hanson et al. "Cyclostationarity and the Cepstrum for Operational Modal Analysis of MIMO Systems - Part I - Modal Parameter Identification". In: *Mechanical Systems and Signal Processing* (2007).

[119]   Hanson et al. "Cyclostationarity and the Cepstrum for Operational Modal Analysis of MIMO Systems - Part II - Obtaining Scaled Mode Shapes Through Finite Element Model Updating". In: *Mechanical Systems and Signal Processing* (2007).

[120]   Hasbun, Saberi, and Blumenstein. "Modal Elastic Component Enhancements for RCAS". In: *Vertical Flight Society Annual Forum*. 2020.

[121]   Hazra et al. "Modified Cross-Correlation Method for the Blind Identification of Structures". In: *Journal of Engineering Mechanics* (2010).

[122]   Heath and Imregun. "A Review of Analysis Techniques for Blade Tip-Timing Measurements". In: *The American Society of Mechanical Engineers* (1997).

Bibliography

[123] Hermans, Van der Auweraer, and Guillaume. "A Frequency-Domain Maximum Likelihood Approach for the Extraction of Modal Parameters from Output-Only Data". In: *International Conference on Noise and Vibration Engineering ISMA*. 1998.

[124] Hess. "A Simplified and Approximate Technique for Scaling Rotorcraft Control Inputs for Turbulence Modeling". In: *Journal of the American Helicopter Society* (2004).

[125] Hess. "Rotorcraft Handling Qualities in Turbulence". In: *Journal of Guidance, Control and Dynamics* (1995).

[126] Ho and Yeo. "An Evaluation of Finite-State Dynamic Inflow for Usage in Design". In: *Vertical Flight Society Annual Forum*. 2020.

[127] Ho, Yeo, and Ormiston. "Investigation of Rotor Blade Structural Dynamics and Modeling Based on Measured Airloads". In: *American Helicopter Society Annual Forum*. 2007.

[128] Hoblit. *Gust Loads on Aircraft: Concepts and Applications*. AIAA Education Series, 1988.

[129] Hodges. *Nonlinear Composite Beam Theory*. AIAA, 2006.

[130] Hohenemser. *The Role of Rotor Impedance in the Vibration Analysis of Rotorcraft*. Tech. rep. Washington University, 1978.

[131] Hohenemser and Yin. *Concepts for a Theoretical and Experimental Study of Lifting Rotor Random Loads and Vibrations*. Tech. rep. Washington University, 1972.

[132] Holopainen et al. "Comparison of Modal Parameter Estimation Techniques for Electromechanical Rotordynamics of Cage Induction Motors". In: *ASME International Design Engineering Technical Conferences & Computers and Information in Engineering Conference IDETC/CIE*. 2007.

[133] Holton. *An Introduction to Dynamic Meteorology*. Elsevier, 2004.

[134] Houbolt. "Atmospheric Turbulence". In: *AIAA Journal* (1973).

[135] Howland, Durno, and Twomey. *Ground Shake Test of the UH-60A Helicopter Airframe and Comparison with Nastran Finite Element Model Predictions*. Tech. rep. NASA Contractor Report, 1990.

[136] Howlett. *UH-60A Black Hawk Engineering Simulation Program - Volume I - Mathematical Model*. Tech. rep. NASA Contractor Report, 1981.

[137] Hsu and Peters. "Coupled Rotor-Airframe Vibration Analysis by a Combined Harmonic-Balance Impedance-Matching Method". In: *American Helicopter Society Annual Forum*. 1980.

[138] Huecas, White, and Barakos. "A Turbulence Model for Flight Simulation and Handling Qualities Analysis based on a Synthetic Eddy Method". In: *Vertical Flight Society Annual Forum*. 2020.

[139] Hyvaerinen. "Complexity Pursuit - Separating Interesting Components from Time-Series". In: *Neural Computation* (2001).

[140] Hyvaerinen and Oja. "Independent Component Analysis: Algorithms and Applications". In: *Neural Networks* (2000).

[141] Ibrahim. "Random Decrement Technique for Modal Identification of Structures". In: *Journal of Spacecraft* (1977).

[142] Iliff. "Identification and Stochastic Control of an Aircraft Flying in Turbulence". In: *Journal of Guidance and Control* (1978).

[143] Jacobsen and Andersen. "Operational Modal Analsis on Structures with Rotating Parts". In: *International Conference on Noise and Vibration Engineering ISMA*. 2008.

[144] Jacobsen, Andersen, and Brincker. "Eliminating the Influence of Harmonic Components in Operational Modal Analysis". In: *Proceedings of the IMAC conference*. 2007.

[145] Jacobson et al. "Evaluation of Time-Domain Damping Identification Methods for Flutter-Constrained Optimization". In: *Preprint submitted to Journal of Fluids and Structures* (2019).

[146] James, Carne, and Lauffer. *The Natural Excitation Technique (NExT) for Modal Parameter Extraction From Operating Wind Turbines*. Tech. rep. Sandia National Laboratories, 1993.

[147] Jarrin et al. "A Synthetic-Eddy-Method for Generating Inflow Conditions for Large-Eddy Simulations". In: *International Journal of Heat and Fluid Flow* (2006).

[148] Jhinaoui, Mevel, and Morlier. "A New SSI Algorithm for LPVT Systems - Application to a Hinged-Bladed Helicopter". In: *Mechanical Systems and Signal Processing* (2014).

[149] Ji, Chen, and Li. "Analysis of Helicopter Handling Quality in Turbulence with Recursive Von Karman Model". In: *Journal of Aircraft* (2017).

[150] Ji, Chen, and Li. "Distributed Atmospheric Turbulence Model for Helicopter Flight Simulation and Handling-Quality Analysis". In: *Journal of Aircraft* (2016).

[151] Ji et al. "Pilot Workload Investigation for Rotorcraft Operation in Low-Altitude Atmospheric Turbulence". In: *Aerospace Science and Technology* (2021).

[152] Johnson. *Rotorcraft Aeromechanics*. Cambridge University Press, 2013.

[153] Jones. "Modelling of Gusts and Wind Shear for Aircraft Assessment and Certification". In: *Proceedings of the Indian Academy of Sciences Section C: Engineering Sciences* (1980).

[154] Jones. "Statistical-Discrete-Gust Method for Predicting Aircraft Loads and Dynamic Response". In: *Journal of Aircraft* (1989).

[155] Jones, Watson, and Foster. "Non-Gaussian Statistics of Atmospheric Turbulence and Related Effects on Aircraft Loads". In: *AIAA Journal* (2004).

[156] Jonkman. *TurbSim Users Guide - Version 1.50*. Tech. rep. NREL Technical Report, 2009.

[157] Juang and Pappa. "An Eigensystem Realization Algorithm for Modal Parameter Identification and Model Reduction". In: *Journal of Guidance, Control and Dynamics* (1985).

[158] Jurdic, Joseph, and Antoni. "Investigation of Rotor Wake Turbulence Through Cyclostationary Spectral Analysis". In: *AIAA Journal* (2009).

[159] Kana, Yeakley, and Dalzell. "An Experimental Model for Studying Dynamic Responses of a Rotating Beam under Spatially Distributed Random Excitation". In: *Experimental Mechanics* (1968).

[160] Kelley. "Full Vector (3-D) Inflow Simulation in Natural and Wind Farm Environments Using Expanded Version of the SNLWIND (VEERS) Turbulence Code". In: *12th ASME Wind Energy Symposium.* 1993.

[161] Kelley and Jonkman. *Overview of the TurbSim Stochastic Inflow Turbulence Simulator.* Tech. rep. NREL Technical Report, 2007.

[162] Kerschen. "Modal Analysis of Nonlinear Vibrating Systems - Recent Progress and Challenges". In: *Proceedings of the 8th Conference on Structural Dynamics.* 2011.

[163] Kerschen, Poncelet, and Golinval. "Physical Interpretation of Independent Component Analysis in Structural Dynamics". In: *Mechanical Systems and Signal Processing* (2007).

[164] Kirschneck et al. "In-Situ Experimental Modal Analysis of a Direct-Drive Wind Turbine Generator". In: *Experimental Techniques, Rotating Machinery, and Acoustics.* 2015.

[165] Kocan. "A Comparative Study on In-Flight Modal Identification of an Aircraft Using Time- and Frequency-Domain Techniques". In: *Journal of Vibration and Control* (2020).

[166] Krishnan and Gaonkar. "A Framework for Modeling Two-Point Statistics of Coherence from a Database for Airwake With Helicopter Downwash". In: *Vertical Flight Society Annual Forum.* 2019.

[167] Kumar. "Design and Analysis of Composite Rotor Blades for Active-Passive Vibration Reduction". PhD thesis. University of Michigan, 2013.

[168] Labows. "UH-60 Black Hawk Disturbance Rejection Study For Hover/Low Speed Handling Qualities Criteria and Turbulence Modeling". MA thesis. US Naval Postgraduate School, 2000.

[169] Langley. "Application of the Dynamic Stiffness Method to the Free and Forced Vibrations of Aircraft Panels". In: *Journal of Sound and Vibration* (1989).

[170] Lee. "Simulation and Control of a Helicopter Operating in a Ship Airwake". PhD thesis. Pennsylvania State University, 2005.

[171] Lee and Horn. "Simulation of Pilot Workload for a Helicopter Operating in a Turbulent Ship Airwake". In: *Journal Aerospace Engineering* (2005).

[172] Leoni. *Black Hawk The Story of a World Class Helicopter.* AIAA, 2007.

[173] Li et al. "A Frequency Domain Blind Identification Method for Operational Modal Analysis Using a Limited Number of Sensors". In: *Journal of Vibration and Control* (2020).

[174] Lin, Fujimori, and Ariaratnam. "Rotor Blade Stability in Turbulent Flows - Part I". In: *AIAA Journal* (1979).

[175] Loewy. "Review of Rotray-Wing VSTOL Dynamic and Aeroelastic Problems". In: *Journal of the American Helicopter Society* (1969).

Bibliography

[176] Di Lorenzo. "Operational Modal Analysis for Rotating Machines". PhD thesis. Katholieke Universiteit Leuven, 2017.

[177] Di Lorenzo et al. "Virtual Assessment of Damage Detection Techniques for Operational Wind Turbines". In: *Advances in Condition Monitoring of Machinery in Non-Stationary Operations*. 2013.

[178] Di Lorenzo et al. "Virtual Structural Monitoring of Wind Turbines Using Operational Modal Analysis Techniques". In: *Key Engineering Materials* (2013).

[179] Lusardi et al. "Empirically Derived Helicopter Response Model and Control System Requirements for Flight in Turbulence". In: *Journal of the American Helicopter Society* (2004).

[180] Lutes and Sarkani. *Random Vibrations Analysis of Structural and Mechanical Systems*. Elsevier, 2004.

[181] Maamar et al. "Modal Identification of a Machine Tool Structure During Machining Operations". In: *International Journal of Advanced Manufacturing Technology* (2019).

[182] Manzato et al. "A Review of Harmonic Removal Methods for Improved Operational Modal Analysis of Wind Turbines". In: *International Conference on Noise and Vibration Engineering ISMA, USD*. 2012.

[183] Manzato et al. "Dealing with Harmonics and Noise for Advanced Dynamic Identification Using In-Flight Helicopter Data". In: *International Forum of Aeroelasticity and Structural Dynamics*. 2013.

[184] Manzato et al. "Order Based Modal Analysis vs. Standard Techniques to Extract Modal Parameters of Operational Wind Turbine Gearboxes". In: *Topics in Modal Analysis*. 2015.

[185] Masjedia and Keshmiri. "A Review on Operational Modal Analysis Researches - Classification of Methods and Applications". In: *3rd International Operational Modal Analysis Conference*. 2009.

[186] McComb. *The Physics of Fluid Turbulence*. Oxford Engineering Science Series, 1990.

[187] McFarland. *A Standard Lineatic Model For Flight Simulation at NASA-Ames*. Tech. rep. NASA Contractor Report, 1975.

[188] McFarland and Duisenberg. "Simulation of Rotor Blade Element Turbulence". In: *NASA Technical Memorandum*. 1995.

[189] McNeill and Zimmermann. "Relating Independent Components to Free-Vibration Modal Responses". In: *Shock and Vibration* (2010).

[190] Mellinger, Döhler, and Mevel. "Variance Estimation of Modal Parameters from Output-Only and Input-Output Subspace-Based System Identification". In: *Journal of Sound and Vibration* (2016).

[191] Meng et al. "Comparison of System Identification Techniques for Predicting Dynamic Properties of Large Scale Wind Turbines by Using the Simulated Time Response". In: *Structural Dynamics and Renewable Energy*. 2011.

[192] Mevel et al. "Input-Output Versus Output-Only Data Processing for Structural Identification - Application to In-Flight Data Analysis". In: *Journal of Sound and Vibration* (2006).

Bibliography

[193]   Mezic. "Analysis of Fluid Flows via Spectral Properties of the Koopman Operator". In: *Annual Review of Fluid Mechanics* (2013).

[194]   Mezic. "Spectral Properties of Dynamical Systems, Model Reduction and Decompositions". In: *Nonlinear Dynamics* (2005).

[195]   Miao and Mouzakis. *Bifilar Analysis Study - Volume I*. Tech. rep. NASA Contractor Report, 1980.

[196]   Millott et al. "Risk Reduction Flight Test of a Pre-Production Active Vibration Control System for the UH-60M". In: *American Helicopter Society 59th Annual Forum*. 2003.

[197]   Mironovs, Mironov, and Chate. "Harmonic Components Extraction Influence on Resulting Modal Parameters of Vibrating Structures". In: *13th International Conference Modern Building Material, Structures and Techniques*. 2019.

[198]   Mohanty. "Operational Modal Analysis in the Presence of Harmonic Excitations". PhD thesis. Technische Universiteit Delft, 2005.

[199]   Mohanty and Rixen. "Modified ERA Method for Operational Modal Analysis in the Presence of Harmonic Excitations". In: *Mechanical Systems and Signal Processing* (2006).

[200]   Monico, DiOttavio, and Kakaley. "Achieving Near Zero N/Rev Vibration with Zero-Vibe Technology". In: *American Helicopter Society Annual Forum*. 2018.

[201]   Moore. "Ergodic Theorem, Ergodic Theory, and Statistical Mechanics". In: *Proceedings of the National Academy of Sciences* (2015).

[202]   Moore, Lai, and Shankar. "ARMAX Modal Parameter Estimation Using Random and Periodic Excitation". In: *Proceedings of the 1st International Operational Modal Analysis Conference*. 2005.

[203]   Moorhouse and Heffley. "The Status of Military Specifications with Regard to Atmospheric Turbulence". In: *NASA Langley Research Center Atmospheric Turbulence Relative to Aviation, Missile and Space Programs Conference*. 1987.

[204]   Motte et al. "Operational Modal Analysis in the Presence of Harmonic Excitations - A Review". In: *Dynamics of Civil Structures*. 2015.

[205]   Müller and Schiehlen. *Linear Vibrations - A theoretical Treatment of Multi-Degree-of-Freedom Vibrating Systems*. Martinus Nijhoff Publishers, 1985.

[206]   Murthy and Kvaternik. "Experiences at Langley Research Center in the Application of Optimization Techniques to Helicopter Airframes For Vibration Reduction". In: *America Helicopter Society National Technical Specialists' Meeting on Rotorcraft Structures*. 1991.

[207]   Neu. "Vibration-Based Structural Health Monitoring of Cantilever-Like Structures under Varying Wind Conditions". PhD thesis. Royal Melbourne Institute of Technology, 2016.

[208]   Ngo. "Constrained Control for Helicopter Shipboard Operations and Moored Ocean Current Turbine Flight Control". PhD thesis. Virginia State Universtiy, 2016.

[209] Nieto, ElSayed, and Walch. "Modal Participation Factors and Their Potential Applications in Aerospace - A Review". In: *The Canadian Society for Mechanical Engineering International Congress*. 2018.

[210] Norman et al. "Full-Scale Wind Tunnel Test of a UH-60 Individual Blade Control System for Performance Improvement and Vibration, Loads and Noise Control". In: *American Helicopter Society Annual Forum*. 2009.

[211] Oberinger. "Modellbildung und Berechnung von Rotor-Zelle Kopplungserscheinungen am Hubschrauber und deren Interpretation mittels Energieflussmethoden". PhD thesis. Technical University of Munich, 2016.

[212] Oezbek. "Optical Monitoring and Operational Modal Analysis of Large Wind Turbines". PhD thesis. Technische Universiteit Delft, 2013.

[213] Oliveira et al. "Continuous Dynamic Monitoring of an Onshore Wind Turbine". In: *Engineering Structures* (2018).

[214] Oliveira et al. "Vibration-Based Damage Detection in a Wind Turbine Using 1 Year of Data". In: *Structural Control and Health Monitoring* (2017).

[215] Osgood et al. "Full-Scale Modal Wind Turbine Tests - Comparing Shaker Excitation with Wind Excitation". In: *Proceedings of the IMAC conference*. 2010.

[216] Van Overschee and De Moor. "Subspace Algorithms for the Stochastic Identification Problem". In: *30th IEEE Conference on Decision and Control*. 1991.

[217] Van Overschee and De Moor. *Subspace Identification for Linear Systems*. Kluwer Academic Publishers, 1996.

[218] Ozbek and Rixen. "Operational Modal Analysis of a 2.5 MW Wind Turbine Using Optical Measurement Techniques and Strain Gauges". In: *Wind Energy* (2012).

[219] Papakos and Fassois. "Multichannel Identification of Aircraft Skeleton Structures Under Unobservable Excitation - A Vector AR-ARMA Framework". In: *Mechanical Systems and Signal Processing* (2003).

[220] Pappa, Elliott, and Schenk. "Consistent-Mode Indicator for the Eigensystem Realization Algorithm". In: *Journal of Guidance, Control, and Dynamics* (1993).

[221] Peeters. "System Identification and Damage Detection in Civil Engineering". PhD thesis. Katholieke Universiteit Leuven, 2000.

[222] Peeters, El-kafafy, and Guillaume. "The new PolyMAX Plus Method - Confident Modal Parameter Estimation Even in Very Noisy Cases". In: *International Conference on Noise and Vibration Engineering ISMA, USD*. 2012.

[223] Peeters, Manzato, and Van der Auweraer. "Solutions to Deal with Harmonics and Noise For Helicopter In-Flight Data Dynamic Identification". In: *International Operational Modal Analysis Conference*. 2013.

[224] Peeters and De Roeck. "Reference-Based Stochastic Subspace Identification for Output-Only Modal Analysis". In: *Mechanical Systems and Signal Processing* (1999).

[225] Peeters and De Roeck. "Stochastic System Identification for Operational Modal Analysis - A Review". In: *Journal of Dynamic Systems, Measurement, and Control* (2001).

[226] Peeters et al. "A New Procedure for Modal Parameter Estimation". In: *Journal of Sound and Vibration* (2004).

[227] Peeters et al. "In-Flight Modal Analysis - A Comparison Between Sweep and Turbulence Excitation". In: *International Conference on Noise and Vibration Engineering*. 2006.

[228] Peeters et al. "Removing Disturbing Harmonics in Operational Modal Analysis". In: *International Operational Modal Analysis Conference*. 2007.

[229] Peeters et al. "The PolyMAX Frequency-Domain Method - A New Standard for Modal Parameter Estimation". In: *Journal of Shock and Vibration* (2004).

[230] Perlmutter, Frost, and Fichtl. "Three Velocity Component, Nonhomogeneous Atmospheric Boundary Layer Turbulence Modeling". In: *AIAA Journal* (1977).

[231] Perry, Pototzky, and Woods. "NASA Investigation of a Claimed Overlap Between Two Gust Response Analysis Methods". In: *Journal of Aircraft* (1990).

[232] Peters. "Fast Floquet Theory and Trim for Multi-Bladed Rotorcraft". In: *Journal of the American Helicopter Society* (1994).

[233] Peters and Barwey. "A General Theory of Rotorcraft Trim". In: *Mathematical Problems in Engineering* (1996).

[234] Peters and He. "Finite State Induced Flow Models Part II - Three-Dimensional Rotor Disk". In: *Journal of Aircraft* (1995).

[235] Peters and Hohenemser. "Application of the Floquet Transition Matrix to Problems of Lifting Rotor Stability". In: *Journal of the American Helicopter Society* (1971).

[236] Petsounis and Fassois. "Parametric Time-Domain Methods for the Identification of Vibrating Structures - A Critical Comparison and Assessment". In: *Journal of Mechanical Systems and Signal Processing* (2001).

[237] Pintelon, Peeters, and Guillaume. "Continuous-Time Operational Modal Analysis in the Presence of Harmonics Disturbances". In: *IEEE International Instrumentation and Measurement Technology Conference*. 2008.

[238] Pintelon, Peeters, and Guillaume. "Multivariate Continuous-Time Operational Modal Analysis in the Presence of Harmonic Disturbances". In: *15th IFAC Symposium on System Identification*. 2009.

[239] Poirion. "Response of an Airplane to Non-Gaussian Atmospheric Turbulence". In: *Journal of Aircraft* (1991).

[240] Poncelet et al. "Output-Only Modal Analysis Using Blind Source Separation Techniques". In: *Mechanical Systems and Signal Processing* (2007).

[241] Prasad et al. "Real Time Implementation Aspects of a Rotorcraft Turbulence Simulation Method". In: *American Helicopter Society Annual Forum*. 1993.

[242] Prasad et al. *Rotorcraft Turbulence Modeling and Simulation*. Tech. rep. Georgia Institute of Technology, 1994.

[243] Prelewicz. "Response of Linear Periodically Time Varying Systems to Random Excitation". In: *AIAA Journal* (1972).

[244]   Proctor, Brunton, and Kutz. "Dynamic Mode Decomposition with Control". In: *SIAM Journal on Applied Dynamical Systems* (2016).

[245]   Prowell. "An Experimental and Numerical Study of Wind Turbine Seismic Behavior". PhD thesis. University of California, San Diego, 2011.

[246]   Prowell et al. "In-situ Ambient Vibration Study of a 900-kW Wind Turbine". In: *Journal of Earthquake Engineering* (2018).

[247]   Prussing and Lin. "A Closed-Form Analysis of Rotor Blade Flap-Lag Stability in Hover and Low-Speed Forward Flight in Turbulent Flow". In: *Journal of the American Helicopter Society* (1983).

[248]   Prussing and Lin. "Rotor Blade Flap-Lag Stability in Turbulent Flows". In: *Journal of the American Helicopter Society* (1982).

[249]   Qin, Guo, and Zhu. "Sparse Component Analysis Using Time-Frequency Representations for Operational Modal Analysis". In: *Sensors* (2015).

[250]   Rainieri. "Perspectives of Second-Order Blind Identification for Operational Modal Analysis of Civil Structures". In: *Shock and Vibration* (2014).

[251]   Randall, Antoni, and Smith. "A Survey of the Application of the Ceptrum to Structural Modal Analysis". In: *Mechanical Systems and Signal Processing* (2019).

[252]   Rath and Fichter. "A Closer Look at the Impact of Helicopter Vibrations on Ride Quality". In: *American Helicopter Society Annual Forum*. 2017.

[253]   Reeves. *A Non-Gaussian Turbulence Simulation*. Tech. rep. Technical Report Air Force Flight Dynamics Laboratory, 1969.

[254]   Reichert. "Helicopter Vibration Control - A Survey". In: *European Rotorcraft Forum*. 1980.

[255]   Reveles et al. "Aeroelastic Simulation of the UH-60M Fuselage". In: *VFS Aeromechanics for Advanced Vertical Flight Technical Meeting*. 2020.

[256]   Reveles et al. "Comparison of Fully Coupled Aeroelastic Fuselage Simulations to UH-60A Airloads Program Data". In: *Vertical Flight Society Annual Forum*. 2020.

[257]   Rex and Hajek. "Influence of Atmospheric Turbulence on Helicopter Elastic Rotor Hub Vibrations". In: *VFS Aeromechanics for Advanced Vertical Flight Technical Meeting*. 2020.

[258]   Rex, Pflumm, and Hajek. "UH-60A Rotor and Coupled Rotor-Fuselage Simulation Framework Validation and Analysis". In: *European Rotorcraft Forum*. 2019.

[259]   Rex, Rinker, and Hajek. "Sensitivity Study of Helicopter Vibrations and Loads with Elastic Fuselage Coupling and Empennage Loads from Free Wake Analysis". In: *Vertical Flight Society Annual Forum*. 2020.

[260]   Reynders. "System Identification and Modal Analysis in Structural Mechanics". PhD thesis. Katholieke Universiteit Leuven, 2009.

[261]   Reynders. "System Identification Methods for (Operational) Modal Analysis - Review and Comparison". In: *Archives of Computational Methods in Engineering* (2012).

[262]   Reynders, Houbrechts, and De Roeck. "Fully Automated (Operational) Modal Analysis". In: *Mechanical Systems and Signal Processing* (2012).

[263] Reynders, Pintelon, and De Roeck. "Uncertainty Bounds on Modal Parameters Obtained From Stochastic Subspace Identification". In: *Mechanical Systems and Signal Processing* (2008).

[264] Reynders and De Roeck. "Reference-based Combined Deterministic-Stochastic Subspace Identification for Experimental and Operational Modal Analysis". In: *Mechanical Systems and Signal Processing* (2008).

[265] Reynders et al. "Uncertainty Quantification in Operational Modal Analysis with Stochastic Subspace Identification - Validation and Applications". In: *Mechanical Systems and Signal Processing* (2016).

[266] Riaz. "A Simulation Model of Atmospheric Turbulence For Rotorcraft Applications". PhD thesis. Georgia Institute of Technology, 1992.

[267] Riaz et al. "Atmospheric Turbulence Simulation for Rotorcraft Applications". In: *Journal of the American Helicopter Society* (1993).

[268] Rigo et al. "Numerical Evaluation of Gust Loads on Tiltrotor". In: *American Helicopter Society Annual Forum*. 2018.

[269] Rizo-Patron and Sirohi. "Operational Modal Analysis of a Helicopter Rotor Blade Using Digital Image Correlation". In: *Experimental Mechanics* (2017).

[270] Robinson. "Real-Time Simulation of Full-Field Atmospheric Turbulence for a Piloted Rotorcraft Simulator". MA thesis. Massachusetts Institute of Technology, 1994.

[271] Roy and Girard. "Impact of Residual Modes in Structural Dynamics". In: *European Conference on Space Structures*. 2005.

[272] Rybicki. "The Sikorsky Elastomeric Rotor". In: *Journal of the American Helicopter Society* (1981).

[273] Sadhu, Narasimhan, and Antoni. "A Review of Output-Only Structural Mode Identification Literature Employing Blind Source Separation Methods". In: *Mechanical Systems and Signal Processing* (2017).

[274] Schwochow and Jelicic. "Automatic Operational Modal Analysis for Aeroelastic Applications". In: *International Operational Modal Analysis Conference*. 2015.

[275] Scionti et al. "Tools to Improve Detection of Structural Changes From In-Flight Flutter Data". In: *International Conference on Recent Advances in Structural Dynamics*. 2013.

[276] Seher-Weiss. "ACT-FHS System Identification Including Rotor and Engine Dynamics". In: *Journal of the American Helicopter Society* (2019).

[277] Seher-Weiss and von Gruenhagen. "Development of EC 135 Turbulence Models via System Identification". In: *European Rotorcraft Forum*. 2009.

[278] Shi, Jiang, and Yin. "Generalized Complexity Pursuit". In: *Fourth International Conference on Natural Computation*. 2008.

[279] Shinoda, Yeo, and Norman. "Rotor Performance of a UH-60 Rotor System in the NASA Ames 80- by 120-Foot Wind Tunnel". In: *American Helicopter Society Annual Forum*. 2002.

[280] Shinozuka. "Simulation of Multivariate and Multi-Dimensional Random Processes". In: *The Journal of the Acoustical Society of America* (1971).

[281] Shinozuka and Jan. "Digital Simulation of Random Processes and its Applications". In: *Journal of Sound and Vibration* (1972).

[282] Shinozuka and Yang. "Peak Structural Response to Non-Stationary Random Excitations". In: *Journal of Sound and Vibration* (1971).

[283] Siddigi. "Identification of the Harmonic Transfer Function of a Helicopter Rotor". MA thesis. Massachesetts Institute of Technology, 1999.

[284] Sidle, Sridharan, and Chopra. "Coupled Vibration Prediction of Rotor-Airframe–Drivetrain-Engine Dynamics". In: *American Helicopter Society Annual Forum*. 2018.

[285] Sitaraman. "CFD Based Unsteady Aerodynamic Modeling for Rotor Aeroelastic Analysis". PhD thesis. University of Maryland, 2003.

[286] Sitaraman and Roget. "Prediction of Helicopter Maneuver Loads Using a Fluid-Structure Analysis". In: *Journal of Aircraft* (2009).

[287] Skjoldan. "Aeroelastic Modal Dynamics of Wind Turbines Including Anisotropic Effects". PhD thesis. Danmarks Tekniske Universitet, 2011.

[288] Skjoldan and Bauchau. "Determination of Modal Parameters in Complex Nonlinear Systems". In: *Journal of Computational and Nonlinear Dynamics* (2010).

[289] Skjoldan and Hansen. "On the Similarity of the Coleman and Lyapunov-Floquet Transformations for Modal Analysis of Bladed Rotor Structures". In: *Journal of Sound and Vibration* (2009).

[290] Solovyev et al. "Mathematical Modeling and Experimental Investigations of a Main Rotor made from Layered Composite Materials". In: *Mechanics of Composite Materials* (2020).

[291] Studebaker. "A Survey of Hub Vibration for the UH-60A Airloads Research Aircraft". In: *American Helicopter Society Aeromechanics Specialists Conference*. 1994.

[292] Stull. *An Introduction to Boundary Layer Meteorology*. Kluwer Academic Publishers, 1988.

[293] Süelözgen and Wüstenhagen. "Operational Modal Analysis For Simulated Flight Flutter Test of an Unconventional Aircraft". In: *International Forum of Aeroelasticity and Structural Dynamics*. 2019.

[294] Sutton and Bennett. "Aeroelastic/Aerodynamic Optimization of High Speed Helicopter/Compound Rotor". In: *NASA Langley Research Center Recent Experiences in Multidisciplinary Analysis and Optimization*. 1984.

[295] Talbot et al. *A Mathematical Model of a Single Main Rotor Helicopter for Piloted Simulation*. Tech. rep. NASA Technical Memorandum, 1982.

[296] Tcherniak, Chauhan, and Hansen. "Applicability Limits of Operational Modal Analysis to Operational Wind Turbines". In: *International Modal Analysis Conference*. 2010.

[297] Tcherniak et al. "Output-Only Modal Analysis on Operating Wind Turbines - Application to Simulated Data". In: *European Wind Energy Conference*. 2010.

[298] Tong et al. "AMUSE A New Blind Identification Algorithm". In: *IEEE International Symposium on Circuits and Systems* (1990).

[299] Uehara. "Estimation of Helicopter Rotor Loads from Blade Structural Response". PhD thesis. University of Texas at Austin, 2019.

[300] Uehara, Cameron, and Sirohi. "Deformation Measurement and Modal Identification of an Extremely Flexible Rotor Blade". In: *6th Asian-Australian Rotorcraft Forum/Heli Japan*. 2017.

[301] Uehara, Eitner, and Sirohi. "Automated Operational Modal Identification of a Rotor Blade". In: *AHS International 74th Annual Forum and Technology Display*. 2018.

[302] Vandiver et al. "A Mathematical Basis for the Random Decrement Vibration Signature Analysis Technique". In: *Journal of Mechanical Design* (1982).

[303] Veers. *Three-Dimensional Wind Simulation*. Tech. rep. Sandia Report, 1988.

[304] Verboven et al. "Autonomous Structural Health Monitoring - Part I: Modal Parameter Estimation and Tracking". In: *Mechnical Systems and Signal Processing* (2002).

[305] Wachspress, Quackenbush, and Boschitsch. "First-Principles Free-Vortex Wake Analysis for Helicopters and Tiltrotors". In: *American Helicopter Society Annual Forum*. 2003.

[306] Wang and Frost. *Atmospheric Turbulence Simulation Techniques With Application to Flight Analysis*. Tech. rep. NASA Contractor Report, 1980.

[307] Wax and Sheinvald. "A Least-Squares Approach to Joint Diagonalization". In: *IEEE Signal Processing Letters* (1997).

[308] Wijker. *Mechanical Vibrations in Spacecraft Design*. Springer, 2004.

[309] Williams, Kevrekidis, and Rowley. "A Data-Driven Approximation of the Koopman Operator - Extending Dynamic Mode Decomposition". In: *Journal of Nonlinear Science* (2015).

[310] Wilson. *Turbulence Models and the Synthesis of Random Fields for Acoustic Wave Propagation Calculations*. Tech. rep. Army Research Laboratory Technical Report, 1998.

[311] Yang and Nagarajaiah. "Blind Modal Identification of Output-Only Structures in Time-Domain Based on Complexity Pursuit". In: *Earthquake Engineering and Structural Dynamics* (2013).

[312] Yang and Nagarajaiah. "Time-Frequency Blind Source Separation Using Independent Component Analysis for Output-Only Modal Identification of Highly Damped Structures". In: *Journal of Structural Engineering* (2013).

[313] Yeager. *Implementation and Testing of Turbulence Models for the F18-HARV Simulation*. Tech. rep. NASA Contractor Report, 1998.

[314] Yeo, Bousman, and Johnson. "Performance Analysis of a Utility Helicopter with Standard and Advanced Rotors". In: *Journal of the American Helicopter Society* (2004).

[315] Yeo, Romander, and Norman. "Investigation of Rotor Performance and Loads of a UH-60A Individual Blade Control System". In: *American Helicopter Society Annual Forum*. 2010.

[316] Yeo and Shinoda. "Investigation of Rotor Loads and Vibration at Transition Speed". In: *American Helicopter Society Annual Forum*. 2002.

[317]   Yu, Yang, and Bai. "Estimation of Modal Parameters Using the Sparse Component Analysis Based Underdetermined Blind Source Separation". In: *Mechanical Systems and Signal Processing* (2014).

[318]   Yun and Bauchau. "Improving Modal Parameter Predictions for Joint Airframe Panels. Part I- Experiments". In: *Journal of the American Helicopter Society* (1997).

[319]   Zhang, Brincker, and Anderson. "An Overview of Operational Modal Analysis - Major Development and Issues". In: *Proceedings of the 1st International Operational Modal Ananlysis Conference*. 2005.

[320]   Zhang, Tang, and Tang. "An Improved Stochastic Subspace Identification for Operational Modal Analysis". In: *Measurement* (2012).

[321]   Zhou and Chelidze. "Blind Source Separation Based Vibration Mode Identification". In: *Mechanical Systems and Signal Processing* (2007).